Università degli Studi Roma Tre
Dipartimento di Matematica e Fisica
Scuola di Dottorato

The Mu2e calorimeter: R&D and calibration strategies

Relatori
Dott. Stefano Miscetti
Dott. Gianantonio Pezzullo

Candidata
Raffaella Donghia

XXXI ciclo di dottorato

Introduction

The Mu2e experiment at Fermi National Laboratory will search for Charged Lepton Flavor Violation (CLFV), looking for the conversion of a muon into an electron in the field of an aluminum nucleus. About 6×10^{17} muons, provided by a dedicated muon beam line, will be stopped in the aluminum target in three years of running. The experiment single event sensitivity will be 3×10^{-17} [1]. This process is forbidden in the Standard Model [2]. When considering diagrams with neutrinos oscillation, the process is allowed but the expected rate is negligible (BR $\sim 10^{-52}$). Therefore observation of this process would be a clear evidence of New Physics beyond the Standard Model. Several extensions of the Standard Model predict a rate in the range of $10^{-14} - 10^{-18}$ [3]. The current best experimental limit, set by the SINDRUM II experiment, is 7×10^{-13} at 90% Confidence Level. The Mu2e experiment plans to improve this limit by four orders of magnitude to test many of the possible Standard Model extensions. To reach this ambitious goal, the Mu2e experiment will use an intense pulsed muon beam and a detector system composed of a very precise straw tube tracker and a calorimeter made of pure CsI crystals. The calorimeter plays a crucial role in the Mu2e measurement, providing particle identification capabilities that are necessary for rejecting two of the most dangerous background sources that can mimic an electron from muon conversion: cosmic muons and anti-protons induced background. The calorimeter information allows also to improve the tracking performances and it is needed to confirm the signal measurement. Moreover, it provides a fast standalone trigger for the experiment.

The calorimeter is composed by 1348 undoped CsI crystals arranged in two annular disks with a read out system constituted by two UV-extended Silicon Photomultipliers per crystal. The calorimeter performance has been determined by exposing a 51-channels calorimeter prototype to an electron beam with energy from 80 to 140 MeV, at the Beam Test Facility of Laboratori Nazionali di Frascati (INFN, Italy). Both energy and time resolution have been measured. An energy resolution of $\sigma_E/E \sim 5.4\%$ and a timing resolution $\sigma_T < 200$ ps have been obtained at 100 MeV.

The INFN group has leaded the R&D phase and is now in charge for the production phase, where all calorimeter components will be tested and assembled. Albeit all individual calorimeter components will be completely characterised before calorimeter assembly, an equalization and calibration of all channels will be carried out during the commissioning and data taking periods. Two dedicated calibration systems are already included in the calorimeter design: 1) a fluorinert-based liquid radioactive source emitting 6 MeV photons will circulate in pipes mounted on the calorimeter front face to irradiate uniformly all crystals and providing an absolute calibration and energy scale; 2) a laser system will send light to each crystal for calibration of the SiPMs' gain, time alignment of the calorimeter time offsets and resolution monitoring purposes. Other "in-situ" calibration sources have been investigated for their possible usage during experiment running:

- cosmic ray muons offer a constant energy deposition (about 21 MeV per crystal) in the calorimeter cells that can be exploited for response equalization. Moreover, cosmic ray traces could be used for timing alignment;
- electrons from muon decay in orbit can provide a uniform calibration in the high energy range (above 50 MeV) with an accuracy lower than 1%, during dedicated calibration runs at low beam intensity and reduced magnetic field.

Contents

Chapter 1

Intoduction to Charged Lepton Flavor Violation searches

1.1 Theoretical introduction

The Standard Model (SM) is currently the best theoretical model describing our particle physics understanding. It is a quantum field theory that describes matter's basic constituents and the interactions among them [2]. Matter's building blocks consist of fermions (leptons and quarks). The quarks and leptons are both organized in three flavor generations, where transitions from one generation to another have been observed both in the quark sector and in the neutral lepton sector, but not for charged leptons.

This model was developed in the early 1970s and since then it has explained almost all the experimental results [4], including the existence of the Higgs boson (discovered in the LHC at CERN in 2012 [5][6]). However, even though it is currently the best description of the subatomic world and no obvious contradictions have been found so far, the SM incorporates only three of the fundamental forces, excluding gravity. Indeed, the it is not a complete theory of the universe. It lacks an explanation for: the flavor structure, neutrino mass, dark matter or dark energy and it does not provide a mechanism which could explain the observed baryon asymmetry in the Universe. Nowadays, the SM is regarded as a low-energy approximation

of a more general theory. It is also clear that there must be physics Beyond the Standard Model (BSM), waiting to be discovered.

1.1.1 Charged Lepton Flavor Violation causes

The gauge symmetry of the SM is a $SU(3)_C \times SU(2)_L \times U(1)_Y$ gauge group, where C indicates color charge, L indicates that only left-handed fields participate in the weak interaction and Y is the hypercharge. The $SU(2)_L \times U(1)_Y$ electroweak part of the gauge group breaks down to the $U(1)_{EM}$ of electromagnetism via the Higgs mechanism.

In the SM, the lepton flavour conservation is accidental, not related to the gauge structure of the theory, but arising from its particle content, in particular from the absence of right-handed neutrinos. It is an automatic consequence of the gauge invariance and the renormalizability of the SM Lagrangian.

However, the discovery of neutrino oscillations and the measurements of the neutrino mixing parameters performed during the last decades demonstrated the lepton family numbers are not conserved [7][8]. It calls for an extension of the SM to include neutrino mass terms. This has no practical effect in inducing transitions among charged leptons within the SM framework. In principle, the neutrino mixing matrix, U_{PMNS} (usually called Pontecovo-Maki-Nagasaki-Sakata) [9], can give rise to CLFV as well. U_{PMNS} is the matrix that diagonalises the neutrino mass matrix in the basis of diagonal charged lepton masses, thus connecting neutrino flavour and mass eigenstates:

$$\nu_\alpha = \sum_{k=1,3} U_{\alpha k} \nu_k \quad , \qquad \alpha = e, \mu, \tau \quad . \tag{1.1}$$

This violation can only occur through loop diagrams involving neutrinos and W bosons. For example, a Feynmann diagram contributing to the $\mu \to e\gamma$ decay is shown in Figure 1.1. In this process, the incoming muon decays and emits a muon neutrino and a W boson, which gets reabsorbed after the neutrino oscillates into an electron neutrino, creating an electron. Since the neutrino is oscillating in a virtual loop (much shorter length scale than the distance that neutrinos have

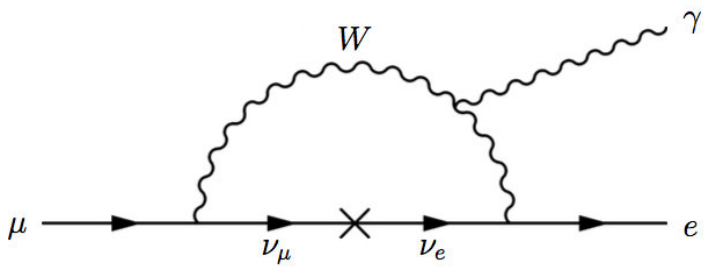

Figure 1.1: Feynmann diagram for the charged lepton flavor violating process $\mu \to e\gamma$ in the Standard Model.

actually been observed oscillating over), this process is massively suppressed by a factor of $m^2_{\nu_i}/M^2_W$ [10], as shown in eq. 1.2, where the branching ratio (BR) of this process is given:

$$BR(\mu \to e\gamma) = \left| \frac{3\alpha}{32\pi} \sum_i U^*_{\mu i} U_{ei} \frac{m^2_{\nu i}}{M^2_W} \right| < 10^{-54} \quad [11], \tag{1.2}$$

where α is the electromagnetic coupling constant, U is the PMNS neutrino mixing matrix and m_{ν_i} and M_W are the masses of the neutrinos and W boson respectively.

On the other hand, many New Physics (NP) models predict significant enhancements to CLFV rates. Indeed, the minute BR of eq. 1.2 makes searches for CLFV processes very appealing, since it means that there is no SM background to take account of and so any observation of CLFV would be a clear evidence of physics BSM.

LFV searches, in process involving charged leptons, started decades ago, both in dedicated and general purpose experiments, but there is still no evidence of such violation.

1.2 Lepton flavor violating processes in muon sector

In general, CLFV can be studied via a large variety of processes:

- muon decays, such as $\mu^+ \to e^+\gamma$, $\mu^\pm \to e^\pm e^- e^+$ and muon conversion;

- tau decays, such as $\tau^+ \to e^+\gamma$, $\tau^\pm \to e^\pm e^- e^+$, ecc;
- meson decays: $\pi^0 \to \mu e$, $K_L^0 \to \mu e$, $K^+ \to \pi^+ \mu^+ e^-$, ecc;
- Z^0 decays, such as $Z^0 \to \mu e$, ecc.

Table 1.1 shows the current upper limits on the branching ratios of various CLFV processes. The muon processes have been intensely studied in the CLFV for several reasons:

- low energy muon beams can be produced at high-intensity proton accelerator facilities;

Process	Upper limit	references
$\mu^+ \to e^+\gamma$	$< 5.7 \times 10^{-13}$	[12]
$\mu^\pm \to e^\pm e^+ e^-$	$< 1.0 \times 10^{-12}$	[14]
$\mu^- Ti \to e^- Ti$	$< 1.7 \times 10^{-12}$	[14]
$\mu^- Au \to e^- Au$	$< 7 \times 10^{-13}$	[15]
$\mu^+ e^- \to \mu^- e^+$	$< 3.0 \times 10^{-13}$	[16]
$\tau \to e\gamma$	$< 3.3 \times 10^{-8}$	[16]
$\tau^- \to \mu\gamma$	$< 4.4 \times 10^{-8}$	[16]
$\tau^- \to e^- e^+ e^-$	$< 2.7 \times 10^{-8}$	[17]
$\tau^- \to \mu^- \mu + \mu^-$	$< 2.1 \times 10^{-8}$	[17]
$\tau^- \to e^- \mu^+ \mu^-$	$< 2.7 \times 10^{-8}$	[17]
$\tau^- \to \mu^- e^+ e^-$	$< 1.8 \times 10^{-8}$	[17]
$\tau^- \to e^+ \mu^- \mu^-$	$< 1.7 \times 10^{-8}$	[17]
$\tau^- \to \mu^+ e^- e^-$	$< 1.5 \times 10^{-8}$	[17]
$\pi^0 \to \mu e$	$< 8.6 \times 10^{-9}$	[18]
$K_L^0 \to \mu e$	$< 4.7 \times 10^{-12}$	[20]
$K^+ \to \pi^+ \mu^+ e^-$	$< 2.1 \times 10^{-10}$	[21]
$K_L^0 \to \pi^0 \mu^+ e^-$	$< 4.4 \times 10^{-10}$	[22]
$Z^0 \to \mu e$	$< 1.7 \times 10^{-6}$	[22]
$Z^0 \to \tau e$	$< 9.8 \times 10^{-6}$	[23]
$Z^0 \to \tau \mu$	$< 1.2 \times 10^{-6}$	[23]

Table 1.1: Sample of various CLFV processes. Data from current experimental bounds.

- final state of processes in the muon sector can be precisely measured.

Search for CLFV with muons has been pursued looking for muon decays ($\mu^+ \to e^+\gamma$, $\mu^\pm \to e^\pm e^- e^+$) and muon coherent conversion ($\mu^- N \to e^- N$).

Even if the SM does not predict these processes, within measurable BRs, and because there are so many different NP theoretical models, it is possible to explicitly insert a model-independent CLFV lagrangian in order to study process sensitivities. There are two possible types of interactions between leptons and quarks which contribute to the effective Lagrangian for muon's CLFV processes of $|\Delta L_i| = 1$ (such as the previous cited processes): photonic or loop interaction and four-fermion or contact interaction (Fig. 1.2).

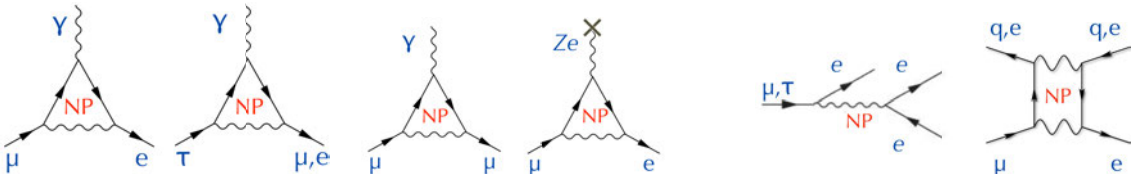

Figure 1.2: Feynmann diagrams for the muon to electron conversion process in a nucleus field. Left: photonic interaction. Right: contact four-fermion interaction.

For the photonic contribution, there is a defined relation between the muon conversion process and $\mu \to e\gamma$ decay. Supposing the photonic contribution is dominant, the BR of the muon conversion process is expected to be smaller than the other process by a factor of a few hundreds due to electromagnetic interaction of a virtual photon. This implies that the search for muon conversion at the level of 10^{-16} is comparable to that for $\mu \to e\gamma$ at the level of 10^{-14}.

If the contact term dominates, the $\mu \to e\gamma$ decay would be small whereas the muon to electron conversion could be sufficiently large to be observed. If a $\mu \to e\gamma$ signal is found, also a conversion signal should be found. The ratio of the branching ratios between $\mu \to e\gamma$ decay and muon to electron conversion carries vital information on the intrinsic physics process. If no $\mu \to e\gamma$ signal is found, there will still be an opportunity to find a $\mu - e$ conversion signal, because of the potential existence of non-photonic contributions.

The effective Lagrangian that includes both the photonic and non-photonic con-

tributions is given by 1.3 [24]:

$$L_{CLFV} = \frac{m_\mu}{(k+1)\Lambda^2}\bar{\mu}_R\sigma_{\mu\nu}e_L F^{\mu\nu} + \frac{k}{(k+1)\Lambda^2}\bar{\mu}_L\gamma_\mu e_L(\bar{u}_L\gamma^\mu u_L + \bar{d}_L\gamma^\mu d_L) \quad , \quad (1.3)$$

where m_μ is the muon mass, $F_{\mu\nu}$ is the electromagnetic field tensor, R and L represent the chirality of the fermion fields. The parameters Λ and k represent the energy scale of new physics and the ratio between the contact four-fermion (non-photonic) and loop-type (photonic) interactions respectively. For $k \ll 1$, the photonic interaction dominates and for $k \gg 1$, the contact interaction dominates.

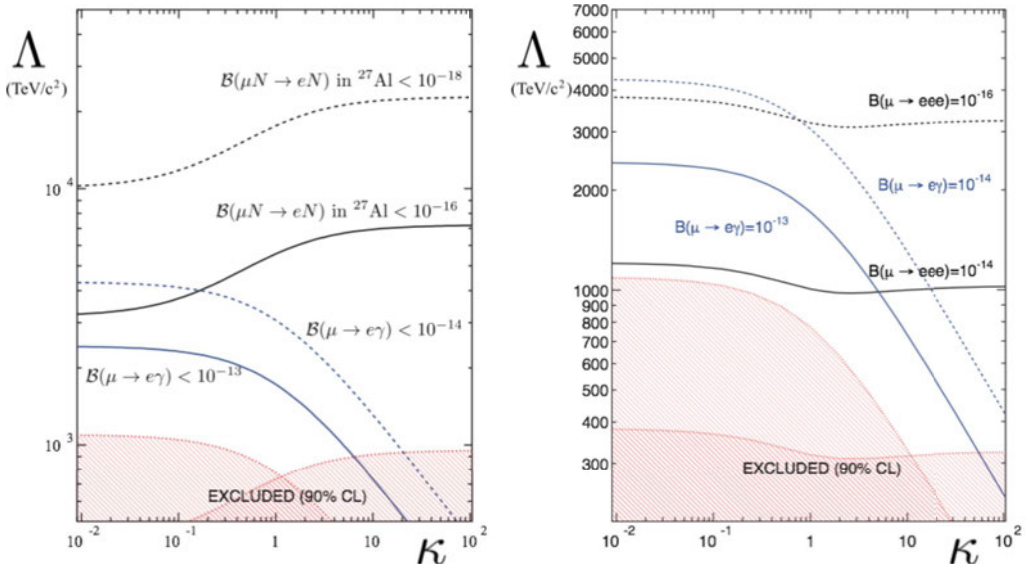

Figure 1.3: The current and future limits expected of $\mu \to e\gamma$ and $\mu - e$ conversion (left) and $\mu \to 3e$ (rigth) in terms of the two parameters Λ and k, where the first one is the energy scale of the new interaction and the second is the ratio between the four-fermion and loop interactions [24].

Figure 1.3 shows the relation between the BRs of $\mu \to e\gamma$ and $\mu - e$ conversion process as a function of the parameter k. The parameter space for muon CLFV that has been excluded by previous experiments and the region that future experiments will be able to probe are also reported. The upper limits expected at 90% C.L. for the future experiments MEG upgrade, Mu2e and Mu2e at PIP II (Proton Improvement Plan-II [25]) are also shown.

It is also important to note that CLFV searches can probe energy scales of $\mathcal{O}(10^4)$ TeV, which are much higher than what can currently, or in the next future, be directly probed at colliders.

A second thing to note from Figure 1.3 is that an observation in a single channel would not give any indication to the form of the new interaction. For example, if a signal is seen in muon conversion alone with a branching ratio of 10^{-16} then the value of k would not be known until a signal is observed or excluded in $\mu \to e\gamma$ at a sensitivity greater than 10^{-14}. Obviously, an observation of CLFV would lend some weight to these theories. However, a non-observation of CLFV would also restrict the large parameter space of these theories and possibly exclude most of them.

1.2.1 New physics models

The discovery of CLFV events, or just a better constraint on the BR, could give strong indications on which NP model is preferred.

SUSY models have recently received much attention. Other examples include extra-dimension models, little Higgs models, models with new gauge Z' bosons, models with new heavy leptons, leptoquark models, etc[26]. Some NP examples and their CLFV effects are reported in the following.

SO(10) SUSY Grand Unified Model In the Supersymmetric version of the SM (SUSY), the origin of CLFV could be interactions at a very high energy scale, such as the GUT scale or the mass scale of a heavy right-handed Majorana neutrino that appears in the seesaw mechanism [27].

SUSY can lead to sensibly large rates of CLFV process. It is possible to relate the $\mu^- N \to e^- N$ rate in titanium to that of SO(10) SUSY GUT breaking parameters [28], taking into account the measured value of the neutrino mixing angle θ_{13} value and Higgs mass with different hypothesis of the neutrino Yukawa couplings (Fig. 1.4). In fact, SUSY models predicts $\mu^- N \to e^- N$ conversion through a penguin diagram, as shown in Figure 1.5, where the photon then interacts with nuclei quarks.

Higgs-induced lepton flavor violation Some NP models include LFV processes induced by Higgs exchange. Compared to $\mu \to e\gamma$ and $\mu \to 3e$, muon conversion is more sensitive because of the smallness of the Yukawa couplings in the first two cases [33]. The conversion can be induced with a tree-contribution involving light quark or with a loop-induced effect of heavy quarks to the gluons

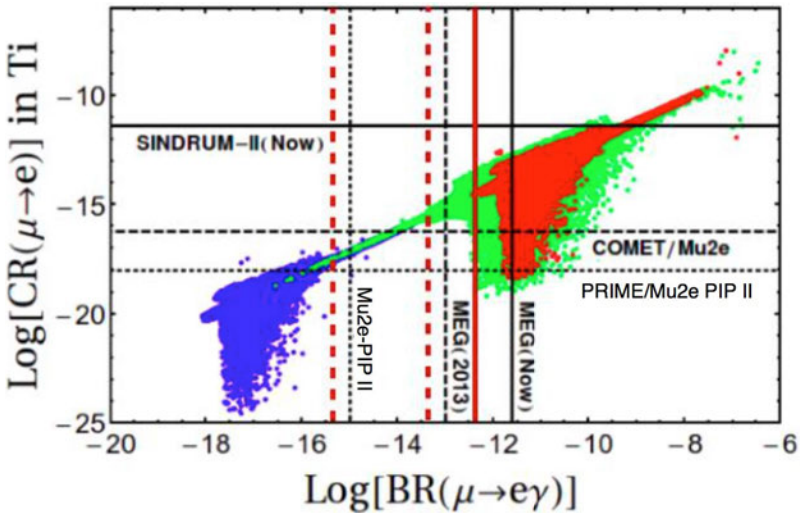

Figure 1.4: Muon Conversion Rate CR($\mu \to e$) in titanium versus BR($\mu \to e\gamma$) for the PMNS-like neutrino Yukawa coupling in mSUGRA (red), Non Universal Higgs Mass (green) and for CKM-like neutrino Yukawa coupling (blue) for tan$\beta = 10$. Red vertical lines represent the present limit given by MEG [30], the expected result for the MEG upgrade (dashed) [31] and the expected result for a conceptual new $\mu \to e\gamma$ experiment [31]. Horizontal black lines, instead, represent limit on muon-to-electon conversion rate from SINDRUM II [15] result and Mu2e/COMET planned results. Project X, now PIP-II, is related to an improvement of 10 times the beam intensity, currently under study at Fermilab. Adapted from [28].

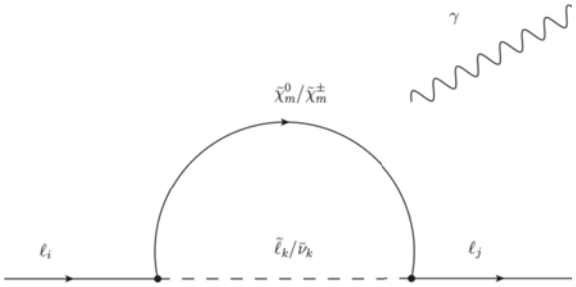

Figure 1.5: Supersymmetric contribution to $l_i \to l_j\gamma$, $l_i - N \to l_j N$. It is understood that the photon attaches to the fermion or the scalar in the loop, depending on which field is charged.

(Fig. 1.6, right). The muon conversion in nucleus is also the most sensitive channel for the study of Yukawa couplings $|Y_{\mu e}|$ and $|Y_{e\mu}|$ (Fig. 1.6, left).

Littlest Higgs model with T-parity In the Littlest Higgs model with T-parity (LHT), the Higgs boson is considered an exact Goldstone boson under several symmetries [34]. Only if the symmetries are all broken (collective symmetry breaking, CSB), the Higgs boson picks up a contribution to its mass.

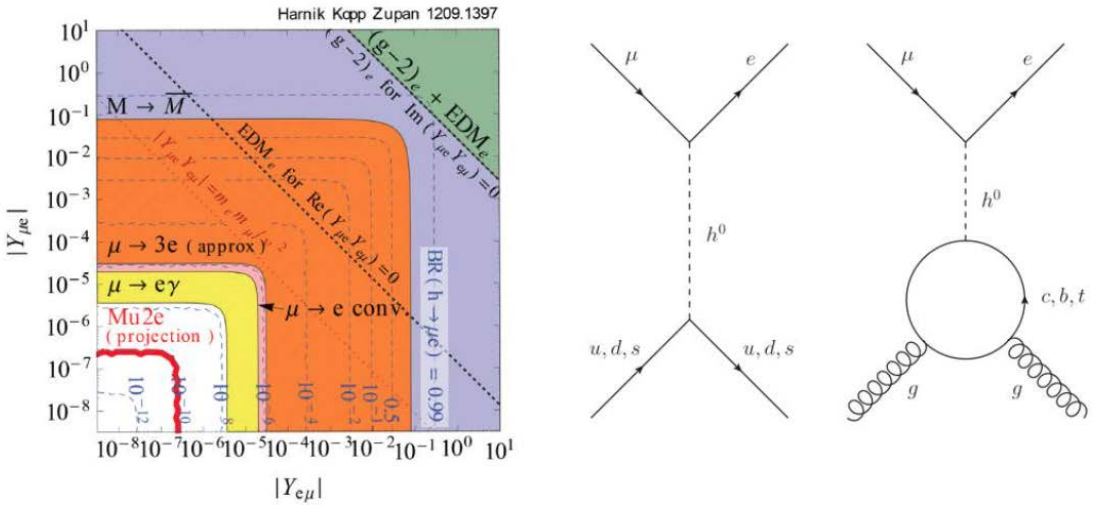

Figure 1.6: Left: constraints on the flavor-violating Yukawa couplings $|Y_{\mu e}|$ and $|Y_{e\mu}|$ for a 125 GeV Higgs boson [33]. Thin blue dashed lines are contours of constant BR for $h \to \mu e$, while the thick red line is the projected Mu2e limit. Constraints from $\mu \to e\gamma$ process are not updated to the latest MEG result [30]. Right: Higgs-induced LFV for a muon conversion can involve light quarks with a tree diagram (on left) or gluons with a loop of heavy quarks (on right).

In order to avoid fine tuning from electroweak precision data, a discrete symmetry, analogous to SUSY R-parity and called T-parity, is introduced. The scanning of the parameters of this model provides measurable BRs both for $\mu \to e\gamma$ and for $\mu N \to eN$ (Fig. 1.7, left) [35].

The $\mu - e$ conversion sensitivity for this process is extremely good. Indeed, for most of the parameter space, if observed by MEG upgrade, the $\mu - e$ conversion will observe it with a much larger statistics. In case of no observation, this model will be excluded.

Heavy neutrinos As previously stated, neutrino oscillation gives the first proof of LFV interactions. However, rates for CLFV processes are not immediately related to neutrino masses, because they strongly depend on the undergoing mechanism. The presence of new heavy neutrino mass states [36], different from mass eigenstates ν_1, ν_2, ν_3, is related to a muon conversion process through the neutrino oscillation in Feynman loop (Fig. 1.5).

Scalar Leptoquark model The presence of scalar leptoquars at TeV scale could modify CLFV conversion rate processes through a new coupling λ [37], without

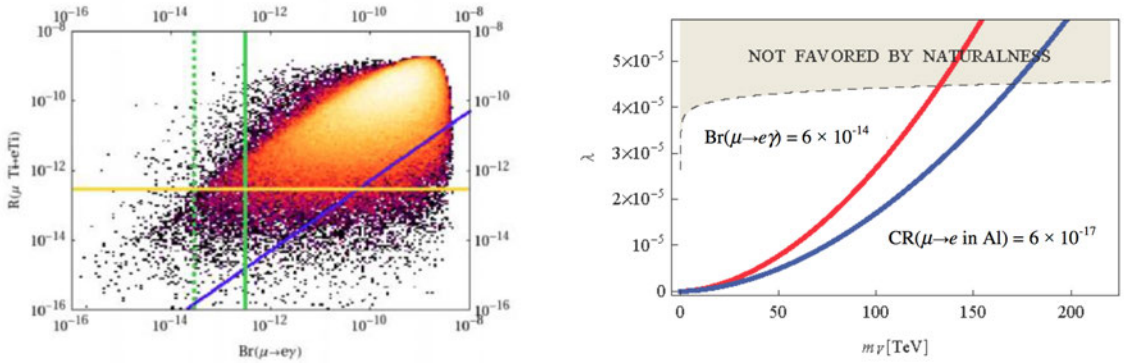

Figure 1.7: Left: Correlation between $\mu \to e\gamma$ and $\mu - e$ conversion rates in Ti obtained from a general scan over the LHT parameters. The blue line represents the MSSM dipole contribution, the green lines are the present (solid) and expected (dashed) upper limits by the MEG upgrade and the yellow solid line is the SINDRUM II upper limit. The Mu2e experiment would cover all the parameters of this scan. Adapted from [35]. Right: value of the coupling constant λ from [37] as a function of the scalar leptoquark mass. The blu line represents the limit for the muon conversion rate in Al and the red one the limit for $\mu \to e\gamma$ process. The shaded area corresponds to values which do not satisfy the naturalness criterion as defined in [37].

violating all the other constraints from quark flavor physics (Fig. 1.7, right). In this case, the mass and λ coverage of $\mu - e$ conversion is much higher than in MEG upgrade results. With Mu2e the sensitivity will be even larger.

Left-Right Symmetric Models Left-Right symmetric models are extensions of the SM useful to restore parity at short distances. A recent study [38] predicts the CLFV rates assuming a new mass breaking scale at around 5 TeV. From the correlation between the BR for the MEG upgrade and BR of muon conversion from Mu2e, it is possible to cover the full phase space of this theory: the observation of $\mu \to e\gamma$ with a branching ratio of 10^{-13} would imply a $\mu - e$ conversion rate around of 10^{-14} and then several hundreds of events in the Mu2e experiment (Fig. 1.8).

1.3 Experimental searches

The first CLFV searches was made by Hincks and Pontecorvo in 1947 in the muon sector, with the first search in $\mu \to e\gamma$ [29]. They stopped Cosmic Ray muons in a

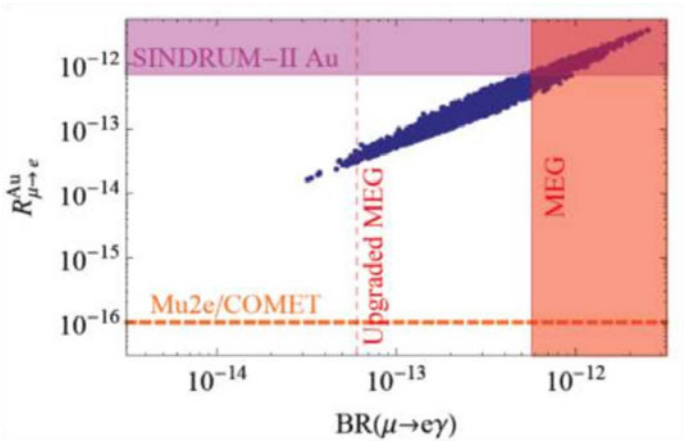

Figure 1.8: Expected BR and $BR_{\mu e}$ for Left-Right symmetric models for the MEG upgrade and the muon conversion experiments [38].

lead absorber and measured the coincidence between signals from two Geiger-Muller counters: they gave as a limit the inverse of the number of observed muons, having seen no such coincidence.

Soon afterwards, the search for the neutrinoless muon to electron conversion process in a nucleus field, $\mu\, N(A,Z) \rightarrow e\, N(A,Z)$, where $N(A,Z)$ is a nucleus capturing the muon, was also carried out. Such searches were significantly improved when muons became artificially produced at accelerators, stopping pion beams first (until the 1970s) and starting directly with muon beams afterwards.

The history of the limit on the probability of CLFV processes involving muons is shown in Figure 1.9. The sensitivity on the CLFV search has been increased by many order of magnitude over the years and in the next decade new limits will emerge from several experiments under construction or upgrade.

1.3.1 $\mu^+ \rightarrow e^+\gamma$

The $\mu^+ \rightarrow e^+\gamma$ process is a two-body decay, so the positron and the photon are emitted back to back in the rest frame of the decaying muon. Neglecting the tiny positron mass, each product carries an energy equal to half of the muon mass ($E_e = E_\gamma = 52.8$ MeV). Variation in the expected energy spectrum can occur in case of muon decays in flight, where a boost needs to be taken into account for

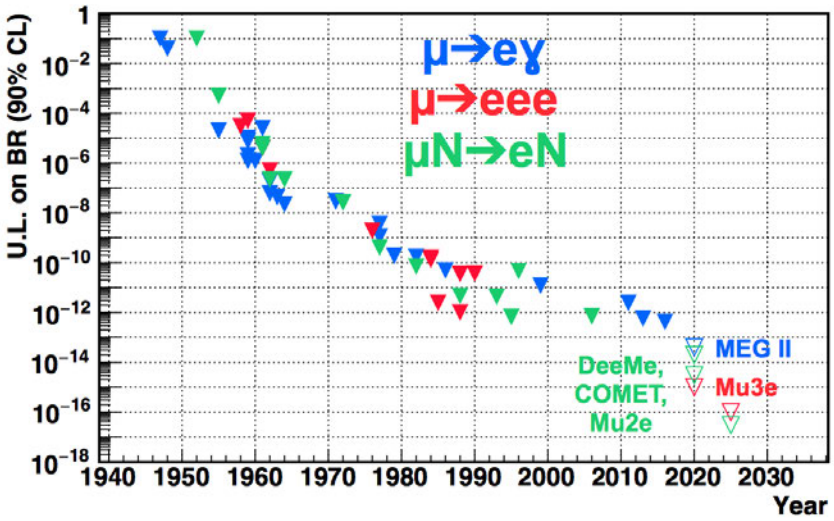

Figure 1.9: Limits on the branching ratio of the CLFV processes involving muon evaluated experimentally during last years and in future experiments (empty triangles).

re-evaluating both the energy spectra and the emission distributions. Boost related problems are avoided if low energy muons are stopped in a target.

The two background sources to this decay measurement are:

- irreducible background: Radiative Muon Decays (RMDs) $\mu^+ \to e^+\gamma\overline{\nu}_\mu\nu_e$ in which the neutrinos carry away little energy;
- accidental background: coincidence of a positron from the standard Michel decay of muons, $\mu \to e\nu\nu^-$, and a relatively high energy photon from radiative muon decay, $\mu \to e\nu\nu^-$, both carrying an energy close to half the muon mass energy, being time-coincident and moving in opposite directions within the detector resolutions.

The largest background is the second one and because it increases quadratically with the muon rate, a continuous muon beam with a low instantaneous rate is preferable for the $\mu^+ \to e^+\gamma$ search.

The current best limit on $\mu^+ \to e^+\gamma$ branching ratio is $\mathrm{B}(\mu^+ \to e^+\gamma) < 4.2\times 10^{-13}$ at 90% C.L. [30] [12], obtained by the MEG experiment in 2013. An upgrade of the detector system is underway for improving the detector performance. The goal is to improve sensitivity by another order of magnitude [32].

1.3.2 $\mu^{\pm} \to e^{\pm}e^{-}e^{+}$

The $\mu^{\pm} \to e^{\pm}e^{-}e^{+}$ signal event signature consists of two positrons and one electron emitted from a common vertex in space and time. Momentum conservation implies that the momentum vectors of the three particles have to lie in a plane. The maximum energy that can be carried away by a positron/electron is equal to half the muon mass energy. The phase space distribution of the decay particles depends on the new physics inducing CLFV and is therefore not known a priori.

The search for such kind of decay requires a detector system characterized by a large acceptance for low momenta electrons and positrons, and the consequent capability to tolerate the positron flux from the Michel muon decay. The main source of background is represented by accidental coincidences of positrons from the Michel decay with e^- e^+ pairs either from gamma ray conversions, or from Bhabha scattering of Michael positrons with atomic electrons. The current best upper limit on $\mu^{\pm} \to e^{\pm}e^{-}e^{+}$ branching ratio is BR($\mu^{\pm} \to e^{\pm}e^{-}e^{+}$) $< 1 \times 10^{-12}$, at 90% C.L. [39]. It was obtained by the SINDRUM experiment at PSI in 1988.

A new experiment, named Mu3e, has been proposed at PSI for lowering the sensitivity down to the level of about 10^{-16} [40].

1.3.3 Negative muon conversion

From an experimental point of view, the $\mu - e$ conversion is very attractive. Its signature signal corresponds to a monoenergetic electron to be separated by a fast falling spectrum background. Since it does not suffer from accidental background, as in the case of $\mu \to e\gamma$ and $\mu \to 3e$, its systematic is completely different from the other two decays. Indeed, this kind of search has the potential to improve the sensitivity in a linear way with the muon beam intensity.

The current best experimental limit in muon conversion process is settled by SINDRUM II experiment (PSI, 2006) [41]:

$$BR(\mu^- \,\mathrm{Au} \,\to e^- \,\mathrm{Au}) < 7 \times 10^{-13}\,, \;\; at \;\; 90\%\,\mathrm{C.L.} \;\; . \tag{1.4}$$

Each of these rare muon decay searches uses the same experimental method: large numbers of muons are brought to rest hitting a thin target and allowed to decay;

the stopped muons are in a well known initial kinematic state (all the energy is in its mass) so that, the decay kinematics is well defined.

1.3.3.1 Signature

The event signature of the coherent $\mu - e$ conversion in a muonic atom is a monoenergetic single electron emitted from the conversion with an energy of:

$$E_e = m_\mu - B_\mu - E^0_{rec} \approx m_\mu - B_\mu \ , \tag{1.5}$$

where m_μ is the muon mass (105.6 MeV), $B_\mu \simeq Z^2\alpha^2 m_\mu/2$ is the 1s muonic atom for a nucleus with atomic number Z, and E^0_{rec} is the nuclear-recoil energy. The nuclear-recoil energy is approximately $E^0_{rec} \approx (m_\mu - B_\mu)^2/(2M_N)$, where M_N is the atomic mass of the recoiling nucleus. Since B is different for various nuclei, the peak energy of the conversion electron signal changes. For instance, it varies from $E_e = 104.3$ MeV, for titanium, to $E_e = 94.9$ MeV for lead.

In the Mu2e experiment, muons are stopped in a thin Al target, where they can form muonic atoms. Then, the muons immediately fall into the 1s ground state, emitting photons. Finally, muons can interact coherently with the whole nucleus and, in the case of $\mu - e$ conversion, will transform into a single electron with a muon life-time of ∼864 ns and a well-defined energy, 104.96 MeV ($Z(Al) = 13$, $A(Al) = 27$).

The choice of Al results from a tradeoff between conflicting requirements. Muon conversion process scales as Z^5 (the interaction itself scales by Z^2 and then the probability of the wavefunctions overlapping scales as Z^3) and the BR is normalized to the rate of muon capture (proportional to Z^4). So that, the rate of the muon conversion process scales linearly in Z and so a high-Z material would be preferred. On the other hand, a long muonic atom lifetime is needed. In this way, experiments can collect data in a delayed time window, which means that low-Z materials would be preferred. Considering both previous statements, the search for the conversion process will be initially conducted using an aluminum target. Other materials will be investigated later, since the rate of a given CLFV operator has a Z-dependence and this study would allow to distinguish among all the NP models beyond the SM.

The Mu2e experiment has also the possibility to measure a similar process with $\Delta L = 2$ [42], where L is the lepton number:

$$\mu^- + N(Z, A) \rightarrow e^+ + N(Z-2, A) \quad , \tag{1.6}$$

which violates both total lepton number and lepton flavor numbers L_e and L_μ and it is related to the the neutrinoless double-β decay. Some theoretical models predict a rate of this reaction between 10^{-12} and 10^{-14}. The current best limit for the BR compared to ordinary muon capture is $< 4.9 \cdot 10^{-10}$ (at 90% CL), settled by TRIUMF experiment [43].

1.3.3.2 Conversion Rate and Sensitivity

The aim of the Mu2e experiment is to measure the conversion rate of the $\mu - e$ coherent conversion process in a nucleus field, $R_{\mu e}$, defined as the ratio of muon conversion events normalized to the number of muon captures rather than the total number of decays (eq. 1.7):

$$R_{\mu e} = \frac{N(\mu^- + N(Z, A) \rightarrow e^- + N(Z, A))}{\mu^- + N(Z, A) \rightarrow \nu_\mu + N(Z-1, A)} \quad . \tag{1.7}$$

If conversion signals will not be observed, the Mu2e experiment will set an upper limit on $R_{\mu e} < 8 \times 10^{-17}$ [1].

The Single Event Sensitivity (SES) is defined as that conversion rate for which the expected number of events will be one. It depends on the total number of stopped muons, on the fraction between stopped and captured muons (this depends on the nucleus) and by the efficiency of the experiment. The Mu2e experiment will reach a SES of $\sim\ 2.7 \times 10^{-17}$.

1.3.3.3 Physics background

To reach experimental sensitivity, it is mandatory to keep under control all the background events. There are many different processes which might obscure or mimic a conversion signal:

- intrinsic physics backgrounds arising from muons stopping in the target, where they are captured in an atomic excited state and promptly fall to the ground state. For aluminum, about 39% of the muons will decay in orbit (DIO), while the remaining 61% will be captured on the nucleus, producing electrons, photons and neutrons from the atomic cascade (Fig. 1.10). DIO events are the most important intrinsic physics background processes. A high resolution detector reduces the effect of these backgrounds since, neglecting resolution effects, there are no intrinsic physics backgrounds that have the same energy as the electron from conversion signal energy;

- beam-related prompt backgrounds arising from contamination of the muon beam, causing electrons with an energy close to the region of conversion electrons. The impact of these events are greatly reduced by using a bunched beam and recording only data in a delayed time window (Sec. 2.3), an example is the radiative pion capture process (RPC). However, these prompt backgrounds could still cause problems if there are protons leaking out of the main proton pulses and into the gaps between them. Therefore, a high level of "extinction", defined as the ratio of beam between pulses to the beam contained in a pulse, is required to achieve the design SES. This contamination is due to three main sources. Pions that have not decayed by the time reaches the stopping target can be captured immediately by the nucleus. Secondly, a small fraction of pions can decay directly in high energy electrons (despite having a small BR of 1.23×10^{-4}) and are important for the high intensity beam that will be used. Finally, muons can decay in flight and, if they have a momentum greater than 77 MeV, could produce an electron with an energy in the conversion signal region;

- beam-related delayed backgrounds are events from the main proton pulse, but which arrive late at the stopping target section, for example, antiprotons or neutrons. If produced on the primary target, antiprotons can be a background source due to their lower speed thus arriving in delay on the detector surface. These backgrounds can be reduced by having a sufficiently long muon beam line and using a time delayed acquisition window. Antiprotons are reduced to a negligible contribution by means of a specific absorber;

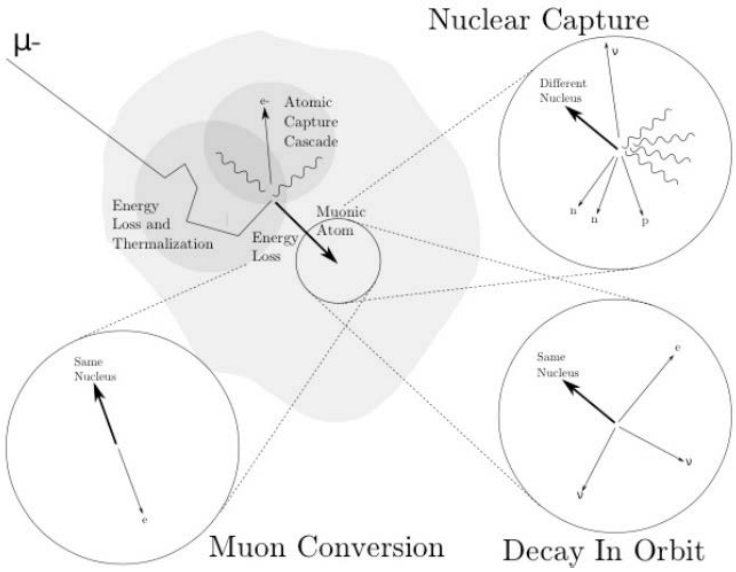

Figure 1.10: A muon stopped in the aluminum target can be captured in an atomic excited state and promptly fall to the ground state. For aluminum, in addition to the electron conversion process, $\sim 39\%$ of the muons will decay in orbit, while the remaining $\sim 61\%$ will be captured on the nucleus, producing electrons, photons and neutrons from the atomic cascade.

- other backgrounds are caused by electrons or muons initiated by cosmic rays, which can induce a background event in the detector but can be reduced and accounted for by using a cosmic ray veto.

The Mu2e rate of background activity scales linearly with beam intensity and the main sources are described in more detail in the following sections.

Decay in Orbit

In the SM, a muon bound in the atom can undergo a decay-in-orbit (DIO). In this case, the electron from decay can exchange momentum with the nucleus, because the muon is captured in the atomic orbit. This results in a small, but not null, probability to reach the same energy of a conversion electron.

In a free muon decay, the electron energy would not exceed 52.8 MeV, which occurs when the electron and two neutrinos are emitted in opposite directions. However, in the DIO case the nucleus can take away some of the electron momentum, which, being non-relativistic, means it can take momentum out of the system with-

out taking any significant energy. Therefore, electrons can essentially recoil off the nucleus and thus have more energy than the free muon decay limit. However, the electrons cannot take all of the energy (the two neutrinos will take some) and so the end point of the DIO spectrum is slightly lower than the energy of the conversion signal.

The DIO electron energy spectrum has been calculated by Czarnecki et al. [44] and is shown in Figure 1.11 .The nucleus recoil results then in a small tail after 52.8 MeV (going as $1/m_\mu^5$) and appears to vanish at 60 MeV. However, looking at the DIO spectrum on a log scale, it can be seen that the occurrence of DIO electrons above 100 MeV is still at an appreciable level relative to a signal with a branching ratio of $\mathcal{O}(10^{-17})$.

To date, there are no measurements of DIO spectrum near the conversion electron energy, because of the high muon rate needed. However, a recent theoretical calculation [44], which takes into account nuclear effects, gives an uncertainty near the endpoint smaller than 20%.

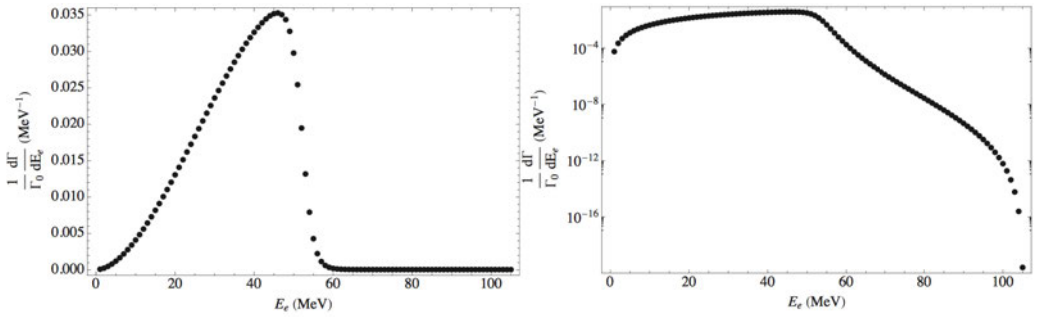

Figure 1.11: The signature of $\mu - e$ conversion is a monoenergetic electron near the muon rest mass. Moreover, muons captured by the nucleus target can decay-in-orbit. DIOs spectrum shape (left) is a distorted Michel spectrum with a long tail to high energies. On right, the DIO spectrum on a log scale is reported: it extends all of the way out to the endpoint energy, about 0.5 MeV less than the muon mass, for this reason these events represent an important background for the Mu2e experiment.

Radiative muon captures

The muons can be absorbed by the nuclei of the target, emitting a high energy photon, $\mu + N(Z, A) \rightarrow \gamma + \nu_\mu + N(Z - 1, A)$, which can convert to e^+e^- pairs.

It is possible, however, to choose the target material in order to reduce the energy of the resulting photon. For example, the resulting photon energy endpoint for an aluminum target is 101.9 MeV, which is about 3.1 MeV below the conversion electron signal energy, because the minimum mass of the Mg (Z=12) is a couple of MeV above the rest mass of Al (Z=13).

Antiprotons induced backgrounds

Antiprotons, which can be generated along with the muons by the parent proton beam or by cosmic rays, can be coincident in time with a conversion electron, having also the same energy. The products of their interaction with the matter can be also a source of background because they do not decay and carry a negative electric charge.

Antiprotons with momenta less than 100 MeV can propagate and reach the stopping target. Those with momenta less than 100 MeV spiral slowly, consequently the expected flux of antiprotons at the muon stopping aluminum target is nearly constant in time so that the delayed live gate and the extinction systems do not effectively mitigate the resulting backgrounds. Moreover, antiprotons will annihilate on nuclei, releasing significant energy and producing a significant number of secondary particles. These secondaries can include electrons themselves, or they can produce electrons in tertiary interactions such as capture or decay.

To prevent antiprotons reach the stopping target region, a thin absorbers will be placed before this region (upstream in the Transport Solenoid, see Ch. 2.3.2).

Radiative pion capture

Pions can induce background events when they are captured in the stopping target or surrounding material and produce a high energy photon through RPC:

$$\pi^- + N \rightarrow \gamma + N^* \quad . \tag{1.8}$$

The kinetic endpoint of the emitted photons peaks at $\sim$ 110 MeV, which can also produce e^+e^- pairs. If the photon then converts in the stopping material, one sees

an electron-positron pair and in the case of an asymmetric conversion, the outgoing electron can be near the conversion energy, thus appearing to be a conversion electron. In addition, the photon can internally convert:

$$\pi^- + N \rightarrow e^+ \, e^- \, + N^* \tag{1.9}$$

Thus electrons resulting from photon conversions, both internal and external, can produce background.

RPC occurs in 2.1% of pion captures for an aluminum target. This kind of background can be reduced using a pulsed beam and an appropriate delayed acquisition time-window.

Other environmental backgrounds

Other activity in the detector might affect track reconstruction, thus causing tails in the energy resolution response function that can move low-energy DIO electrons into the signal momentum window. Additional activities in the detector are primarily originated from the muon beam, from multiple DIO electrons and from muon capture on target nucleus that results in the emission of photons, neutrons and protons.

The protons ejected from the nucleus following muon capture have a very small kinetic energy and are highly ionizing, so the large pulses they leave behind in tracking chambers can shadow hits from low energy electrons, potentially adding to the likelihood of reconstruction errors. Ejected neutrons can be captured on hydrogen or other atoms and produce low-energy photons.

Low-momentum electrons can be created in the tracker by photons that undergo Compton scattering, photo-production, or pair production, and by delta-ray emission from electrons and protons. Because of the low mass of the tracker, these electrons can spiral a considerable distance through the detector before they range out, generating a substantial number of in-time hits.

Electron-generated hits caused by neutron-generated photons are the most common and difficult to remove form of background activity.

Chapter 2

The Mu2e Experiment

The Mu2e experiment will study the CLFV neutrinoless muon to electron conversion in the field of an Aluminum nucleus. The goal of the experiment is to measure the ratio of the conversion rate normalized to the number of nuclear muon captures, improving by four orders of magnitude the present limit [41]:

$$R_{\mu e} = \frac{\mu^- + N(Z,A) \rightarrow e^- + N(Z,A)}{\mu^- + N(Z,A) \rightarrow \nu_\mu + N(Z-1,A)*} < 8 \times 10^{-17} \quad (at\ 90\%\ C.L.). \tag{2.1}$$

2.1 Setup overview

The "S-shaped" layout of the Mu2e apparatus is shown in Figure 2.1. The entire experimental setup is extensively described in the Technical Design Report of the experiment [1].

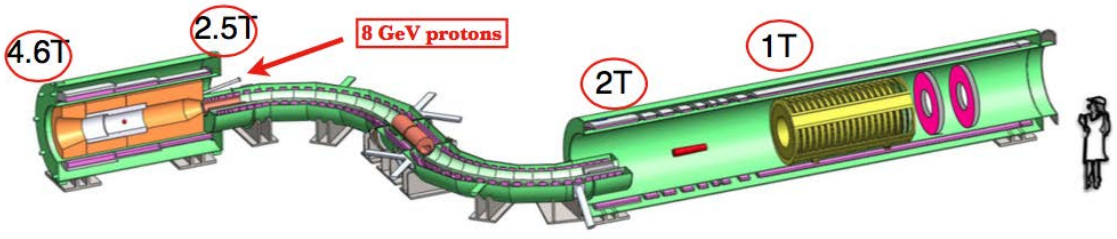

Figure 2.1: Layout of the Mu2e experiment. It consists of three superconducting solenoid magnets: from left to right, the production solenoid, the transport solenoid and the detector solenoid.

It consists of three superconducting solenoid magnets:

- the Production Solenoid (PS), where an 8 GeV pulsed proton beam coming from the Fermilab accelerator system [46] strikes the production tungsten target, producing mostly pions;
- the Transport Solenoid (TS), which efficiently captures charged pions and selects and transports negatively charged secondary muons to a stopping target located in the next solenoid. The S-shaped Transport Solenoid is long enough to allow the decay of almost all hadrons and to suppress line-of-sight particles. The momentum spectrum of the transported muon beam must be low enough to ensure that a significant fraction of the muons can be brought to rest in a thin target;
- the Detector Solenoid (DS) that houses the Al muon stopping target and the detectors needed to efficiently identify 105 MeV/c electrons coming from muon conversion (CEs). Moreover its design allows backgrounds rejection from conventional processes and cosmic rays.

The inner bore of the solenoids is evacuated to 10^{-4} Torr, in order to limit backgrounds from muons that might stop on gas atoms and to reduce the contribution of multiple scattering for low momentum particles.

So that, the Mu2e experimental concept is simple. Protons interact with the primary tungsten target in the PS creating charged pions, which are focused and collected by the lens provided by the graded magnetic field in the TS. Inside the TS, pions mainly decay into muons. Low momentum and negative charged muons are transported by the TS to the thin stopping aluminum target housed by the DS, where they stop at high rate ($\sim$ 10 GHz). Active detector components (tracker + calorimeter) measure the momentum and energy of the particles originating from the stopping target-beam interactions and discriminate CEs from background processes. The initial proton beam has a bunched structure that provides enough time for most of the stopped muons to decay before the next pulse arrival. Outside the DS, a stopping target monitor is used to measure the total number of muon captures. A Cosmic Ray Veto (CRV) system surrounds the DS and part of the TS in order to detect and reject Cosmic Rays events.

The construction of the experimental hall facility, which houses the entire apparatus, has started on April 2015 and was concluded in 2017. Similarly the procurement of the entire production of superconductive cables have been completed.

2.2 The accelerator system

A high intensity and bunched proton beam is used to produce low energy muon beam needed for the Mu2e experiment. The Mu2e key features for the secondary beam are:

- intensity and time structure;
- beam transport efficiency;
- purity.

2.2.1 The proton beam

The existing Fermilab accelerator complex [46] is exploited to spill protons for the Mu2e experiment. Figure 2.2 shows the layout of this infrastructure. The proton spill stages for Mu2e are the following:

- boosted protons batches, each containing 4×10^{12} protons with a kinetic energy of 8 GeV, are extracted into the Main Injector (MI-8) beamline and injected into the Recycler Ring;
- a re-bunching is performed in the Recycler Ring using a RF manipulation sequence;
- bunches are slow-extracted and synchronously transferred to the Delivery Ring;
- a resonant extraction system injects $\sim 3 \times 10^7$ protons into the Mu2e beam line each 1.7 μs (revolution period in the Delivery Ring). The proton beam time structure is illustrated in Figure 2.3. After the resonant extraction sequence is complete, a cleanup abort kicker is fired to remove any remaining beam.

This accelerating facility is now called Muon Campus and supports the operation of both the Muon g-2 [47] and the Mu2e experiments.

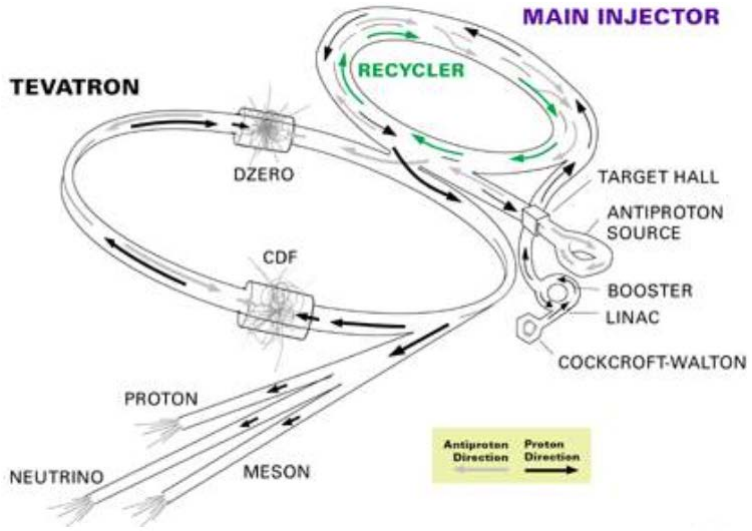

Figure 2.2: Layout of the accelerator complex providing the proton beam to Mu2e. Protons are transported from the Booster through the MI-8 beamline to the Recycler Ring where they will circulate while they are re-bunched by a 2.5 MHz RF system. The reformatted bunches are kicked into the P1 line and transported to the Delivery Ring where they are slow extracted to the Mu2e detector through a new external beamline.

Mu2e will collect about 4×10^{20} protons on target in three years of running, resulting in about 10^{18} stopped muons, which will yield the required SES for coherent muon conversion.

An important parameter used to estimate the proton beam quality is the "extinction factor", EF, that is defined as the ratio between the number of protons in time and out-of-time with respect to the 250 ns full-width of the bunch itself. A

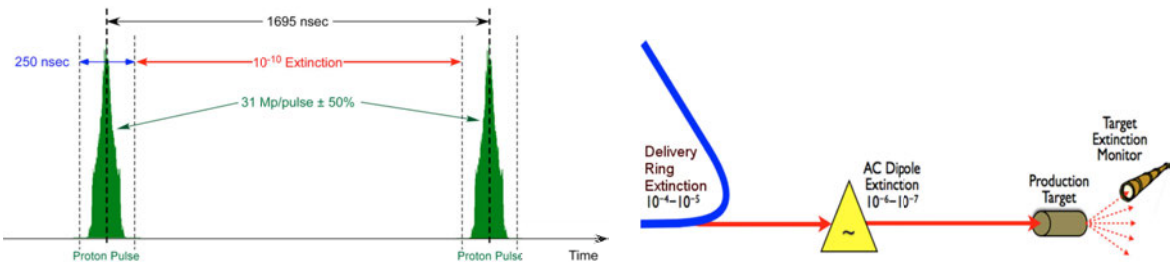

Figure 2.3: Left: The proton bunch structure required by the Mu2e experiment. Right: Concept for the statistical extinction monitoring technique.

EF $>$ 10^{10} is needed to keep the "prompt" background negligible. These protons are a potential source of radiative pion capture background, which is not suppressed by a delayed "live gate". The combination of "proton pulse" shaping and a high frequency AC dipole allows to achieve a proton extinction factor of about 10^{12} [1].

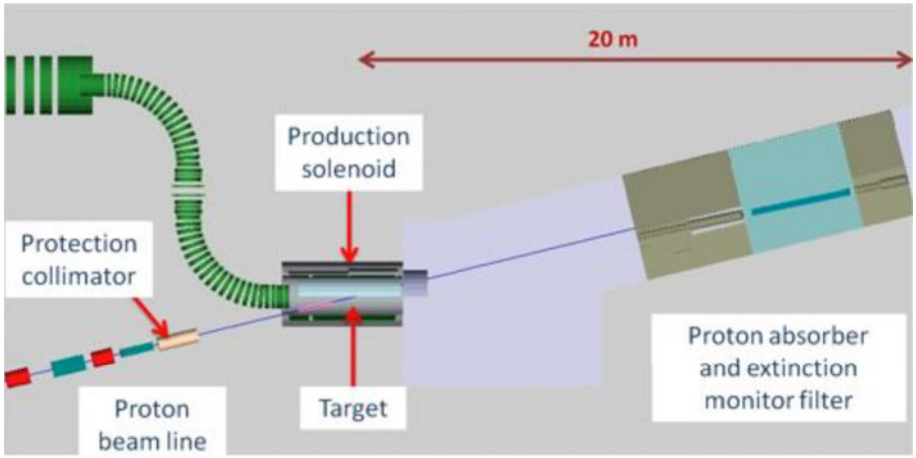

Figure 2.4: Location of the extinction monitor system.

An extinction monitor system, located above the production target, is used to check that this level of extinction is achieved (Fig. 2.3, right). It measures the number of scattered protons as a function of time, so providing a direct measurement of the residual beam between the batches. Figure 2.4 shows the orientation of the Extinction Monitor within the experiment. It is composed of:

- a filter magnet, which selects particles with an average momentum of 4.2 GeV/c;
- two collimators, placed in front of the filter magnet;
- a spectrometer magnet, placed in between two series of Si pixel detectors to allow momentum measurements;
- scintillating counters to trigger the Si read out in case of out-of-time particles and time stamp them;
- a sampling calorimeter to identify muons.

2.3 The muon beam line

In order to achieve the designed SES, the secondary muon beam should satisfy the following strict requirements:

- have a high rate, in order to obtain a large number of muons stopped. It is essential to improve previous experiments results. The present proposed rate is of 4.21×10^{10} μ^-/s.

- have a pulsed structure in order to suppress the prompt background. The muons hitting the stopping target should be distributed in a narrow time bursts (< 250 ns), ~ 1700 ns separated (larger than the muonic aluminum lifetime), in order to suppress the prompt background.

- have a TDAQ late window. The result of SINDRUM II experiment was ultimately limited by the presence of the veto counters, necessary for the suppression of the prompt background. Mu2e, instead, will take data 670 ns after the injection bursts, to let decay the prompt background (especially pion capture). The data-taking time window will then close 925 ns after, just before the arrival of the next bunch. Veto counters are then no longer needed. The muon capture time in Al maximizes the total number of muons on target, given the time scheme provided by the Fermilab accelerator complex, as shown in Figure 2.5.

- between-bursts extinction is fundamental to suppress background generated by unwanted beam between pulses.

The Mu2e solenoid system takes its basic design idea from the pioneering work by R.M. Djilkibaev and V.M. Lobashev, proposed in 1989 for the MELC experiment [48], later cancelled. The basic idea is to convoy pions, produced from the proton-target interaction, in a long transport channel where they undergo a decay to muons. The decay channel acts also as a sign-selector removing positive particles.

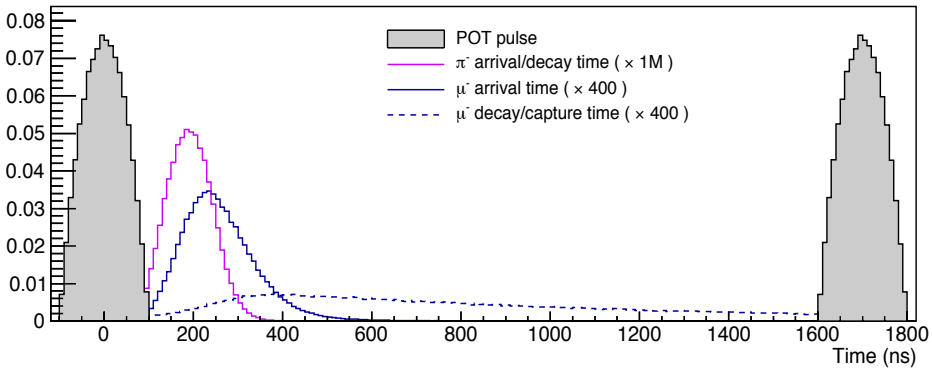

Figure 2.5: The proton beam hits the production target with bursts 200 ns large and separated from the next one by ∼1700 ns. The detector system starts taking data after 670 ns from the arrival of the proton pulse, when almost all pions are decayed. Muon capture time in Al (dashed blue line) best matches this timing scheme.

2.3.1 The Production Solenoid

The Production Solenoid is the first stage of the Mu2e Superconducting Solenoid Magnet system. It is approximately 4 m long, with a graded magnetic field varying from 4.6 to 2.5 T. It has an inner bore diameter of about 1.5 m. A shield structure made of bronze is placed in between the inner bore and the PS coil to limit the radiation damage. Figure 2.6 shows the PS structure.

The 8 GeV bunched proton beam coming from the accumulator ring enters in the PS and hits the tungsten target placed in the center of the solenoid (Fig. 2.6, right), producing mostly pions. The production target consists of a 160 mm long tungsten rod, with a 6.3 mm diameter, placed within a titanium support ring. The tungsten has been chosen as target material because of its thermal properties: it has a high melting point and a low thermal expansion coefficient. The PS coils, made of Al-stabilized NbTi cables, are then protected from radiation damage by a bronze shield.

The flux of particles coming from the proton pulse striking the production target during the early burst is referred as "beam flash". In order to reduce the flux of secondary particles, the primary proton beam enters the PS from the opposite direction of the Transport Solenoid. The axially graded magnetic field reflects the charged particles toward the low magnetic field region, to recover some interaction

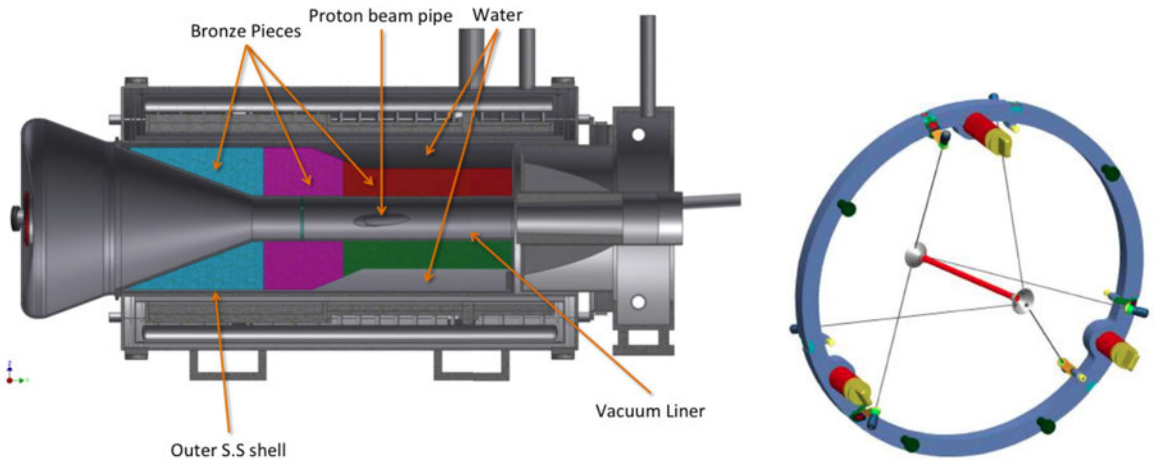

Figure 2.6: Left: layout of the Production Solenoid. Right: tungsten stopping target for the primary proton beam.

products emitted backwards: the p_t/p ratio, in fact, decreases as the magnetic field decreases, enhancing the particle movement in the direction of decreasing gradient. This approach has been already validated by the MuSIC experiment R&D (at J-Park) [49] and according to many simulation studies, the capture efficiency in Mu2e is expected to be of about 1000 times larger than in conventional muon facilities [1] [50].

2.3.2 The Transport Solenoid

The Transport Solenoid consists of several superconducting straight and toroidal sections. It is needed to select and transmit low energy negatively charged muons ($p < 80$ MeV/c) from the PS to the DS, using a series of collimators and absorbers installed inside. Figure 2.7 shows the sketch of the TS and its main components, which are:

- the TS1 links the PS to the TS and houses a collimator that selects particles with momentum lower than 100 MeV/c;
- the TS2 is a quarter of toroid, avoiding neutral particle from the PS to propagate into the DS;
- the TS3 is a straight solenoid containing two collimators, for filtering particles

based on sign and momentum, separated by a beryllium window, needed for stopping antiprotons produced in the PS;

- the TS4 is another quarter of toroid, similar to the TS2, which does not allow neutral particles from the beam interactions in the TS3 to reach the DS;
- the TS5 interfaces the beam line with the DS and is equipped with a collimator for momentum selection.

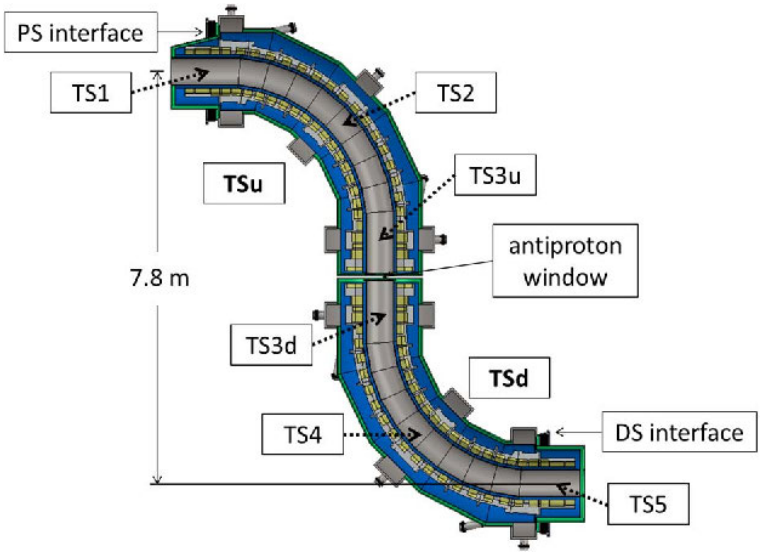

Figure 2.7: Trasnsport Solenoid schematic drawing.

The magnetic field in the TS has a negative gradient, from 2.5 T to 2 T, in order to minimise the transport of particles spending a long time in the magnetic system. This technique eliminates possible traps, where the particle bounces for a while between two local field maxima and allows to accelerate particles from the PS region thorough the DS [1].

A cosmic ray veto device covers the part of the TS close to the DS entrance.

2.4 The Detector Solenoid

The Detector Solenoid is ∼11 m long and houses the muon stopping target, the tracker, which measures the particles momentum, and the calorimeter, which measures particles energy and their arrival time. Moreover, in the downstream part of

the DS, the muon beam stop is located. This system is made by a high-Z material in order to absorb all the muon beam energy that does survive the stopping target. The layout of the DS is reported in Figure 2.8.

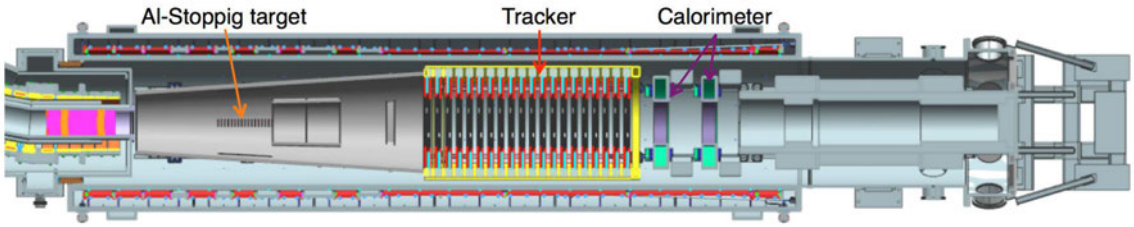

Figure 2.8: Drawing of the Detector Solenoid, which is a low field magnet that houses the muon stopping target and the components required to identify and analyze CEs emitted by the stopping aluminum target.

All these devices have to operate in a graded magnetic field, which is around 2.5 T, at the beginning of the solenoid, and is about 1 T in the region occupied by the detectors, becoming almost uniform till the end of the DS. The graded field allows to accelerate particles from the TS to the detector area, helps in rejecting beam-related backgrounds and increases the acceptance for conversion electrons: the conversion electrons emitted in the direction opposite the detector components are gradually reflected backwards. Not all of these reflected electrons will be used in the final data sample, because many of them will pass through nearby material, losing energy or scattering and failing the analysis selections.

2.4.1 The muon stopping target

The muon stopping target has to be massive enough to stop a significant fraction of muons coming from the TS, but not so high-Z to corrupt the momentum measurement of conversion electrons emerging and traversing part of it. Thus, the design of the stopping target is the result of a trade off between the stopping efficiency and the amount of material traversed by the eventual conversion electron. The dependence of the CE rate from the target material could help to identify the physics mechanism responsible for the process.

Figure 2.9 (left) shows the final design of the stopping target that has been chosen to optimize the sensitivity of the experiment. It is composed by 17 thin

aluminum foils and placed along the first part of the DS axis. The foils are 0.22 mm thick, spaced 5 cm. The disks radius decreases from 8.3 cm, upstream, to 6.3 cm, downstream. Aluminum is the selected material for the stopping target because the mean life-time of a muon captured in an Al nucleus is 864 ns, which is of about one half of the proton bunch spacing.

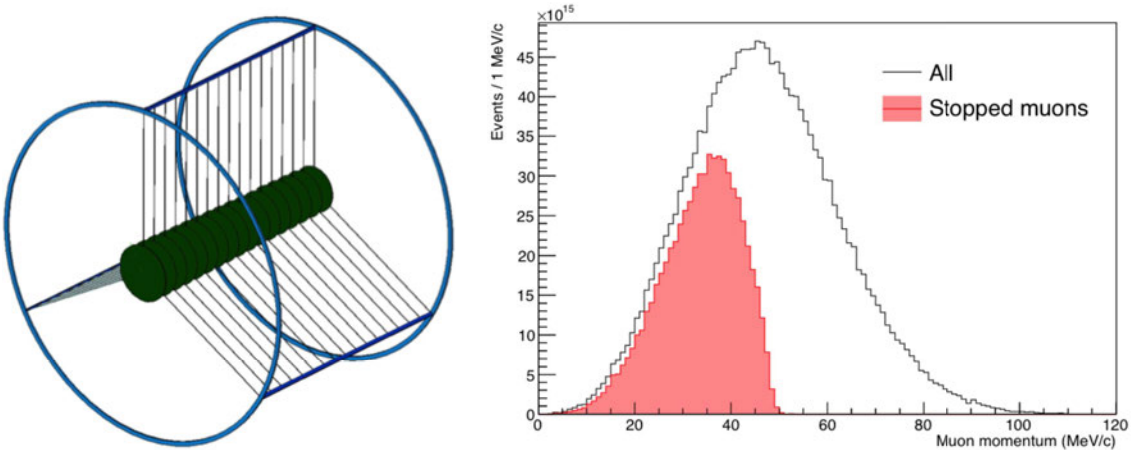

Figure 2.9: Left: schematic layout of the Mu2e stopping target and its mechanical support. It is made by 17 aluminum disks, 0.22 mm thick, spaced 5 cm along the DS axis. The disks radius decreases from 8.3 cm upstream to 6.3 cm downstream. Right: momentum distribution of muons delivered to the stopping target as well as the distribution of muons that stop (red) in the Al foils.

Figure 2.9 (right) shows the resulting momentum distributions for muons delivered to the Al target and stopped in the foils.

2.4.2 Stopping target monitor

The Mu2e stopping target monitor has been designed to measure the total number of stopped muons with a relative accuracy of 10%, by counting the X-ray emitted by muonic atoms [1]. It is important for the normalization of the conversion rate, $R_{\mu e}$. The highest X-ray yield is due to the 2p→1s radiative transition, corresponding to the arrival of a muon into the ground state. Other lines are also available with significant yields: like the 3p→1s and the 4p→1s transitions. Moreover, muons that stop in impurities of the Al foils (non Al atoms), can be identified from their typical X-ray emission. The rates and spectra of these nuclear capture products are being studied by the AlCap experiment at PSI [52]. A solid-state Ge detector is used to

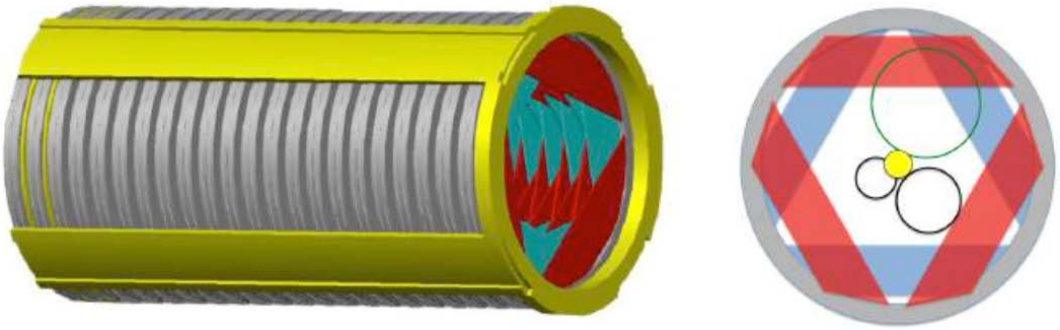

Figure 2.10: Left: The Mu2e straw tube tracker. The straws are oriented transverse to the solenoid axis. Right: cross sectional view of the Mu2e tracker station with the trajectories of a 105 MeV CE (top) and a 53 MeV Michel electron (lower right) superimposed. The disk in the center is the stopping target. Electrons with energies smaller than 53 MeV (lower left) miss the tracker entirely.

perform the X-rays detection with sufficient accuracy to distinguish and identify all contributions. It is housed in a concrete box, placed downstream to the outer part of the DS to minimize the background fluxes.

2.4.2.1 The Tracker

The Mu2e tracker has to accurately measure the trajectory curvature of ∼105 MeV/c CE, in order to calculate their momentum [53]. The material of the tracker must be as low as possible to minimize multiple scattering, which is the main source of reconstruction errors. Moreover, the high rates of the Mu2e environment can generate background from spurious hits of low energy particles, which can combine mimicking a CE trajectory. Indeed, a low mass and highly segmented detector is required to minimize multiple scattering and handle the high rates.

Figure 2.10 illustrates the final tracker design. It consists of straw tubes aligned transversely to the DS axis. The basic detector element is a 25 μm sense wire inside a 5 mm diameter tube, made of 15 μm thick metalized Mylar (Fig. 2.11, right). The tracker consists of about 20000 straws divided in 18 measurement stations, which are distributed over a length of $\sim$ 3 m and assembled to resemble an annular disk. In this configuration all the electrons with low momentum, $p < 53$ MeV, will pass through the central hole, increasing the tracker purity (black tracks in Fig. 2.10,

right). A large fraction of them (97%) do not reach the tracker, because most of the electrons have energy smaller than 60 MeV.

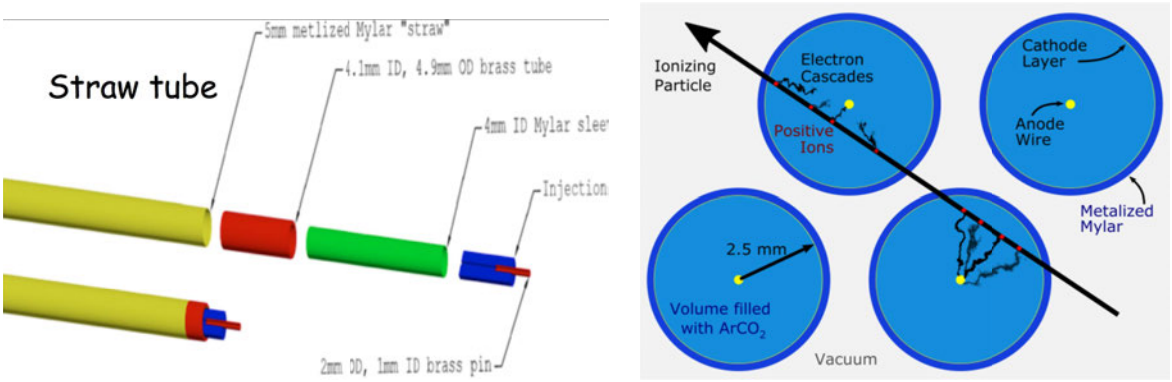

Figure 2.11: Left: exploded view of a Mu2e tracker straw tube. Right: cross section of straw drift tubes.

The assembling element of a station is the panel, which consists of two layers of straws, to provide mechanical rigidity. Six panels, rotated by 60 degrees, define a plane (Fig. 2.10, right) and, finally, two rotated planes form a station.

A 1.25 mm gap is maintained between straws to allow diameter expansion due to gas pressure and manufacturing tolerance. The straws are designed to withstand changes in differential pressure ranging from 0 to 1 atmosphere for operation in vacuum. Each straw is read out on both sides by means of pre-amplifiers and TDCs for timing and one ADC is used for dE/dx capability. The position along the straws is obtained by charge deposition and time informations. The required tracker position measurements resolution on drift radius is about 100 μm. The straws are supported at their ends by a large radius ring, outside of the active detector region.

Signal digitization in the vacuum region is performed near the tracker, and transmitted though optical fibers, in order to minimize the amount of feed-throughs. A liquid cooling system is required to maintain an appropriate operating temperature of the electronics in vacuum.

Tracker momentum resolution is crucial to determine the level of several critical backgrounds. The required resolution is $\sigma < 200$ keV/c. Simulations indicate that the net resolution of the tracker is smaller than the estimated deterioration due to the energy loss in the upstream material (Fig. 2.12).

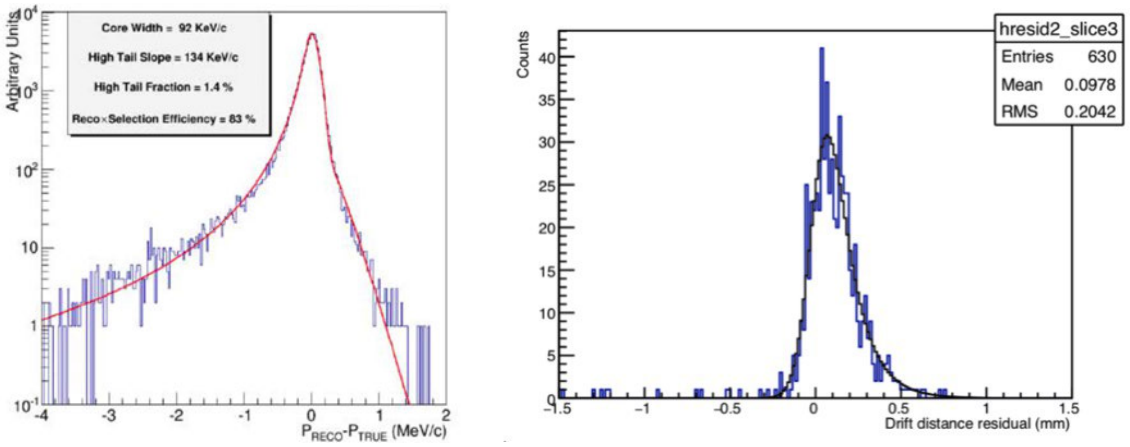

Figure 2.12: Tracker momentum resolution with simulated CEs. Full background overlay and pattern recognition included. Fit to a split double Gaussian with standard track fit quality cuts. The core width satisfies the Mu2e momentum resolution requirements [1].

A small panel prototype with 8 straws was built at Lawrence Berkeley Laboratories to measure the performance using cosmic rays and radioactive sources [54]. The straw resolution was measured for each of the 8 straws using cosmic rays. The Mu2e official Monte Carlo simulation implements a detailed model of physical and electronics responses to GEANT4 energy deposition. This model includes all the chain electron Clusters → Drift → Current pulse → Voltage waveform → Digitization. Figure 2.12 shows the distribution of the drift distance residual (blue line) of the cosmic ray data. The transverse resolution is found to have a full-width at half maximum of 283 μm.

The R&D phase of the tracker is mature and the panel assembly has started in summer 2018.

2.4.2.2 The Calorimeter

High rates of hits in the tracker may cause pattern recognition errors that add tails to the resolution function. Accidental hits combined with low energy particles might reconstruct to a trajectory consistent with a CE. A calorimeter downstream to the tracker allows particle identification and rejection of such kind of background, combining the fitted helix trajectory extrapolated by tracker information with the measured energy deposit, timing and position. In particular, energy and timing mea-

surements from the calorimeter provide information critical for efficient separation of electrons and muons in the detector.

Besides the Particle Identification (PID), the calorimeter allows:

- track seeding;
- rejection of the background due to cosmic ray muons, not vetoed by the CRV;
- to perform a fast and stand alone high level trigger, based on energy measurements;
- reduction of the total volume and rate of the data storage.

A more detailed description of the Mu2e crystal calorimeter and its expected performance is given in the next chapter.

2.4.2.3 The Muon Beam Stop

The DS final component is the muon beam stop (MBS), where about 60% of the muons stop. It is designed to absorb the energy of beam particles that reach the downstream end of the solenoid, while minimizing the muon decays background to the detectors. Structurally, the MBS consists of several concentric cylindrical structures of stainless steel and high density polyethylene. The MBS is coaxial with the DS bore and is plugged on the downstream end [1].

2.4.2.4 The Cosmic Ray Veto

Cosmic rays muons are a known source of background for the Mu2e experiment. They could produce particles mimicking a CE emitted from the stopping target or produce 105 MeV/c electrons and positrons through secondary and delta-ray production in the detector region material, as well as from muon decay-in-flight. Such kind of background events occur at a rate of about one per day and must be suppressed in order to achieve the required SES.

The CRV system is a passive shielding needed to eliminate background sources other than penetrating muons [55]. On each side, the CRS system consists of four

layers of extruded scintillator strips bars (Fig. 2.13, left) with embedded wavelength shifting fibbers that are read out with Silicon photomultipliers (SiPMs) on both strip ends. The strips are 2 cm thick, providing ample light yield to allow a low enough light threshold to be set to suppress most of the backgrounds. Aluminum absorbers between the layers are used and designed to suppress background from electrons.

The CRV surrounds the DS on 3 sides (Fig. 2.13, right) and extends up to the midpoint of the TS. The Veto signal is produced by the coincidence of adjacent counters in different layers. In the region of the muon stopping target the CRV efficiency is 99.99%, reducing the Cosmic Ray induced background rate to 0.10 events during the entire running period. The light yield has to be around 15 photoelectrons/cm/SiPM to meet the above requirement, with a signal rise time faster than 5 ns.

The passive shielding, between the CRV and the DS and part of the TS, has been designed in order to minimize the CRV dead time, generated by the intense neutron flux, coming primarily from the muon stopping target. Most of the neutrons have kinetic energies below 10 MeV, with the most probable energy value at 1 MeV. Simulations [1] show that the rate in the counters comes primarily from gammas that are produced from neutron capture on hydrogen. The passive shielding moderates and capture most of the neutrons. The magnitude and pattern of energy deposition in multiple layers of scintillator is expected to be different for neutrons and muons, and therefore false veto signals from neutrons can be reduced to an acceptable level.

A pulsed beam of 120 GeV protons provided at the Fermilab Test Beam Facility was used to measure properties of a CRV prototype counters [56]. The average light yield was measured to be $\sim$50 photoelectrons per SiPM for normal incident protons at a position 1 m from the end of a 3 m-long counter. Longitudinal and transverse beam scans were used to study properties of the prototypes. Single-channel timing resolution based on a 79.5 MHz sampling rate was demonstrated to be better than 2 ns. This test concluded the CRV R&D phase demonstrating that this configuration will meet the Mu2e experiment requirements. The counters production phase is starting in 2020.

b!

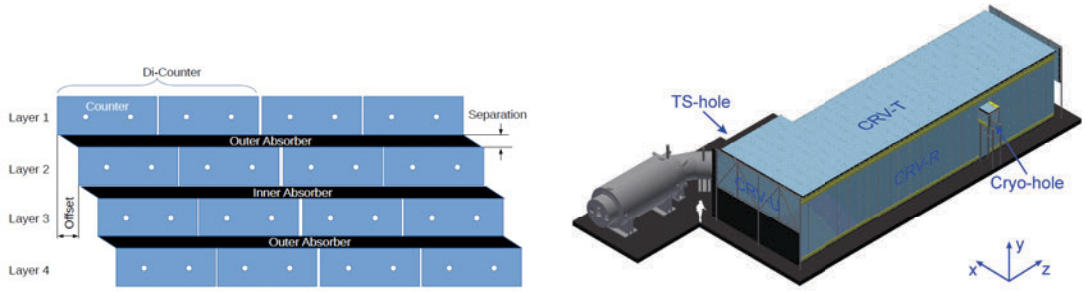

Figure 2.13: Left: the CRV system is an active veto made by a system of four layers of long scintillator strips, with an aluminum layer between them. Right: the cosmic ray veto covering the Detector Solenoid and half of the Transport Solenoid.

Chapter 3

The Mu2e crystal electromagnetic calorimeter

The Mu2e calorimeter provides information about energy, timing and position to validate the charged particle reconstructed by the tracker, reject muons mimicking the signal and antiprotons interactions. The design of the calorimeter is driven by the need to reject backgrounds to reach the required SES for the muon conversion process and also to maximize the acceptance for $\sim$ 105 MeV/c CE tracks.

3.1 Requirements

The previously stated tasks were translated in the following calorimeter performances requirements [1]:

- an energy resolution better than $\mathcal{O}(10\%)$ (at 105 MeV), to confirm the electron momentum measurement from the tracker, which is much more precise (160 keV/c, at 105 MeV/c), and distinguish it from the $\sim$40 MeV energy deposit from 105 MeV/c muons mimicking the signal;
- a timing resolution better than $\sim$ 0.5 ns (at 105 MeV), to ensure the energy depositions in the calorimeter are in time with the conversion electrons reconstructed by the tracker;

- a position resolution ($\sigma_{r,z}$) better than 1 cm, to match the position of the energy deposit with the extrapolated trajectory of a reconstructed track;
- keep an efficient operation in the high-radiation Mu2e environment, maintaining its functionality for radiation exposures up to ∼15 krad/year in the hottest region and for a neutron flux equivalent to 10^{11} MeV/cm^2, inside an evacuated region (10^{-4} Torr) of the Detector Solenoid that provides 1 T axial magnetic field;
- a fast enough response in order to handle the experimental high rate ($\tau < 40$ ns);
- a temperature and gain stability within ± 0.5%, to not deteriorate the energy resolution.

Moreover, the calorimeter has to be able to provide:

- an independent trigger, either in hardware, software, which can be used to identify signal events with significant energy deposits;
- a seed to drive the pattern recognition in the track reconstruction.

3.2 Design

In the 105 MeV energy regime, a total absorption calorimeter employing a homogeneous continuous medium is required to meet the Mu2e requirements. A long R&D phase has been carried out to define the detector design, that was concluded in 2015 with the final technical choice [57][58]. The Mu2e calorimeter final design consists of two disks whose dimensions were optimized to maximize the acceptance for CEs. Figure 3.1 shows its design: two identical annular disks with an inner (outer) radius of 35 cm (66 cm) and a relative distance of 70 cm, corresponding to about half pitch of the helicoidal CE trajectory. Each disk is composed of 674 square based scintillating crystals of $3.4 \times 3.4 \times 20$ cm^3 dimensions. Each crystal is readout by two solid state photosensors and wrapped with a 150 μm foil of Tyvek. The Front-End Electronics (FEE) is mounted on the rear of each disk, while voltage distribution, slow control and digitizer electronics are housed behind each disk

in custom crates. A laser flasher system provides light to each crystal for relative calibration and monitoring purposes. A pipes system, mounted on the front side (opposite to the front-end) of each disk, with a radioactive liquid source circulating inside, provides absolute calibration and energy scale channel by channel.

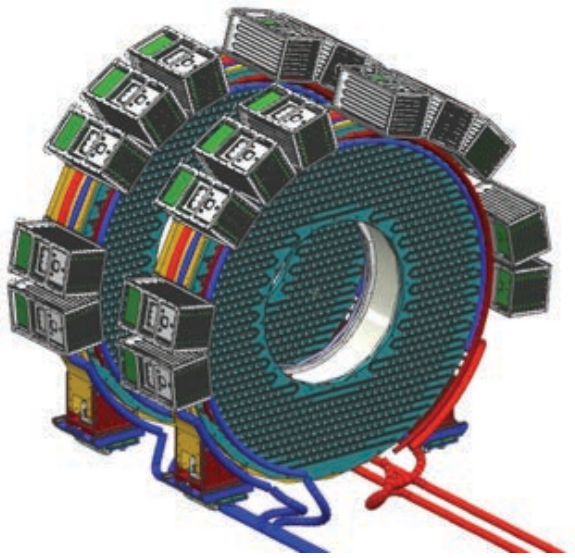

Figure 3.1: Calorimeter design.

3.2.1 Crystals

Different types of crystals have been considered for the Mu2e calorimeter: lutetium-yttrium oxyorthosilicate (LYSO) [59], lead tungstate ($PbWO_4$), barium fluoride (BaF_2) [60] and pure cesium iodide (CsI). Table 3.1 compares properties of the crystals taken in consideration.

In the Mu2e Conceptual Design Report [61] of 2012, the calorimeter baseline choice was based on LYSO crystals. Since then, an extensive R&D program has been carried out to study this option [62][63]. The cost of a LYSO calorimeter became unaffordable, due to the salt price increase. $PbWO_4$ option was excluded for its low light yield. As an alternative, BaF_2 and CsI crystals were considered having very similar properties in terms of light output and radiation length. BaF_2 emits at 218 nm, but presents an important slow component above 280 nm (decay

Property	BaF_2	LYSO	CsI	$PbWO_4$
Density [g/cm^3]	4.89	7.28	4.51	8.28
Radiation length X_0 [cm]	2.03	1.14	1.86	0.9
Molière radius [cm]	3.10	2.07	3.57	2.0
Interaction length [cm]	30.7	20.9	39.3	20.7
dE/dx [MeV/cm]	6.5	10.0	5.56	13.0
Refractive Index at λ_{max}	1.50	1.82	1.95	2.20
Peak luminescence [nm]	220, 300	402	310	420
Decay time τ [ns]	0.9, 650	40	26	30,10
Light yield (compared to NaI(Tl)) [%]	4.1, 36	85	3.6	0.3,0.1
Hygroscopy	None	None	Slight	None

Table 3.1: Comparison of crystal properties for LYSO, BaF_2, pure CsI and $PbWO_4$.

time ∼650 ns). Therefore, it needs to be coupled with a photosensor able to suppress this onr. The absence of a "solar-blind" photosensor in this wavelength region made this option too risky to be chosen. On the other side, CsI proven to be a good compromise for its properties and for a good matching with new generation photosensors. For these reasons, it has been selected has the final scintillator choice [64][65].

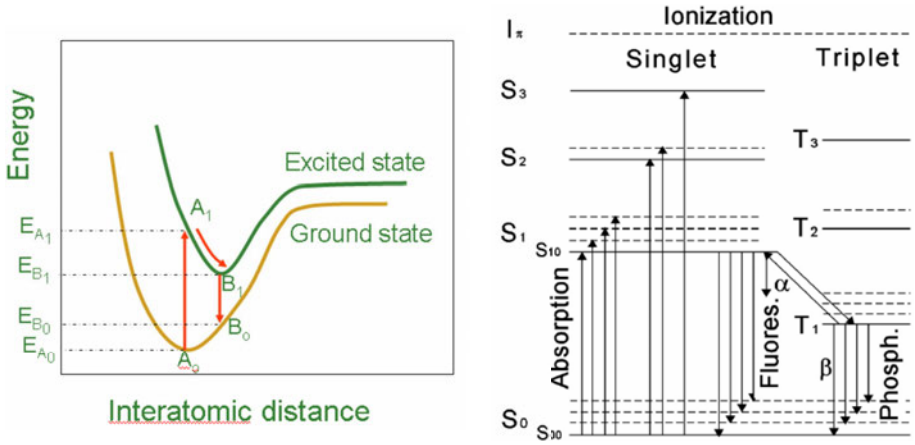

Figure 3.2: Energy levels of organic molecules.

Pure CsI is an organic scintillator material: it exhibits scintillation, the property of luminescence, when excited by ionizing particles. The scintillation mechanism in organic materials arises because of the structure of the crystal lattice [66], from transitions in the energy levels of a single molecule (Fig. 3.2, left). Practically organic scintillators are organic molecules that have symmetrical properties associated with the electron structure. Energy from a charged particle is absorbed and excites the electron into a variety of excited states. Spacing between singlet states (spin = 0) is 3-4 eV (i.e. S_0 and S_1 in Figure 3.2 right) and spacing in vibrational structure is 0.15 eV: each of the S levels is subdivided into a series of levels with much finer structure, corresponding to the vibrational states of the molecule. At room temperature, average energy is approximately 0.025 eV, so all molecules are in the S_{00} state. When the charged particle passes through the crystal, molecules absorb its kinetic energy and electrons are excited to the upper levels. The higher states, S_2, S_3, de-excite quickly ($\sim$ ps) to S_1 state through radiation-less transitions (internal conversion). States such as S_{11}, S_{12} that have extra vibrational energy and are not in thermal equilibrium with neighbouring molecules, quickly lose energy. After negligibly short time a population of excited molecules in S_{10} state is produced as the net effect of the excitation process.

The prompt fluorescence intensity, I, at time t following excitation is described by an exponential decay, $I = I_0\ e^{-t/\tau}$, with a decay time, τ, that depends by the scintillator material. In most organic scintillators, the decay time is of the order of a few nanoseconds, therefore organic scintillators are fast.

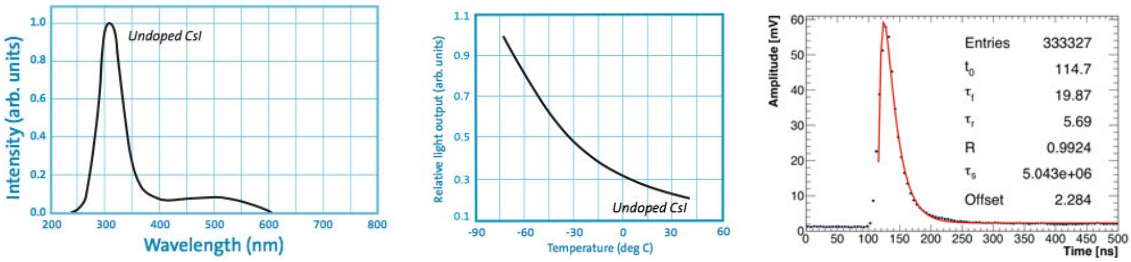

Figure 3.3: Left: scintillation emission spectrum of pure CsI. Middle: relative light output as a function of temperature. Right: CsI signal with a super imposed double exponential fit function (red), showing the fast (τ_f) and slow (τ_s) decay times

Pure CsI has an emission spectrum characterised by (Fig. 3.3, left) [67]: a fast

emission peak at 315 nm, with a decay time of about 30 ns, and a slow emission at around 500 nm with a decay time of ~ 1 μs due to impurities in crystal growth. The 315 nm maximum can be described to self-trapped exciton luminescence of the pure material whereas the slow component can be explained by the presence of I^- vacancies (lattice defects). The intensity of the 500 nm component is significantly smaller for the high purity crystals.

The chosen length of the crystals (200 mm) corresponds to just 10 radiation lengths (X_0), however when considering the average CE incidence angle (50°), the effective length becomes ~ 300 mm that corresponding to an acceptable containment of $15X_0$.

Figure 3.3 (right) shows the signal of a CsI sample crystal tested with a ^{22}Na source and readout with a UV-extended Photomultiplier. The red line represents a triple exponential fit function, used to evaluate the decay times. The fast one resulted to be around 20 ns, while the slow one is the order of 1 μs. Figure 3.3 (middle) shows the CsI scintillation intensity as a function of the temperature. The light output, though, is heavily quenched at room temperature, and cooling to -77° would give ten times higher light output. Moreover this crystal is slightly hygroscopic, which means that a particular attention is needed during the operations with it. During test and assembly a dry atmosphere is to be used. Crystals will be inserted in calorimeter wrapped with a 150 μm tick Tyvek foil. Water vapour can pass through Tyvek, but liquid water cannot. Dedicated studies showed that Tyvek is approximately 90% reflective for the CsI emission wavelength. Moreover, an air gap of 2 mm will be present between the crystal and the sensor readout unit, to reduce thermal coupling and to avoid the usage any kind of glue or material that can produce outgassing in vacuum or deteriorate with radiation.

A detailed description on the crystals requirements and tests is reported in the following chapter.

3.2.2 Readout sensor

The Mu2e calorimeter photosensors has to operate in a 1 T magnetic field, which force us to use of solid state photodetector such as Silicon PhotoMultipliers (SiPMs),

and with a good quantum efficiency at 315 nm for optimal coupling with the CsI scintillation emission. The detector will be accessible only once a year, so the photosensors must have a good reliability to avoid any deterioration of the expected calorimeter performance. Redundancy is a good mean to increase reliability, so each crystal is equipped with two photosensors readout independently for a total of 2696 channels.

SiPMs are photon-counting devices made by one planar matrix of several APD photodiode pixels of the same shape, dimensions and construction features operating in Geiger mode. The APD is a semiconductor device made of a simple p-n junction, working in inverse polarization mode, at a voltage just below the breakdown level (Fig. 3.4). It consists of a thin layer of silicon in which the light is absorbed and free charge carriers (electrons and holes) are created and amplified. Electron and holes are collected at the anode and cathode of the diode, respectively. The primary electrons, produced by the incident radiation, are made to attain high velocities under the influence of an externally applied high electric field. If the energy obtained by an electron is large enough, it can free one or more secondary electrons, thereby creating an avalanche of charge pairs. Theoretically, such a process is only possible if the incident electron gains energy at least equal to the band gap energy of the material. However, since an electron also loses energy through non-radiative scatterings, on average, the electron energy should be much higher than the band gap energy. For most semiconductors an energy difference of a factor of 3 is normally required. The secondary electrons, being under the influence of the same electric field, produce tertiary charge pairs and so on. Once started, this process of charge multiplication grows and eventually causes avalanche multiplication of charge pairs (Fig. 3.4, right).

The ability to ionize of charge carriers is described by two ionization coefficients: α_e for the electrons and α_h for the holes, defined as the probability per unit length for a ionization impact. This probability is directly proportional to the electric field in the depletion region and inversely proportional to the temperature: the increase of internal vibrations in the crystal lattice can cause uncontrolled impacts before the electric field acceleration.

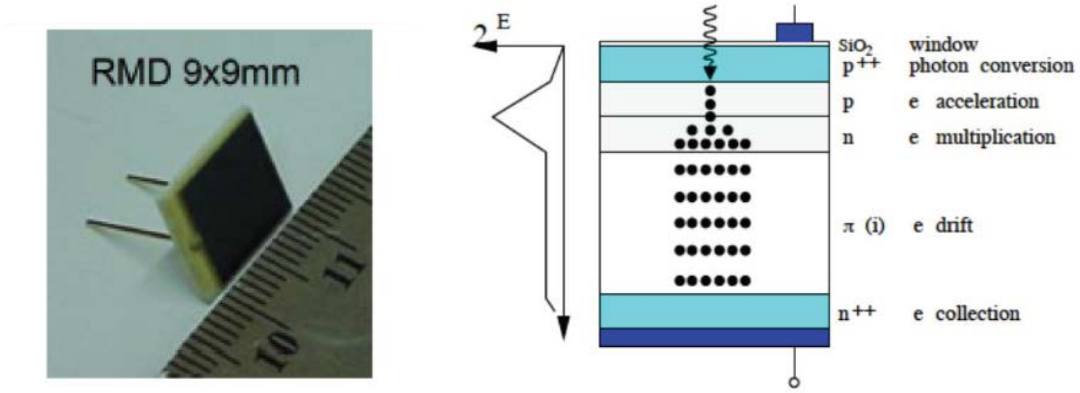

Figure 3.4: Left: picture of an APD sample. Right: Schematic layout of the Avalanche Photodiode. An intrinsic (or lightly doped p-type) material π sandwiched between a heavy doped p-side and a heavy doped n-side. Another p-type region is also established between the intrinsic material and the heavily doped n side. A strong reverse bias between the two ends creates an electric field E.

The gain, G, of the APD is quantified trough the formula:

$$G = \frac{1-\rho}{e^{-(1-\rho)\alpha_e w} - \rho} \ , \tag{3.1}$$

where $\rho = \alpha_h/\alpha_e$ and w is the width of the depletion region, it is possible to observe that with $\rho = 0$ the gain grows exponentially with the $\alpha_e w$ factor, while in the limit $\rho \to +\infty$, the gain is unitary. If electrons and holes have similar ionization coefficients ($\rho = 1$), they can both produce new electron-hole pairs along their tracks, thus increasing the gain. However, this process can slow down the avalanche envelope and increase the photodiode intrinsic noise: for this reason, APDs usually exploit only one type of charge carriers, generally electrons, because they maximize the device temporal response. These photodetectors have low gain (< 1000), so that inorganic, high light response scintillators are mandatory.

In a SiPM device, the APDs of the array operate with a reverse-bias voltage well above the breakdown voltage [69]. This kind of operation is also called Geiger-mode, as opposed to the linear-mode for the case of a single APD. In this way, the silicon will break down and become conductive, effectively amplifying the original electron-hole pair into a macroscopic current flow and a high gain is achievable. A single APD operating in Geiger mode works as a photon trigger switch. To overcome this lack of proportionality, the SiPM integrates a dense array of small APD sensors, each

with its own quenching resistor. When an APD+quenching resistor microcell in the SiPM fires in response to an absorbed photon, a Geiger avalanche is initiated causing a photocurrent to flow through the microcell. This results in a voltage drop across the quench resistor, which in turn reduces the bias across the diode to a value below the breakdown, thus quenching the photocurrent and preventing further Geiger-mode avalanches from occurring. Once the photocurrent has been quenched, the voltage across the diode recharges to the nominal bias value. The Geiger avalanche will be confined to the single microcell in which it was initiated in. During the avalanche process, all other microcells will remain fully charged and ready to detect photons. A typical SiPM has microcell densities of between 100 and several 1000 per mm^2. Each microcell detects photons identically and independently. The sum of the photocurrents from each of these individual microcells combines to form a quasi-analog output, providing information on the intensity of an instantaneous photon flux.

The Photon Detection Efficiency (PDE) is a measure of the SiPM response sensitivity and in silicon depends on the wavelength of the incident light, as shown in Figure 3.5 (left), the applied over voltage and microcell fill factor. The PDE is defined as the statistical probability that an incident photon interacts with a microcell to produce an avalanche:

$$PDE(\lambda, V_{bd}) = QE(\lambda) \cdot \epsilon_{av}(V_{bd}) \cdot F \quad , \tag{3.2}$$

where QE(λ) is the quantum efficiency os silicon at a given wavelength λ, $\epsilon_{av}(Vbd)$ is the efficiency to trigger an avalanche process in the depletion region produced by V_{bd} and F (filling factor) is the ratio between the sensitive area and the sensor dimension. The chosen photosensor for the Mu2e calorimeter is a TSV-SPL SiPM from Hamamatsu [70]. SPL stands for Silicon Protection Layer, meaning an optical layer different from the standard epoxy used for blue wavelenghts. The blue markers in Figure 3.5 show its PDE compared to similar devices [71]. In the UV range 250-350 nm, the PDE of this UV-enhanced SiPM is of O(30)%, which is a factor ~ 6 better than a standard Hamamatsu SiPM.

These devices operate at low voltage (< 60V) while featuring a very high gain, a high PDE, a high-speed of response, an excellent time resolution and a wide spectral response range.

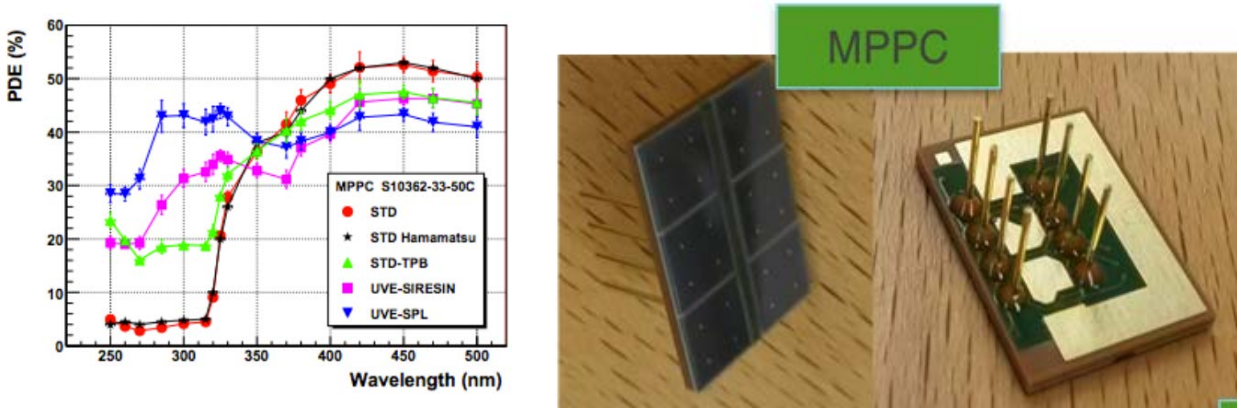

Figure 3.5: Left: photodetection efficiency as a function of the wavelength for four SiPM prototypes. The typical PDE values of the standard SiPM S10362-33-50C from Hamamatsu are shown for comparison. These measurements were performed at 25° and include effects of cross-talk and after-pulses. Right: picture of Mu2e array SiPM.

Over the breakdown voltage, the SiPM gain is directly related to its inverse polarization voltage:

$$G = \frac{Q}{e} = \frac{(V_{bias} - V_{bd}) \cdot C_{pixel}}{e}\,, \tag{3.3}$$

where V_{bias} is the voltage applied to the SiPM, V_{bd} is the breakdown voltage and C_{pixel} is the capacitance of a single pixel. The overall resistance of the photodetector, and then its breakdown voltage V_{bd}, is a function of the temperature:

$$R = R_0(1 - \alpha T)\,, \quad \alpha = \beta/T_0^2\,, \tag{3.4}$$

where β is a parameter depending on the device.

The analog sum of the output of each pixel forms the SiPM output. Assuming all pixels to be identical and producing the same charge, the number of impinging photons is directly proportional to the charge output. When a SiPM is hit by one photon, there is a dead time (also called recovery or quenching time), due to the presence of the quenching circuit. Thus, if there is a large flux of incident photons on the SiPM area, the number of fired pixels will saturate with the relation:

$$N = N_{max}(1 - e^{-\frac{\mu}{N_{max}}})\,, \tag{3.5}$$

where N is the number of active pixels, N_{max} is the total number of SiPM pixels and $\mu = N_\gamma \cdot PDE$ is the number of incident photons rescaled with the PDE.

A detailed discussion about the photosensors requirements and selection tests are discussed in details in Chapter 5.

3.2.3 Front End Electronics

The Front-End Electronics (FEE) consists of two discrete and independent chips (Amp-HV) for each crystal that are directly connected to the back of the photosensor pins. These provide both the amplification and shaping stage and a local linear regulation of the photosensor bias voltage (Fig. 3.6).

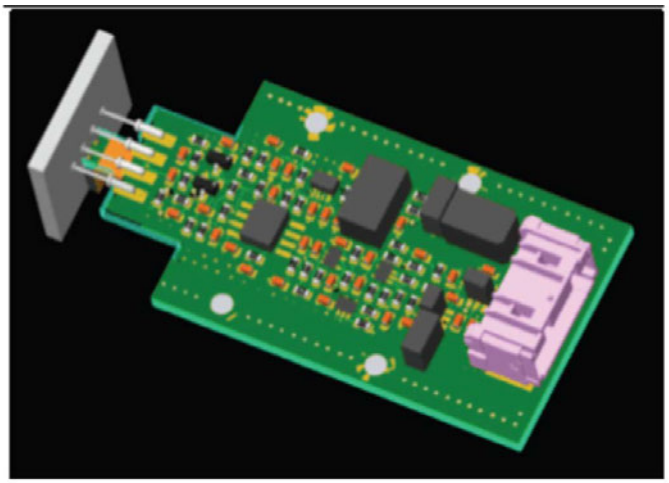

Figure 3.6: CAD drawing of the the AMP-HV integrated circuit.

The FEE board implements also the readout of current and temperature sensors whose values are then transferred to the Data Control System. The possibility to trigger a charge pulse test allows to monitor in time the gain of the amplifier, so to disentangle its contribution in the calibration phase. The Amp-HV board requirements are the following:

- two settable amplification values: 4 or 8, with low noise;
- a signal rise time comparable with 25 ns (5 times the digitizer sampling time) in order to allow at least five points to determine with precision the signal leading edge and therefore a good time resolution;
- a short falling time to improve pileup rejection;

- a high precision and stability in regulating and keeping the operation voltage of the photosensors;
- sustain a rate of 500 kHz/channel, while maintaining its gain, signal shape and the pileup rejection capability stable;
- a stable output regardless to the increase of the average current due to irradiation of the photosensors or to the radiation induced noise in the crystals, assuming those contributions to be contained below 2 mA;
- a low power consumption.

The FEE equivalent circuit, satisfying the requirements, is reported in Figure 3.7.

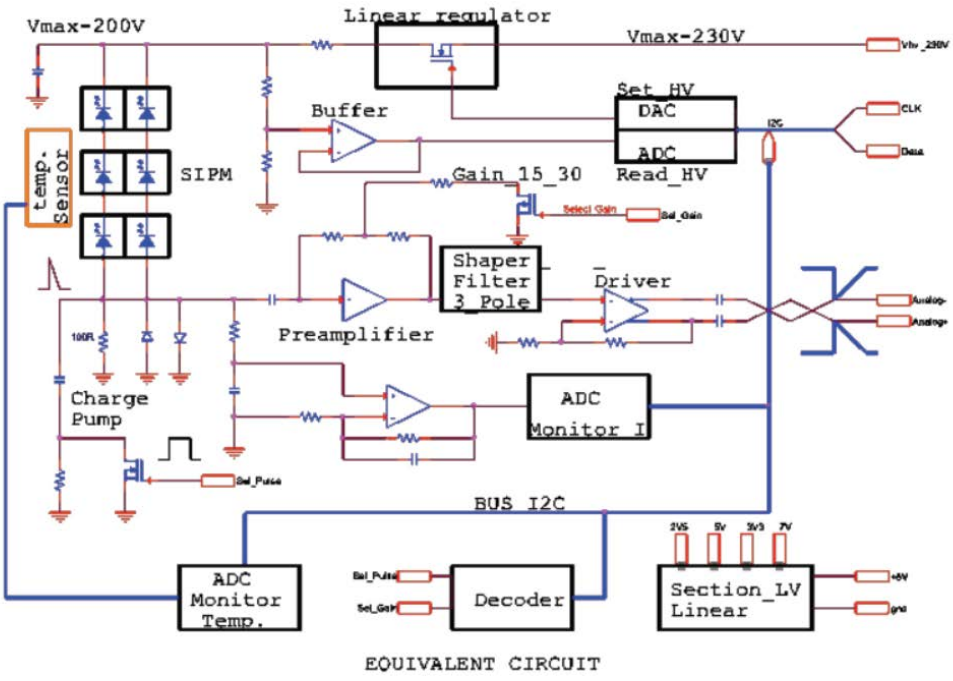

Figure 3.7: Layout of the equivalent circuit for the AMP-HV chip.

A pair of Amp-HV chips and one of photosensors are arranged in a modular unit as shown in Figure 3.8 called SiPM-holder. This holder is composed by a copper support where the two SiPMs of each crystal are plugged. The support holds also the two FEE electronic boards in thermal contact by means of bridge resistors. The FEE boards are shielded by a surrounding copper Faraday cage. The last

component of the holders is the optical fiber needle that will bring the light from the laser calibration system in front of the crystal; diffusion on the Tyvek provide a uniform illumination of the sensors.

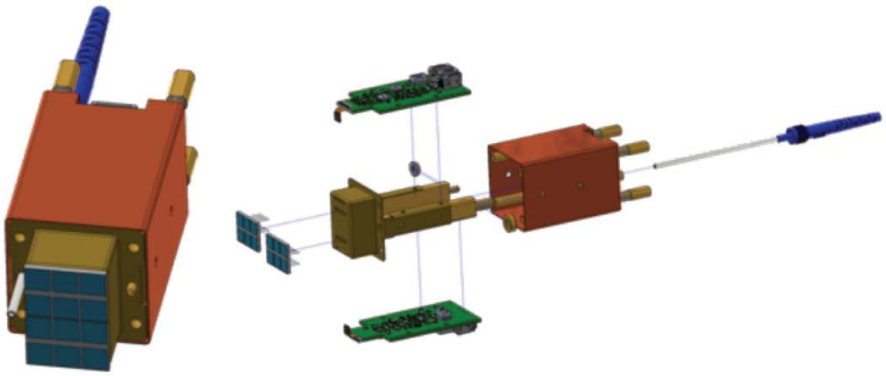

Figure 3.8: Left: assembly of the FEE holder. Right: exploded view of the FEE holder with all the components. Two SiPMs glued on the inner cupper support, FEE AMP-HV boards, Faraday cage and needle for insertion of the optical fiber.

Groups of 20 Amp-HV boards are controlled by a dedicated mezzanine board (MB), where an ARM controller distributes the low and high voltages reference values, while setting and reading back the locally regulated voltages. From MB, sets of 20 signals are sent in differential way to the Waveform Digitizer (WD) board (see next section). The parameters read out/set by the MB pass to the WD boards, which then communicate with the Detector Control System through an optical link. Both disks are subdivided into 34 similar pseudo-azimuthal sectors, each one grouping 20 crystals.

3.2.4 Data Acquisition System

The calorimeter has a total of 2696 fast analog signals to be digitized after being amplified and shaped by the FEE. An average pulses of 150 ns maximum width with a rise time of 20 ns is expected as input to the digitization state with a dynamic range of 2 V. The simulated shape of signals is shown in Figure 3.9; this width and shape are the results of convolution between the CsI emission time, the SiPM quenching time and the FEE amplification and shaping parameters.

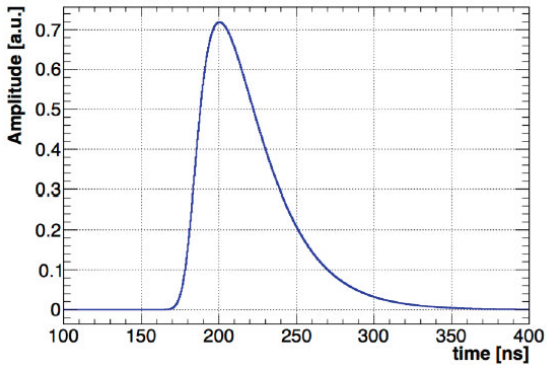

Figure 3.9: Monte Carlo simulation of the CsI + SiPM + FEE waveform.

The digitizing system contains 140 WD boards arranged in 10 crates per disk. Each WD board is cooled through an aluminum cold plate that is kept in thermal contact with the highest dissipation components. The cold plate will be thermally connected to the crate structure through card locks.

Simulations were used to optimize the digitization frequency and the bit resolution required to satisfy the Mu2e requirements: 200 Msps and 12 bits of resolution are a good compromise between performance, power dissipation and costs.

3.2.5 Waveform Digitizer Board

The WD has to digitize and serialize analog data and send them upstream to the DAQ system through a transceiver optic fiber. The WD board must also perform the zero suppression, to remove signals below threshold, and provide the mean charge and time for each channel by means of running averages.

Each board will handle 20 channels. The WD block diagram is shown in Figure 3.10. The design is based on a SoC component (FPGA + CPU integrated in the same package) belonging to the Microsemi Smartfusion 2 family, model SM2150T1152F. A very accurate jitter cleaner (LMK04828) will reduce the incoming clock jitter to less then 100 ps and distribute it to the ADCs and to the SoC. Signals will be sampled by 10 double-channels high-speed ADCs (ADS4229) and the FPGA will perform the online operation on data and the transmission to the servers [72]. At the moment of writing, a new radiation harder FPGA (Polar-Fire always from MicroSemi) is under

evaluation to improve the radiation hardness of the board.

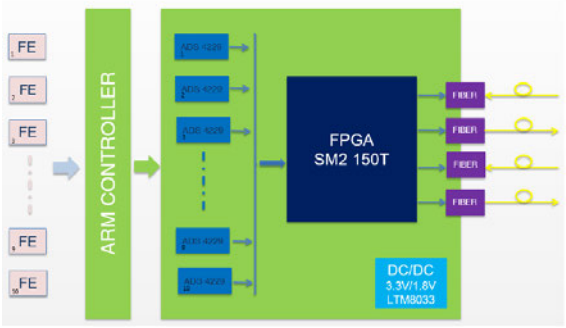

Figure 3.10: Block diagram for the Calorimeter Waveform Digitizer board, comprehending the MB and the Amp-HV chips: the principal components used are shown.

3.3 Mechanical Structure

The calorimeter mechanical structure is designed to support the layout of the crystals by piling then up in a self-standing array organized in consecutive staggered rows. The active area of the Mu2e calorimeter consists of two annular disks of 674 staggered crystals with a square prism shape, each one wrapped with a 150 μm thickness reflective Tyvek sheet for a total weight of 700 Kg.

Figure 3.11 is an exploded view of all the elements composing each annulus. Each crystals array is supported by two coaxial cylinders. The inner cylinder must be as thin and light as possible in order to minimize the passive material in the region where spiralling background electrons are concentrated. The outer cylinder is as robust as required to support the load of the crystals. Each disk has two cover plates. The plate facing the beam is made of Carbon Fiber to minimize the degradation of the electron energy, while the back plate can be also very robust. The back plate is needed also to support the SiPMs, the FEE and the SiPM cooling lines.

The crystal arrangement is self-supporting, with the load carried primarily by the outer ring. A catenary structure resembling a Roman arch is constructed to reduce the overall load on the inner cylinder. The back plane will be built of plastic material with good outgassing properties, like PEEK. It provides support for the

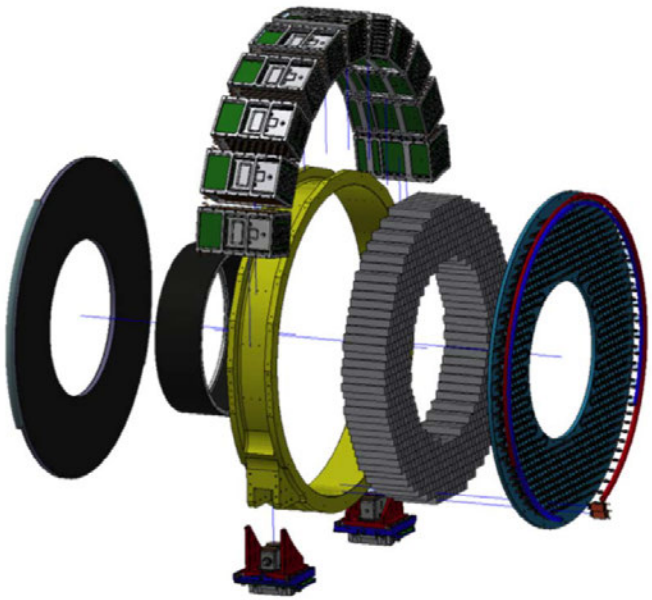

Figure 3.11: Exploded view of the components of the Mu2e calorimeter annular disks.

FEE electronics and SiPM holders and hosts the cooling pipes to dissipate the power of the electronics and cool down the sensors. A readout unit is composed of a crystal, two SiPMs and two AMP-HV chips. The back plate will provide visual access to each crystal. The Front Plate will be made of Carbon Fiber and will embed the piping for running the source calibration fluid.

3.3.1 Vacuum system and test

To reduce multiple scattering of CEs on air molecules and prevent discharge from detector high voltage, the entire muon beam-line, DS included, must have an internal pressure of 10^{-4} Torr ($\sim 10^{-7}$ atm) at most. To reach this value, the required limit for the outgassing rate of the whole calorimeter has been set at 8×10^{-3} Torr liter/s. This value is 1/10 of the allowed tracker outgassing (that has to deal also with gas leaks from the straws) in order to make the calorimeter contribution negligible.

The outgassing contribution of the calorimeter not-standard materials has been measured at the LNF-vacuum facility using the "known conductance" method [73], to determine the overall calorimeter outgassing level.

The outgassing measured values are summarized in Table 3.2.

Component	Q [Torr·liters/s]
Crystal+Tyvek	2.4×10^{-3}
FEE-MB + Cables	1.9×10^{-3}
Diffusive Spheres	1.2×10^{-4}
Full Holders	2.6×10^{-4}
Patch Panel Services - IFB cables	1×10^{-4}
Total	7.1×10^{-3}

Table 3.2: Outgassing measurements of calorimeter components.

To quantify contributions from virtual leaks, a parallel measurements campaign has been carried out by testing a large calorimeter prototype (Module-0) in vacuum. The 51 channels prototype was composed with components very similar to the ones of the final calorimeter. The difference between the direct measurement of its outgassing value and the sum of the single components' contributions provides an estimate of the contribution from virtual leaks. A total outgassing rate of 9×10^{-4} mbar·liters/s is obtained, that practically satisfies the calorimeter vacuum rate requirement.

3.3.2 Cooling System

Because electronics operate inside a vacuum cryostat at 10^{-4} Torr, the cooling is a crucial element of the calorimeter. The power generated by SiPMs, FEE and read out electronics must be removed within temperature values acceptable for the correct operation of each device. Furthermore, the difficult access to components requires a cooling system free of fault and maintenance for at least one year. The cooling system has to maintain SiPM temperature below 0°C to minimize their dark current: this is obtained by choosing as refrigerating fluid a mixture of 35% mono propylene and water that has the freezing temperature of -17°C. To ensure a good

thermal contact, the cooling pipes are vacuum brazed to a C profile posed on the backplane and the SiPM holders are directly bolted to it, as shown in Figure 3.12.

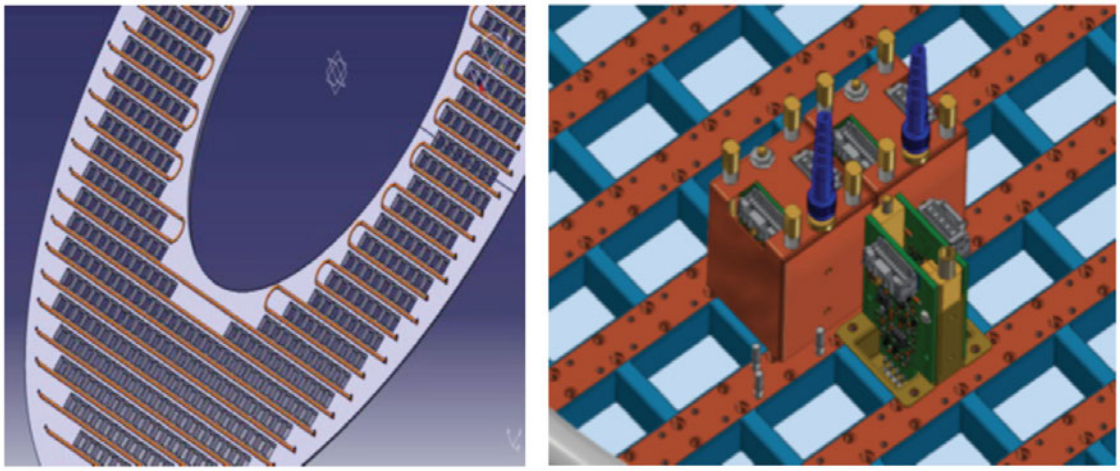

Figure 3.12: Left: Views of the cooling back plate with zoom of the small cooling lines. Right: Details of the SiPM/FEE holders connected to the cooling lines.

In air, the electronic components on the WD board can operate at 120°C, but to improve the reliability the operating temperature is set to 60°C. The cooling solution for the WD boards crate is shown in Figure 3.13: the two crate plates are maintained at low temperature by a brazed cooling coil; a custom aluminum plate over each board, fixed to the crate with two card locks, ensures the thermal contact between the integrated components and the crate.

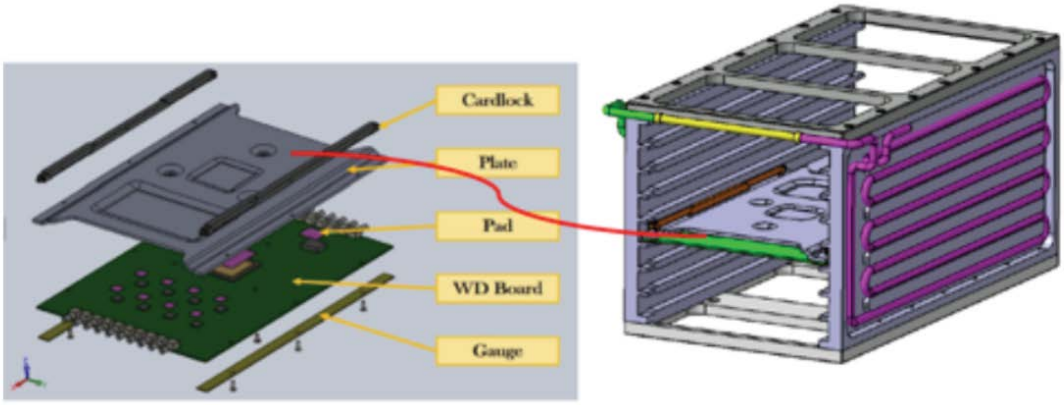

Figure 3.13: Left: views of the cooling back plate with zoom of the small cooling lines. Right: details of the SiPM/FEE holders connected to the cooling lines.

To guarantee the mechanical detector precision, the uniformity of the temperature of the cooling fluid inside the pipes has been set at the level of 2°C. A long set of thermal measurements have been carried out on prototypes (board, SiPM sensors and crates) at INFN Pisa and on the full size calorimeter prototype at the National Laboratory of Frascati. These studies have shown that: 1) the temperature gradient on the crystals is under control; 2) an equilibrium temperature of the mechanical structure is achievable; 3) the SiPMs can be cooled down at the required level with circuit losses in good agreement with the thermal simulation.

3.4 The calibration systems

The high sensitivity required to the Mu2e experiment implies a special care in detector calibration to avoid any systematic effects. In the calorimeter either time and energy need calibration. To monitor the calorimeter performance, different independent calibration methods will be followed using:

- a radioactive source;
- a laser pulsing system;
- the decays of stopped muons and pions;
- cosmic-ray muons.

3.4.1 Radioactive source

A liquid radioactive source (Fluorinert^{TM}) is used to provide an absolute energy scale and the response equalization between crystals. This liquid source circulates through aluminum pipes on both disks surface, and is activated by a neutron source, producing the following decay chain:

$$\begin{aligned} {}^{19}F + n &\rightarrow {}^{16}N + \alpha \\ {}^{16}N &\rightarrow {}^{16}O^{*} + \beta^{-} + \bar{\nu}_e \ (\tau_{1/2} = 7\text{s}) \\ {}^{16}O^{*} &\rightarrow {}^{16}O + \gamma(6.13 \text{ MeV}) \end{aligned}$$

The liquid source circuit consists of 12 Al pipes, 0.5 mm thick, with a diameter of 3/8 inches and a length which ranges from 1.5 to 1.7 m. The selected geometry allows to have an uniform illumination of the disk with a variation in the intensity smaller than 5% [74].

The 6.13 MeV photons interact with the crystals: the overall energy distribution as reconstructed by the calorimeter is shown in Figure 3.14. In this distribution the different contributions are shown: the full absorption peak at 6.13 MeV, the two escape peaks [1] respectively at 5.62 MeV and at 5.11 MeV; these peaks are then superimposed with the Compton spectrum.

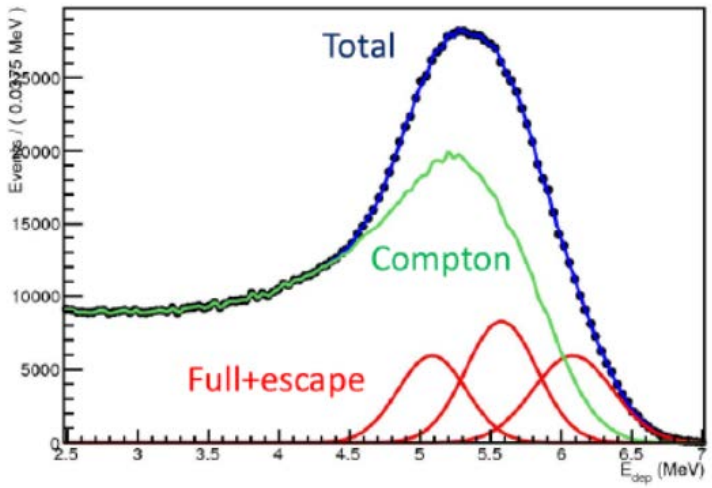

Figure 3.14: Energy spectrum for a crystal irradiated with 6.13 MeV photons from an $^{16}O^{*}$ source.

The source rate is expected to be $\sim 10^4$ photons/crystal/10 minutes. The level of the equalisation that could be reach is of about 1.5%. This 10 minutes long calibration will be performed once a week, to check the absolute energy scale of the calorimeter, at low energy.

3.4.2 Laser system

A laser monitor system is used to control photosensors' gains, charge and timing resolutions, as well as to perform a fast equalization of time offsets. A green light laser has been chosen. The overall system is described in Figure 3.15. A pulsed

laser sends light through standard collimation optics to an optical splitting system to subdivide the beam into 8 equal sub-beams.

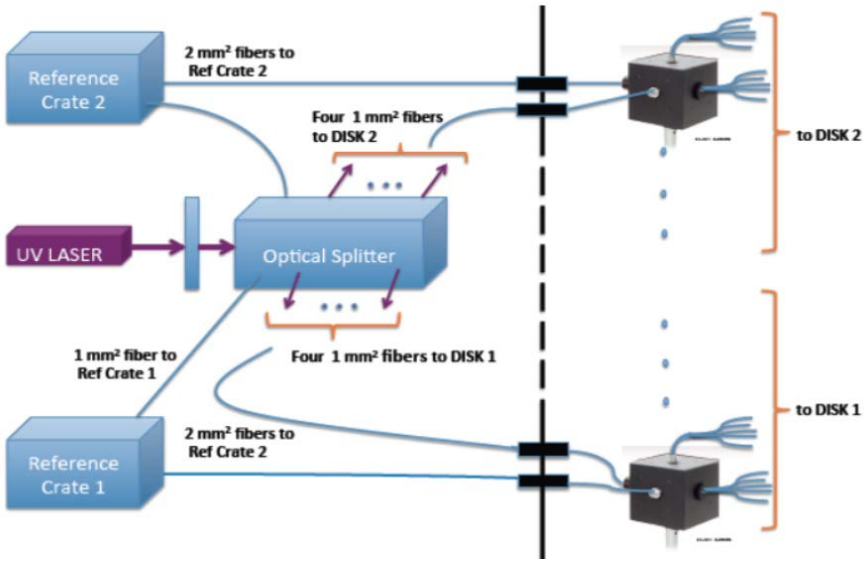

Figure 3.15: Schematics of the Laser Monitoring System.

By means of eight 1 mm diameter, 60 m long quartz fibers, the light is brought inside the DS. On each disk, there are four integrating spheres with one input for the incoming fiber and three outputs for fibers bundles. Each bundle is composed of 70 silica fibers with 200 μm diameter, for a total of 840 fibers/disk. 674 of these fibers are used for calibration, the remaining 166 are spares. The end of each optical fiber arrives up to the readout side of the detector, where is inserted in the FEE/SiPM holders. In this way, the light arriving from the fiber illuminates the crystal and is readout by the photosensors.

A laser pulse corresponding to an energy deposition of 50 MeV is sent at each spill-off period, i.e. once each 1.33 s. The laser system is expected to provide a 0.5% equalization of all channels in 25 minutes.

3.4.3 DIO Muons and Pion Decays

For energy calibration at a scale closer to 100 MeV, muons and pions decays will be used. The most promising decay channels are:

- $\pi^+ \to e^+\nu_e$ decays of pions, that produces a monochromatic positron of about 69.8 MeV;
- electrons from decay in orbit muons (DIOs), $\mu^- \to e^-\nu_\mu\bar{\nu_e}$ that have a characteristic spectrum edge at 52.8 MeV.

After matching the calorimeter cluster with the electron/positron track, the particle momentum is derived by the tracker with an accuracy much better than 0.5%, so allowing an energy calibration of the calorimeter with similar accuracy.

Unfortunately, at nominal field, both particles decay illuminate only a reduced part of the detector, due to the relation between the particle momentum and the radial coordinate. Dedicated runs at reduced magnetic fields will be required to provide a uniform coverage of all calorimeter crystals. Furthermore, when the magnetic field is reduced, the rate of particles on the detectors dramatically increases and the tracker resolution deteriorates: a reduction of the beam intensity is therefore required. Therefore the calibration with pions and muons presents also some drawbacks as shown below.

The calibration with the $\pi^+ \to e^+\nu_e$ decays requires: 1) a modification to the beam line by rotating the collimator in the TS for a positive charge particle selection; 2) a different time window for data acquisition; 3) a reduced magnetic field down to 0.7 T; 4) a reduction of the beam intensity and a degrader located before the muon Stopping Target to increase the number of total stops, since the branching ratio of the process is $\sim 10^{-4}$ and only 10^{-6} pions per proton on target are stopped.

DIO electron calibration does not require any modification of the beam line and can be performed in shorter times due to the larger available statistics. For this calibration, the magnetic field must be reduced to 0.5 T and the intensity at 50% of the nominal value. A detailed description of this procedure has been studed by simulation as a part of this thesis and it is reported in Chapter 7.

3.4.4 Cosmic Rays

Cosmic rays calibration in the Mu2e calorimeter is complementary to all other calibration techniques described before. Cosmic ray events can be acquired during nor-

mal run operations with a dedicated trigger. The energy calibration is performed by reconstructing the cosmic muon path length and measuring the energy deposit released on the calorimeter crystals. The distribution of deposited energy in a single crystal is shown in Figure 3.16: the minimum ionizing particle peak for the Mu2e CsI crystals corresponds to a 20 MeV energy deposition.

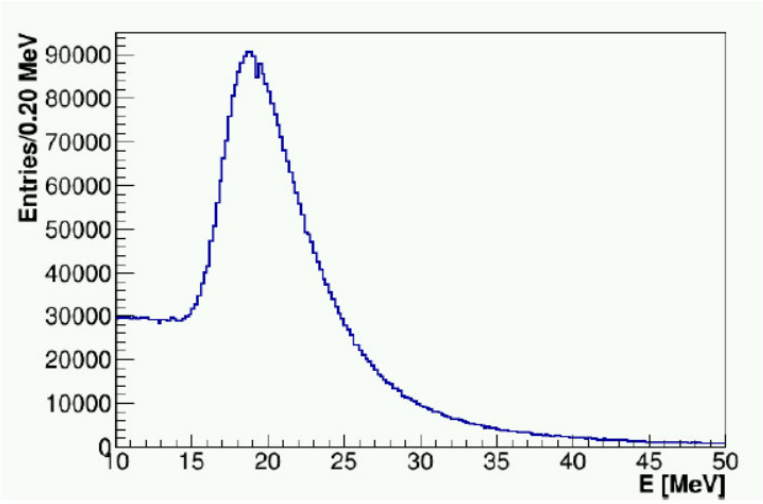

Figure 3.16: Distribution of the energy released by a cosmic muons in a single crystal.

The expected energy equalization is at the level of ∼1%, providing a small contribution to the calorimeter energy resolution. Since cosmic muons are relativistic particles, the time they take to cross the calorimeter can be used to align the time offsets among channels without relying to any external time reference. Following this procedure, the alignment of the time offsets alignment is expected to be within ∼50 ps. Simulation shows a rate of 15 Hz for cosmic events useful for calibration purposes, corresponding to 1000 events/crystal after ∼5 hours.

3.5 Simulation of the calorimeter performance

Calorimeter performance has been studied using Monte Carlo. Event simulation proceeds in several steps. The interaction of the incident particle with the crystals is first simulated by GEANT4 [75] and the deposited energy is then converted into optical photons, taking into account an average photoelectron yield of 30 p.e./MeV and a Longitudinal Response Uniformity of few % along the crystal axis. The

response of each SiPM is then simulated, including a Poissonian photostatistic fluctuation and a gaussian distributed electronic noise (150 keV equivalent). A fully digitized waveform shape is introduced as a function of number of photoelectrons. The individual hits are extracted by the single waveforms, including the possibility of multiple pile-up contributions, to form the final crystal hits. The generated pulses are then processed for reconstructing timing and energy. Time is reconstructed by performing a fit to the leading edge with an analytic function, while energy is reconstructed by integrating the pulse (detailed description of both algorithms is reported in the next chapter). Calorimeter clusters are finally formed by means of a dedicated algorithm described in the next section.

3.5.1 Geometry

The dimension and shape of the calorimeter disks were the first issue addressed by the simulation. A simplified algorithm to estimate the signal efficiency as a function of the disk dimension was used to select the acceptable configurations. The separation between disks was set to 70 cm, corresponding approximately to a half CE wavelength. A full simulation was performed to confirm the preliminary results and select the final geometry: a crystal size of 34 mm with inner and outer disk radii of 374 mm and 660 mm, respectively. This solution is robust against small variations of the crystal size. The distance between the disks was then re-evaluated, confirming the value of 70 cm as optimal. The position of the disk with respect to the tracker has a negligible impact on the efficiency, as expected from translational invariance. Finally, the crystal length was studied, and a value of 20 cm, corresponding to approximately 10 X_0 chosen. This geometry ensures sufficient space to mount the readout at the back of the crystals while maintaining high reconstruction efficiency and limiting the number of readout channels.

3.5.2 Cluster reconstruction

The clustering algorithm starts by taking the crystal with the largest reconstructed energy as a seed, and adding one by one crystals that satisfies the following requirements:

- have a common side with the crystals already included;
- have reconstructed time within ±10 ns from the seed crystal time;
- have reconstructed energy 3 times larger than the expected electronic noise.

3.5.3 Energy resolution

The energy resolution has been estimated by simulating $\mu\ N \rightarrow e\ N$ conversion electrons (E=104.97 MeV) together with the expected background.

The distribution of the difference between the true signal electron energy obtained by simulation (EMC) and the reconstructed cluster energy (E) is plotted in Figure 3.17 (left). The distribution shows an higher left tail due to leakage. The energy resolution has been estimated as FWHM/2.35 = 3.8±0.1 of the distribution, which is about 5 MeV RMS.

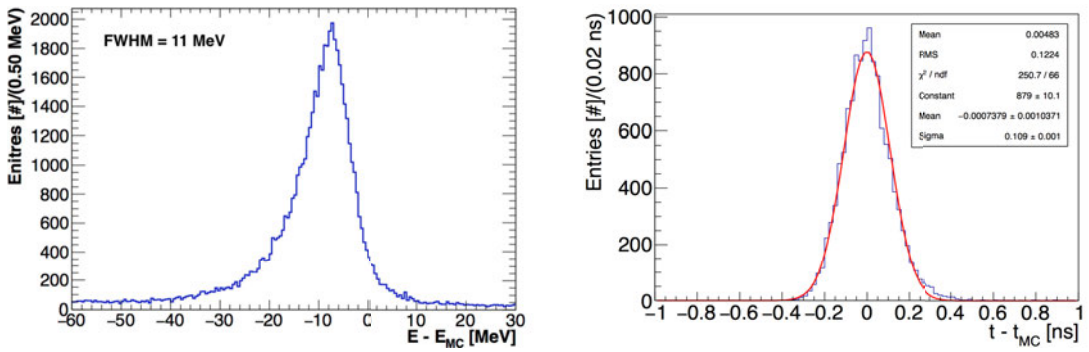

Figure 3.17: Left: distribution in energy residuals between the reconstructed cluster energy and the Monte Carlo value. Right: distribution of the time residuals between the reconstructed cluster time (t) and the Monte Carlo truth (t_{MC}).

The resolution depends on crystals characteristics, such as light yield e longitudinal response uniformity. A dedicated simulation study (Fig. 3.18) showed that a longitudinal response uniformity below 5% and a light yield above 20 30 p.e/MeV are sufficient to achieve good resolution.

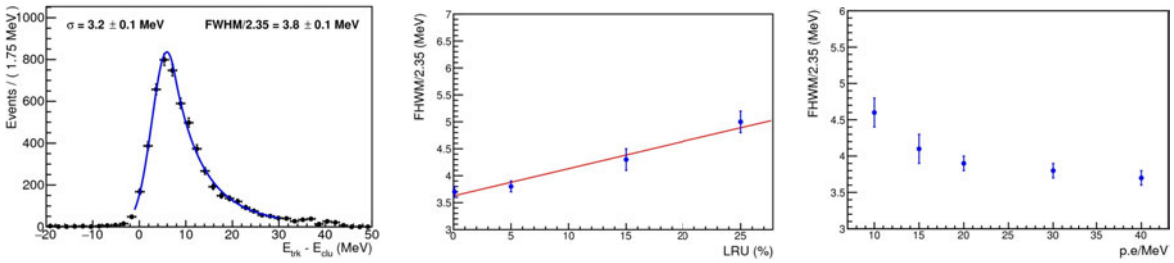

Figure 3.18: Left: energy resolution fit with a double-sided Crystal Ball function, quoting both core resolution (σ) and FHWM/2.35. The core resolution is more sensitive to the pile-up, while the FHWM is more representative of the "total" resolution. Middle: FHWM/2.35 as a function of crystal longitudinal response uniformity. Right: FHWM/2.35 as a function of crystal lyght yield

3.5.4 Coordinate resolution

The cluster position is necessary to match the reconstructed tracks with the calorimeter cluster. These coordinates are obtained using the linear energy weighted mean. The coordinate resolution has been estimated by simulating $\mu\, N \rightarrow e\, N$ conversion electrons together with the expected background. The distribution of the difference between the predicted and actual position of the track at the calorimeter surface demonstrates that a coordinate resolution of about 6 mm can be achieved [1].

3.5.5 Time resolution

As already mentioned, the simulation of the signal digitization process has been modeled using as input the waveform acquired with an experimental test. Assuming a constant pulse shape, the best accuracy is achieved by setting the signal time at a threshold corresponding to a constant fraction (CF) of the pulse height.

The cluster time is then defined as the linear energy weighted time of all the crystals belonging to the cluster. The time resolution has been estimated by simulating conversion electrons. Figure 3.17 (right) shows the time residuals between the reconstructed cluster time and the Monte Carlo truth. A Gaussian fit to this distribution shows that the expected time resolution is of about 110 ps.

3.5.6 Radiation environment

A large flux of charged particles, photons, and neutrons can affect crystals, sensors and readout electronics performances.

In general, all known crystals suffer from some radiation damage. There are three possible damage effects [93] in scintillator crystals:

- damage to the scintillation-mechanism;
- radiation-induced absorption;
- radiation-induced phosphorescence.

A damaged scintillation mechanism would reduce LY and may also change the LRU along the crystal if the radiation profile is not uniform along the crystal axis. Photons' absorption induced by radiation reduces the light attenuation length. Contrary to other crystals, in CsI thermal annealing and optical bleaching were found to be not effective to recover this effect [94]. Moreover, radiation-induced afterglow causes a Readout Induced Noise (RIN) that can increase the dark current in photo-detectors.

In order to understand the radiation environment of the Mu2e calorimeter crystals, a detailed simulation was performed to include all expected radiation sources as summarized in the following list:

- beam flash;
- DIO electrons;
- neutrons, protons and photons produced in the stopping target via nuclear capture;
- particles produced by muons stopped outside the Al stopping target (OOT).

3.5.6.1 Ionizing dose

The Mu2e radiation environment is calculated with a GEANT-4 based full simulation. The dose is dominated by the contribution of the beam flash, with a smaller

component due to electrons from muons decaying in orbit, neutrons, protons, and photons. The expected dose rate for each crystal of the calorimeter disks is shown in Figure 3.19, where the dose as a function of the disks radius is reported [95]. The average dose in the calorimeter is about 3 and 0.5 krad/year in the front and back disk respectively, with 6 krad (5 krad) for the innermost crystals (SiPMs) in the front disk. The expected rate results is of ∼1 rad/h in the hottest region.

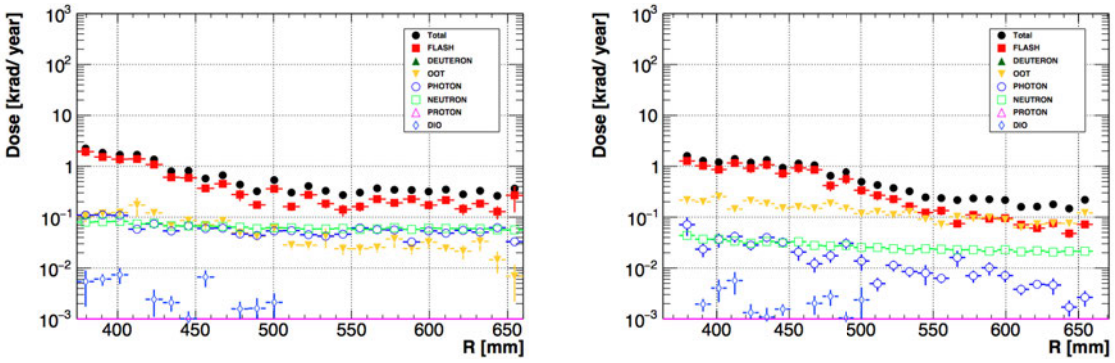

Figure 3.19: Expected dose in the front (left) and back (right) CsI disks as a function the radius where the crystals are located.

3.5.6.2 Neutron fluence

In neutron interactions, the energy is primarily deposited by non-ionizing processes, resulting in damage from atoms displaced from their position in the lattice structure. For neutron energies between 50 keV and 14 MeV, the neutron-matter interaction mainly proceeds through neutron-neutron elastic scattering (n,n), or inelastic neutron-neutron scattering (n,n'), neutron-proton (n, p) and neutron-alpha (n,α) interactions. About half of the neutron energy is transferred to the nucleus (detailed calculations are given in [76]). The displacement damage induced by neutrons in Si based devices is usually normalized to the damage induced by 1 MeV neutrons, referred to as "1 MeV equivalent damage" [77]. The neutron flux at the front face of each disk is fairly uniform around 2×10^{11} neutrons/cm^2/year. In the second disk, the neutron flux peaks at about 10^{11} neutrons/cm^2/year in the innermost region, being not shielded by the first disk, and gets reduced down to 4×10^{10} neutrons/cm^2/year in the outermost part, thanks to the shielding provided by the first disk. Thus the number of neutrons absorbed by the crystals is at most 10^{11} neutrons/cm^2/year.

The expected neutron fluence on SiPMs as a function of their position in radius is shown in Figure 3.20.

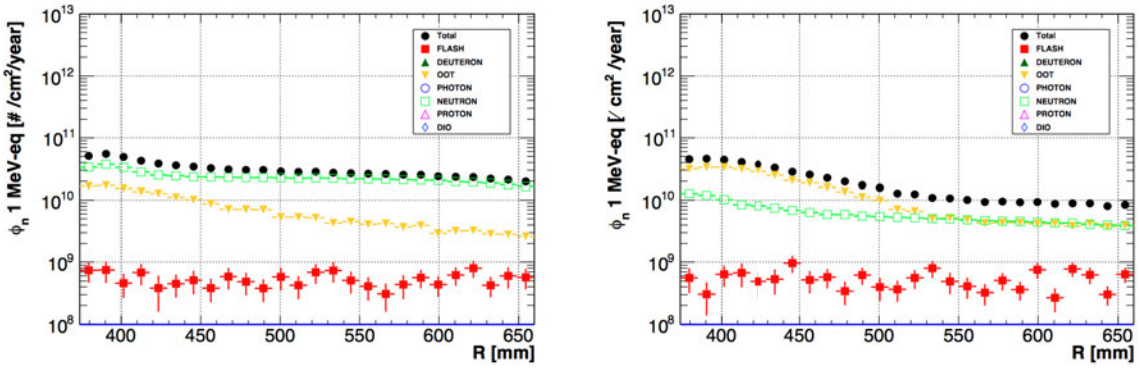

Figure 3.20: 1 MeV-equivalent neutron flux as a function of the radial position at the back face of the front (left) and back (right) disk. The backgrounds representing less than 1% of the total flux are not drawn.

3.5.7 Particle identification and muon rejection

Even if the tracker momentum resolution is sufficient to distinguish a CE signal from background, a combination of hits from lower energy particles could result in an erroneously reconstructed CE signal: even a coarse confirmation of the particle's energy will then be fundamental to reject this kind of background from spurious combinations of hits from lower energy particles. Indeed, the tracker can measure charged particle momenta with a good resolution (<200 KeV/c at 100 MeV), but this single information is not enough to distinguish among particles types. This is doable combining together tracker and calorimeter informations. The signals from the tracker and from the calorimeter are correlated in time. The time of the calorimeter signal should be comparable to the time of impact of the extrapolated tracks from the tracker. The difference between these two times should be less than 0.5 ns and this value drives the timing resolution requirement of the calorimeter [1].

The calorimeter timing information can be used by the cluster reconstruction algorithm in several ways: for the cluster reconstruction itself, a good time resolution helps in the connection and rejection of cells to the cluster and in the cluster merging. Moreover, timing information can also be used to improve the pattern recognition in the tracker and add discriminating power to the particle identification of μ with respect to the electrons (PID). Figure 3.21 shows how the calorimeter allows a simplification of the pattern recognition: the speed and efficiency of tracker reconstruction is improved by selecting tracker hits compatible with the time ($|\Delta\, t| < 0.5$ ns) and azimuthal angle of calorimeter clusters.

The main goal of the PID in Mu2e is to separate potential electron candidates from muons which could be associated with the beam or produced in the showers generated by cosmic rays. Cosmic rays generate two distinct categories of background events: muons trapped in the magnetic field of the DS and electrons produced in a cosmic muon interaction with detector material.

Studies on cosmic ray induced background, assuming a CRV inefficiency of about 10^{-4}, showed that after three years of data taking one could expect about three events in which negative cosmic muons in the momentum range $103.5 < p < 105$ MeV/c enter the detector, while not being detected by the CRV counters and sur-

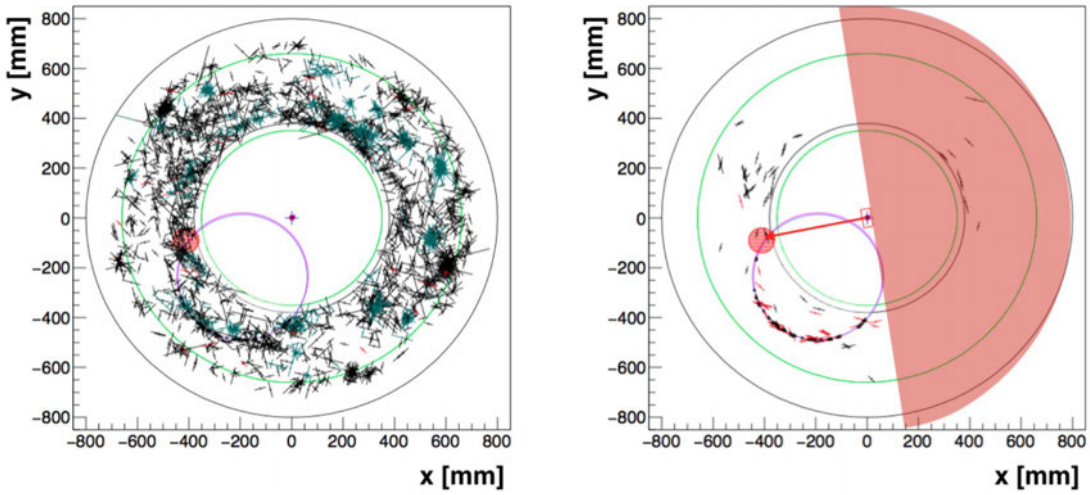

Figure 3.21: Distribution of the hits in the tracker before (left) and after (right) the application of a timing window based on timing information in the calorimeter. The situation for the pattern recognition is dramatically improved: fitting a helix to the selected tracker hits and calorimeter cluster increases the tracking efficiency by 9%

viving all analysis cuts [78]. The event display of a such kind of event is shown in Figure 3.22.

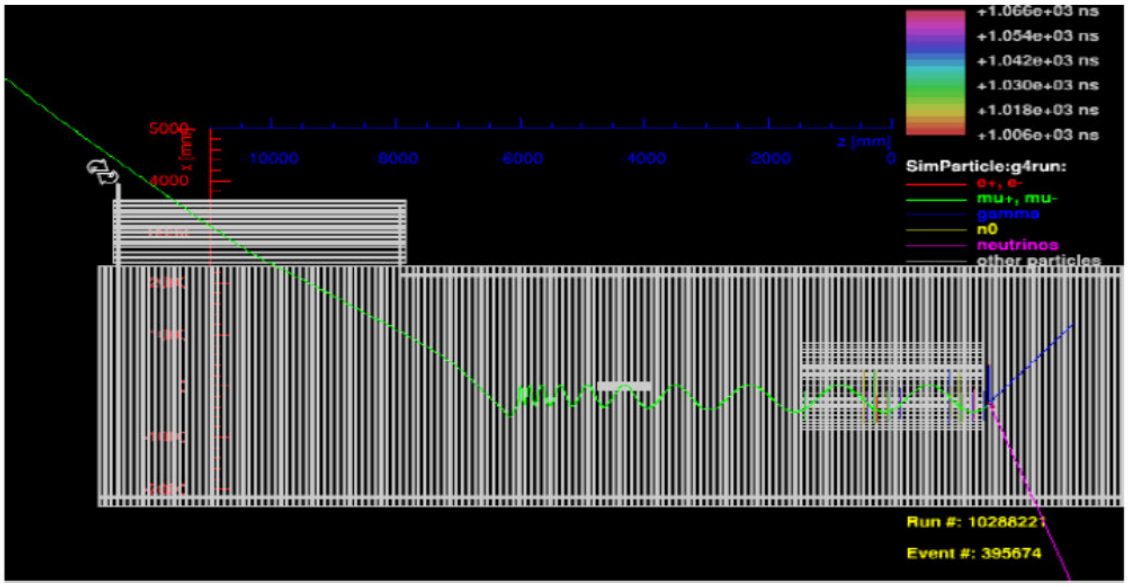

Figure 3.22: Event display of a negative muon from cosmic rays mimicking a CE signal.

Thus, to keep the total background from cosmic rays at a level below 0.01 events, a muon rejection factor > 200 is required. The dE/dx information from the Mu2e

tracker provides minor PID capabilities [79]. To reach a muon rejection factor of 200, the efficiency of the electron identification based on tracker-only information would be below 50%. The energy measurement from the calorimeter and the time-of-flight measurement that results from the both detectors measurements provide information for an efficient separation of electrons from muons. In Figure 3.23 the distributions of the time difference between the track and cluster times and the E/p are reported both for muons and electrons at 105 MeV/c, showing a clear separation between the two particles. A PID likelihood is built combining these two variables.

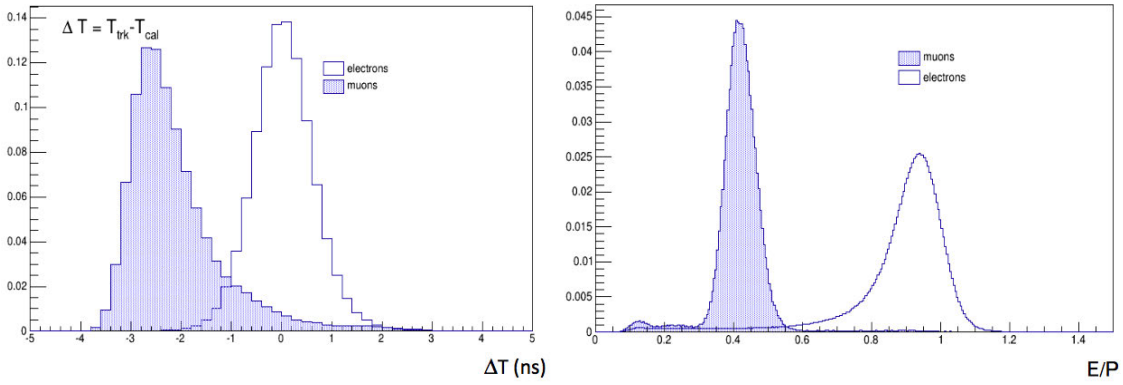

Figure 3.23: Distributions of time difference, Δt, between the track and the cluster (left) and E/P (right) for 105 MeV/c electrons and muons [1].

The calorimeter acceptance has been optimized to reveal 99.4±0.1 % of the CEs produced from the stopping target, with tracks passing "Set C" quality cuts [82] and producing a calorimeter cluster with $E > 10$ MeV from the conversion electron. Therefore a reconstructed CE candidate event is required to have a calorimeter cluster, pointed to by a track.

In Figure 3.24 the dependence of the electron identification efficiency, for the case with a rejection factor set at 200, on the timing resolution for different values of the calorimeter energy resolution is reported.In the expected operational range, $\sigma_E/E < 0.1$ and $\sigma_T < 0.5$ ns, the PID is robust as a function of the time resolution and energy resolution values, while keeping the electron identification efficiency variations below 2% in this region of parameter space.

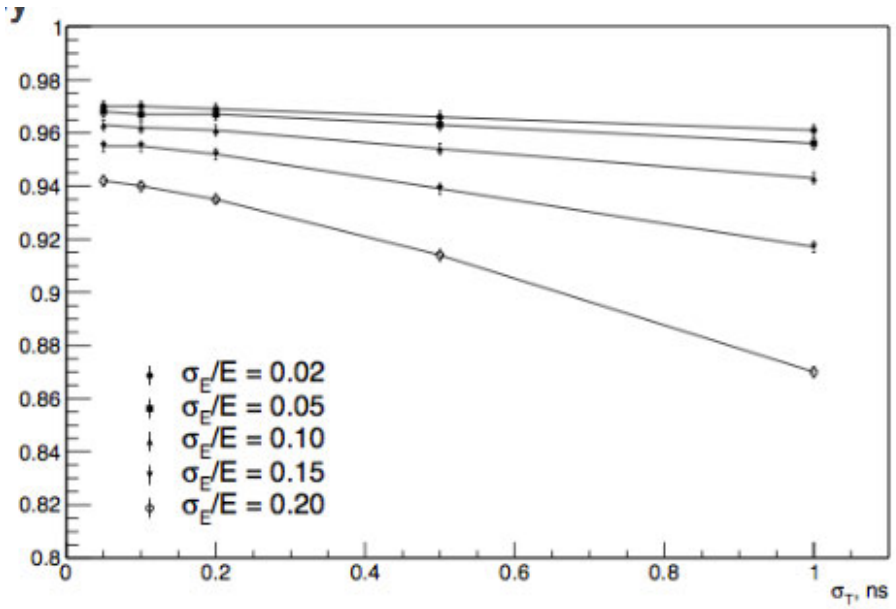

Figure 3.24: PID efficiency for CEs for muon rejection factor of 200 and different assumptions about the calorimeter energy and timing resolution.

3.5.8 The calorimeter trigger

In the current design, the Mu2e trigger consists of a set of software algorithms, aiming to filter with the highest possible efficiency the events of physics interest, while keeping the total rate under 2 kHz and the data rate to tape below 0.7 GB/s.

Among the events of physics interest one has to include the control samples needed to calibrate the tracker and the calorimeter (i.e. DIO events and cosmic rays) or to evaluate the backgrounds for the conversion electron analysis (like the radiative pion capture events). The global requirements for the Mu2e trigger are: i) an efficiency better than 90% on the Mu2e physics data set; ii) a background rejection factor larger than 100; iii) a processing time shorter than 3.6 ms/event.

A dedicated study, based on a boost decision tree (BDT) multivariate classifier, demonstrated that a calorimeter standalone trigger can fulfill all these requirements [80] [81], by combining timing, radial position, energy and cluster topology information. The BDT classification training for the trigger has been performed using the 4.1.2 TMVA (Toolkit for Multivariate Data Analysis) libraries, provided by ROOT analysis tools [103]. The trigger classifier has been trained using ∼12000 events

with CEs mixed with the expected spurious hits coming from the majority of the background sources and the same amount of pure background events. In order to optimize the efficiency on the Mu2e physics dataset, the standard Mu2e quality cuts [82] have been applied to define the CE training sample. No preselection cuts were applied to the background training sample. Different training categories have been used for the two calorimeter disks, to take into account their different occupancy and signal to background ratio. Figure 3.25 reports on left the classifier efficiency on CEs versus the radial position of the electron impact point on the calorimeter. The efficiency drops below 80% when the radial position goes below 425 mm: this corresponds to the radius of the inner ring of crystals in the calorimeter disks. A small efficiency drop is also seen when the shower peak approaches the external edge of the disk and can be explained by the lateral energy leakage effect. On right, the classifier efficiency on CEs versus the electron impact time on the calorimeter: the efficiency is above 80% also before of the live gate starting from 700 ns that is used for the analysis and is steadily above 90% above 900 ns. The overall trigger efficiency is 90.5%. The final background rejection is 100.

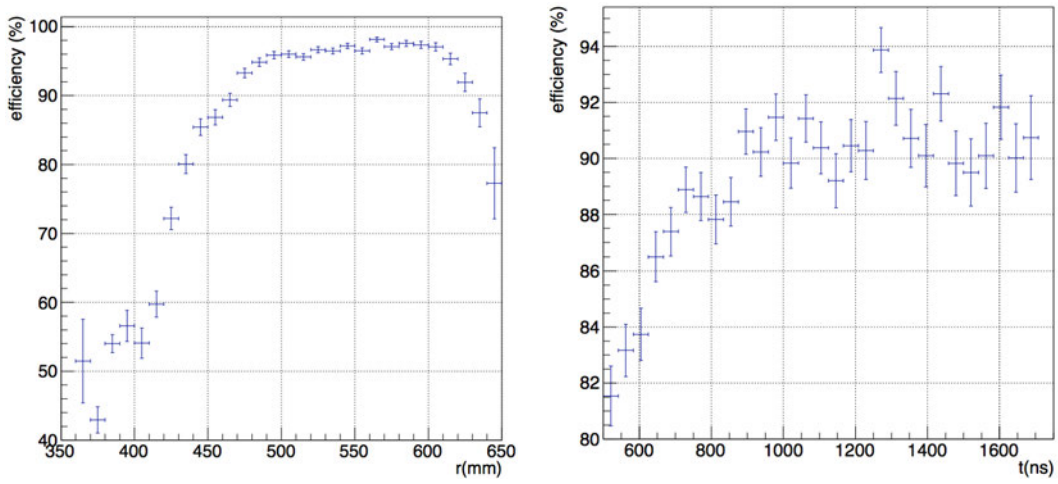

Figure 3.25: Left: CE BDT efficiency versus the conversion electron impact radial position after preselection. Right: CE BDT efficiency versus the conversion electron time position after preselection.

This trigger will take the form of a High Level Trigger filter that will be used after streaming the events to the online computing farm, but before storing data on disk. The most important aspect of this filter is that it is fully independent from

the tracker. It is important for smooth start-up of the experiment when running conditions are not perfectly known and for determining the tracker trigger efficiency. The average processing time is 0.9 ms/event and may be improved by performing the digitizer waveform peak search at the FPGA level.

Chapter 4

Quality assurance of undoped CsI crystals

Figure 4.1: Picture of the pre-production crystals received from Amcrys, Saint Gobain and Siccas vendors.

The Mu2e calorimeter consists of 1348 undoped CsI crystals with parallelepiped shape of $34 \times 34 \times 200$ mm^3 dimensions. The physics requirements discussed in

Section 3 were used to define a set of requirements on the mechanical, scintillation and radiation hardness properties of the crystals. The mechanical dimensions are critical to allow a correct stacking and alignment of the crystals inside the calorimeter disks. The optical properties are crucial to reach the required time and energy resolution of the detector. The radiation hardness ensures operation in the Mu2e environment.

4.1 Pre-production crystals

At the end of 2016, beginning of 2017, a pre-production from three international vendors has been organised to control quality and select the best provider for the calorimeter construction. The vendors selected for the Mu2e preproduction crystals were (Fig. 4.1): Amcrys (Ukraine), Saint Gobain (France) and Siccas (China). In the following sections, a detailed description of the tests done to qualify these crystals and improve our Quality Assurance (QA) procedures in view of the large size production is reported.

4.1.1 Mechanical Properties

Each calorimeter disk is composed by an external annular mechanical shell in aluminum that provides a self-supporting structure. The crystals will be piled up inside this shell without any dedicated alveolar structure. An inner ring in Carbon Fiber will allow to keep stacking crystals around the center hole. Because of this procedure, the tolerance on the crystal dimensions and shapes are critical to allow a correct stacking and alignment of the 674 crystal units.

Due to the operation in vacuum and to grant feasibility for access and replacement of the photosensors, we avoid gluing the SiPMs to the crystal read out face and housed them in an independent rigid structure (back or FEE-disk). Therefore the crystal-to-photosensor alignment is highly sensitive to the crystal position and tolerances. A right 3D shape of the crystal is also useful to ensure coplanarity among the crystals in the same layer, so to reduce the mechanical stress among crystals. A detailed engineering study defined a set of requirement as reported below:

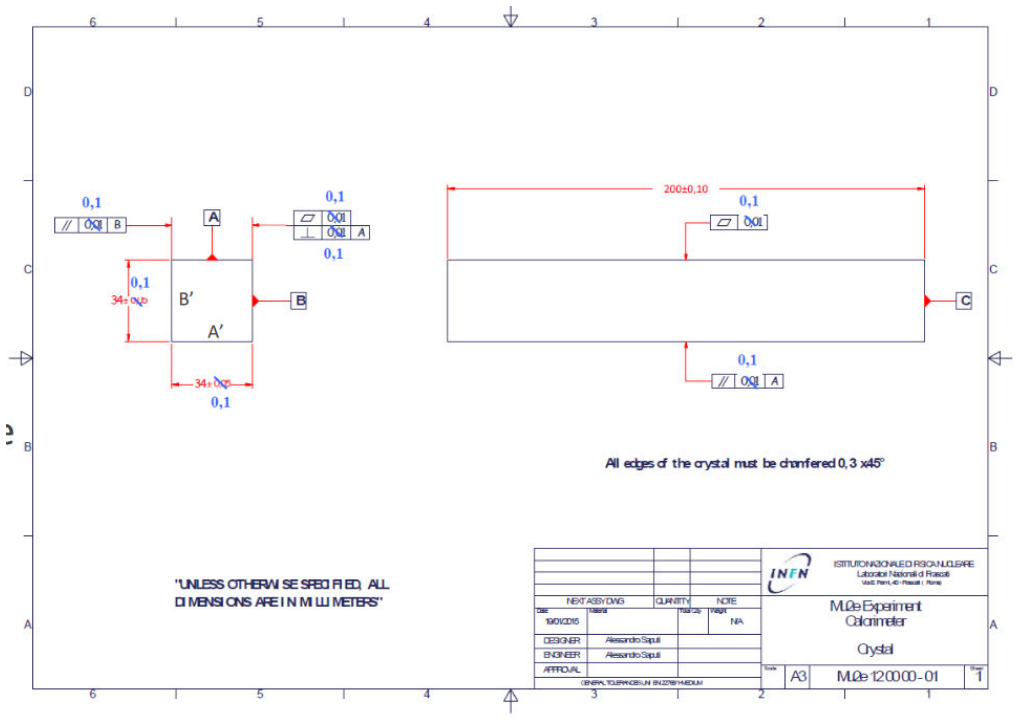

Figure 4.2: Technical draw of a Mu2e crystals. Dimensional tolerances are within 0.1 mm.

- preserved mechanical integrity of the crystal (no cracks, chips, fingerprints or bubbles);
- the deviation from a perfect 3-dimensional parallelepiped has to be less than 100 μm;
- the mechanical tolerances for the transversal (longitudinal) dimensions has to be of $\pm$ 100 (200) μm.

These requirements are also summarized in Figure 4.2.

4.1.1.1 Geometrical measurements

In November 2016, 72 crystals have been shipped at Fermilab, 24 from each of the three preproduction vendors. The mechanical properties of these crystals were checked with a visual inspection and by means of a Coordinate Measuring Machine (CMM): 112 points have been acquired, 20 on each long face and 16 on each small

one. Starting from these measurements, the flatness of every face, the perpendicularity and the parallelism between faces have been also determined. The aim of this first test was to check if all vendors were able to provide crystals with the required mechanical specifications.

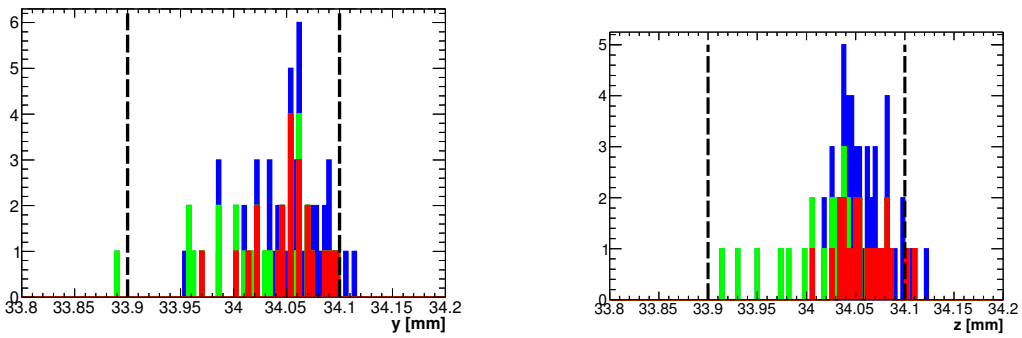

Figure 4.3: Stack distribution of the transverse dimensions along the horizontal (left) and vertical (right) axis with respect to the measurement table of the CMM. Black dashed lines shows the limits imposed by the mechanical requirements.

Figure 4.3 and 4.4 show the results of the CMM measurements. The black dotted line represents the requirement limits. Only one SICCAS crystal did not satisfy the required cross-sectional dimension. All the units satisfied the flatness limit, but few of them exceeded the parallelism and perpendicularity ones, i.e. the requirements on the 3D-shape. At the end of this CMM control, 12 crystals per vendors have been sent to LNF in order to measure their light emission performance. A similar sample has been sent to Caltech to compare and tune the measurement results.

4.1.2 Scintillation properties

One of the most relevant characteristic property of a scintillator is the Light Yield (LY), which is defined as the number of photons produced by an ionising particle per unit of energy deposited in the scintillator. The absolute value (LY_{abs}) is a material specific constant and depends mainly by the energy band gap of the scintillation mechanism. The experimental number assigned to each crystal is the number of detected photo-electrons per MeV (LY_{pe}). This number is related to LY_{abs} according

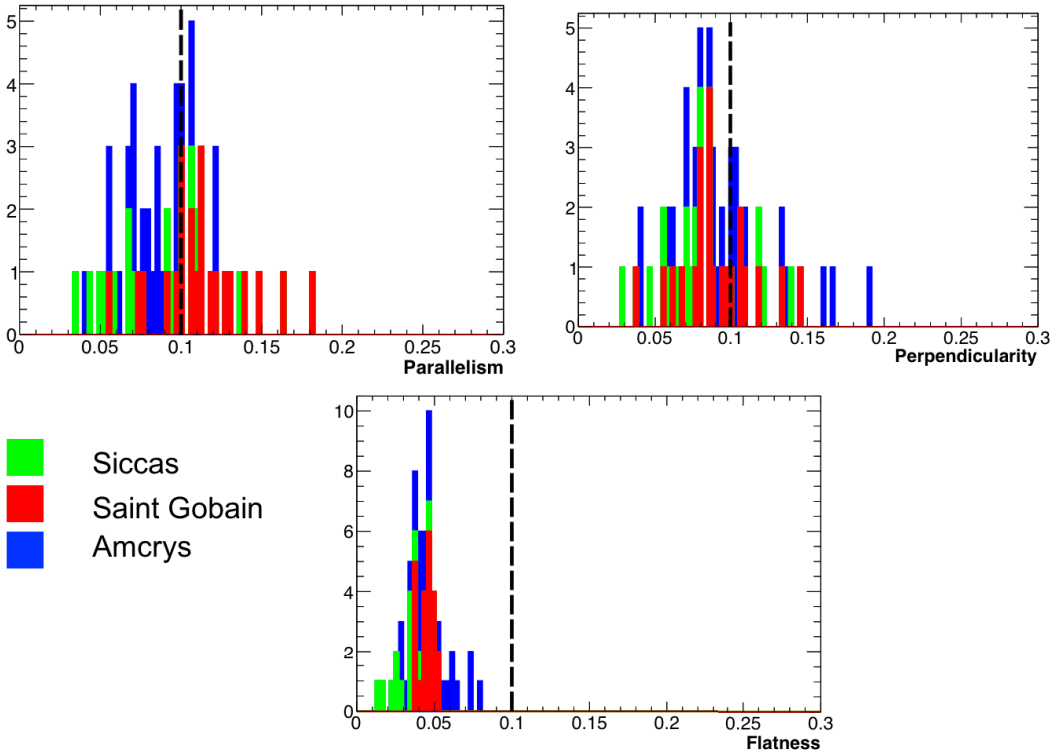

Figure 4.4: Stack distribution of the shape tolerances for the 72 pre-production crystals. Black dashed lines shows the limits imposed by the mechanical requirements.

to the following relation:

$$LY_{pe} = LY_{abs} \cdot \epsilon_L \cdot \epsilon_{QE} \cdot \epsilon_A \quad ,$$

where

- ϵ_L is the optical transmission efficiency of the scintillating photons from the interaction point through the end of the crystal where the photosensor is located;
- ϵ_A is a geometrical coupling factor between the crystal and the photodetector active area;
- ϵ_{QE} represents the quantum efficiency of the photodetector coupled to the crystal.

The light transmission within the crystal depends also on the presence of impurities that might produce internal absorption: therefore another important optical prop-

erty to control is the Longitudinal Response Uniformity (LRU), that describes the dependence of the LY_{pe} on the interaction position of the incident particle along the crystal longitudinal axis. The LRU is a convolution of several effects: internal absorption, reflection, wrapping and sensor coupling medium.

Undoped CsI has an emission spectrum characterised by a fast emission peak at 315 nm with a time structure composed of a decay component of 20÷30 ns. In addition to this fast scintillation component, commercially available undoped CsI crystals may present a slow one due to the presence impurities or defects. This slow component have a decay time of a few μs in the wavelength region above 400 nm [105] and could be source of harmful pileup effects if not kept under control. In Figure 4.5, the study of the emission components from some crystal samples is shown with an analysis done with a spectrofotometer.

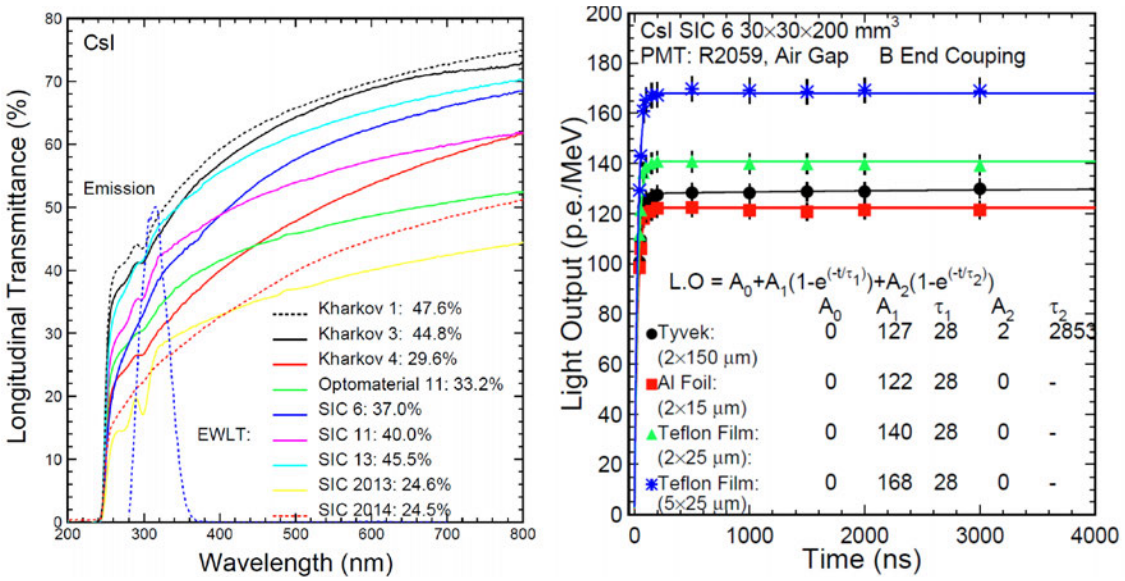

Figure 4.5: CsI EWLT (left) and light output (right).

A large divergence in the longitudinal transmission spectra for undoped CsI crystal samples from several vendors is measured. In this plot the emission spectrum (blue dashed lines) is also shown together with the numerical values of the emission weighted longitudinal transmittance (EWLT), which is defined as:

$$EWLT = \frac{\int LT(\lambda)\ Em(\lambda)\ d\lambda}{\int Em(\lambda)\ d\lambda} \quad , \tag{4.1}$$

where LT(λ) is the light transmittance at the wavelength λ and Em(λ) is the emission

spectrum. The corresponding EWLT at the emission peak is below 50%. The large diversity of EWLT indicates that longitudinal transmission of CsI can not be used to represent crystals optical quality. We thus concentrate on light output measurement for CsI quality control.

Figure 4.5 (right) shows the LY (or light output, LO) as a function of the integration time for a 20 cm long CsI sample with different wrapping materials. The dependence of the response on the integration time is well described by the function:

$$LY(t) = A_0 + A_1(1 - e^{-t/\tau}) \quad , \tag{4.2}$$

where A_0 and A_1 are the LY of the slow and fast component respectively, and τ is the decay time of the fast component. Fit results show that the slow component is negligible. While the overall decay time of this CsI sample can be fit well to a single component with a fast decay time of 28 ns.

The LRU has been studied by measuring the LY along the axis: the corresponding data (Fig. 4.6, top left) is well fit by a linear function. CsI shows a LY increment smaller than 6% toward the side closer to the read out.

The fraction (F/T) of light due to the fast scintillation mechanism with respect to the total one is an observable commonly used in crystal calorimetry to quote the quality of the crystals and to evaluate the relevance of the slow component [104]. A tight requirement on the F/T variable has been set for the Mu2e crystals.

The bottom plot of Figiure 4.6 (left) shows the Fast/Total (F/T) ratios for 100 and 200 ns gate versus 3000 ns gate. The average F/T ratio of these seven points is 73% and 75% respectively, indicating significant slow scintillation. Figure 4.6 (right) summarizes the F/T ratio of LO(200)/LO(3000) for all samples. Also shown in Figure is the Mu2e specification of 75% (dashed line). It is clear that all samples satisfy this specification.

The slow scintillation in undoped CsI is found to be peaked at 450 nm, so can be eliminated by inserting a band-pass filter. This is also highly correlated to the radiation induced read out noise (RIN), discussed in Section 4.2.1. Reducing slow scintillation component thus will also reduce the radiation induced read out noise.

In order to improve the light collection efficiency (i.e. the LY_{pe}) and avoid optical

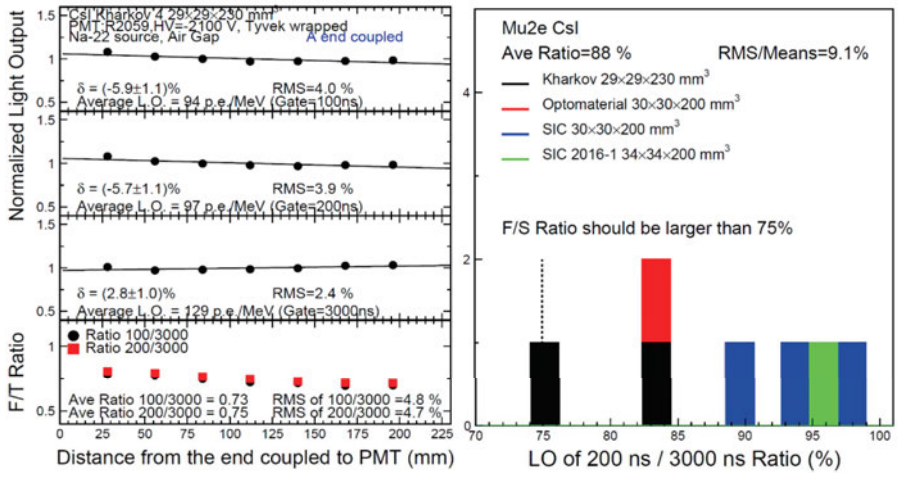

Figure 4.6: Left: CsI LRU (top three) measured with 100, 200 and 3000 ns integration gates respectively, and the F/T ratio (bottom) of LO(100 ns) and LO(200 ns) versus LO(3000 ns). Right: Summary of the F/T ratio of LO(200 ns)/LO(3000 ns).

crosstalk between different channels, each crystal has to be wrapped with a dedicated reflector material. A study of different wrapping materials were performed to: (a) test their radiation resistance and (b) to improve light collection.

The amplitude of CsI LY depends on the wrapping materials used (Fig. 4.7, left). At the end of this optimisation study, the found solution was of using a wrapping of 150 μm thick Tyvek paper foils around each crystal. Tyvek$^{\textcircled{r}}$ is a brand of flash-spun high-density polyethylene fibers. This wrapping is very strong and difficult to tear

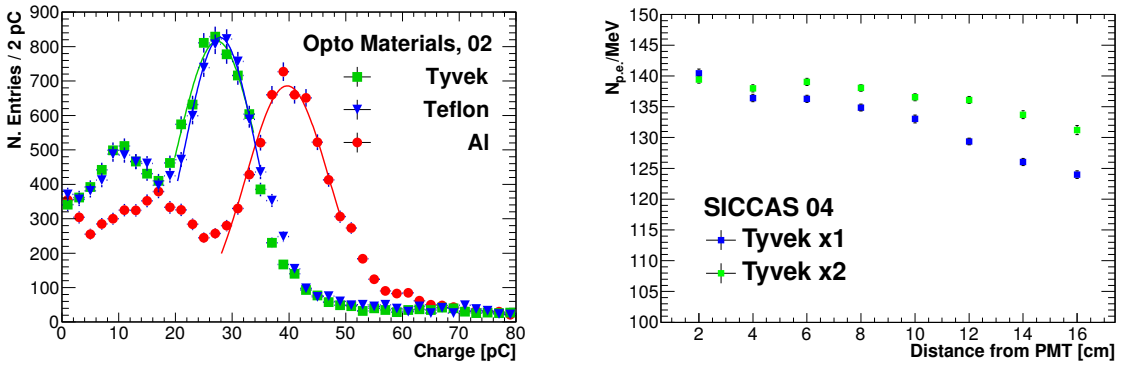

Figure 4.7: Left: Reconstructed charge of a CsI crystal from Opto Materials when tested with a ^{22}Na source and wrapped with different materials. Right: light yield of a CsI crystal sample from SICCAS when wrapped with one or two layers of a 150 μm tick Tyvek foil.

but can easily be cut with scissors. Figure 4.7 (right) shows a single layer is enough to collect the crystal scintillation light. Water vapour can pass through Tyvek, but liquid water cannot. This feature matches very well with the small hygroscopicity of CsI crystals.

4.1.2.1 Requirements

From a Monte Carlo study and from a preliminary test on few commercially available CsI crystals, a set of selection criteria on the crystal optical parameters has been derived. These selection requirements have been applied in the following measurement conditions:

- each crystal is wrapped, on all faces excluding the read out one, with a 150 μm thick Tyvek foil;
- each crystal is read out with an UV-extended PMT, such as an Hamamatsu-R2059 or a ET-9202QB, through an air-gap. No optical glue or grease are applied to the read out sensors.

In these conditions, our technical specifications for acceptance are:

- a LY_{det} above 100 p.e./MeV;
- an energy resolution better than 19% at 511 keV;
- an LRU, defined as the RMS of the LY measured in 8 or more points along the longitudinal axis, less than 5%;
- a ratio between fast and total light yield components, F/T, above 75 %.

Crystals that do not meet these selection requirements will be discarded.

4.1.2.2 Experimental setup

To measure the LY and LRU of each crystal, we use a low intensity collimated ^{22}Na source which irradiates the crystal in a region of few mm^2. The ^{22}Na source

produces two 511 keV electron-positron annihilation photons and it is placed between the crystals and a small tagging system, constituted by a $(3 \times 3 \times 10)$ mm^3 LYSO crystal, read out by a (3×3) mm^2 MPPC. One of the two back-to-back 511 keV photons is tagged by this monitor, while the second photon is used to calibrate the crystal under test. The crystal under test is read out by means of a 2" UV extended photomultiplier tube (PMT) from ET Enterprises, ET-9202QB. The ET-9202QB quantum efficiency curve is shown in Figure 4.8, reaching $\sim 30\%$ at 310 nm, which is the wavelength where the undoped CsI emits. The whole system is inside a light tight black box.

For each crystal, a longitudinal scan is done irradiating eight points, of 2 cm step, from the read out system. In the scan, the source and the tag are moved together along the axis of the crystal under test with a manual movement. A detail of the setup is shown in Fig. 4.8. The crystal under test is placed inside a holder, while the hand-cart contains both the source and the tag crystal.

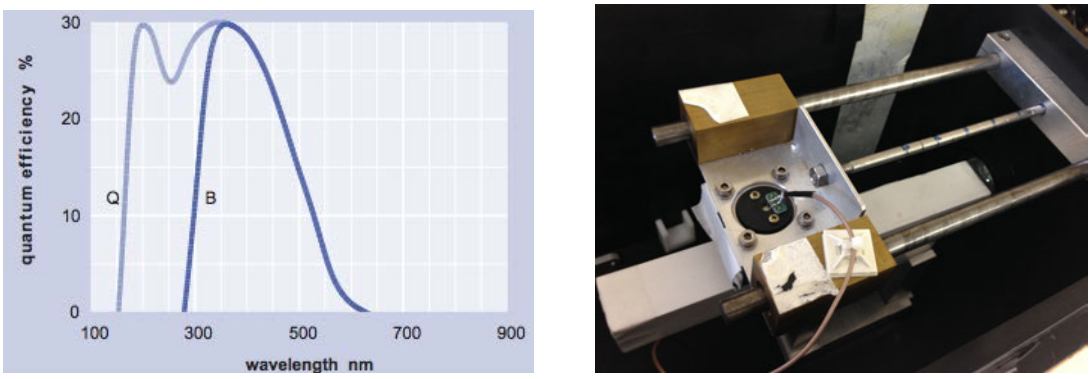

Figure 4.8: Left: efficiency curve of the UV-extended photomultiplier tube used for the measurements. Right: detail of the setup used to test crystals. The coupling of a wrapped crystal with the PMT is visible. The cart bringing the source is also visible.

The data acquisition system is composed by a trigger board, which starts the recording of the events by applying a threshold of 20 mV on the tag signal, and a CAEN DT5751 digitizer at 10^9 samples per second (1 Gsps), which acquires both the tag and test signals. We take ~ 20000 events per point at an acquisition rate of ~ 500 Hz. Each point is completed in about one minute with the adjustment of the next position taking few seconds. A program analyses data for all points as soon as the scan is completed. A complete longitudinal scan takes about 10 minutes.

4.1.2.3 LY, LRU, Energy Resolution and F/T measurements

An example of recorded waveforms for the LYSO tagging system and a crystal under test (CUT) are reported in Figure 6.19, on left and right respectively. LYSO signals are typically within 400 ns from the trigger, with a 50 ns delay, so that the charge is obtained integrating in the range between 50 and 450 ns. The baseline is evaluated using the interval region below 50 ns.

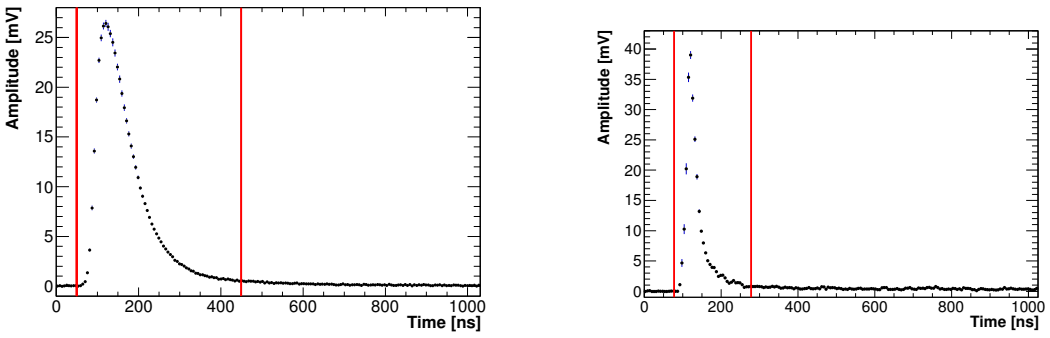

Figure 4.9: Left: Digitized waveform of the LYSO tag system. Right: Digitized waveform produced by the 511 keV photon in the pure CsI crystal. The red lines represent the integration range.

An example of the resulting charge distribution is shown in Figure 4.10. The peak of the 511 keV photons for the tag is extracted performing an asymmetric Gaussian fit around the maximum of the charge distribution. Events for further processing are selected by applying a cut of 2 σ's around the tag distribution peak.

The CUT charge is obtained integrating the signal in the range between 40 ns before and 160 ns after the amplitude peak, T_{mean}. The baseline is evaluated using the interval region below 40 ns. To reduce random coincidences, a cut on T_{mean} is used. Signals are selected only if their peak time is around $\pm 3\,\sigma$ of the time distribution mean value evaluated with a gaussian fit (see Figure 4.11, left). In Figure 4.11 (right), a charge distribution example for one of the CUT, after this selection criteria, is reported. The spectra is very clean and the peak due to the 511 keV photon is clearly visible. An asymmetric Gaussian fit is performed around the 511 keV photon peak to extract the peak position, μ_Q, with a few per mil

precision.

Since the number of photoelectrons follows the Poisson statistics, the LY is obtained from the formula:

$$LY = \frac{N_{p.e.}}{MeV} = \frac{\mu_Q}{G_{PMT} \times E_\gamma \times q_e}, \tag{4.3}$$

where G_{PMT} is the PMT gain at the operational voltage, E_γ is the energy of the ^{22}Na photon and q_e is the elementary charge of the electron. The cart with the

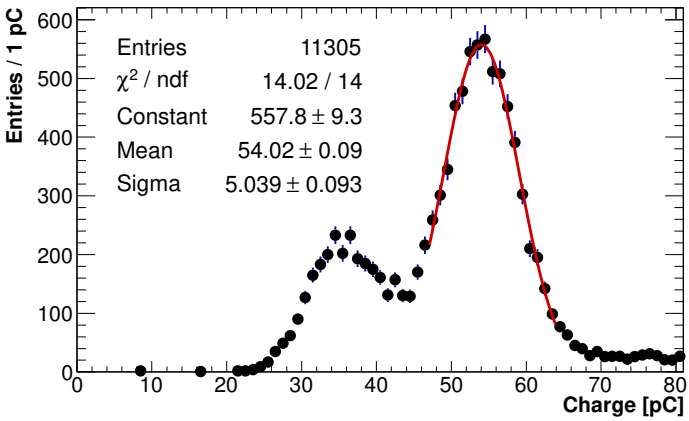

Figure 4.10: Charge distribution of the LYSO-tag system. The distribution red fit is a gaussian function used to evaluate the mean value and the σ of the distribution. Events are selected only if their peak time is around $\pm 2\,\sigma$ of the mean value.

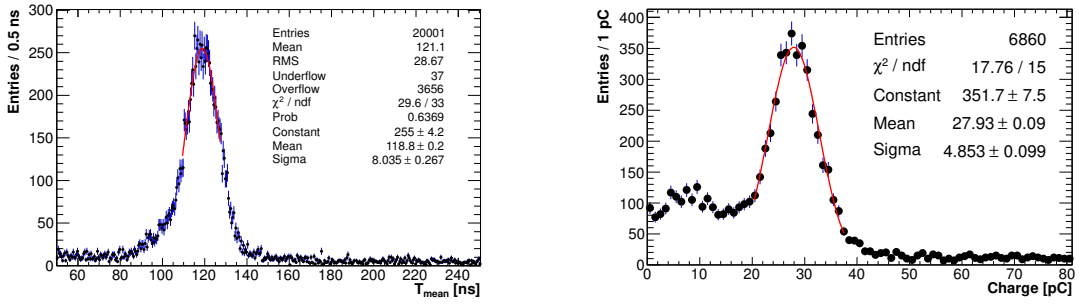

Figure 4.11: Left: Time distribution mean value, fitted with a gaussian function to evaluate the mean value and the σ of the distribution. Events are selected only if their peak time is around $\pm 3\,\sigma$ of the mean value. Right: Charge distribution of the crystal under test after the timing selection and the TAG charge cuts.

source and the tag is moved by 2 cm steps, starting from the center of the crystal, along the crystal axis for a total of 8 points. The LRU is defined as the RMS of the eight LY values. Each crystal is measured two times, by coupling the PMT on the different read out sides. An example of the result of this procedure for six different crystals (two per vendor) is shown in Figure 4.12, where the LY is reported as a function of the distance of the ^{22}Na source from the PMT for both crystal sides.

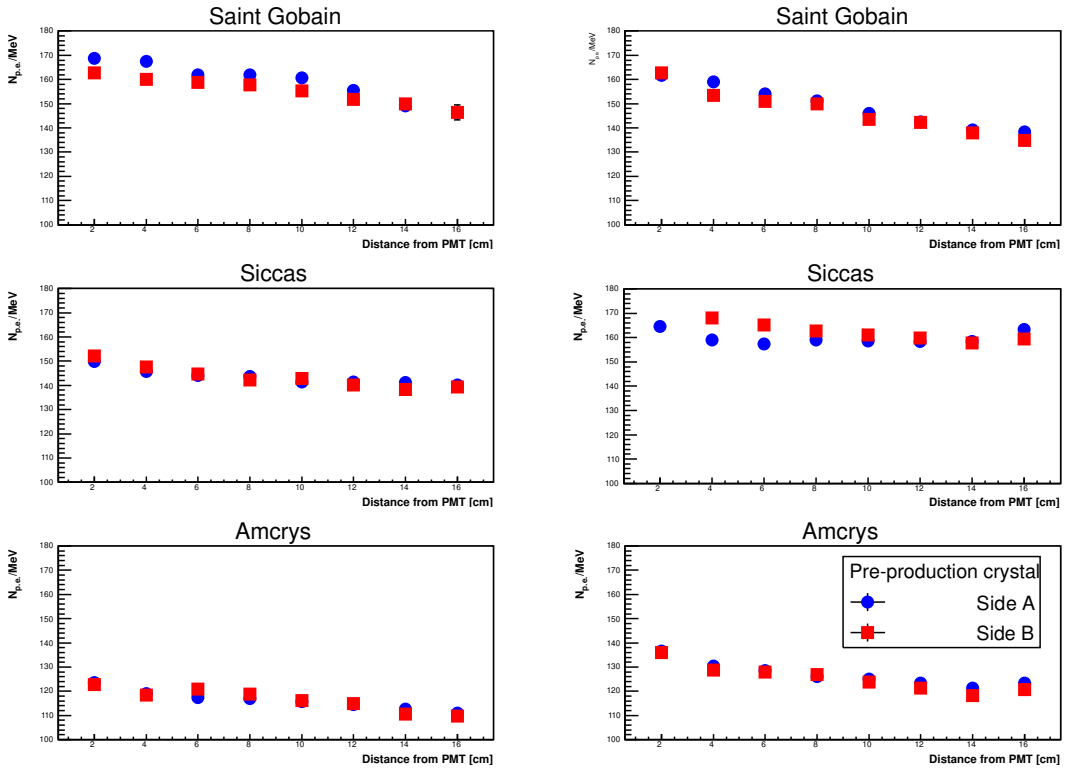

Figure 4.12: Example of LRU measurement for 6 different crystals: 2 Sain Gobain cystals (top), 2 from Siccas (middle) and two from Amcrys (bottom). Blu points are taken with the PMT coupled with A side, red squares with B side.

Summary results of the LY and LRU measurements for the entire pre-production crystals batch are shown in Figure 4.13, top left and right respectively. The LY requirements are well satisfied by all crystals. On the contrary, the LRU distributions shows four Siccas and one Saint Gobain crystals out of specification, underlying the importance of testing each single unit in order to monitor each batch quality.

The intrinsic energy resolution of the crystal at 511 keV is obtained by fitting the ^{22}Na photon peak in each charge spectra of the longitudinal scan and by averaging

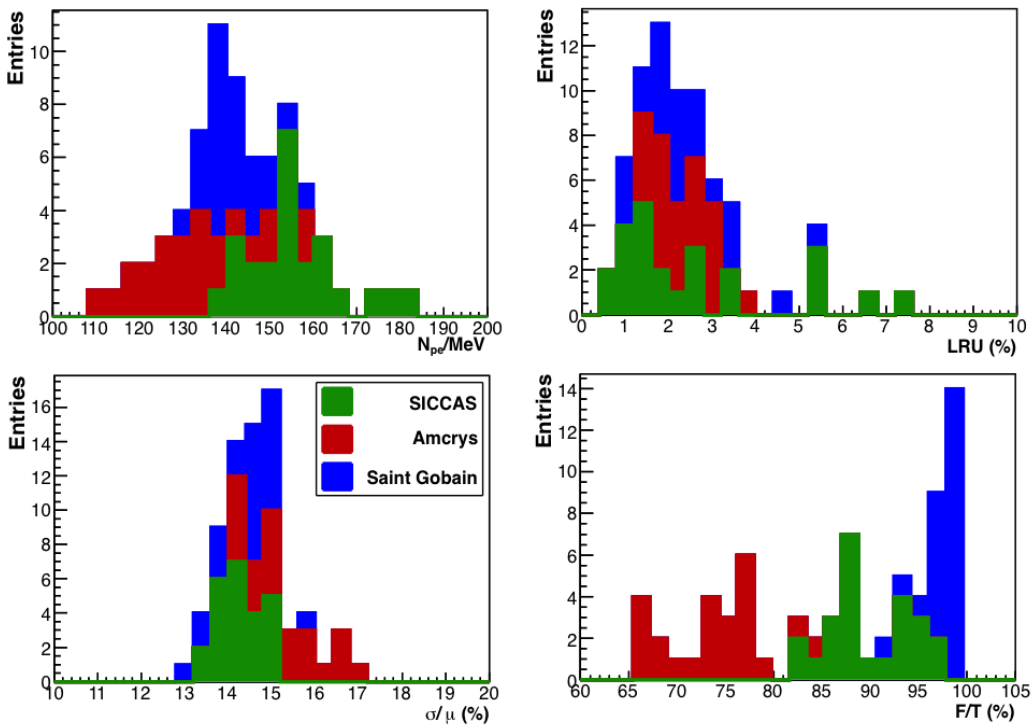

Figure 4.13: Left: Distribution of measured LY for pre-production crystals. Right: Distribution of measured LRU for pre-production crystals. Red lines indicate the selection requirement threshold.

the obtained resolutions. Results of these measurements are shown in Figure 4.13 (bottom, left): most of the crystals satisfy our selection criteria.

The fast and slow components have been studied looking at the distribution of the ratio Q_{INT}/Q_{TOT} as a function of the integration gate in steps of 20 ns. Q_{INT} is the charge integrated from the beginning of the signal up to the step under consideration, while Q_{TOT} is the charge integrated over 1 μs range (Fig. 4.14, left). In order to be sensitive also to few μs scintillation components, the full length of the acquired signal is fixed at 3 μs and measured by means of CAMAC ADC module. A CAMAC based technique is used in Caltech at a similar QA-station thus allowing a comparison and a relative calibration of the measurement results.

For each Q_{INT}, a profile histogram is constructed. The profile is then fit accord-

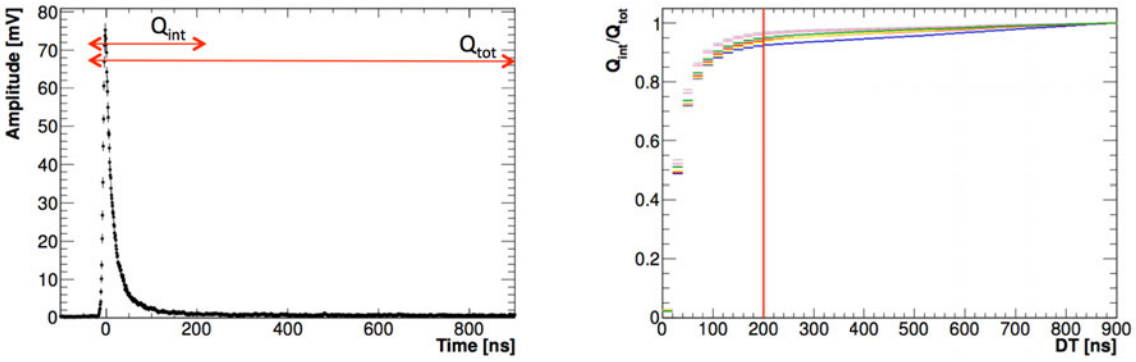

Figure 4.14: Left: Definition of the F/T ratio. Right: Ratio between Q_{INT} and the total charge Q_{TOT} as a function of the integration gate for some SICCAS pre-production crystals.

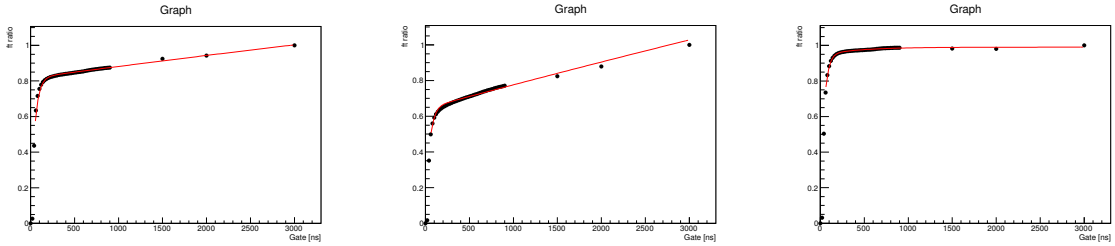

Figure 4.15: Ratio between Q_{INT} and the total charge Q_{TOT} evaluated in a 3 μs gate as a function of the integration gate for a SICCAS (left), Amcrys (middle) and Saint Gobain (right) crystal. The profile is fitted with the function in Equation 4.4.

ing to the following parametrisation:

$$\frac{Q_{INT}}{Q_{TOT}} = P_0 \cdot (1 - e^{-\Delta_t/\tau_1}) + P_2 \cdot (1 - e^{-\Delta_t/\tau_2}) \tag{4.4}$$

where τ_1 and τ_2 are respectively the decay time of fast and slow components. Figure 4.14 (right) shows an example of such a profile for some SICCAS crystals. The relative contribution of the fast component can be monitored on different CsI crystals by calculating the F/T ratio when a 200 ns integration gate is used for Q_{INT}. Figure 4.15 shows the fit method applied on a SICCAS (left), Amcrys (middle) and a Saint Gobain crystal. The Saint Gobain sample has the highest F/T ratio. The Amcrys one shows a long slow component instead.

All the results of the F/T ratio measurements on a batch of pre-production crystals is shown in Figure 4.13 (bottom, right). Many of the Amcrys crystals do

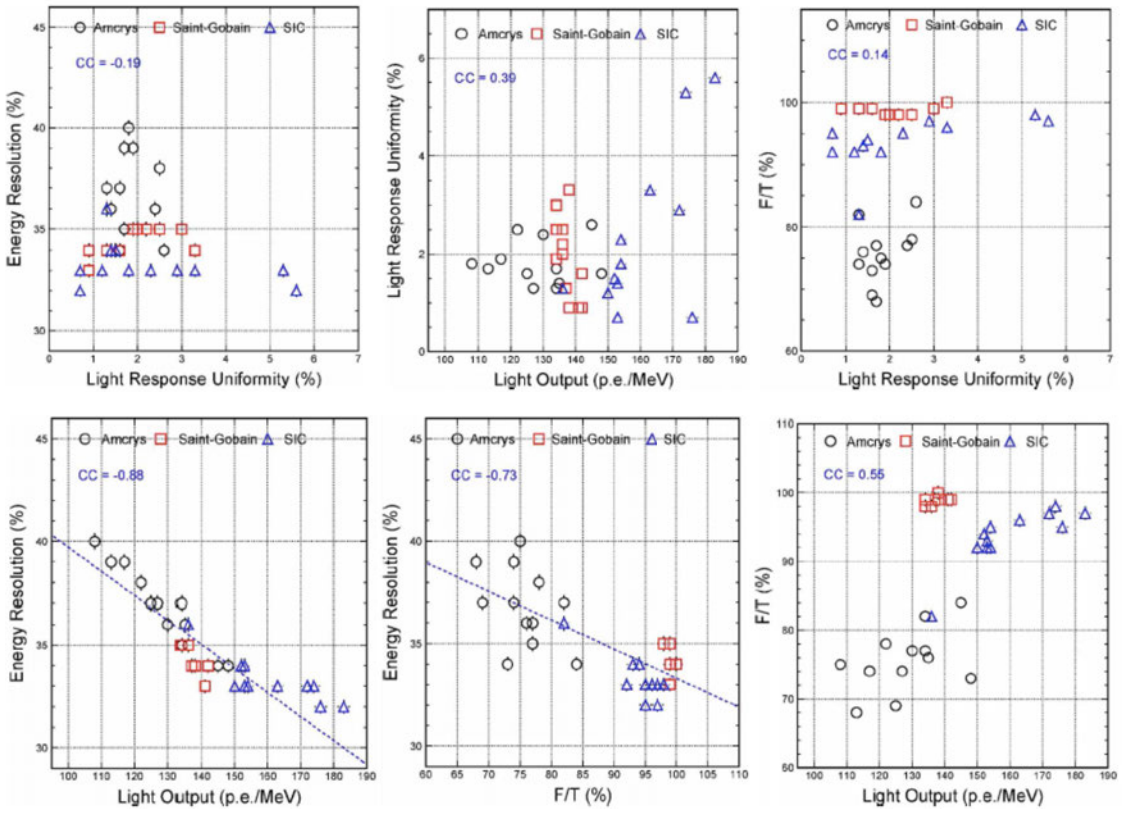

Figure 4.16: Left:Correlation observed between LY, resolution and F/T ratio. Right: Correlation plots between LRU and LY, resolution and F/T ratio.

not satisfy this selection criteria. For this reason this vendor has been discarded for the final calorimeter crystal production.

The average decay times observed during production resulted to be ∼30 ns for the slow component and larger than 400 ns for the slow one.

In Figure 4.16, the correlations between crystals optical properties are reported. Correlations observed between LY, resolution and F/T ratio indicate the importance of keeping a small slow component (top). No correlation observed between LRU and light yield, resolution and F/T ratio (bottom).

The distribution of F/T ratios suggests a strong dependence of the slow component from the manufacturing process, that can be optimised by means of an accurate selection of the material.

4.2 Radiation Hardness of undoped CsI crystals

Another important feature to be checked for the chosen crystal is its radiation hardness, since the light output and the other optical properties can change in a high radiation environment, thus degrading time and energy resolution. As discussed in Chapter 3, the expected ionising dose in the hottest region of the front disk is $\sim$6 krad/year, with an average rate of 1 rad/hour. While the expected neutron fluence at 1 MeV equivalent energy is 10^{11} neutrons/cm^2/year.

In dedicated irradiation studies [106], neutrons resulted to negligibly damage CsI properties with respect to the total ionisation dose (TID): a negligible variations in the EWLT and the LO has been measured, testing crystals after an exposure up to 10^{11} neutrons/cm^2.

In 20 cm long undoped CsI crystals ionisation dose resulted to reduce the light output of 70% - 80% after a TID exposure of 1 Mrad.

From preliminary tests, the RIN due to ionization is larger than that induced by neutrons.

In conclusion, the final quality control on radiation hardness can be carried out only using ionisation dose tests. After adding a safety factor to the dose rate evaluated by simulation, the calorimeter radiation hardness requirements become:

- a LY higher than 85% (60%) of the initial value after receiving a TID of 10 krad (100 krad);

- a RIN with PMT read out smaller than 0.6 MeV for a dose rate of 1.8 rad/h.

For the final production crystals, the RIN quality check will be performed over the whole sample in order to identify the ones with smaller fluorescence that can then be positioned in the hottest calorimeter area. All the way around, since exposing a crystal to a TID will permanently degrade the LY, this test will be carried out only on few crystals, randomly selected, from each production batch.

4.2.1 Gamma Radiation Induced Noise

The RIN due to dose has been measured both at LNF and Caltech using a strong ^{137}Cs source that mainly produces 0.66 MeV gamma-rays. The experimental apparatus used at LNF is shown in Figure 4.17: a motorized cart transports the source over the CUT that is coupled to a UV-extended PMT with an air-gap as for the optical properties' measurement. During the source movement, the dark current read out from the PMT anode, I_{rin}, is registered with a picoammeter.

Figure 4.17: Experimental apparatus for RIN measurements: a motorized cart transport a strong ^{137}Cs source over the CUT.

The number of radiation induced photoelectrons per unit of dose rate, F, has been determined according to the formula:

$$F = \frac{I_{rin}}{G_{PMT} \times q_e} \cdot \frac{1}{\phi_{lab}} \tag{4.5}$$

where ϕ_{lab} is the source dose rate. In order to evaluate the number of background photoelectrons due to RIN in the final signal, N_{RIN}, F has to be re-scaled to the dose rate expected in Mu2e operation environment, $\phi_{Mu2e} \sim 1.8$ rad/h, and then integrated in the 200 ns gate of a typical calorimeter signal:

$$N_{RIN} = F \times \phi_{Mu2e} \times 200 \text{ ns}. \tag{4.6}$$

The RIN in MeV is then obtained as the statistical fluctuations of N_{RIN} normalized to the LY:

$$RIN = \frac{\sqrt{N_{p.e.}}}{LY} \tag{4.7}$$

Therefore, the procedure to perform the RIN measurement is the following:

- Acquisition of the dark current without source for ∼5 minutes;
- Measurement of the photocurrent for ∼15 minutes while the crystal is irradiate with the source;
- Measurement of the photocurrent for additional ∼15 minutes without source to check the crystal decay time.

Figure 4.18 shows an example of the result of this measurement for one crystal. The current increases from I_{dark} ∼10 nA when the crystal is not irradiated up to $I_{plateau} \sim \mathcal{O}(10)$ μA. The plateau is used to evaluate the RIN. In Table 4.1, the mean value results of pre-production crystals from each vendor are reported.

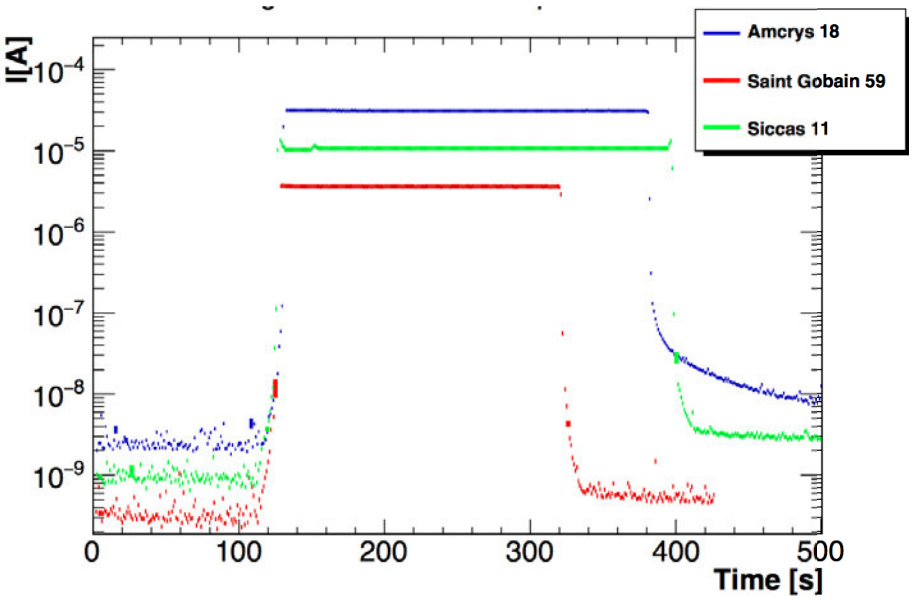

Figure 4.18: Example of RIN measurement for a SICCAS (green), Amcrys (blue) and Saint Gobain (red) crystal. The photocurrent plateau occurs when the ^{137}Cs source cart is over the crystal.

Radiation induced read out noise have been measured for all 72 pre-production CsI crystals. Results are reported in Figure 4.19 (left). All crystals from Saint Gobain and Siccas meet the Mu2e specification, all the crystals shows similar RIN values between 155-300 keV. About half crystals from Amcrys do not. The average RIN value obtained for each vendor are reported in Table 4.1.

Vendor	$I_{plateau}$ *[nA]*	*RIN [keV]*
Saint Gobain	162	202
Siccas	277	237
Amcrys	1620	622

Table 4.1: Mean value results of RIN measurements performed on all the 72 pre-production crystals.

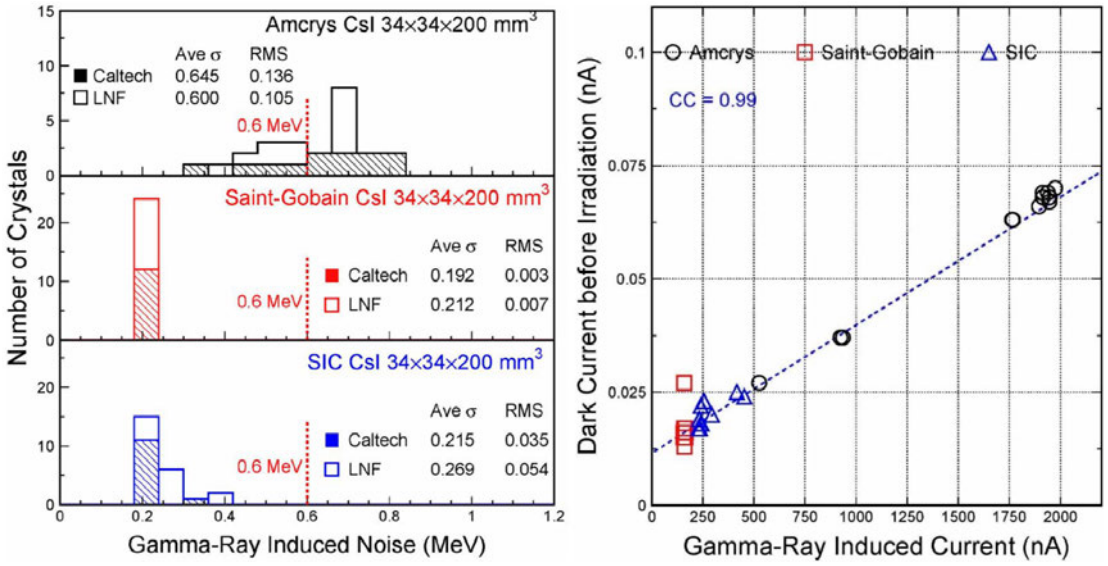

Figure 4.19: Left: results of RIN measurements performed on all the 72 pre-production crystals form Amcrys (top), Saint-Gobain (middle) and SICCAS (bottom). Right: dark current before the irradiation as a function of the dark current measured during crystal exposure.

Figure 4.19 (right) reports the dark current measured before the irradiation as a function of the current measure during crystal exposure. A linear correlation is clearly visible.

Moreover an excellent correlation between the dark current, the radiation induced current, the radiation induced read out noise and the F/T ratio has been

studied and reported in Figure 4.20. This means eliminating slow component in crystals will reduce the RIN.

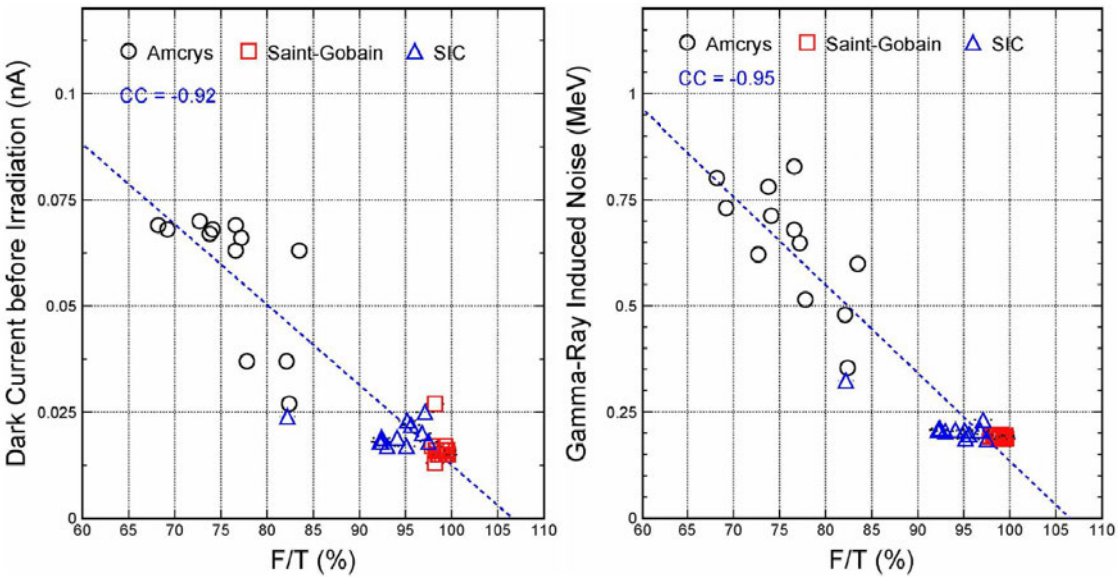

Figure 4.20: Dark current before the irradiation (left) and γ-RIN (right) measurements as a function of the F/T ratio.

4.2.2 Neutron Radiation Induced Noise

Neutron induced radiation damage [106] and RIN are much smaller than the ones from ionisation dose. We demonstrated this during a test performed at the HOTNES facility of ENEA (Frascati), where we measured the noise induced by neutron flux similar to the one expected while running in Mu2e [107].

In May 2016 crystals from several vendors have been tested with thermal neutrons at the HOTNES facility: a single crystal, coupled to a photomultiplier with a gain of 2.1×10^6 at 1400 V, has been inserted inside the AmB sourceand thus irradiated with a uniform flux of 700 n/cm^{2}s, the dark current values are recorded by means of an automatic acquisition program. The experimental setup is shown in Figure 4.21.

A typical measurement took place in three different steps: the dark current measurement of the crystal outside the source for $\sim$5 minutes, then, continuing dark current monitoring, the crystal has been irradiated by the source for 15 minutes and

Figure 4.21: Experimental setup used to determine crystal neutron RIN.

finally current recording continued for 15 minutes after the extraction, to check the crystal decay time. To evaluate the radiation induced noise we are interested in measuring the radiation induced number of photoelectrons/s/neutron flux, F, and the related RIN. The first one is defined as:

$$F = \frac{\frac{I}{e \times G_{PMT}}}{\phi_N} \tag{4.8}$$

To evaluate the noise expected for the Mu2e experiment, we considered a gate of 200 ns and an estimate flux, ϕ_N, of 10^4 n/cm^2/s. The number of collected photoelectrons is defined as:

$$N_{p.e} = F \times \phi_{Mu2e} \times 200 \text{ ns} \tag{4.9}$$

Knowing now the number of collected photoelectrons, the RIN can be obtained using Formula 4.7.

In Figure 4.22, the results of the test performed from crystal sold by different vendors are reported. The value of the current increase from $I_{dark} \sim 10$ nA while the crystal is not irradiated to $I_{neutrons} \sim \mathcal{O}(10)$ μA. All the crystals tested showed a similar behaviour and the RIN values obtained are between 60-85 keV.

Since all the crystal tested largely satisfied the Mu2e requirements of neutron-RIN < 0.6 MeV, we found out not necessary to measure this property for the pre-production and production crystals.

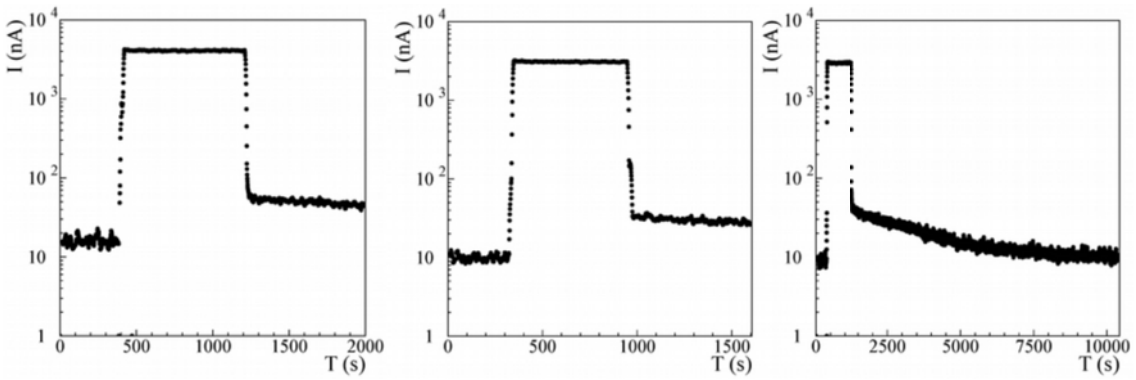

Figure 4.22: Experimental setup used to determine crystal RIN.

4.2.3 Radiation dose test

Irradiation tests to check the degradation of the LY are performed using a very intense source ^{60}Co to produce γ with an energy of 1.17 MeV and 1.33 MeV. As a reference, the LY is measured in the test station of previous Section before to start of irradiation.

Figure 3.19 (left) shows how the EWLT and the LY vary for CsI as a function of the integrated dose. Up to 10 krad, which is the dose/year expected in the inner most rings of the calorimeter (Radius $<$ 38 cm), undoped CsI shows a drop of few percentages in the LY and the EWLT.

At the end of irradiation, corresponding to a total dose of 10^5 rad, just 2 SICCAS crystals satisfied the radiation damage specifications.

Radiation damage study for CsI is a costly exercise, since crystal samples after testing are unusable. For the production phase just few sample per batch will be tested.

4.2.4 Neutron fluence test

In 2015, three CsI crystal samples have been tested with neutrons at the Frascati Neutron Generator Facility (FNG, ENEA). FNG uses a deuteron beam, accelerated up to 300 keV, impinging on a tritiated target to produce a nearly isotropic 14 MeV neutron flux via the T(d,n)α fusion reaction. The maximum neutron intensity

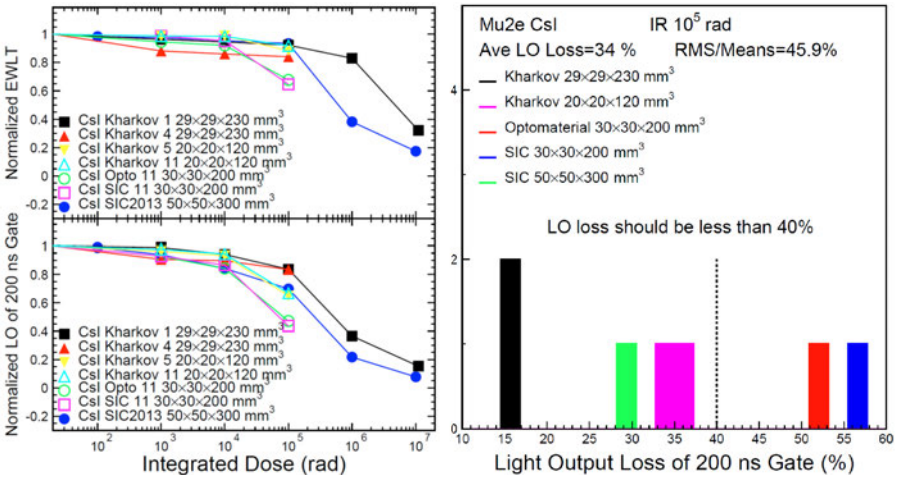

Figure 4.23: Left: normalized emission weighted longitudinal transmission (EWLT, top) and light output (LO, bottom) are shown as a function of integrated dose for undoped CsI crystals from various vendors. Right: summary of the normalized light output loss measured in 200 ns integration time for undoped CsI crystals from different vendors after 100 krad.

is 0.5×10^{11} n/s, close to the target, with a uniform production. The desired neutron intensity is reached by either positioning the crystal at the needed distance or changing the deuteron beam intensity.

During the test, LY and LRU have been measured at different steps of the irradiation program.

The total fluence delivered was 9×10^{11} n/cm^2 in four days [87]. All crystals showed a good LRU after irradiation, with a total uniformity well below 10% and negligible deterioration. This means the Mu2e expected neutron fluence on calorimeter will not affect crystals performances. For this reason we decided to do not repeat the test for other samples.

4.3 Production crystals

A the end of the long characterization and optimization of crystals for the calorimeter construction, crystals from Saint Gobain and SICCAS vendors have been selected, showing to be good compromises between quality and cost.

Test stations have been designed by the Mu2e LNF-INFN group, as automatized

tools to test the optical quality of the 1450 undoped CsI crystals under procurement for the construction of the Mu2e electromagnetic calorimeter.

The Quality Acceptance (QA) procedure of these crystals works as follows: the crystals are shipped from the producers to the Mu2e Calorimeter laboratory at Fermilab. Here a visual survey is carried out to control the absence of big defects such as large notches, dents, scratches or bubbles. Soon after, their mechanical specifications are controlled by means of a CMM. If they do not pass specifications they are rejected and sent back to the producer. The radiation hardness tests are carried out on a small randomly selected sample in Caltech, Pasadena (USA). The optical properties and RIN measurements are instead carried out at Fermilab. Test stations have been designed by the Mu2e LNF-INFN group, as automatized tools to test the optical quality of the 1450 undoped CsI crystals under procurement for the construction of the Mu2e electromagnetic calorimeter.

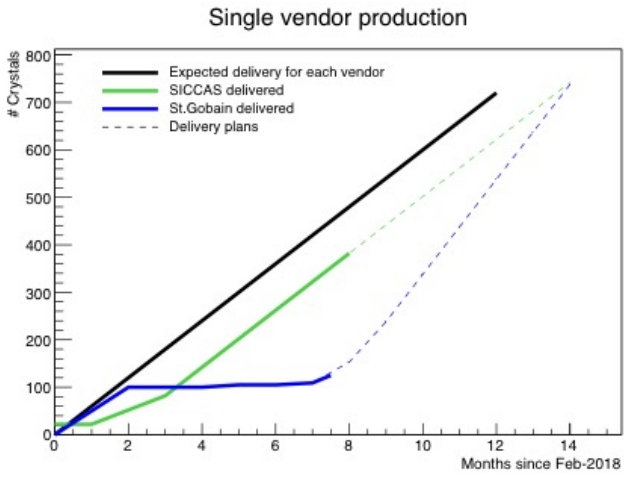

Figure 4.24: Production crystals delivery status.

The QA started on February 2018, 60 crystals per vendor were supposed to arrive each month. At the moment of writing, 507 crystals have been shipped at FNAL, 382 from SICCAS and 125 from Saint Gobain. Figure 4.24 shows the status of crystal delivery. The production phase expected end is May 2019.

4.3.1 Geometrical measurements

Twelve Saint Gobain crystals have been discarded due to the presence of clearly visible defects. The remaining 495 have been measured with the CMM machine, to check the same parameters discussed for the pre-production phase. Figure 4.25 shows on top the results in flatness (left), parallelism (middle) and prependicularity (left) between crystals faces and on bottom the results on longitudinal (X) and transverse (Y,Z) dimensions. The black lines represent the technical requirements and 44 Saint Gobain crystals resulted out of specification. For this reason have been discarded.

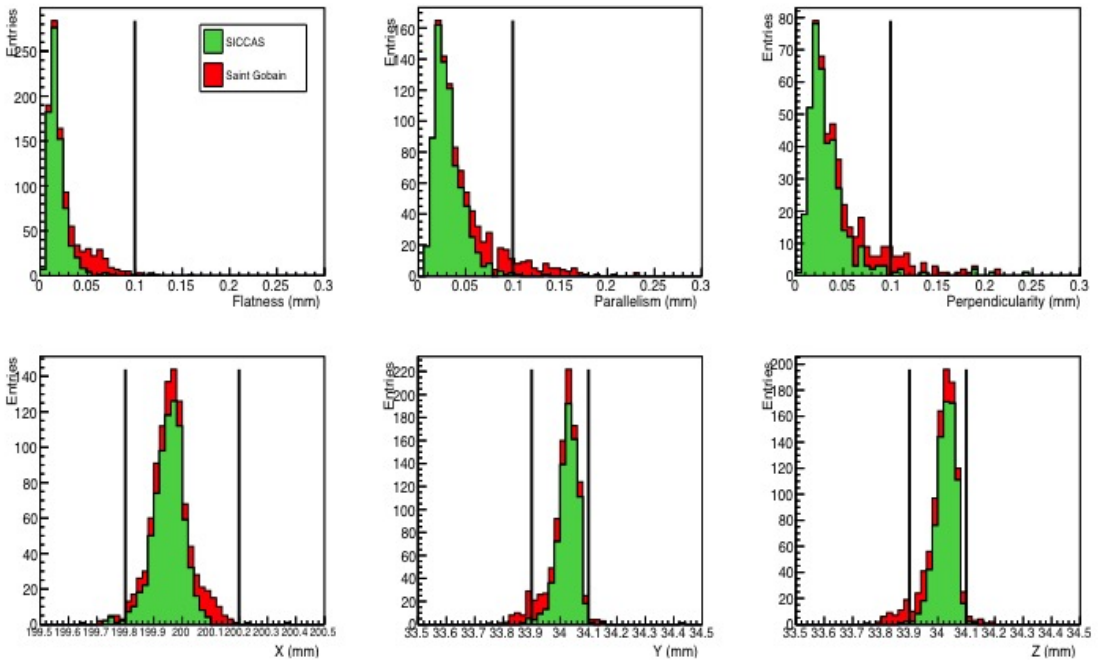

Figure 4.25: Mechanical measurements of the production crystals performed with a CMM machine at Fermilab.

4.3.2 Optical QA

At the end of the mechanical measurements, about 87 crystals were sent to Caltech for a comparison in the measurement of optical properties. The remaining ones have been characterized at FNAL by the LNF group, using the QA optical station shown

in Figure 4.26.

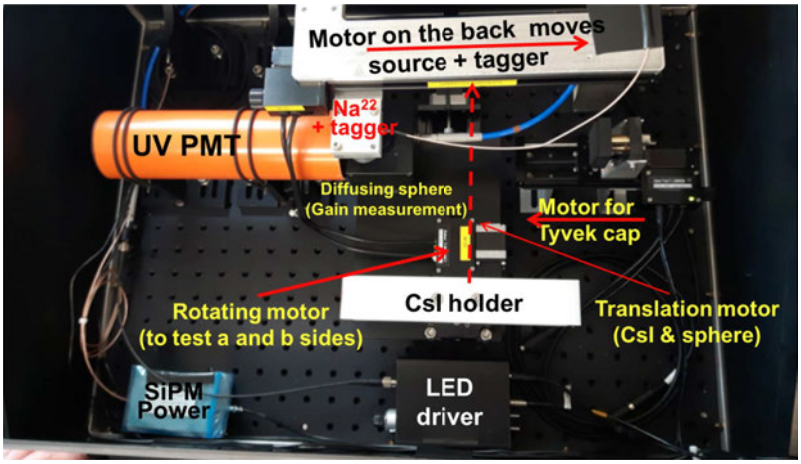

Figure 4.26: Layout of the QA optical automatized station.

It contains four motors which allows to test both read out sides of a crystals in about 20 minutes. The crystal under test is inserted in the white holder that, by means of a translational stepper motor, can be positioned in the center of the PMT photocathode. The crystal is wrapped with Tyvek foils and the lateral edges are protected by a small plastic frame in ASA to avoid folding the Tyvek over the edges. Reflection on the side opposite to the read out is granted by an ASA cap coated with two layers of Tyvek. In the QA station, an additional translational stepper motor is used to move a very precise Tyvek cap in the ASA frame opposite to the read out system. This, together with a rotating motor, allows to test both read out sides. When the crystal is positioned in the right place in front of the PMT, an additional motor moves the ^{22}Na source along the crystal axis and data are acquired with a CAEN Desktop Digitizer. Then the same test procedure describeed in 4.1.2.2 is followed: a LYSO crystals is used to tag the source photon and the analysis algorithms are the same. In addition a LED emitting at 350 nm, driven by a CAEN LED driver, is present in the new station. It is used to fire with a pulsing frequency of 100 Hz the PMT to perform a fast calculation of the gain, thus allowing to follow variations along time.

Figure 4.27 shows the results for the best side in LRU of all the 364 crystals tested (293 from SICCAS and 71 from Saint Gobain). The red lines represent the requirements. All the crystals satisfy the LY specification (top left), some SICCAS

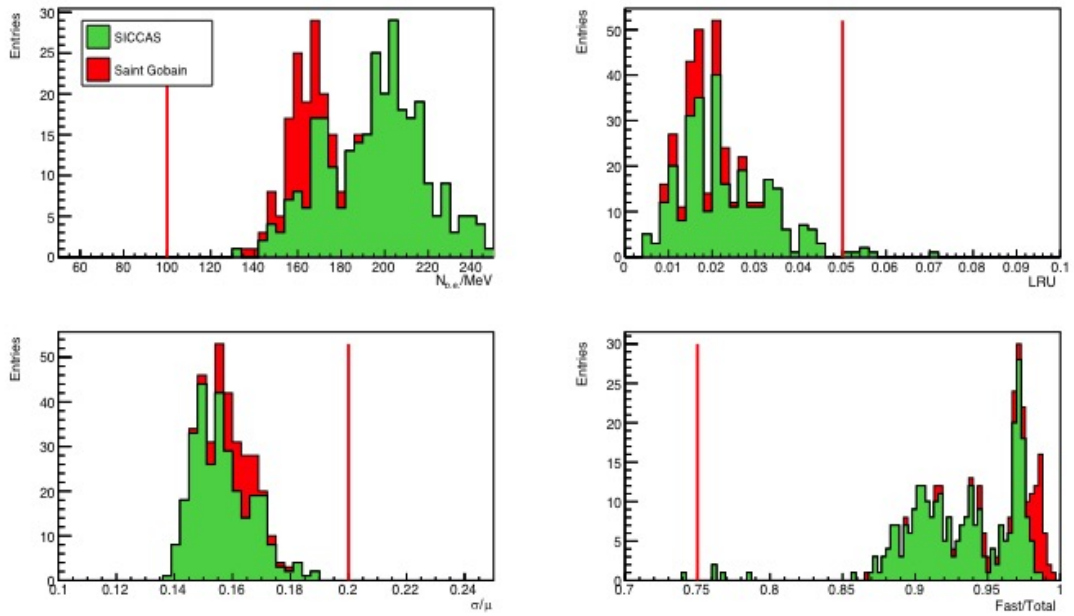

Figure 4.27: Optical properties of the production crystals measured with the automatized station.

samples are out of the LRU (top right) and F/T requirements (bottom right). All the crystals show a good resolution (bottom left).

4.3.3 Radiation induced noise measurements

Crystals that do not pass specifications are rejected and sent back to the producer. For the other, the RIN measurements is performed at FNAL with the station shown in Figure 4.28 (left). This station has been designed by the Mu2e INFN-LNF group to test 6 crystals at the same time. So once the best side in LRU has been evaluated, the crystals are inserted inside the light tight drawer and each of them is coupled to two Mu2e SiPMs. The electrical scheme of the bias and output board for the SiPMs is reported in Figure 4.28 (right). each one read out by two Mu2e SiPMs. After few minutes of acquisition of the SiPM dark current, a ^{137}Cs source, remotely controlled by a translational stepper motor, stops at the center of the top face of each crystal for one minute. Since the activity of the source is 10 mCi and the distance from the crystal is 10 cm, a dose od 42 mrem/h is expected on the top face of the crystals.

The Radiation Induced current is evaluated as the average of the two SiPMs

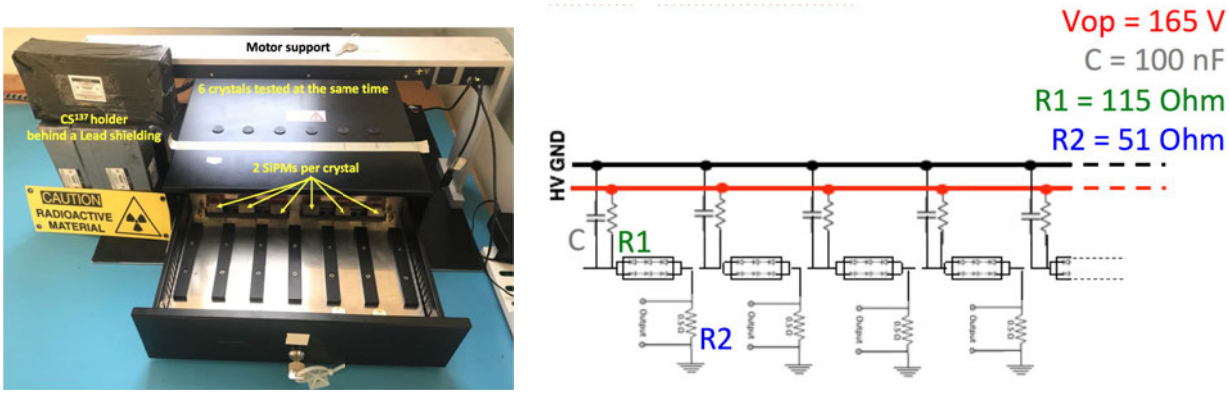

Figure 4.28: Left: picture of the RIN station. Right: sketch of the bias and output board for the SiPMs used in the RIN station. A RC filter is placed in the bias pins using R1 and C, while R2 is placed in the output pin.

ones, when the crystal is exposed. The RIN is evaluated following 4.2.1. In Figure 4.29 (left), the RIN measurements for all the crystals are rported. This value does not constitute a rejection criteria: it was considered as a parameter of preference on the technical evaluation. The goal of the preproduction bid was have a large number of crystals with $\sigma_{RIN}(PMT) < 0.6$ MeV in a 200 ns gate. This translates to $\sigma_{RIN}(SiPM) < 1.2$ MeV.

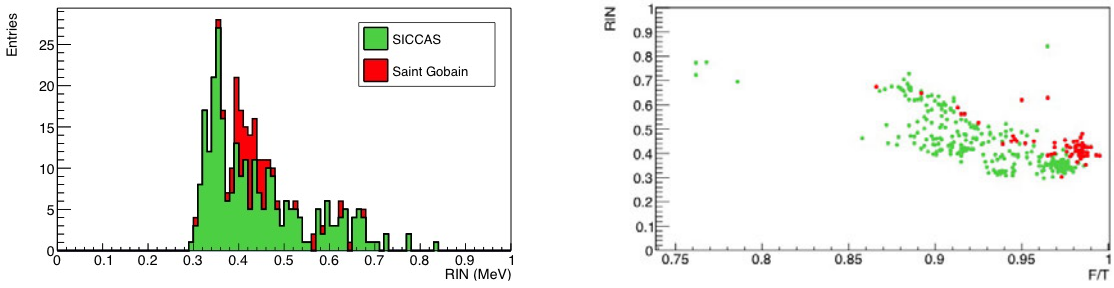

Figure 4.29: Left: RIN measurements of the production crystals, read out by SiPMs. Right: correlation between RIN and F/T values.

A linear RIN correlation to the F/T ratio values is clearly visible in Figure 4.29 (right), as evaluated for the pre-production samples.

At the moment of writin, six SICCAS production crystals were irradiated up to 100 krad. All have more than 100 p.e./MeV after the irradiation, meeting the Mu2e specifications. Three samples lose more than 20% light after 10 krad.

Chapter 5

Silicon Photomultipliers

For the final calorimeter configuration, we designed a custom silicon photo-sensor consisting of a large area 2×3 array of individual UV-extended 6×6 mm^2 Silicon Photomultipliers (SiPMs) cells, as shown in Figure 5.1. Each cell is composed by 14400 pixels of 50×50 μm^2 dimensions and has an effective photosensitive area of 6×6 mm^2. The pixel size has been decided as a good compromise between gain and photo-detection efficiency. We refer to this array as *Mu2e-SiPM*.

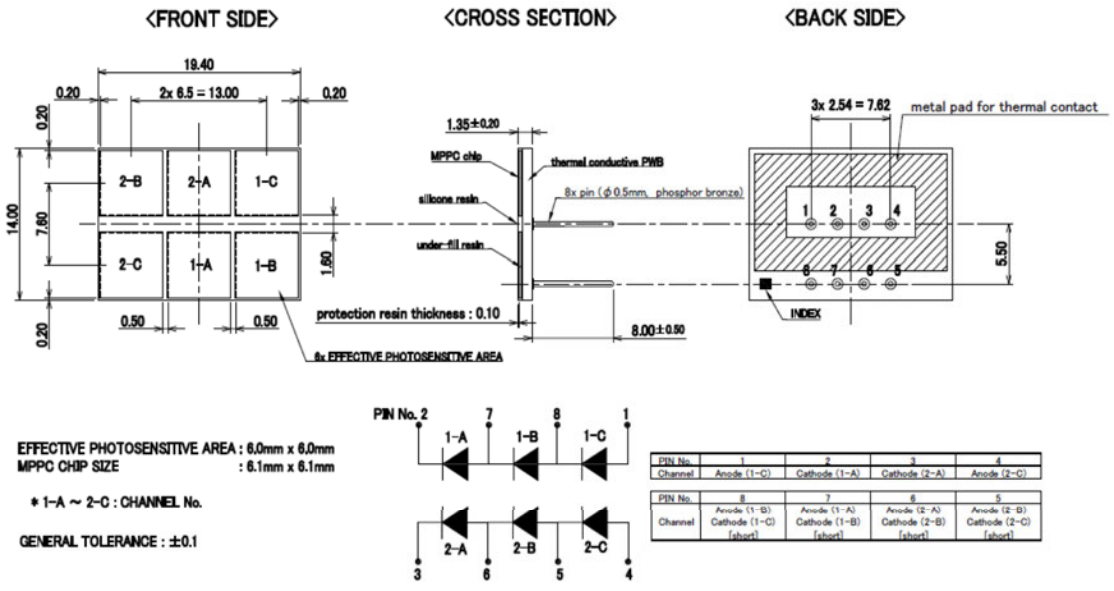

Figure 5.1: Sketch a of the custom Mu2e SiPM array.

The solid-state photodetectors are necessary due to the presence of the high magnetic field, while the choise of an UV-extended detector allows to match, with high efficiency, the wavelength of the scintillation light produced by the CsI crystals ($\sim$ 315 nm). This has been obtained requiring a silicon resin layer as window material.

To meet the request of a short signal width (<40 ns), to avoid pileup effects in the experiment, a small total capacitance of the sensor is needed. The read out is organized as the parallel of two series of three monolithic cells: such a configuration in series allows to reduce (to 2/3) the large capacitance of the parallel configuration that might affect the energy and time measurements. The read out scheme is shown in the bottom part of Figure 5.1. In Figure 5.2, the signal width of a single SiPM cell is compared to the serie of three SiPMs as in our configuration. The second signal is clearly faster and has a width of $\sim 1/3$ of the single cell.

In order to allow reliability of the system, each crystal is read out by two independent Mu2e SiPMs, each one whith its one bias voltage and read out chain. The needs to operate for one year without interruptions inside the DS, while maintaining stable the performances, is translated on a large request of the needed Mean Time To Failure (MTTF).

Each Mu2e SiPM has to fulfil the following specifications, in order to satisfy the Mu2e calorimeter requirements discussed in Chapter 3:

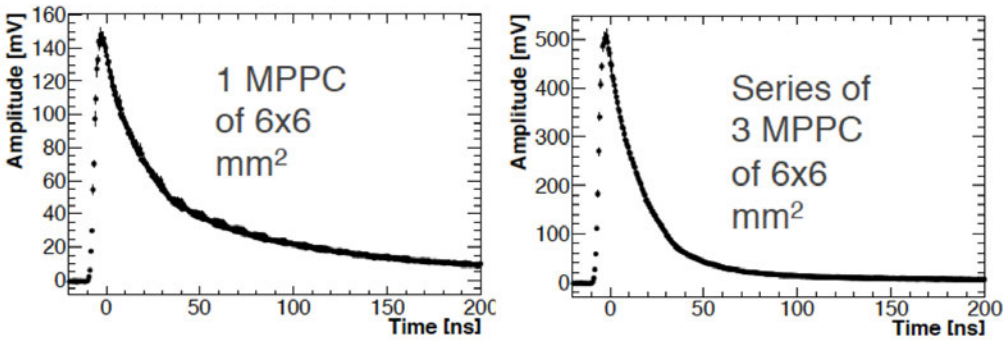

Figure 5.2: Left: digitized waveform of a single 6×6 mm^2 SiPM cell. Right: digitized waveform of a series of three 6×6 mm^2 SiPM cells.

- a Photon Detection Efficiency (PDE) larger than 20%, at 315 nm;
- a gain (G) larger than 10^6 at the operational voltage, $V_{op} = V_{breakdown} + 3$ V ;
- a fast quenching time (τ) smaller than 100 ns for each of the 6×6 mm^2 SiPM cells, when measured on a load larger than 15 Ω;
- a spread in the operation voltage (RMS(V_{op})), among the 6 SiPMs in the array, smaller than ± 0.5 %;
- a spread in the dark current (I_d) at V_{op} (RMS(I_d)) among the 6 SiPMs in the array, smaller than ±15 %;
- a dark current at V_{op} smaller than 10 mA and a gain reduction smaller than a factor of 4 while irradiating SiPMs up to 3×10^{11} n_{1MeV}/cm^2 at 20 °C;
- a Mean Time To Failure (MTTF) better than a million hours while operating at 0 °C.

During the pre-production phase started in November 2016, we procured 50 custom SiPMs from three different vendors: AdvanSid (Italy), Hamamatsu (Japan) and SensL (Ireland). In the following months we characterised all of them, by measuring all quantities needed to check the required technical specifications. At the end of this QA process, this set of measurements was used to select the best vendor for the calorimeter production phase.

5.1 Pre-production SiPMs characterization

A test station able to fully characterized one sensor at a time has been built, due to the large number of measurements to be performed for each SiPM's cell. A schematic view of the station is shown in Figure 5.3. A LabView software [108] was developed controll and provide the DAQ interface.

The SiPM test system was housed in a black box to prevent external light to reach the SiPM Under Test (SUT). The SUT support was encapsulated in a copper

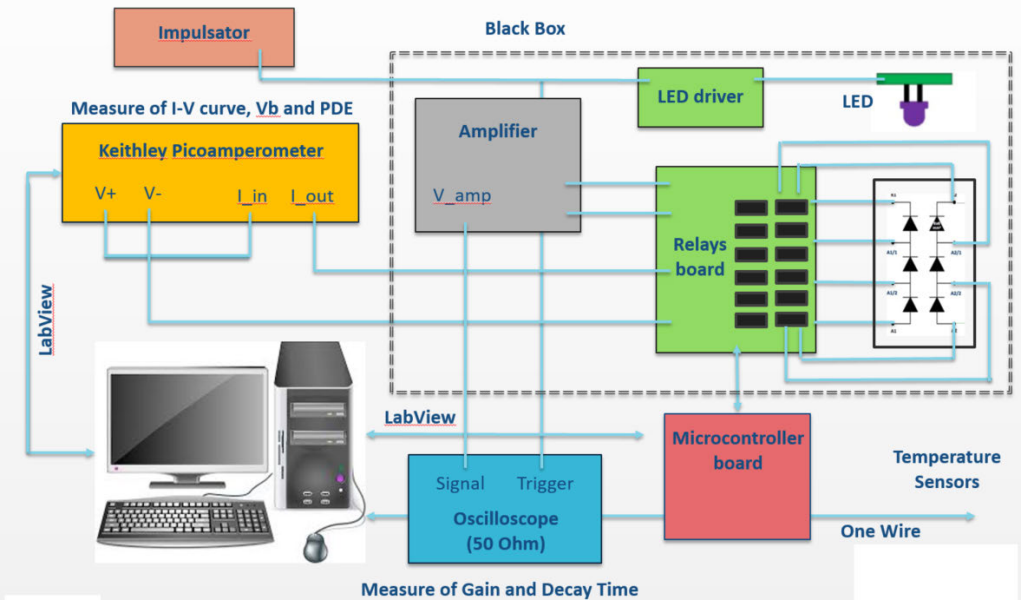

Figure 5.3: Scheme of the experimental setup used for the pre-production SiPMs tests.

box actively cooled with a chiller to stabilize its temperature. To provide a good thermal coupling between the SiPM package and the copper a layer of thermic tape was used. A picture of the final setup is shown in Figure 5.4. The temperature of the copper box was kept stable at 20 °C by a water chiller [109]. The thermal stability of the system was continuously monitored by a one-wire digital thermometer system with an accuracy of 0.3 °C.

The SUT was biased by a KEITHLEY 6487 source meter [110], which was also used to measure the current drained by the SUT itself. The cell to be biased is selected by means of a custom relay board which is photo-coupled to an Arduino Mega2560 Rev3 microcontroller [111]. A serial interface allowed to control both the KEITHLEY and the micro-controller by means of a LabView software able to:

- select the cell;
- set the bias voltage;
- program, record and store the current measurements.

An UV LED emitting at a wavelength of 315 nm was placed inside the copper box to uniformly illuminate all the SUT cells, for PDE and G measurements. The

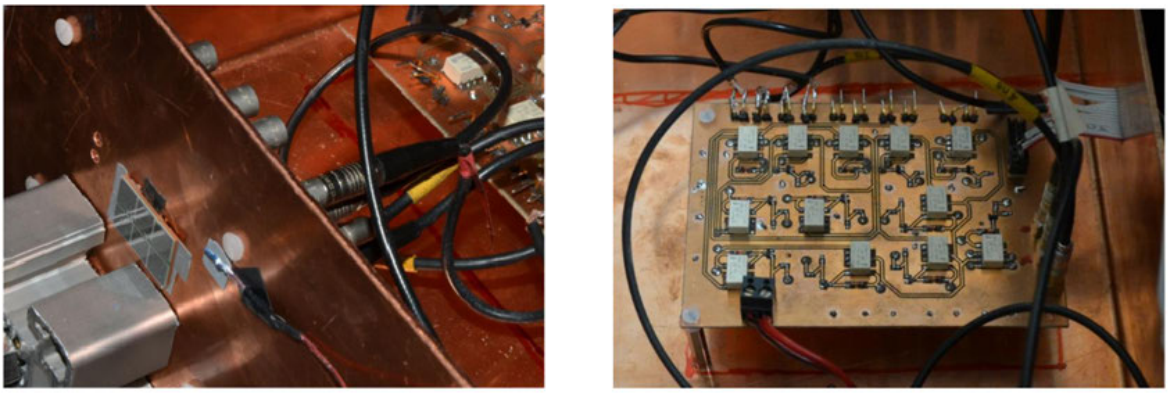

Figure 5.4: Left: Picture of a preproduction Mu2e SIPM mounted on a side of the copper box. Right: Picture of the Relays board controlled by the microcontroller.

LED was pulsed with an external programmable pulse generator, which supplied a sync signal. A cascade of Mar-8 amplifiers, with a total gain of $G_{amp} = 250$, was used in the circuit when performing the gain and PDE measurements. The amplified signal was read out by a WaveRunner 6Zi-LeCroy digital scope on a 50 Ω load [112]. For the PDE measurement, a couple of sanded quartzes was added between the LED and the SUT, in order to improve the uniformity of the diffused light. The light stability was monitored with a reference sensor (LRS) positioned close to the LED, after the first quartz.

5.1.1 Measurement of V-breakdown and Dark Current

To measure the breakdown voltage, an I-V scan was performed for each Mu2e SiPM cell. When V_{bias} starts increasing, the generated carriers have enough energy to impact atoms in the depletion region, but still insufficient to start an avalanche. The current increases more rapidly at each subsequent voltage step. The breakdown voltage, V_{br} is evaluated as the point where the curve behaviour changes from a convex function to a concave one. Therefore, V_{br} is evaluated by finding the maximum of the current Logarithmic Derivative, $LD = d(logI)/dV$ [113]. The peak position is fitted with a Log-Normal function [114]. An example of such a procedure is shown in Figure 5.5.

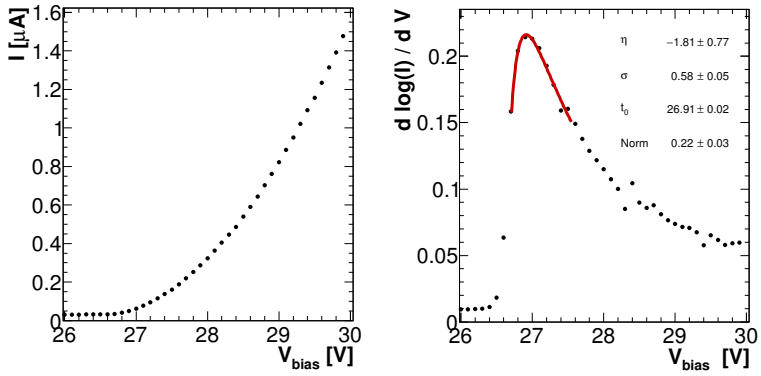

Figure 5.5: Left: example of an I-V scan. Right: dark current logarithmic derivative as function of the SiPM bias voltage. The red line represents the log-Gaussian fit used to extrapolate the breakdown voltage as the peak position value.

The operational voltage value is defined as $V_{op} = V_{br} + 3$ V. Results of the V_{op} measurement for each cell of 3×35 Mu2e-SiPMs are shown in Figure 5.6 (left column). The distribution of the dispersion of the V_{op} within a Mu2e-SiPMs, evaluated as RMS over the six cells values, is shown in Figure 5.6 (right). The red dotted line represents the 0.5% threshold required by the technical specifications. Hamamatsu prototypes showed the best performance with an RMS value of (0.070 $\pm$ 0.005)%.

The value of I_{dark} at V_{op} is obtained from the I-V scan data. Results are shown in Figure 5.7.left. On the right plots the dark current RMS in the array is shown. All sensors well satisfy the selection requirement to have an RMS below 15% apart few SensL sensors. The best performance is shown by the Advansid sensors that provides an I_{dark} RMS mean value of (4.7 $\pm$ 0.4)%.

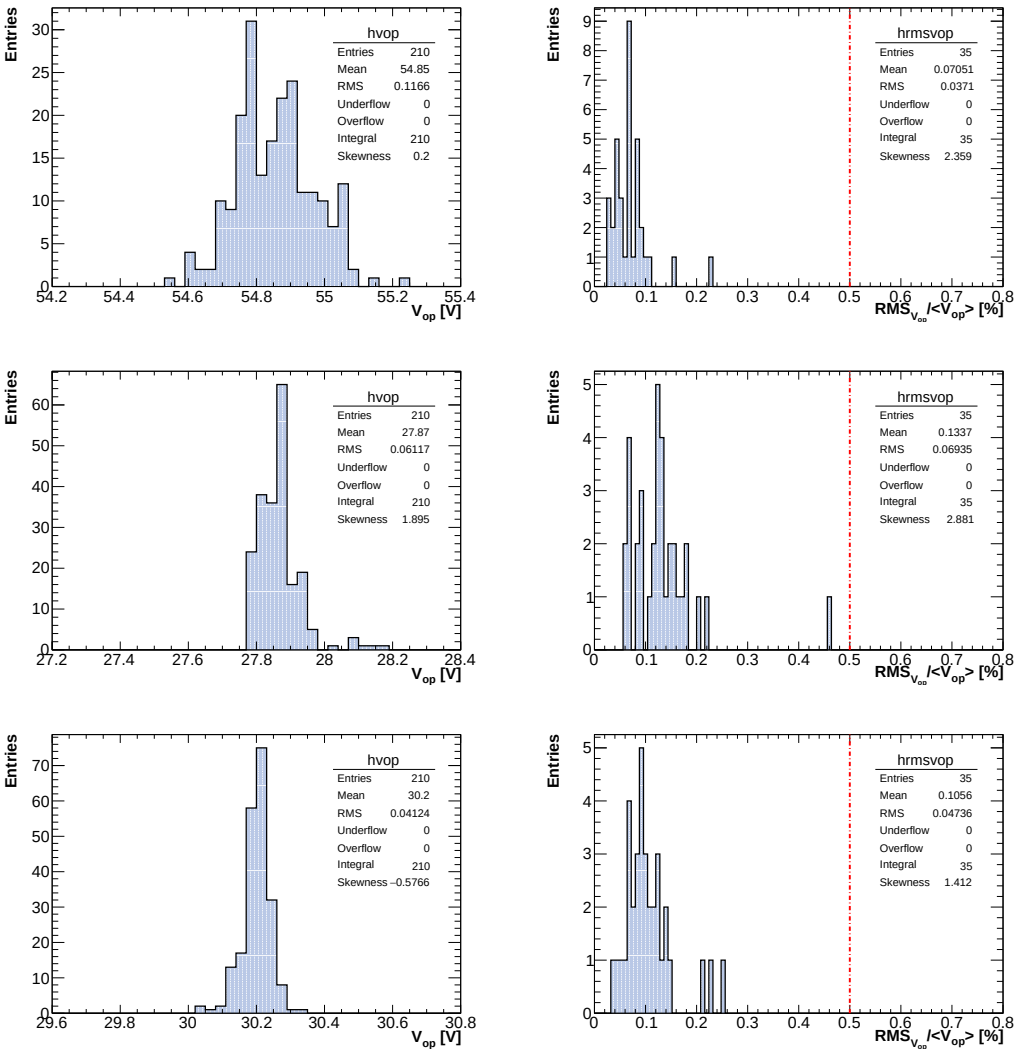

Figure 5.6: Left: Distribution of $V_{op} = V_{br} + 3$ V for all the measured cells of the SiPM from Hamamatsu (top), SensL (middle) and AdvanSiD (bottom) vendors. Right: Distribution of the RMS mean value of V_{op} among each Mu2e-SiPM cell.

5.1.2 Gain

To perform the gain measurement at V_{op}, the LED is driven by 20 ns wide pulses at a frequency of 100 kHz. The same pulse is used to trigger the data acquisition. The pulse amplitude is reduced to send only few photons reaching the photosensor. The SUT signal is increased by a factor 250 in voltage by means of a tranimpedance preamplifier and then acquired with a digital scope. The SiPM signal charge, Q, is obtained by integrating the signal in a 150 ns time window. An example of the

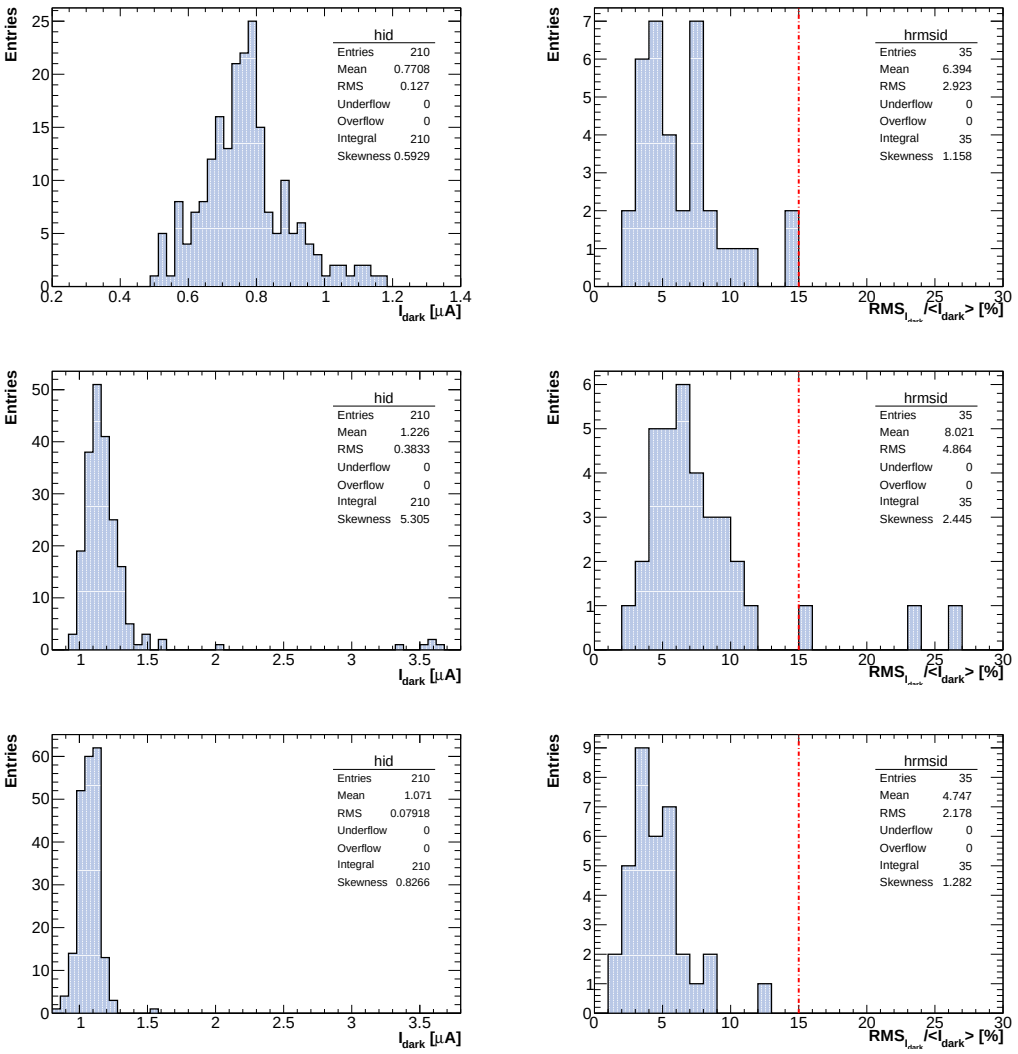

Figure 5.7: Distribution of I_{dark} (left) and distribution of the RMS mean value of I_{dark} (right) within each sensor cell from Hamamatsu (top), SensL (middle) and AdvanSiD (bottom) vendors.

resulting charge distribution for a single cell is reported in Figure 5.8. The distribution of the reconstructed charge is formed by the superposition of many peaks: each peak corresponds to a different number of photons, $n_\gamma = 0, 1, 2, ...$, detected by the SUT and, as expected, the distribution follows a Poissonian statistics. The first peak around 0 represents the pedestal [115]. The underlying noise spectrum is due to afterpulses. The interval ΔQ between adjacent peaks corresponds to the resulting mean charge produced by a single photon. The gain is therefore evaluated

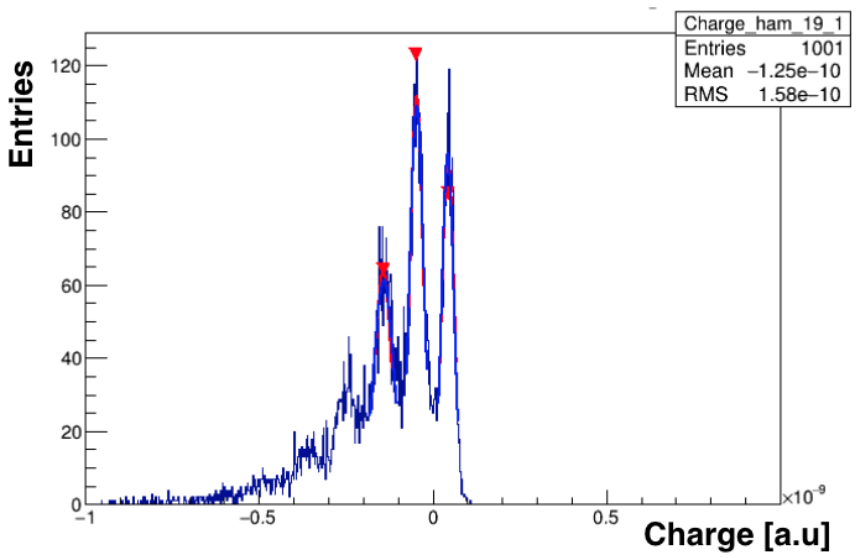

Figure 5.8: Charge distribution distribution for a SiPM's cell illuminated by a LED light. Red markers indicate the distribution's peaks. Thae Gain is evaluated using the peaks distance.

from the following formula:

$$G = \frac{\Delta Q_{01}}{q_e \cdot G_{amp}} \tag{5.1}$$

where ΔQ_{01} is the charge difference between the peaks of 0 and 1 photons, q_e is the electron charge and G_{amp} is the amplifier gain.

Results of the G measurements at the operational voltage are shown in Figure 5.9.left. The higher value of G is shown by the Hamamatsu SiPMs and corresponds to an average gain of $(2.40 \pm 0.01) \cdot 10^6$, largely satisfying the selection requirements. Also the gain RMS mean value among cells of each sensor results to be in specifications. The best result is still provided by the Hamamatsu SiPMs and corresponds to an RMS of $(1.7 \pm 0.2)\%$.

5.1.3 Photon Detection Efficiency

The PDE is defined as the ratio between the average number of detected photoelectrons, n_{pe}, and the average number of incident photons hitting the sensor active region, n_γ [116]. The probability P(n) of detecting n photons by the sensor, in condition of a stable incident photon flux, is described by the Poisson distribution:

$$P(n, n_{pe}, n_{dark}) = \frac{(n_{pe} + n_{dark})^n \cdot e^{-(n_{pe}+n_{dark})}}{n!} \ , \tag{5.2}$$

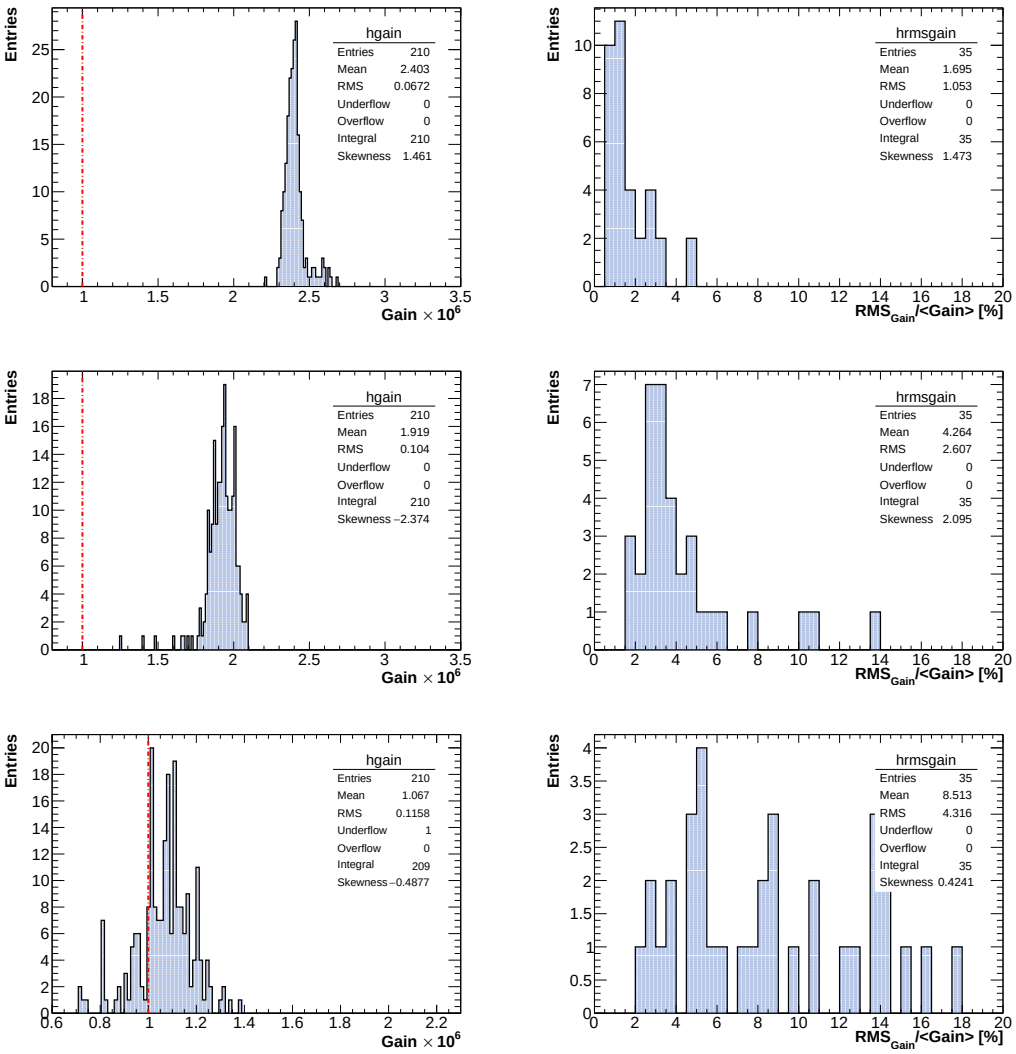

Figure 5.9: Left: Distribution of the gain, G, for all sensors in the prototypes batch from Hamamatsu (top), SensL (middle) and AdvanSiD (bottom) vendors. Right: Distribution of the relative gain RMS in each sensor.

where n_{dark} is the average number of dark pulses in the live time gate of the measurement. Inverting the equation 5.2, n_{pe} is obtained as follow:

$$n_{pe} = -ln(P(0, n_{pe}, n_{dark})) + ln(P(0, 0, n_{dark})) \ , \tag{5.3}$$

where $P(0, 0, n_{dark})$ is the probability of counting zero photons when no light is reaching the sensor. To measure $P(0, n_{pe}, n_{dark})$ and $P(0, 0, n_{dark})$, the LED is powered by 20 ns wide pulses at a frequency of 100 kHz and its amplitude reduced to have a mean of about 1 photon hitting the SUT. The LED intensity is proportional

to N_γ and it is monitored by recording the current of the LRS, that is closer to the LED. The SUT is biased at V_{op} and its signal is amplified by a factor 250. Triggering on the LED pulse, a waveform of 1 μs is recorded with the LED pulse centred at 500 ns after the trigger. To suppress noise, the recorded waveform is smoothed by filtering its Fourier components with frequency higher than 150 MHz; then, a peak search algorithm is applied on the waveform to find the arrival time of dark or LED signals. An example of a waveform is shown in Figure 5.10.

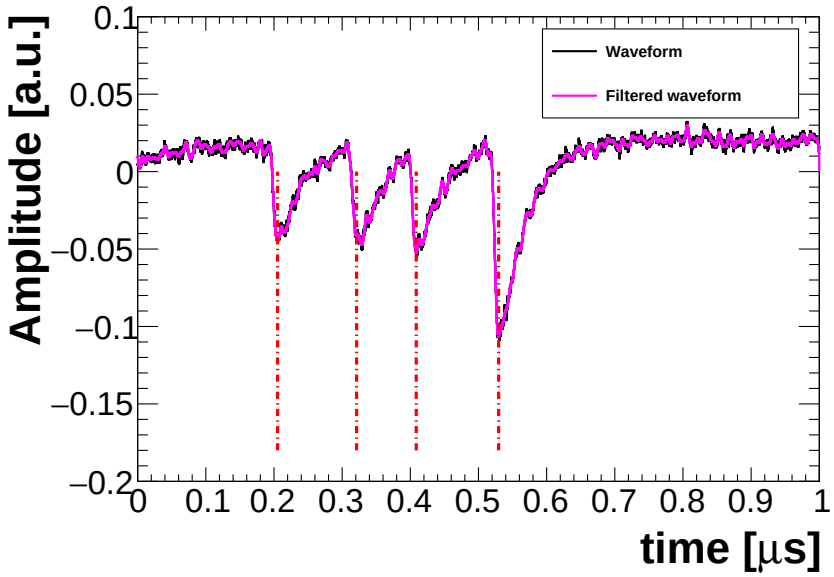

Figure 5.10: Example of a recorded waveform (black). In magenta the same waveform is shown after the cut of the Fourier components larger than 150 MHz. The Red dotted lines indicate the reconstructed time. The LED is positioned at t = 0.5 μs.

The distribution of the recorded waveforms peaks time is shown in Figure 5.11. In this distribution, two time gates 20 ns large are selected: the first (within magenta lines) is used to evaluate the number of dark pulses in the time interval (N_D), while the second (within red lines) is used to estimate the number of LED events with at least one photo-electron ($N_{n\geq 1}$). Using N_D, $N_{n\geq 1}$ and the total number of recorded events N_T, it is possible to write:

$$P(0, n_{pe}, n_{dark}) = 1 - P(n \geq 1, n_{pe}, n_{dark}) = 1 - \frac{N_{n\geq 1}}{N_T} \ , \tag{5.4}$$

$$P(0, 0, n_{dark}) = 1 - P(n \geq 1, 0, n_{dark}) = 1 - \frac{N_D}{N_T} \ . \tag{5.5}$$

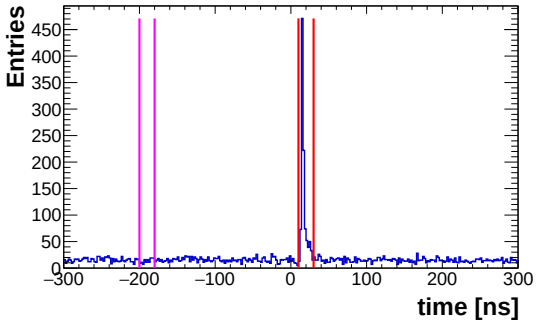

Figure 5.11: Time of the detected peaks. The zero corresponds to the LED pulse. The peak between 10 and 30 ns results from the LED light, while the flat background is due to dark pulses.

Inserting equation 5.4 and 5.5 in equation 5.3, n_{pe} can be obtained as:

$$n_{pe} = -ln(1 - \frac{N_{n\geq 1}}{N_T}) + ln(1 - \frac{N_D}{N_T}) \ . \tag{5.6}$$

All measurements have been performed relatively to a reference sensor (PRS) with a well known PDE of 22% at the LED light wavelength, in order to simplify the absolute number of incident photons. The PRS V_{op}, I_{dark} and gain have been measured with the same procedure applied for the Mu2e-SiPMs. The relative PDE can be written as:

$$\frac{PDE}{PDE^{PRS}} = \frac{n_{pe}}{n_{pe}^{PRS}} \cdot \frac{N_\gamma^{PRS}}{N_\gamma} \ , \tag{5.7}$$

where the N_γ^{PRS}/N_γ ratio is obtained from the ratio of the LRS reference sensor current output at the moment of the two measurements.

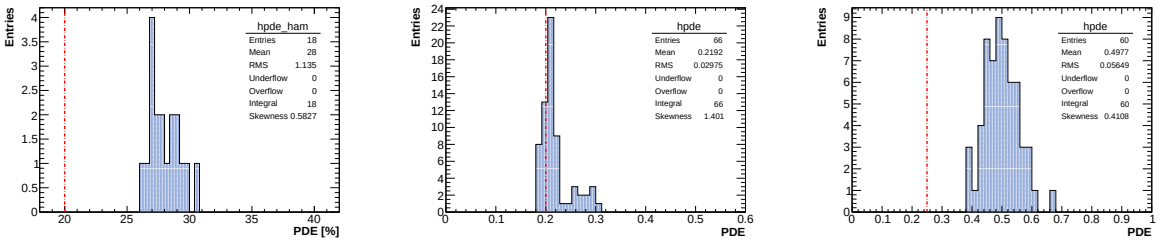

Figure 5.12: Distribution of the PDE for the tested photosensors rom Hamamatsu (left), SensL (middle) and AdvanSiD (right) vendors.

Results of the PDE measurements are shown in Figure 5.12. The Hamamatsu and AdvanSiD SiPMs mean PDE is around (28.0 ± 1.3)% and (49.8 ± 0.6)% re-

spectively, larger than the threshold required by specifications. The SensL SiPMs mean PDE is (21.9 ± 0.3)%, but some samples do not satisfy the requirement.

5.1.4 Recovery Time

The recovery time, or quenching time, is dominated by the value of the basic capacitance, CT, of the SiPMs used, by the pixels size and by the value of the quenching and load resistors. The fast recovery time is due to the recharge of the SiPM pixels, while the slow one can be assigned to the recharge of the SiPM bulk. The pixel recovery time contributes to more than 90% of the recovery process, while the bulk recovery time dominates the tail of the recovery process. The bulk recovery time is more dominant for SiPMs with large pitches [117]. As an example, the single 6×6 mm^2 Hamamatsu cell presents a CT of around 1280 pF. The value of the quenching resistor claimed by the producer is of around R_q = 150 kOhm. The observed tau can be parametrized as a function of the load resistence, R_{load}, and of the number of pixel, $N_{pixel} = 14400$, according to the following formula:

$$\tau = CT \times (R_q/Npixel + R_{load}). \tag{5.8}$$

Inserting the numerical value, we expect around 80 ns for the Hamamatsu cell. We have measured the value of the τ for one sensor of each pre-production firm, both for a single cell and for the series configuration.

The experimental set-up used is reported in Figure 5.13. A SiPM, fixed to a copper support, is kept to 20 °C through a Peltier cell. In order to illuminate it, a optical fiber, fixed to a metallic support, diffused the blue light by an Hamamatsu picosecond laser (C10196) with a rate of 1kHz. In order not to modify the pulse shape, no external preamplifiers were used.

For each SiPM ∼5000 waveforms have been acquired with a CAEN DT5751 digitizer at 1 Gsps. The measurement has been performed using a load of 50 Ω, that is the digitizer input impedance. The final results will be corrected with the ratio between 15 Ω and the used load.

In Figure 5.14 the waveform profiles have been reported. The τ value is obtained by fitting the output waveforms of the sensors with a superposition of three

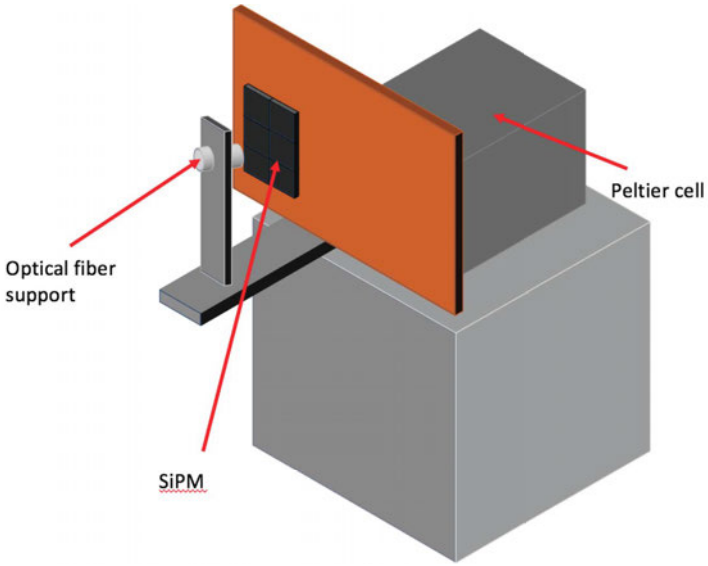

Figure 5.13: Sketch of the experimental setup used for the recovery time measurmenet test.

exponential functions as in the following formula:

$$f(t) = P0[(1 - P4) \times (e^{-(t-P1)/P2} - e^{-(t-P1)/P3}) + P4 \times e^{-(t-P1)/P4} \tag{5.9}$$

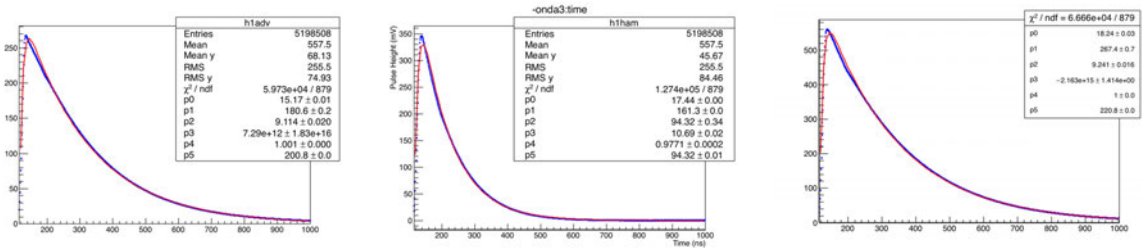

Figure 5.14: Average waveform for a a single cell of the AdvanSiD (left), Hamamatsu (middle) and SensL (right) SiPM.

The fit results for the SiPM recovery time are reported in Table 5.1 as well as the results corrected with the ratio between 15 Ω and the used load (50 Ω).

The same procedure has been repeated also for the series of three cells in order to check how the recovery time improves, as reported in Figure 5.15. The summary of the results is reported in Table 5.2.

SiPM vendor	V_{op} [V]	τ_{cell} (50 Ω) [ns]	τ_{cell} (15 Ω) [ns]
AdvanSiD 40	30	200.8	60.24
Hamamatsu 4	55	94.32	28.3
SenSl 46	27.8	220.8	66.24

Table 5.1: Summary of the V_{op} and the recovery times obtained considering a load of 50 Ω and 15 Ω for a single cell of the SiPM.

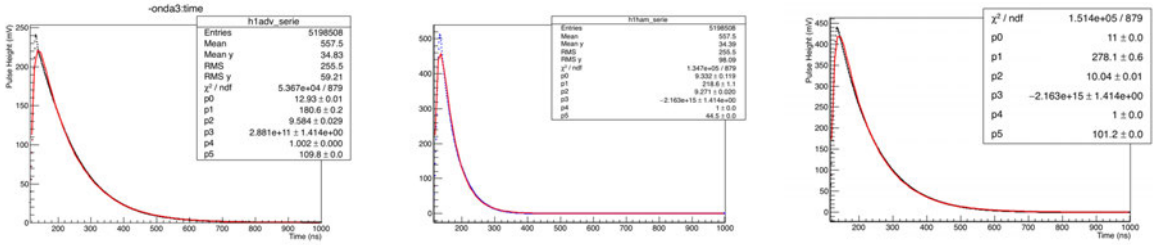

Figure 5.15: Average waveform for a a single cell of the AdvanSiD (left), Hamamatsu (middle) and SensL (right) SiPM.

As shown in the plots AdvanSiD and SensL show very similar decay time both for single cell and for the series configuration. Hamamatsu instead presents a decay times that is a factor of two shorter that the one from the other vendors. When correcting for the impedance value, all vendors pass the requirement.

SiPM vendor	V_{op} [V]	τ_{cell} (50 Ω) [ns]	τ_{cell} (15 Ω) [ns]
AdvanSiD 40	90	109.8	32.94
Hamamatsu 4	165	44.5	13.35
SenSl 46	83.7	101.2	30.36

Table 5.2: Summary of the V_{op} and the recovery times obtained considering a load of 50 Ω and 15 Ω for the series of three SiPM cells.

5.2 Radiation test

5.2.1 Ionizing dose

In November 2015 and in June 2018, two gamma radiation tests of Mu2e SiPMs have been performed, both at the CALLIOPE γ-Facility of ENEA-Casaccia (Bracciano) [118]. Here a where a ^{60}Co source is used to produce γs with an energy of 1.25 MeV. The irradiation plant is a large volume pool-type facility, where the source is arranged in 48 bars with cylindrical shape housed along two concentric cylinders. The activity of the source during our tests was 0.35×10^{15} Bq, allowing to reach from 10 to 2 Gy/h at about 5 m distance.

In 2015, a Mu2e-SiPM was irradiated with these photons for three days, absorbing a total dose of 20 krad. The dose effect on SiPM performances is negligible both in term of leakage current and signal amplitude, as shown in Figure 5.16 and Figure 5.17 (left). The leakage current, which before the irradiation is of 0.15 μA, increases to 0.6 μA as soon as the irradiation started due to the Compton effect on the SiPM active surface. In three days of irradiation the current increased by $\sim$0.15 μA, thus practically doubling the initial dark current [106]. The signal amplitude remained unchanged.

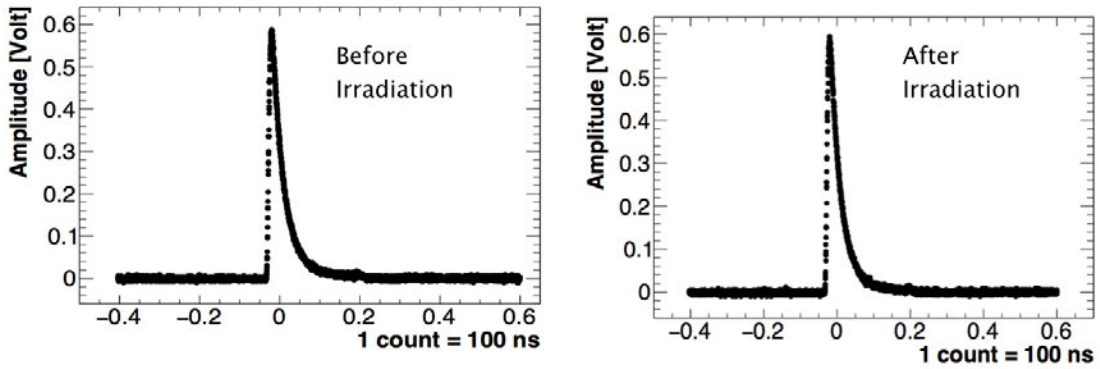

Figure 5.16: SiPM digitized waveform when exposed to LED light before (left) and after (right) gamma radiation exposure.

During the radiation campaign of 2018, another single Hamamatsu Mu2e SiPM has been exposed at 500 rad/h for about 6 days, for a total of 125 hours ($\sim$70 krad).

The SiPM was tested without FEE chip and biased by a power supply protected by lead blocks.

Figure 5.17 (right) shows the result of the test, where the SiPM dark current is reported as a function of the elapsed time, consistently with the old 20 Krad measurement. The dark current observed increase of few μA is negligible compared to the Mu2e requirement and compared to the neutron damage.

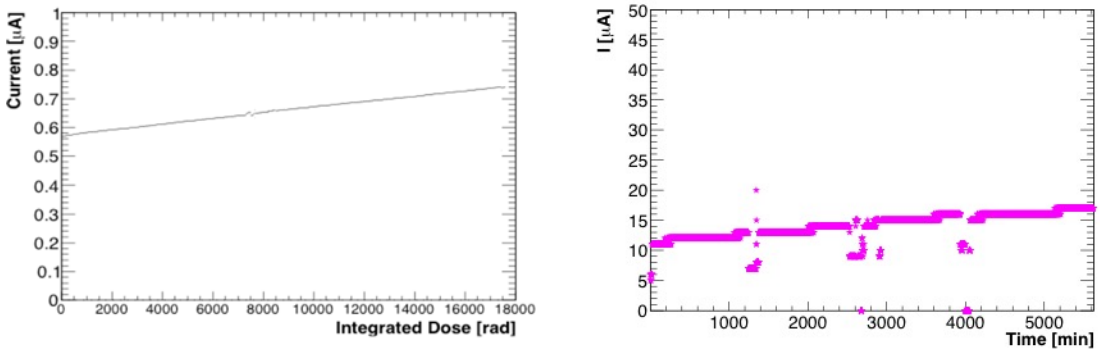

Figure 5.17: SiPM dark current as a function of the integrated dose (left, test 2015) and as a function of the elapsed time (right, test 2018).

In conclusion, a negligible increment of the leakage current and no gain change have been observed with the ionizing dose irradiation tests.

5.2.2 Neutrons

In March 2017 a neutron irradiation test was performed at the Elbe Positron Source facility (EPOS) of the Helmholtz-Zentrum Dresden-Rossendorf [119]. In this facility, a 30 MeV electron beam, of O(100 μA) current, interacts with 1 cm thick Tungsten target and becomes a source of photons and neutrons [120]. In Figure 5.18, the picture of the target with the surrounding shielding of Lead and Borated Polyethylene is shown.

The distribution of the equivalent expected dose for neutrons is shown on Figure5.18.left, while on the right plot the distribution of the expected dose due to photons is presented. The devices under test were located on top of the shielding roof, where the expected photons contribution in dose is negligible. The ratio between the expected photon and neutron induced doses in this region is of $\sim 10^{-4}$.

During the irradiation period, lasted $\sim$ 29 hours, we have continuously recorded the beam current in order to monitor the flux intensity along the data taking time. The neutron fluence has been estimated by a full FLUKA simulation [121] and has been scaled to a 1 MeV equivalent neutron damage on Silicon as a function of the kinetic energy of the simulated neutrons. The spectrum (Figure 5.19, left) is well centred around 1 MeV. Most of the photon produced have an energy below 3 MeV, as shown in Figure 5.19 (right), so they are well shielded by lead.

Experimental setup and measurements

Three Mu2e SiPMs (one for each vendor) have been exposed simultaneously to the same neutron flux. The sketch of the experimental setup used is shown in Figure 5.20, where the details of the SiPM support are shown.

The sketch of the read out circuit is shown in Figure 5.21. To evaluate the dark current, the acquired output voltage has been divided by the value (0.5 Ω) of the load resistor. To maintain the SiPMs' temperature as stable as possible, the sensors under test have been plugged on a copper support, which has been mounted on the cold side of a Peltier cell. In order to assure a good thermal contact, a thermal paste has been used to couple the sensor to the copper plate. The Peltier cell hot side was connected to a very stable chiller system, with water coolant running at (18.3 $\pm$ 0.1) °C. This allowed us to maintain the SiPMs' side at around 20° C.

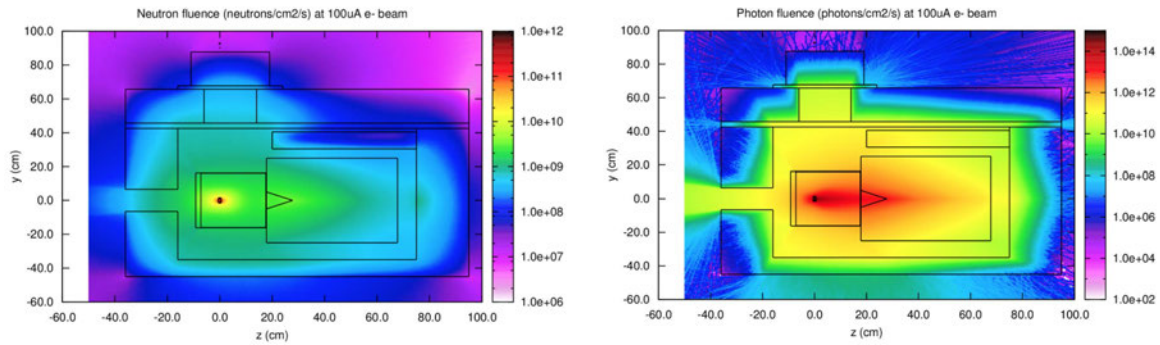

Figure 5.18: Distribution of the neutron (left) and of photon (right) fluences as a function of the position around the shielding for an electron current of 100 μA.

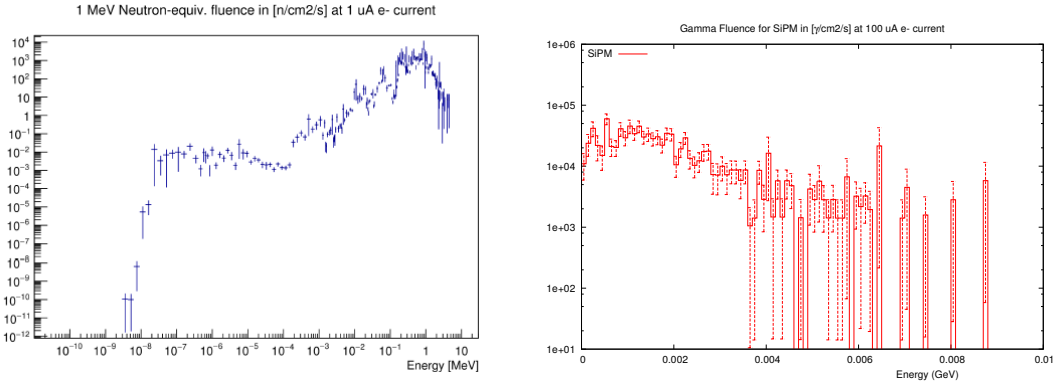

Figure 5.19: 1 MeV equivalent neutron (left) and gamma (right) spectra for an electron current of 1 μA at the SiPMs position.

To monitor the SiPMs temperature along the run, a PT100 resistance-thermometer have been plugged in the middle of the SiPMs in the copper support. The SiPMs' output voltage and the PT100 temperature were acquired by an Agilent 34972A LXI Data Acquisition / Data Logger Switch Unit every 10 s [122]. Pictures of the experimental setup are shown in Figure 5.22.

The SiPMs' support was placed on the top of the EPOS shielding, $\sim$ 90 cm far away from the neutron source, with the sensors active area positioned perpendicularly to the incoming neutron (Fig. 5.23). For each SiPM, only one out of six cells

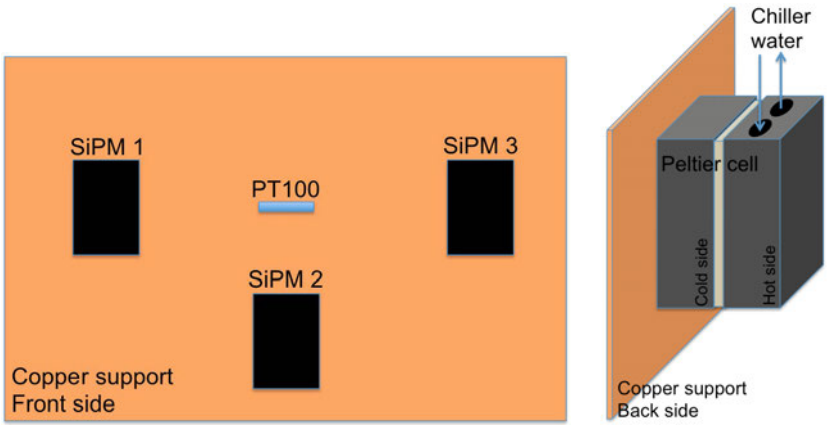

Figure 5.20: Front (left) and back (right) sketch of the experimental setup used for SiPMs irradiation test at EPOS facility of HZDR.

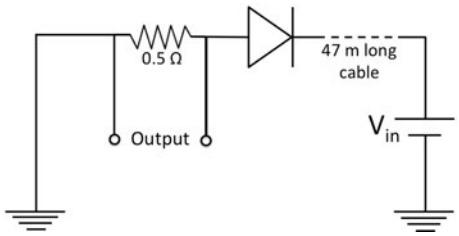

Figure 5.21: Scheme of the circuit used to bias and acquire the voltage output of the SiPM cell under test.

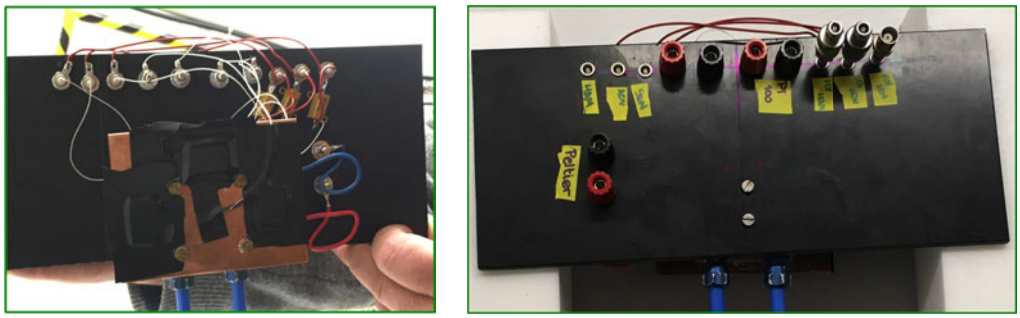

Figure 5.22: Pictures of the front (left) and back (right) side of the experimental setup used for SiPMs irradiation test at EPOS facility of HZDR. The three SiPMs under test are covered by black tape to make them light tight and to not disturb the measurement of dark current.

was biased at the operating voltage, while the other five cells were kept un-biased. During irradiation, we have continuously measured the current drawn by the biased cells.

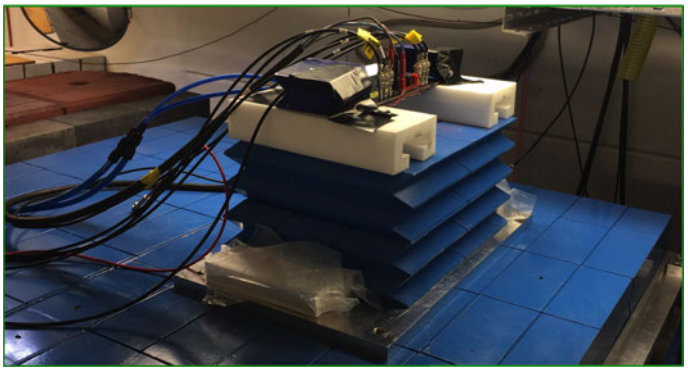

Figure 5.23: Experimental setup mounted in EPOS on top of the shielding. The SiPM surface is located at 2.2 cm from the neutron shielding (blue lead blocks) and 90 cm far away from the neutron source.

As shown in Figure 5.24 (left), the Peltier cell and the chiller system were performing very well and we were able to maintain the copper temperature stable around 20 °C.

The total neutron fluence absorbed by the SiPMs, at the end of the 29 hours long test, was estimated by the simulation to be $\sim$ 8.5 $\times$ 10^{11} n/cm^2. In Figure 5.24 (right), the measured current of the biased cells as a function of the integrated flux are reported for the three tested SiPMs. To summarise the measurement performed at EPOS, the temperature, V_{op} and the dark current (I_d) observed at the end of the irradiation period are reported in Table 5.3 for each biased SiPM.

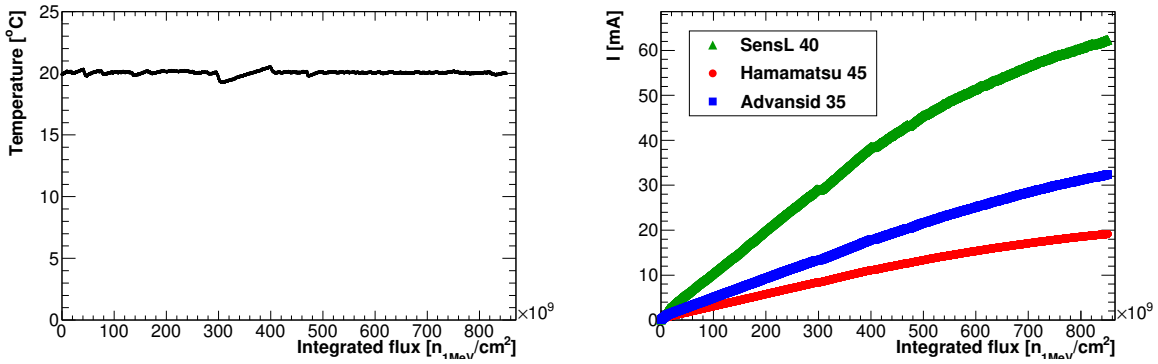

Figure 5.24: Left: temperature behaviour of the SiPM copper support as a function of the integrated neutron flux. Right: Vendor cells dark current as a function of the integrated neutron flux, delivered in $\sim$ 29 hours.

SiPM vendor	T [°C]	V_{op} [V]	I_d [mA]	I_d (after $\sim$ 2 months) [mA]
AdvanSiD 35	20	29.9	32.4	19.1
Hamamatsu 45	20	54.7	19.5	10.0
SenSL 40	20	27.9	62	38.8

Table 5.3: Temperature (T), bias voltage (V_{op}) and dark current (I_d) for each vendor SiPM cell tested at EPOS, at the end of the irradiation period. Total fluence delivered was of $\sim$ 8.5 $\times$ 10^{11}n$_{1\ \mathrm{MeV}}$/cm^2.

The current dependence on the neutron fluence is well represented by a linear

behaviour up to fluence of $3-4 \times 10^{11}$ n/cm^2. At the end of the irradiation period, we have also measured the currents of the unbiased cells that resulted to be few % larger than the biased ones. The dark current increase of the Hamamatsu SiPM looks much smaller than the Advansid and Sensl ones.

Behaviour of irradiate SiPMs with temperature and Vbias

As soon as we turned off the neutron beam, we kept acquiring the I_{dark} for an additional hour, as shown in Figure 5.25. A clear decrease due to self annealing

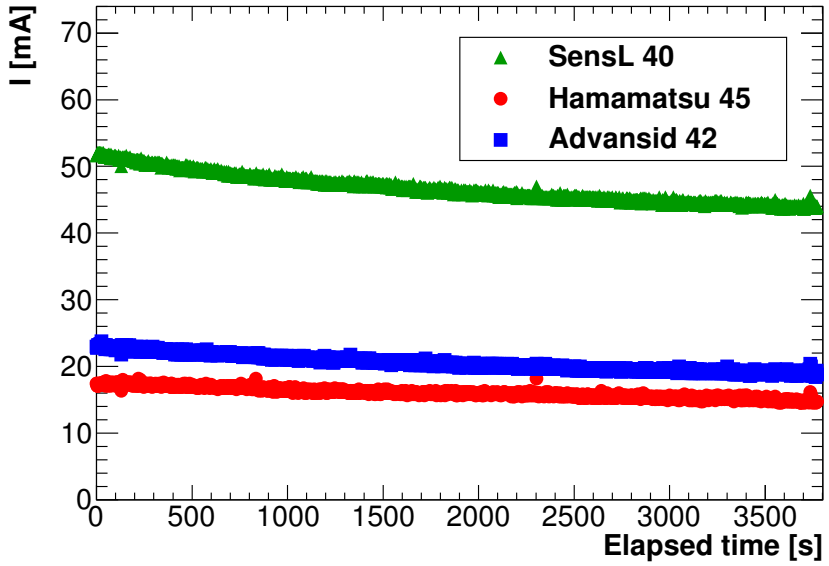

Figure 5.25: Vendors cells current as a function of the elapsed time after the end of the neutron fluence exposure.

is visible. Two months after the irradiation test, a leakage current reduction of about 50% was observed, due to annealing effect at room temperature, as shown in Table 5.3.

After annealing, all irradiated SiPMs were then tested to study the dependence of I_{dark} on temperature and applied bias voltage. The same experimental setup used at EPOS was inserted in a insulated light-tight box fluxed with nitrogen in order to decrease the temperature without reaching the dew point. At first, the dark

current of the cells biased during the irradiation have been measured by varying the temperature of the SiPMs and then varying the operational voltage. The SiPMs temperature were decreased from 20 °C down to -5 °C. In order to keep unchanged the operational point while varying the temperature, the bias voltage was decreased by 0.1 % per degree as from specifications. Moreover this variation has been checked measuring the breakdown voltage at 20, 10 and 0 °C for each SiPM. The change of I_{dark} with respect to temperature is reported in Figure 5.26. A decrease of 10 °C in

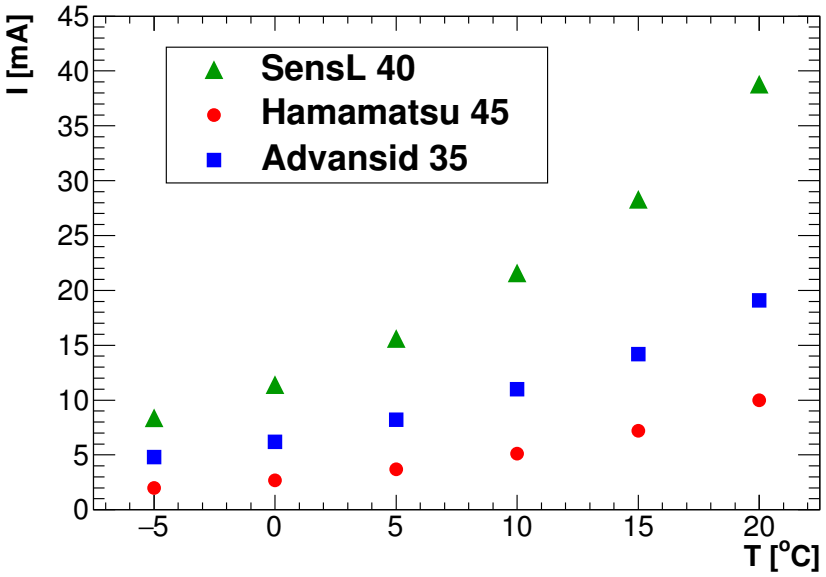

Figure 5.26: Cells current as a function of the temperature at the operational voltage.

the SiPMs'temperature corresponds to a decrease of about 50% in I_d.

After this first measurement, the SiPMs'temperature was fixed to 0 °C and the current was acquired at different bias voltages. Results are reported in Figure 5.27 as a function of the overvoltage (i.e. the difference between bias and breakdown voltages), ΔV.

To check what is the range of reasonable V_{bias} variation, a dedicated test on two channels of the Module-0 has been carried out: The two Hamamatsu and AdvanSiD central channels SiPMs were illuminated with LED light, studying the response and resolution as a function of V_{bias} variation.

Figure 5.28 shows the results for the AdvanSiD SiPMs as a function of $\Delta V =$

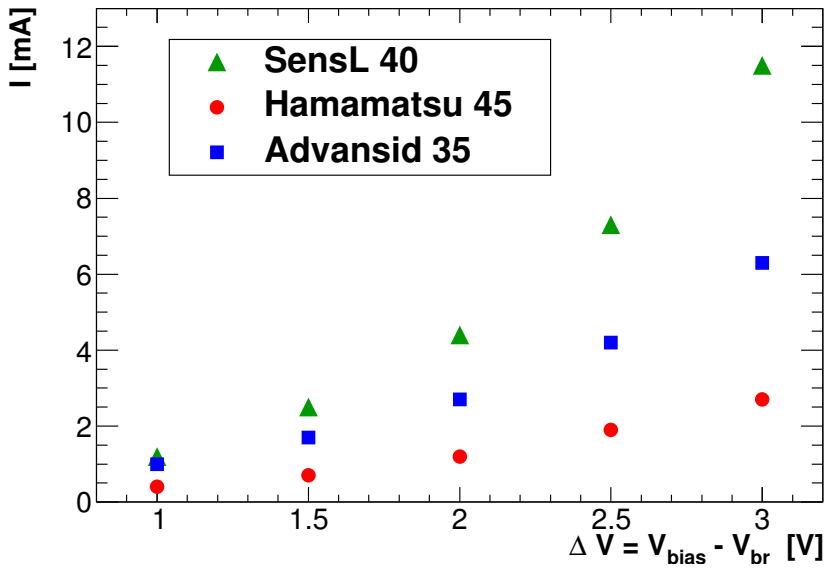

Figure 5.27: Vendor cells current as a function of ΔV. Temperature was kept stable at 0 ° C.

$V_{op} - V_{br}$. On top left, the integrated Charge is reported. "SiPM-1" and "SiPM-2" refer respectively to the left and right SiPM that were used to read out the same crystal. A good agreement between the two channels and their ratio is visible. On the top right plot, the resolution is reported for SiPM-1, SiPM2 and their ratio. On bottom left and right, the LY and the Gain for SiPM-1, SiPM2 and their ratio are reported on left and right respectively. A reduction of 3 V in ΔV corresponds to a gain reduction of a factor 1.8.

Figure 5.29 shows the same results obtained with the two Hamamatsu SiPMs of the Module-0 central channel concerning charge (top left), resolution (top right), LY (bottom left) and Gain (bottom right). In this case, a reduction of 3 V in ΔV corresponds to a gain reduction of a factor 1.6.

However, the highest increase of I_{dark} due to neutron exposure will be in the innermost calorimeter ring. Decreasing the SiPM temperature and/or reducing bias voltage, the dark current is maintained below the 2 mA limit. By testing the Hamamatsu SiPMs of central Module-0 channel with a LED pulse, the MeV equivalent noise as a function of I_{dark} has been evaluated. The I_{dark} value has been increased diffusing additional light into the SiPM holders.

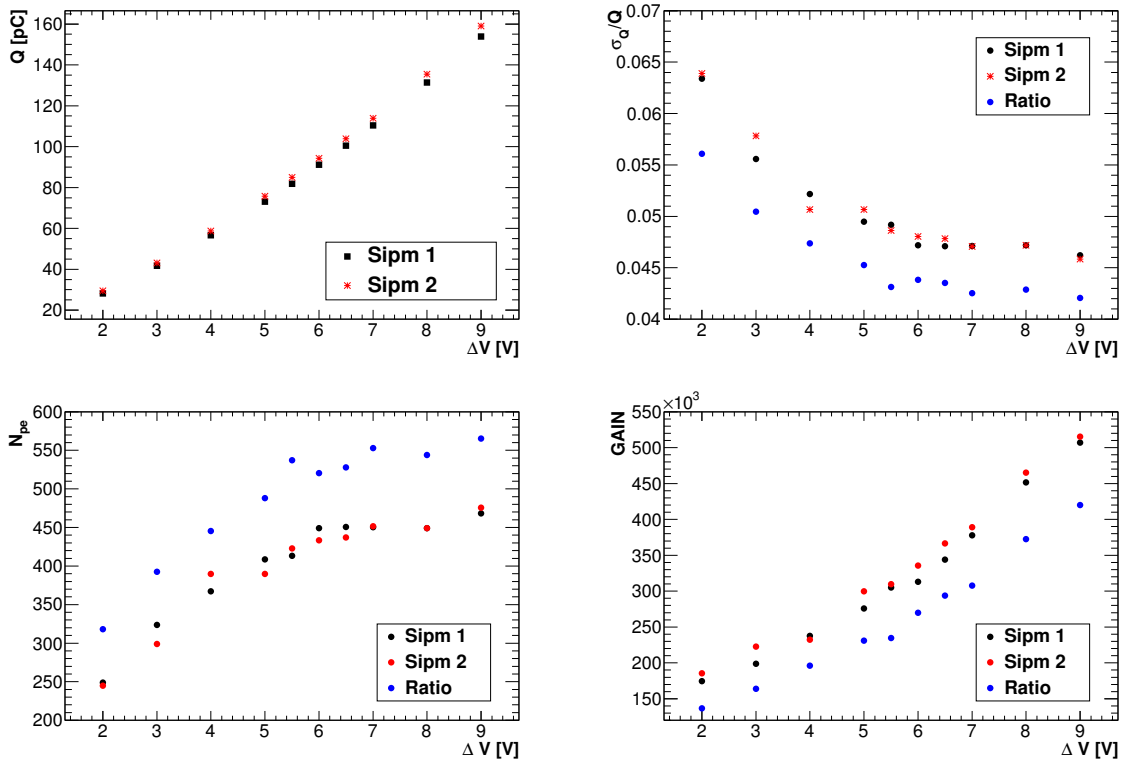

Figure 5.28

Figure 7.18 shows the charge distribution of the two SiPMs when illuminated by LED light, inside a light tight box, corresponding to ∼580 N_{pe} The sensors were biased at their operational voltages. The measured dark currents were ∼ 1 μA. The resolution (sigma/mean) obtained are 4.3% for both left and right distributions.

After this measurement, a bit of external light was let in the experimental box, in order to increase the dark current and simulate the irradiation noise. The results are reported in Figure 7.19. The ambient light induced dark current corresponds to 500 μA and 1500 μA, respectively for the top and bottom plots. All the results are summarized in Table 5.4.

Figure 5.32 shows the same noise distribution, obtained turning off the LED. The sigma is ∼14.5 pC when the induced I_{dark} ∼ 500 μA (top). It increases to ∼25 pC when the induced I_{dark} ∼ 1500 μA (bottom).

The calibration of pC/pe is evaluated from run with LED and without ambient

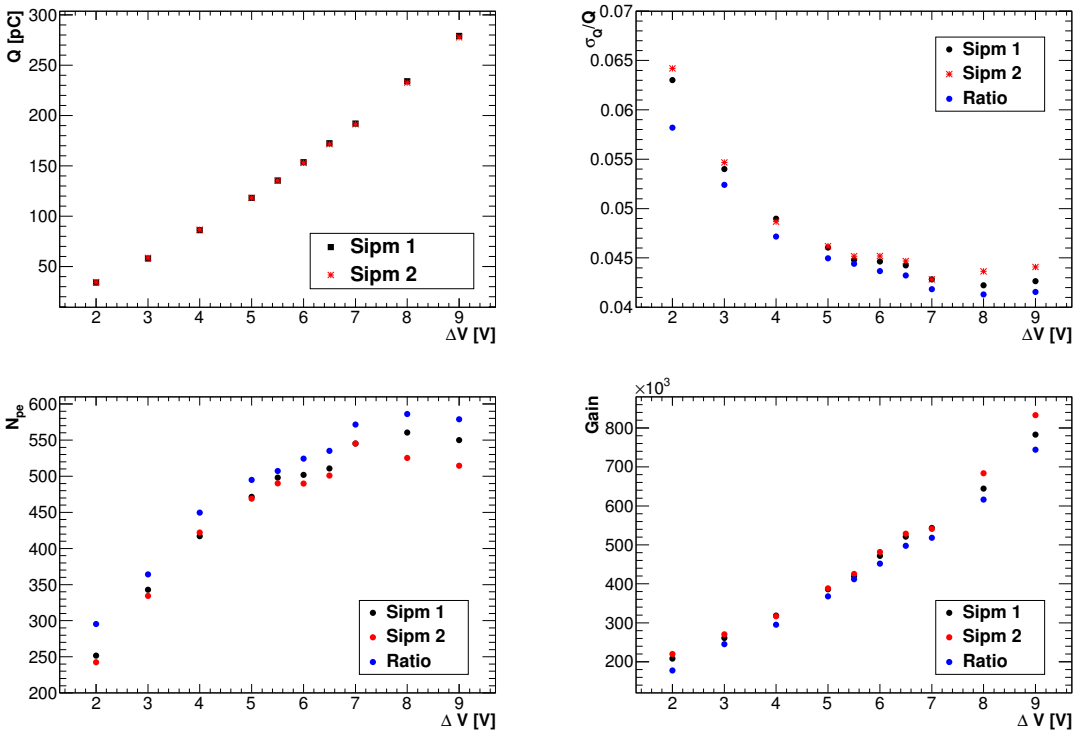

Figure 5.29

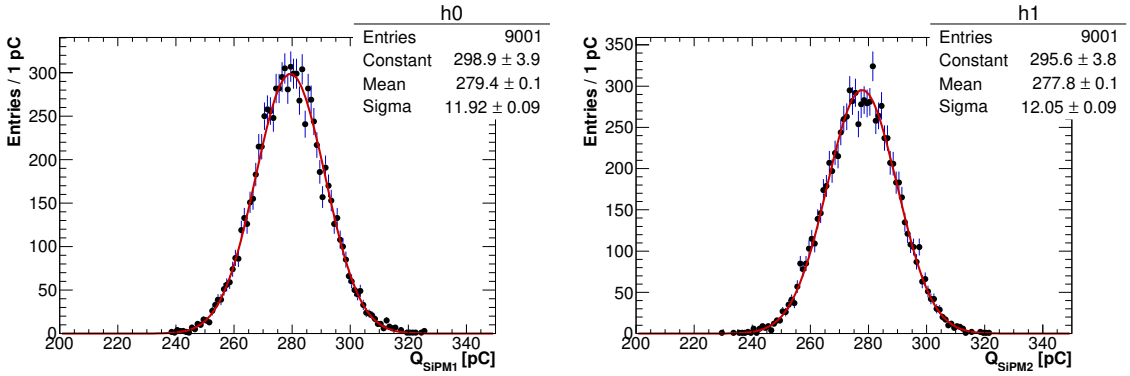

Figure 5.30: Charge distribution of the two Hamamtsu SiPM of the central module-0 channel when illuminated by LED light.

light. A LY around $\sim$ 30 N_{pe}/MeV was measured from the LY measurements done with source, cosmic rays and during the test beam. So that an $I_{dark} \sim 500$ μA corresponds to an equivalent noise of 1 MeV and an $I_{dark} \sim 1500$ μA corresponds to

	$I_d = 0$ mA	$I_d = 0.5$ mA	$I_d = 1.5$ mA
sigma$_{rel}$ (SiPM1)	4.3%	6.5%	11.1%
sigma$_{rel}$ (SiPM1)	4.3%	6.6%	11.4%

Table 5.4: Resolution of the Hamamstsu SiPMs when illuminated by LED light and simulating the neutron induced noise.

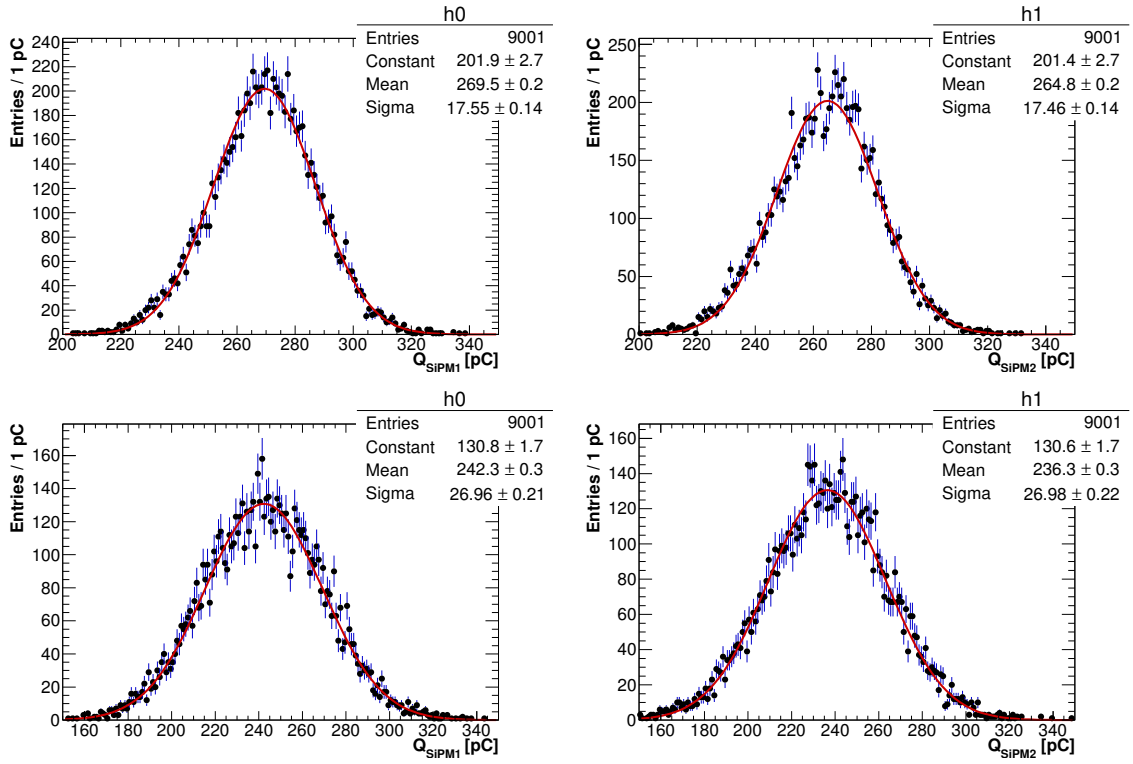

Figure 5.31: Charge distribution of the two Hamamtsu SiPM of the central module-0 channel when illuminated by LED light and ambient light, corresponding to a dark current measurement of 500 μA (top) and 1500 μA (bottom).

an equivalent noise of 1.73 MeV. Extrapolating these values to 2 mA, the equivalent MeV noise results to be around 2 MeV.

In conclusion, it is needed to keep the sensors at 0 ° and lowering of 1 V the overvoltage of each cell in the Mu2e SiPMs during the calorimeter operation, in order to keep the irradiated SiPMs still working after 5 years of running in the innermost region (i.e. to keep a $I_{dark} < 2$ mA). This will correspond to slightly deteriorate the calorimeter performance since the LY (Np.e./MeV) will decrease of

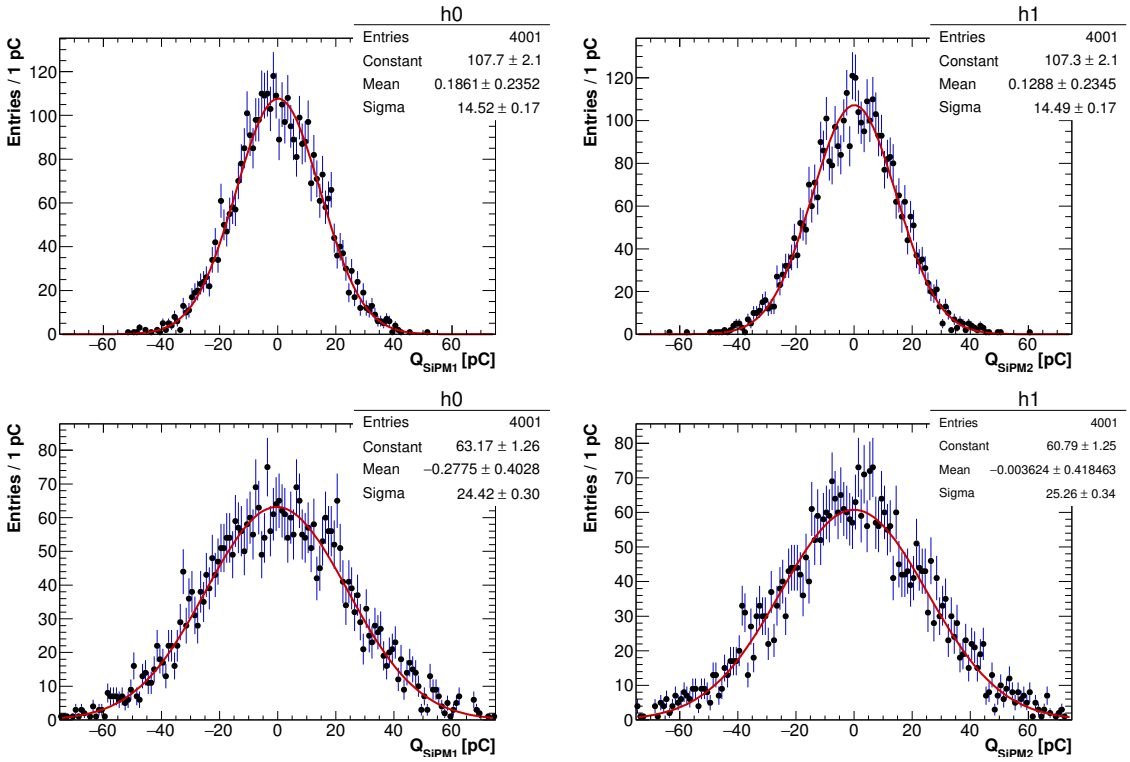

Figure 5.32: Noise distribution of the two Hamamtsu SiPM of the central module-0 channel when illuminated by ambient light, used to simulate the neutron noise and corresponding to a dark current measurement of 500 μA (top) and 1500 μA (bottom).

$\sim$10-15%. Moreover, for the channels reaching 2 mA, the equivalent noise/channel will correspond to $\sim$ 2 MeV.

5.3 Mean Time To Failure evaluation

One of the most important SiPM specification is its reliability. As previously explained, the calorimeter has to remain inside the Detector Solenoid for one year without intervention and without losing performance. The calorimeter reliability was improved by reading out each crystal with a pair of independent Mu2e SiPMs, each one connected to its own, independent, read out chain. With a simulation, we have estimated that the needed Mean Time to Failure (MTTF) for the photosensors has to be larger than 1 million hours. In order to experimentally evaluate the MTTF, we have applied a burn-in measurement to five SiPMs per vendor randomly selected. The MTTF determination was performed between November 28, 2016 and March 13, 2017.

The basic measurement technique consists in accelerating the failure mode of the sensors by operating them at higher temperature. We have used an accelerating temperature of 50°. For a given number of SiPMs under test and assuming to observe no deads at the end of the testing period. the MTTF value is calculated as follows:

$$MTTF = 0.5 \times N_{SIPM} \times AF \times N_{hours}, \tag{5.10}$$

where N_{hours}= 2496 is the number of hours of the test duration, $N_{SIPM} = 5$ is the number of SiPMs under study and the acceleration factor, AF, is obtained from the Arrhenius Equation:

$$AF = exp\left[\frac{E_a}{k}\left(\frac{1}{T_{use}} - \frac{1}{T_{stress}}\right)\right], \tag{5.11}$$

where $E_a = 0.7$ eV is the Silicon activation energy, k is the Boltman constant, T_{use}=273 °K is the temperature fixed for the Mu2e experiment and T_{stress} =323° K is the temperature used during the MTTF test. The acceleration factor is used to derive the failure rate from the thermally accelerated life test conditions to a failure rate indicative of experiment temperature. In our case, the AF is estimated to be $\sim$ 100.

The MTTF test was performed keeping the SiPMs in a light tight box, in thermal contact with a system of two Peltier cells. A constant feedback circuit driving the Peltier cells allowed to maintain the temperature stable at 50 °C. Temperature was

monitored using a PT100 sensor. The aluminum box was surrounded by a Styrofoam support avoiding heat dispersion. An aluminum plate, connected to the cold side of the Peltier, was used as radiator. A schematic view of the experimental set up is reported in Figure 5.33.

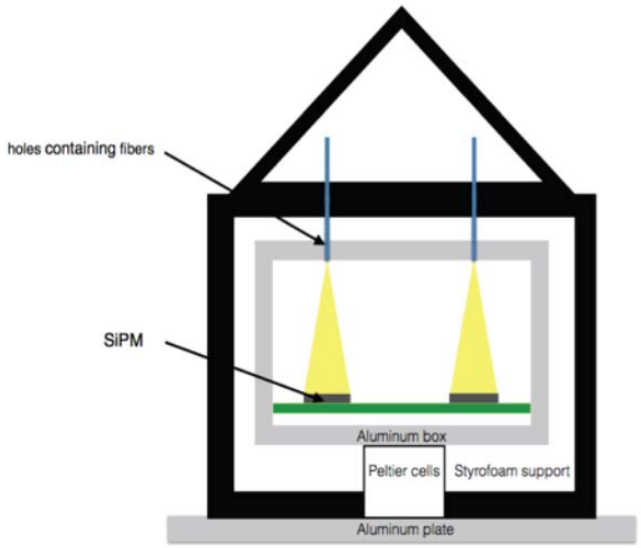

Figure 5.33: Sketch of the box used for the MTTF SiPMs test.

The cathode of each SiPM was connected through a 100 Ω resistor to the high voltage, while the anode was connected to the the ground through a capacitor of 100 nF. The two series were connected in parallel. The Mu2e-SiPMs response to a blue LED, distributed to the sensors by means of 15 optical fibers, was measured every two minutes using a CAEN Flash ADC. The blue LED was driven by a pulse generator supplying a 10 V pulse of 100 ns width. Sensors dark current has been measured once a day by a pico-ammeter for the whole duration of the test. In Figure5.34 the behaviour of the collected charge and of the dark current as a function of the elapsed time is reported. At the end of the test, all SiPMs were alive, without changes in charge or amplitude, so that the MTTF value was evaluated to be greater than 0.6×10^6 hours per each vendor.

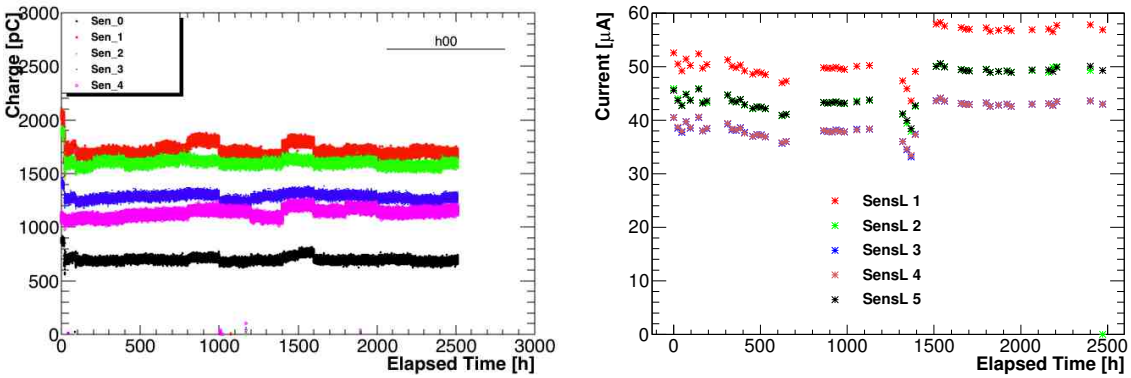

Figure 5.34: Dependence of the SiPM charge (Left) and signal amplitude (Right) as a function of the elapsed time

5.4 Tests on production SiPMs

A the end of the long characterization of pre-production Mu2e SiPMs, the Hamamatsu vendor results the best provider, in particular in terms of radiation hardness.

Test stations have been designed by the Mu2e INFN-Pisa and LNF-INFN groups, as automatized tools to test the SiPMs performances of the 3000 Mu2e SiPMs under procurement for the construction of the Mu2e electromagnetic calorimeter.

The QA procedure of these SiPMs works as the crystals one: 300 SiPMs/month are shipped from the producers to the Mu2e Calorimeter laboratory at Fermilab. Here a visual survey is carried out to control the absence of big defects. Soon after, they their mechanical specifications are controlled by means of a custom laser station with a 100 μm tolerance. If they do not pass specifications they are rejected and sent back to the producer. In the other case, they are tested with the automatized station and the MTTF value is estimated using 18 SiPMs/batch. A subsample of five randomly selected samples are used for neutron irradiation test in HZDR, Dresden (Germany).

5.4.1 Characterization

The QA process requires to characterize 18000 6×6 mm^2 sensors (6×3000). The ones satisfying the visual inspection and the dimensional check are then characterized in

an automitized system, to speed up the process and it is dedicated to measure for each SiPM cell:

- the V_{br} and its spread over the six cell of a SiPM, which is required to be <0.5%(at 20 °C);
- the I_d at the operational voltage and its spread over the six cell of a SiPM, which is required to be <15%(at 20 °C);
- the gain × PDE at 310 nm at the operational voltage and it is required to be $>2 \times 10^5$ for each single cell.

The first two items are measured following the procedure discussed in Section 5.1. The Gain × PDE is evaluated as the ratio of the currents pulled by the SiPM cells and by a fixed reference sensor, while both are illuminated with a stable and uniform LED light.

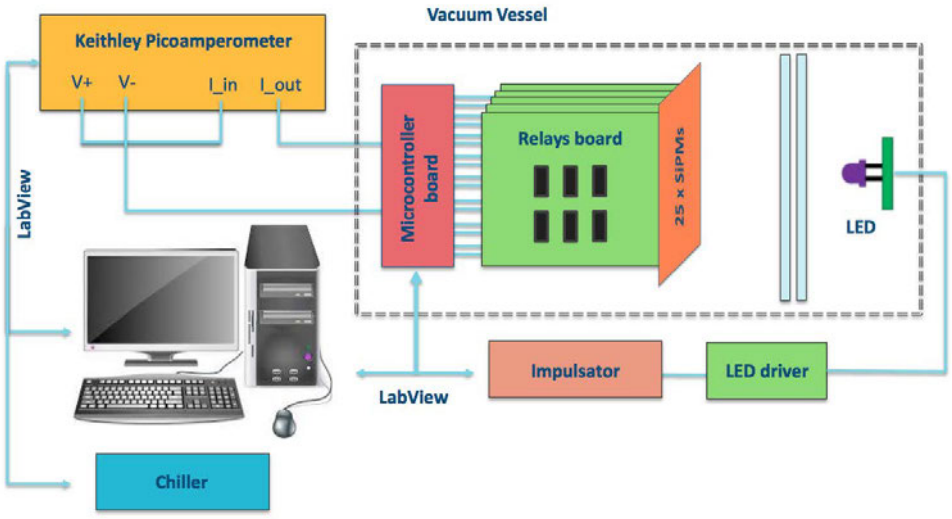

Figure 5.35: Scheme of the experimental setup used for the production Mu2e SiPMs tests.

The scheme of the test system is reported in Figure 5.35. The main difference with the old version is the presence of five relay boards. In this way it is possible to measure 20 Mu2e SiPMs per time, in addition to five fixed reference sernsors. Once the SiPMs are inserted in the vessel reported in Figure 5.36 (left), the test procedure is fully automatized and controlled by a Labview software, analysis included. The

other difference between the old setup is that the light tight box used is a vacuum pump (Fig. 5.36, right). In this way, the measurements can be performed at -10 °C, 0 °C and at 20 °C, since the SiPMs operational temperature in the calorimeter will be 0 °C.

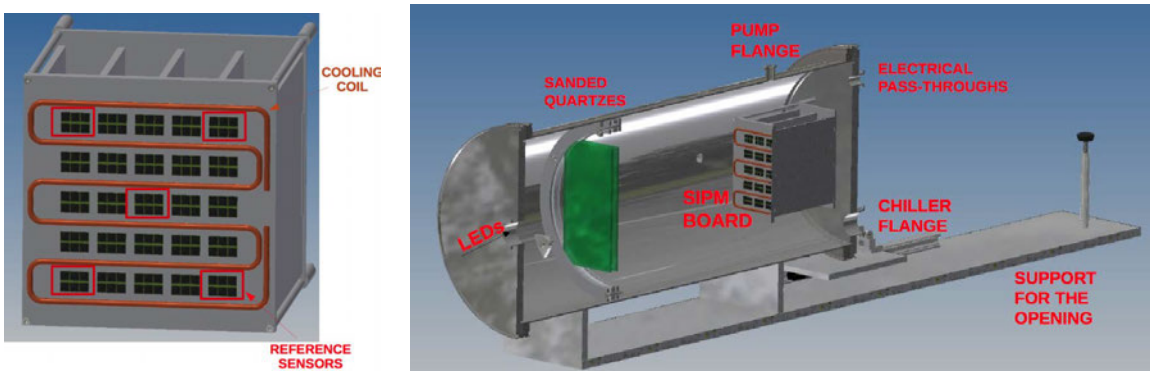

Figure 5.36: CAD drawing of the experimental te

At the moment of writing, 1089 Mu2e SiPMs have been tested. In Figure 5.37, the V_{br} for all the cells is reported as a function of the SiPM identification number. A dependance is clearly visible, probably due to different silicon wafers.

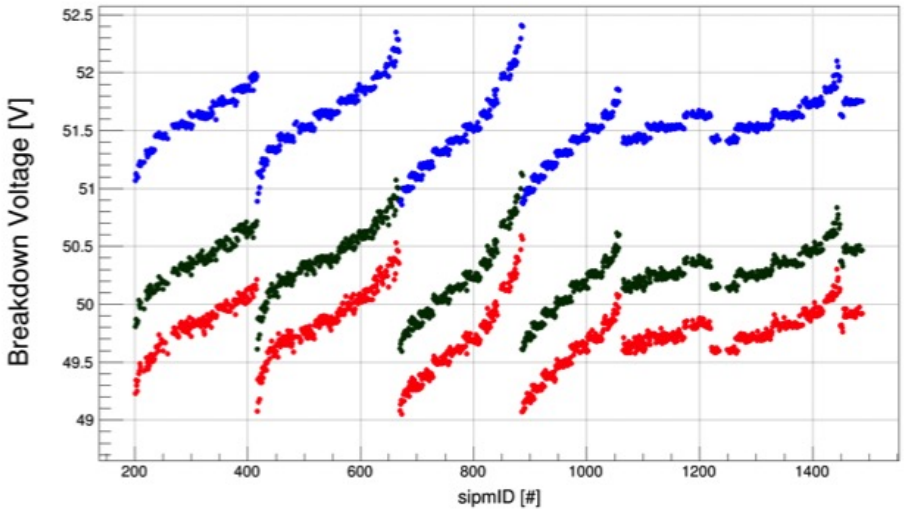

Figure 5.37: Breakdown voltage measured at three different temperature (-10 °Cin red, 0 °C in green, 20 °C in blue) as a function of the SiPM identification number.

Figure 5.38 shows the the V_{br} (top) and I_d at V_{br} (bottom) spread distributions over the six cells of the SiPMs. These measurements have been performed at the

three temperatures over mentioned: -10 °C (left), 0 °C (middle) and at 20 °C (right). The red dotted lines represent the requirement. All the SiPMs satisfy the requirement on V_{br} spread, even at temperature lower than 20 °C. Concerning the requiremen on I_d spread at 20 °C, 38 SiPMs have been rejected, corresponding to 3.4% of the total samples tested.

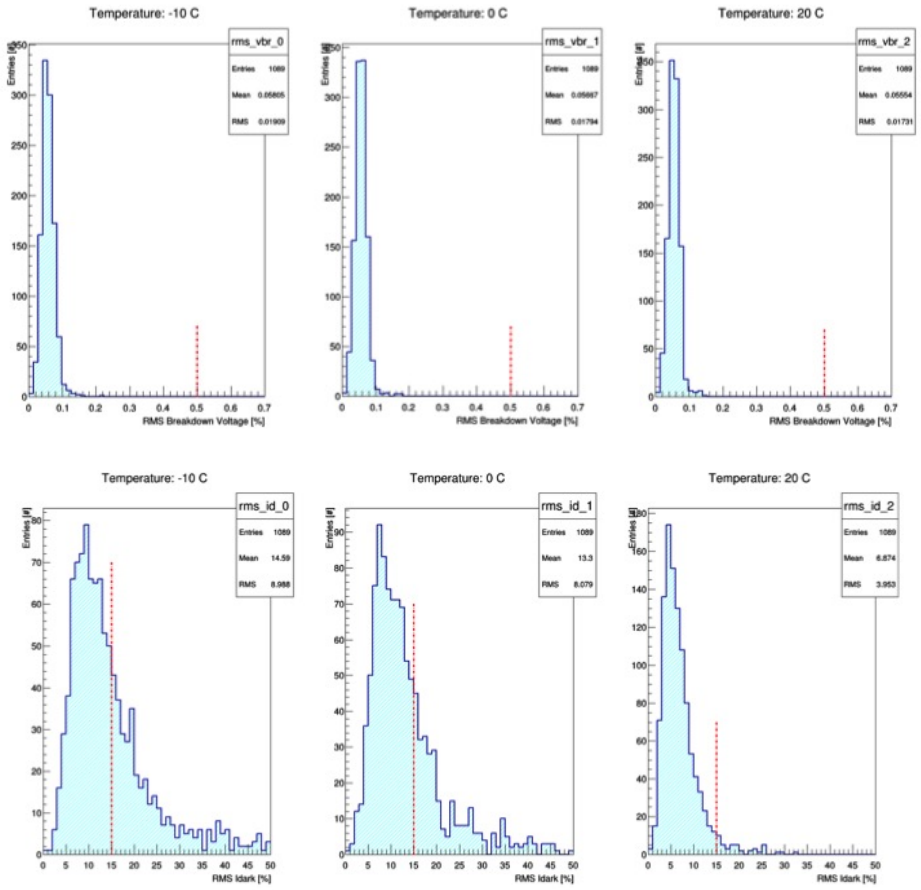

Figure 5.38: Spread on the V_{br}, on top, and on the I_d(at V_{br}), on bottom, measurements performed over the six cells of the Mu2e production SiPMs.

The third step of the test is the measurement of the Gain×PDE, which is performed by means of a LED light and the results are extracted by the following equation:

$$Gain \times PDE = \frac{I_i}{I_{ref}} \times \frac{Light\ Profile(x_{ref}, y_{ref})}{Light\ Profile(x_i, y_i)} \times (G \times PDE)_{ref} \quad , \qquad (5.12)$$

where I_i is the current of the ith SiPM under test and x_i, y_i its coordinates.

I_{ref}, x_{ref}, y_{ref} are respectively the current and positions of the reference sensor, as well as $(G \times PDE)_{ref}$ its Gain×PDE value, which is stable around 4×10^5.

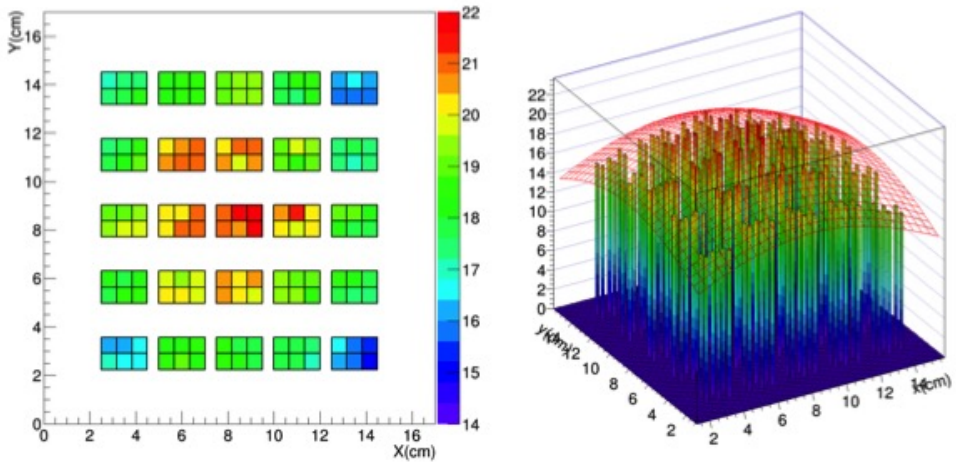

Figure 5.39: LED light intensity reaching the sensors under test.

Figure 5.39, shows the intensity of the light as a function of SiPMs position. The light is not uniform on the sensors plate, but shows a gaussian profile. A good approximation of this profile has been obtained by fitting the sensors current biased at the operative voltage. The resulting residuals have an RMS ∼3%.

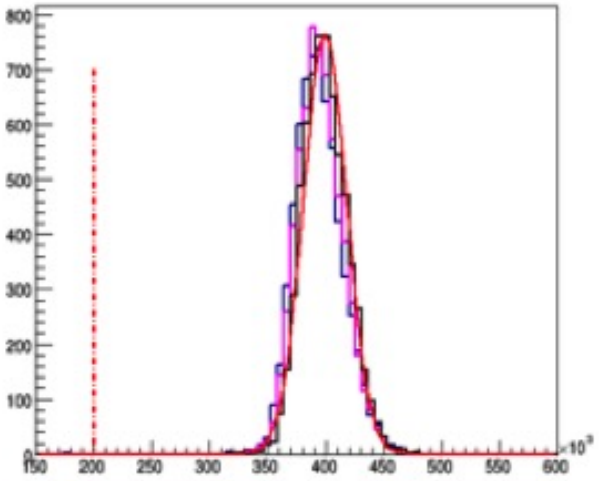

Figure 5.40: $G \times PDE$ measurement results at -10°C (magenta), 0°C (black), 20°C (blue)

In Figure 5.40, the $G \times PDE$ measurement results are reported. All the SiPMs tested satisfy the requirement (red dotted line), at all the three temperatures. The distributions show a mean value of $G \times PDE \sim 4 \times 10^5$, with a resolution, sigma/mean, of about 4%.

Chapter 6

Calorimeter prototype test

To satisfy its requirements, the calorimeter has to have a time resolution better than 0.5 ns and an energy resolution lower than ∼10% for 100 MeV electrons. To demonstrate this, a large scale prototype (Fig. 6.1), called Module-0, was built using 51 crystals and 102 photosensors produced and qualified during the preproduction phase [123][124]. A dedicated test beam was carried out during May 2017

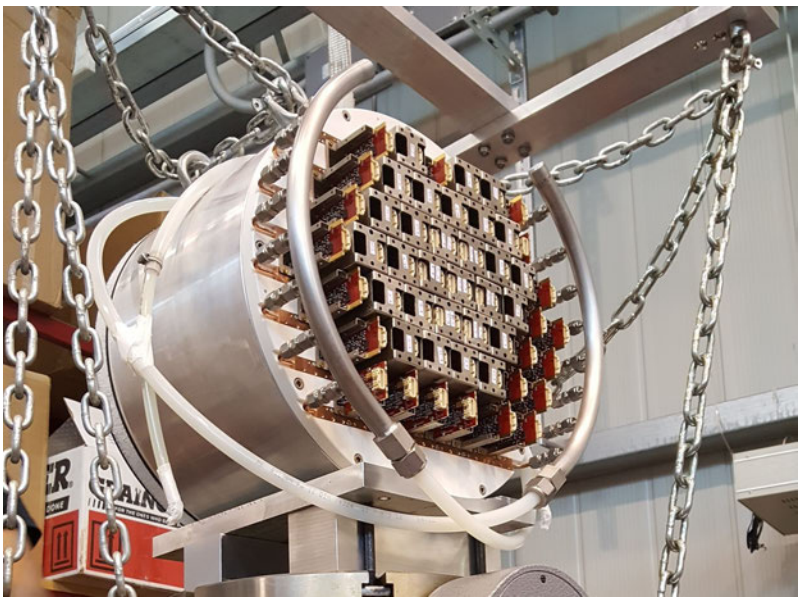

Figure 6.1: The Module 0 installed inside the BTF hall.

at the Beam Test Facility (BTF) of the National Laboratory of Frascati of INFN (Italy) [125]. Determination of time and energy response and resolution were ob-

tained with an electron beam, in the energy range 60-120 MeV. Cosmic Rays were used to equalize the response and provide a calibration point for timing resolution at low energy.

6.1 Mu2e calorimeter Module-0

The Mu2e calorimeter Module-0 was built trying to resemble as much as possible the final calorimeter disks. It is a structure of staggered crystals with a transversal size large enough to contain most of the electromagnetic shower of an electron beam impinging at 45-50°. It consists of 51 crystals of the final size and shape characterized during the pre-production phase (see Chapters 4, 5); each crystal is coupled to two custom Mu2e SiPMs whose signals are amplified by a prototype of the Front End Electronics (FEE) boards. On the same board, a local high voltage (HV) regulator allowed to control and read the bias voltages. An exploded view of Module-0 is shown in Figure 6.2.

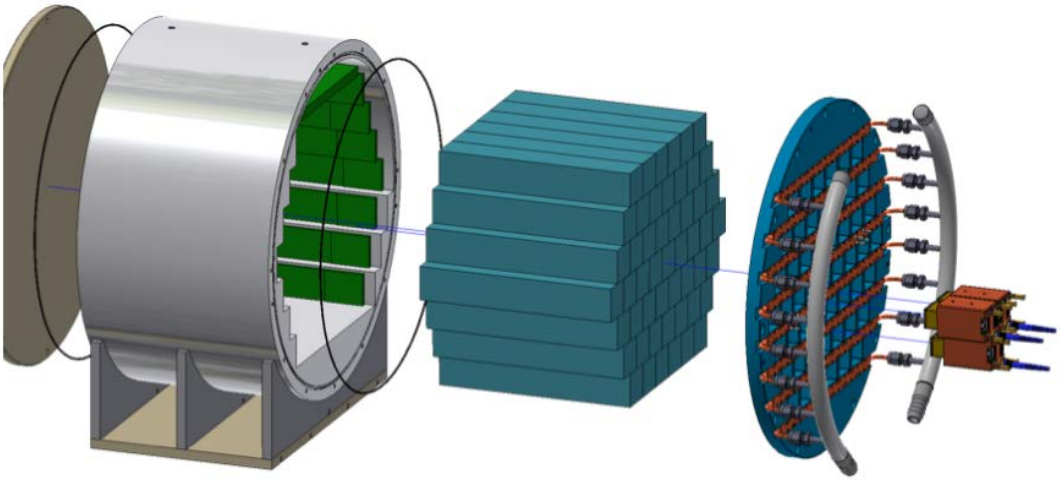

Figure 6.2: Slice view of the Module 0. The picture includes the mechanics, the crystals, the cooling system, the SiPM and the FEE.

Crystals were inserted in Module-0 after being wrapped with a 150 μm thick Tyvek paper foil. An ASA [128] plastic frame was placed on both crystal edges, as shown in Figure 6.3. Light reflection on the side opposite to the readout is granted by an ASA cap coated with two layers of Tyvek. On the other side, a 2 mm2 air gap

distance between the crystal and the SiPMs was present, in order to limit thermal coupling. The mechanical alignment of the crystals was ensured by screws pressing the lateral side on each crystal row.

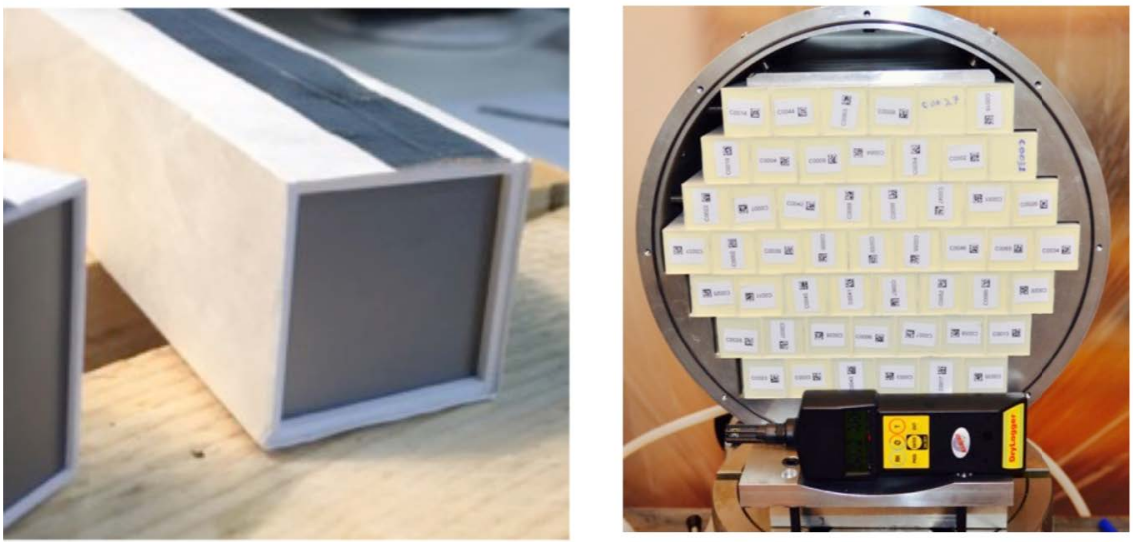

Figure 6.3: Left: Detail of a wrapped crystal. The lateral edges are protected by a small plastic frame in ASA. Right: picture of the mechanical structure of the Module-0 filled with the crystals.

Photosensors were glued with a layer of thermally conductive Masterbond Ep21td-canht epoxy resin [129] on the galvanized copper holders and their pins plugged in the FEE boards, as shown in Figure 6.4 (left). The FEE boards were surrounded by a copper Faraday cage. For calibration purposes, it was also possible to plug an optical fiber on a dedicated insertion in the copper cage to illuminate the crystals with an external light source. As shown in Figure 6.4 (middle, right), the SiPMs+FEE copper holders were inserted into a plastic support (back plate). The Zedex [126] back plate used presents the same specification of the final design (thickness, hole dimensions and piping), but of smaller size. Also the cooling lines connecting the SiPM and FEE holders were made with the final technique, thickness and shape but with a shorter path [127].

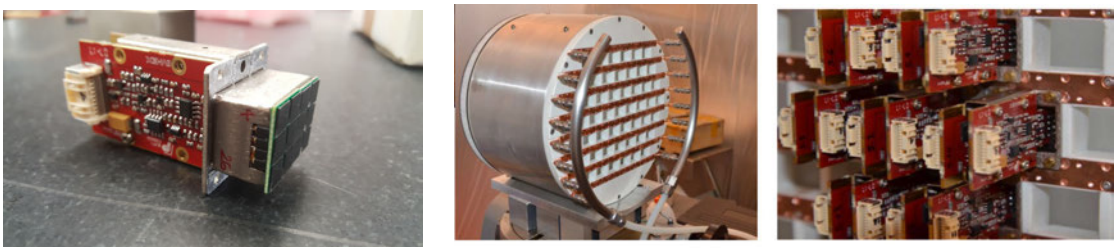

Figure 6.4: Left - Detail of the cooling system: the copper bands are inserted in the backplate. **Right** - Detail of the connection of the holders to the cooling system.

6.2 The Beam Test Facility

The BTF is specifically equipped for testing particle detectors. It uses low momentum beams produced on a Cu target by the 550 MeV e^- (e^+) bunches from the DAΦNE Linac [130]. A system of moving slits and magnets allows to select and deliver a secondary beam with the requested energy and intensity to the BTF hall. For the Module-0 test, the beam was tuned in single-particle configuration, resulting in ∼0.7 particles/bunch with a bunch rate of 50 Hz. The beam energy spread at 100 MeV was of O(1-2)%.

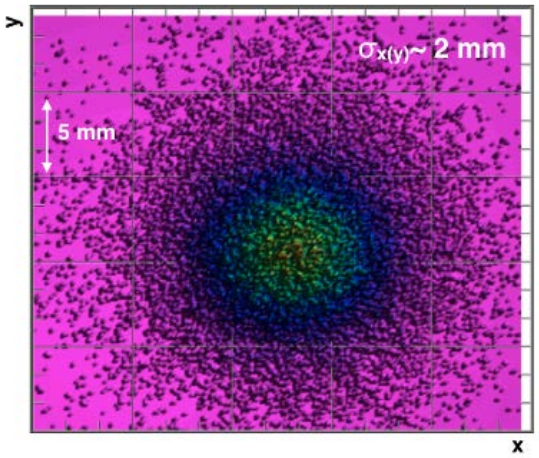

Figure 6.5: Example of beam profile at 100 MeV measured by a Medipix sensor.

The beam divergence was really small: a Gaussian beam profile with a σ_{xy} of ∼2-3 mm was measured with a dedicated Medipix sensor [131](Fig. 6.5) that could be inserted on the beam axis just in front of Module-0.

6.3 Experimental setup

The Module-0 was installed inside the BTF hall, on a two axis mobile table with a step resolution of 0.1 mm. The table was $\sim$ 1 m far from the beam pipe. A picture of the experimental hall is shown in Figure 6.6, where the Module-0 is covered by a black blanket. Two small plastic scintillators (beam counters), of $50 \times 10 \times 20$ mm^3 dimensions, crossed at 90 degrees with respect to each other, were positioned on the beam axis at few centimetres from the Module-0 front face. The coincidence of the scintillation counters was used for triggering the events when the beam was present. To select cosmic rays, we triggered on a $50 \times 50 \times 200$ mm^3 plastic scintillator located above the calorimeter. All the scintillators were read out by photomultipliers.

A calibration laser system was installed to monitor the response of the central crystal during run time. The temperature was kept stable by means of an external chiller connected to the Module-0 cooling system and monitored by dedicated temperature sensors integrated on each FEE board. The data acquisition was triggered by different signals:

- beam trigger (BT), produced by the coincidence of signals from the beam counters put in front of the Module-0. This represents the main trigger for the analysis;
- trigger provided by the signal of the top scintillator plate, used to collect

Figure 6.6: Test Beam experimental setup inside the BTF hall. The Module-0 is covered by a black blanket.

cosmic rays, (CRT);

- laser trigger (LT) in coincidence with the laser pulse, used for calibration purposes.

Two configurations were studied during the test: (i) beam at 0 degrees, which means orthogonal with respect to the Module-0 front face; (ii) beam at 50 degrees with respect to the calorimeter face. The tilted configuration is motivated by the fact that the expected average CE incidence angle on the Mu2e calorimeter is about 50 degrees.

6.3.1 The DAQ system

At the moment of the test beam, the Mu2e custom Waveform Digitizer boards (WD, DIRAC) were still under development, so two commercial CAEN V1742 high-speed digitizers were used to readout all signals coming from the Module-0 SiPMs and from the photomultipliers coupled to the scintillation counters. Each V1742 could acquire up to 32 channels simultaneously, sampling signals through 4 different DRS4 chips [132], which manage 8 channels each. The DRS4 chip is a switched capacitor array that can sample the input signal up to a frequency of 5 GHz. The CAEN digitizers were operating with a 0 - 1 V dynamic scale and at 1 GHz sampling frequency, providing 1024 samples per trigger that resulted in a ~ 1 μs acquisition window.

Due to the limited number of channels available in the DAQ readout system, only 7 central crystals were equipped and readout with two sensors and two FEE chips per crystal, For the outer 44 crystals, one of the sensors was left unbiased and without FEE chip. In total 58 SiPMs were read out. The remaining 6 digitizer channels were used to acquire the trigger and beam counters signals. The two digitizer boards were connected in daisy chain through optical fibers to a CAEN A2818 optical controller installed in the DAQ server [133]. Data from each run were stored in binary format and subsequently converted into a ROOT-compatible format [134].

6.4 Charge reconstruction

The charge was estimated by numerical integration of the waveform. Two different time windows were considered as integration gate:

- 450 ns, from 150 ns up to 600 ns;
- 250 ns, from 150 ns up to 400 ns. The second one resulted better in term of energy resolution because of the reduction of the integrated background level.

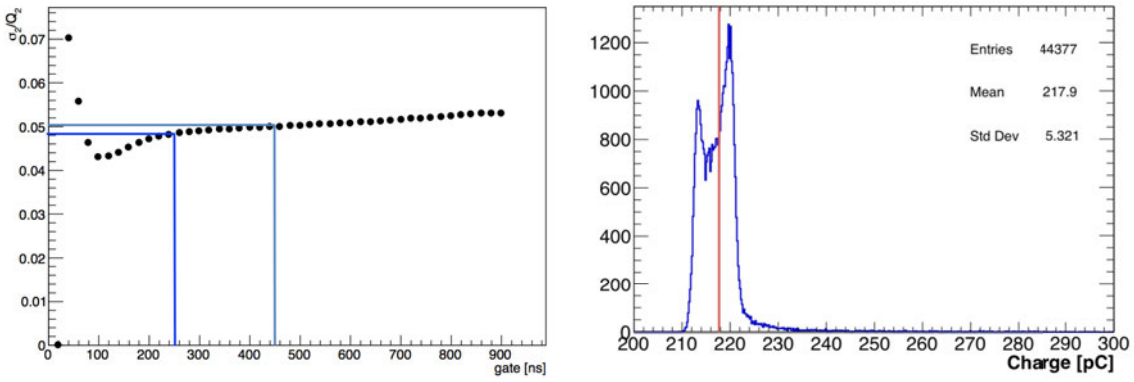

Figure 6.7: Left: charge resolution as a function of the integration range of the waveforms due to laser trigger. Right: initial pedestal charge distribution.

To confirm that an integration gate change did not degrade the matrix performance, the waveform obtained with a laser light firing the Module-0 central crystal was integrated in different time intervals. As shown in Figure 6.7 (left) the charge resolution does not present large variation for the two gates under study.

Pedestal evaluation

During the data taking in BTF hall, the noise level observed resulted much higher ($\times 10$) with respect to that experienced in the clean room with laser and cosmic rays and a reduced number of channels (Sec. 5.2.2). The only difference was on the digitizer system used. Moreover, the shape of the pedestal charge presented a double peak distribution, as observed in Figure 6.7 (right). To study in more detail this effect, a clean set of cuts was applied to better select noise events and better calculate the baseline in a 100 MeV orthogonal run. We required:

- no charge deposit in the beam counters;
- no charge deposit in the scintillator used to veto cosmic ray events;
- no laser light in the central crystal.

A first data correction consisted in fitting the pedestal waveform with a linear function and subtracting it to the signal waveform. Albeit a small improvement was observed, this correction function was not sufficient to eliminate the double peaks in the pedestal charge distribution. To overcome this issue, two correction functions (F_R and F_L, Fig. 6.8) were defined by splitting the pedestal charge distribution using the median (the red line reported in Figure 6.7, right) as separator. In doing this, two different baseline waveforms were obtained for each channel:

- Waveform Right (W_R) average of baseline corresponding to the events that have a pedestal charge greater than its median value;
- Waveform Left (W_L), average of baseline corresponding to the events that have a pedestal charge smaller than its median value.

To determine the correction functions, the Gaussian mean value of the waveform amplitude was evaluated in each time bin. To chose the correct baseline to be

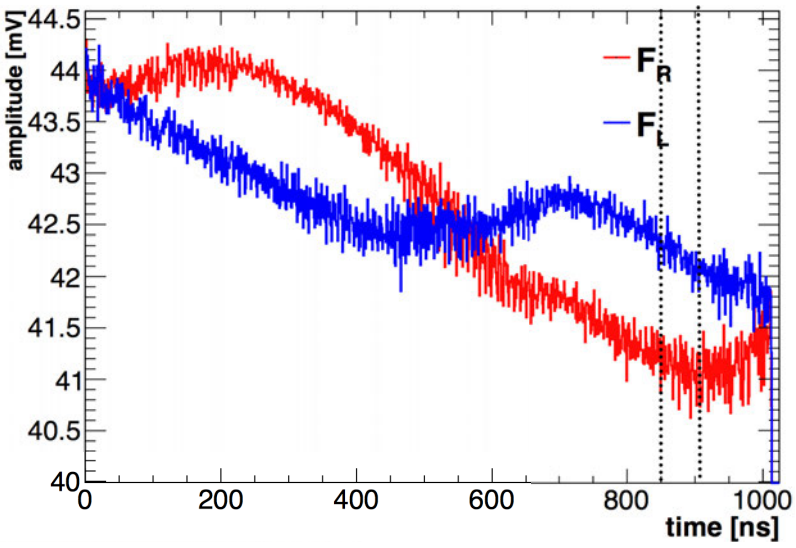

Figure 6.8: Correction functions used to correct the pedestals.

subtracted to each waveform, a comparison between the mean values of the two correction functions and of the waveform under study was then performed in a time interval ([850,900] ns) away from the signal region. The correction selected is the one that minimises the difference between the two compared values. The results of the correction to the baseline is reported in Figure 6.9 where a ZCOL scatter plot of the charge with respect to time is shown before (left) and after (right) the application of the correction. A much flatter behaviour is observed in the second case.

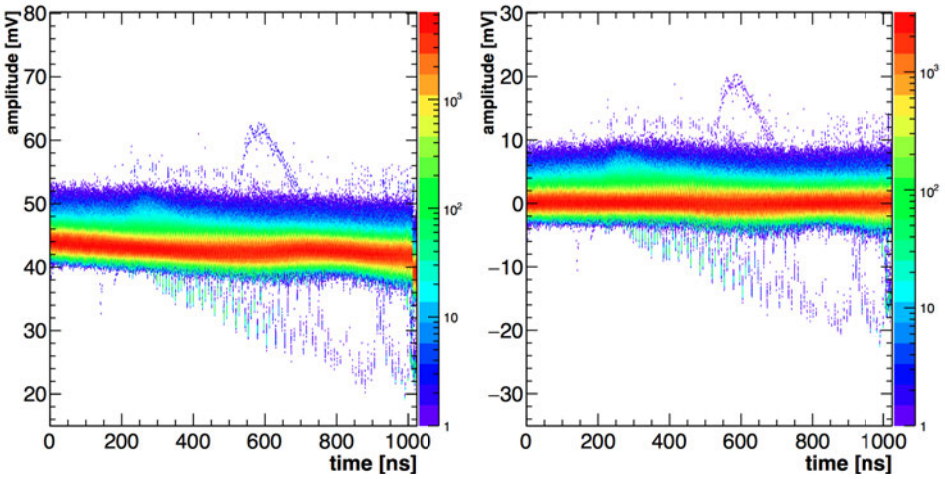

Figure 6.9: Comparison between different reconstruction of the pedestal charge in the central crystal of Module-0. Red: pedestal charge distribution evaluated in 450 ns without any baseline corrections. Black: pedestal charge distribution evaluated in 250 ns with the linear fit correction. Blue: pedestal charge distribution obtained with a 250 ns integration range and baseline correction with the two functions obtained from the waveform shape.

In Figure 6.10 (left), the original noise charge, the noise charge evaluated in the narrowest time interval with the linear fit correction and the noise charge evaluated in the same interval with the baseline corrections applied are reported. The latter correction strongly reduces the two peaks behaviour and the pedestal charge distribution becomes much more similar to a Gaussian.

The Module-0 channels response looked highly correlated, as can be observed in Figure 6.10 (right). Even after the baseline correction, the noise width increases linearly with the number of crystals, nCry, added, not following the expected $1/\sqrt{(}$nCry) behaviour of independendt channels.

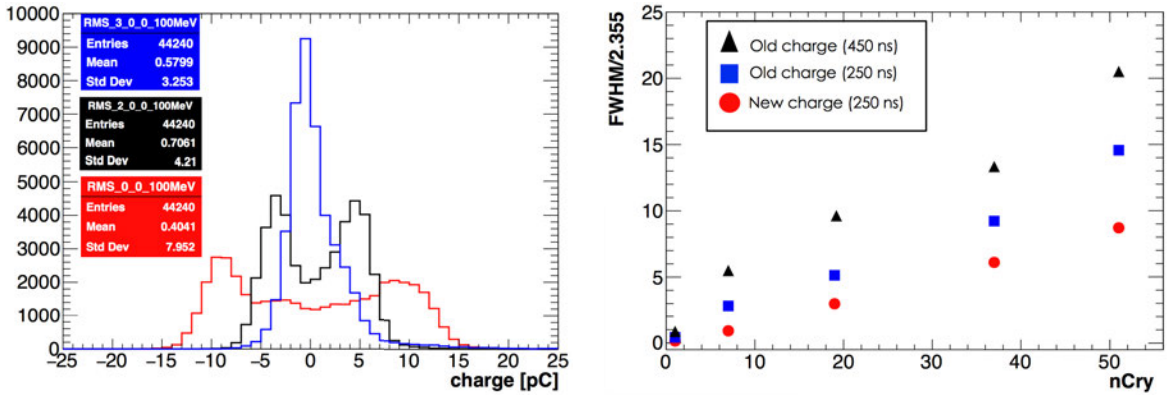

Figure 6.10: Left: Pedestal charge distribution evaluated in 450 ns wf integration range without corrections (black), in the 250 ns range with the linear fit correction (red), in the 250 ns integration range and with the 2-functions based correction (blue). Right: dependence of the RMS of the distribution of the pedestals sum obtained summing up several channels as a function of the number of channels for the three different evaluated charges.

6.4.1 Single electron event selection

Even if the beam collimators were tuned to adjust the beam intensity, a more accurate offline single-particle selection is needed for the time and energy resolution measurements. In order to select single particle events it is necessary to:

- reject event presenting the laser trigger;
- reject event with cosmic trigger;
- ask for a single particle in the beam counters;
- apply a Pulse-Shape Discrimination (PSD) on each crystal waveforms to discard events with one or more channels saturated because of particles pileup.

The PSD is defined as:

$$PSD = \frac{\int_a^b waveform}{Total \quad waveform \quad charge} \quad , \tag{6.1}$$

where a and b correspond to the crossing time samples at 10% of the maximum pulse height on the leading edge, and 90% of the maximum pulse height on the trailing edge. Examples of PSD distributions obtained for the three SiPMs vendors

are reported in Figure 6.11. A PSD limit of 0.5 is required for Hamamatsu SiPMs and of 0.6 for both SensL and AdvanSiD SiPMs.

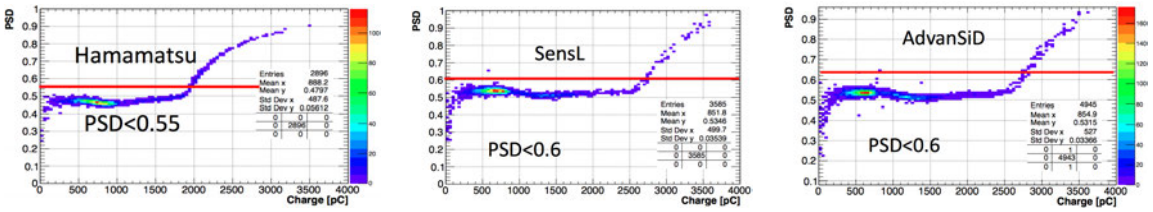

Figure 6.11: Pulse shape discrimination distribution as a function of the reconstructed charge for an Hamamatsu (left), SensL (middle) and AvanSiD (right) SiPM.

6.4.2 Equalization and calibration

To equalize the response of each Module-0 channel, two calibration strategies were followed:

- using the beam energy deposition of a 100 MeV electron beam centered on the crystal under calibration. This was carried out only for the innermost 19 crystals (26 SiPMs).
- using the energy deposition from Minimum Ionizing Particles (MIP) selected from the CRT. This technique allowed to equalize all Module-0 channels.

The crystals involved in each equalization are shown in Figure 6.12.

In the beam equalization procedure, the SiPM charge distribution of each calibrated crystal (i) was fit with a Log-Normal fit [114] and the charge peak was used to evaluate the calibration factor, B_i/B_0. For the crystals with two sensors their average was used as calibration factor. The equalization parameter in the energy sum A_{i-0} is obtained as the ratio of the beam calibration factor with respect to the central crystal, $A_{i-0} = B_i/B_0$. The statistical error associated to this procedure was of $\sim$1.5% for each channel. An example of the fit performed is shown in Figure 6.13 (left).

The cosmic ray equalization was performed by selecting minimum ionizing particles with the Cosmic trigger. The statistical error of each cosmic equalization

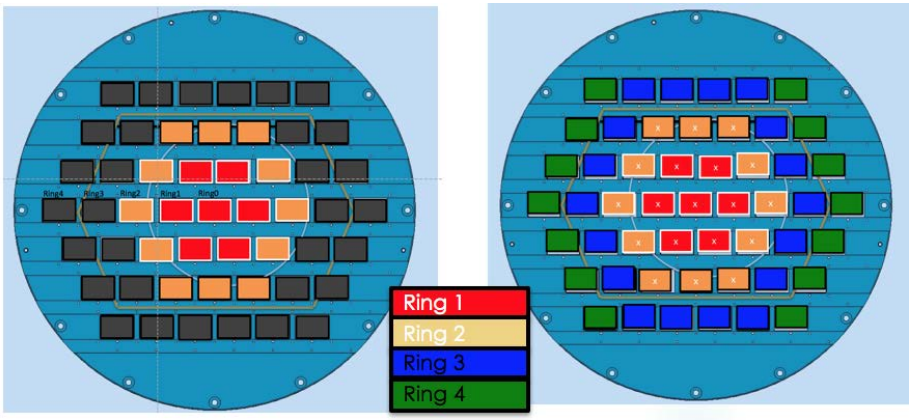

Figure 6.12: Crystals involved in the beam (right) and cosmic (left) equalization

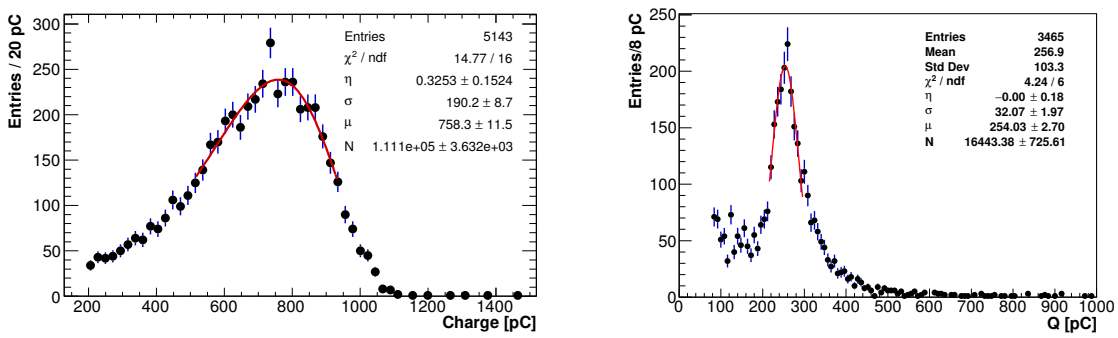

Figure 6.13: Charge deposited by 100 MeV electron beam (left) and cosmic (right) events.

parameter, C_i, was of ∼0.5%. An example of the fit performed is shown in Figure 6.13 (right). The ratio of the A_i factors for beam and cosmic strategies of the 26 innermost channels have been used to compare the systematics of the two methods (Fig. 6.14, left). The average ratio resulted to be well centered around 1 and the sigma of this distribution was of about 3%.

For the final analysis, the calibration factors obtained with the CRT sample were applied. The energy scale was set, after the equalization, by comparing the reconstructed charge in the whole matrix, Q_{rec}, with the expected energy deposited in the Module-0, from a Geant4 based Monte Carlo (MC) simulation where we included all the passive material that the beam was crossing before reaching the detector (scintillating counters, front plate) [135]. A good linearity in response was obtained, as shown in Figure 6.13(right). The energy scale factor is obtained by a linear fit and resulted to be $E_{sc} = (12.07 \pm 0.11)$ pC/MeV. This factor was

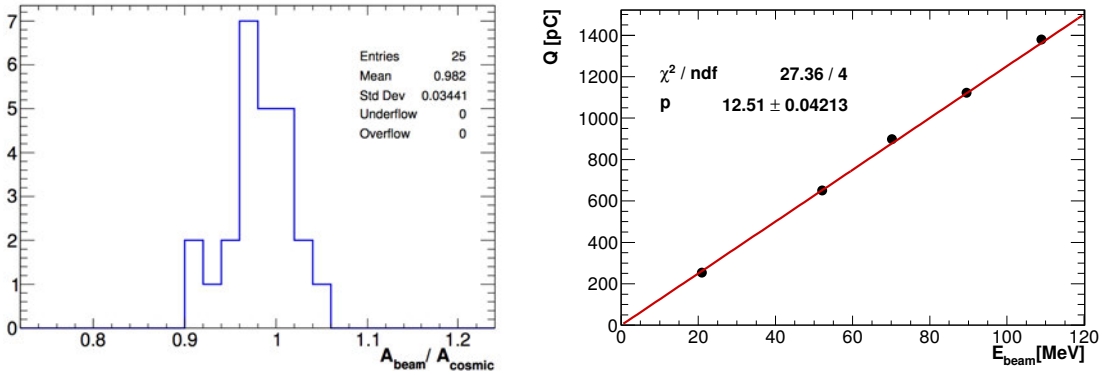

Figure 6.14: Left: Ratio of Ai factors for beam and cosmic calibration techniques. Right: mean value of the charge reconstructed at different beam energy as a function of the expected energy deposit at different beam energy.

then applied to all reconstructed charges to convert the reconstructed charges into reconstructed energies, $E = Q_{rec}/E_{sc}$.

6.5 Energy resolution measurement

In addition to the Gaussian noise added to the MC simulation, the fluctuation of the number of photoelectrons and a cross-talk between the neighbouring crystals of the most energetic one (in the orthogonal run) were taken into account. After having verified, with a laser run, that the cross-talk observed in the data sample was an optical cross-talk, its value was evaluated by dividing the maximum waveform pulse height of each channel with the maximum of the waveform on the central ring. The cross-talk parameters found are reported in Table 6.1.

In Figure 6.15 the comparison between the data and the Monte-Carlo simulation for the energy deposition in the first ring is shown. A good data-Monte Carlo agreement is visible. In Figure 6.16 (left), the distribution of energy deposited in the entire Module-0 by a 100 MeV electron beam entering at 0° in the central crystal is shown. The non-gaussian behaviour is mostly do to leakage and energy loss in the material. Monte Carlo simulation is also reported (red line) and it is in well agreement with data. A similar distribution for the 100 MeV electron beam impinging at 50° degrees is shown in the left plot.

Crystal number	Cross-Talk parameter
1	2.5
2	2.7
3	1.8
4	0.7
5	2.5
6	1.2

Table 6.1: Cross-Talk parameters of the 6 crystals surrounding the central one (with the highest energy deposit) evaluated by the 100 MeV beam data in the orthogonal configuration.

The energy resolution (σ_E/E) is evaluated as the ratio between the sigma and the peak of a Log-Normal fit applied to the energy distribution. An energy resolution of $\sim 5.4\%$ (7.5%) is obtained at 100 MeV for 0 (50) degrees, well satisfying the Mu2e requirements.

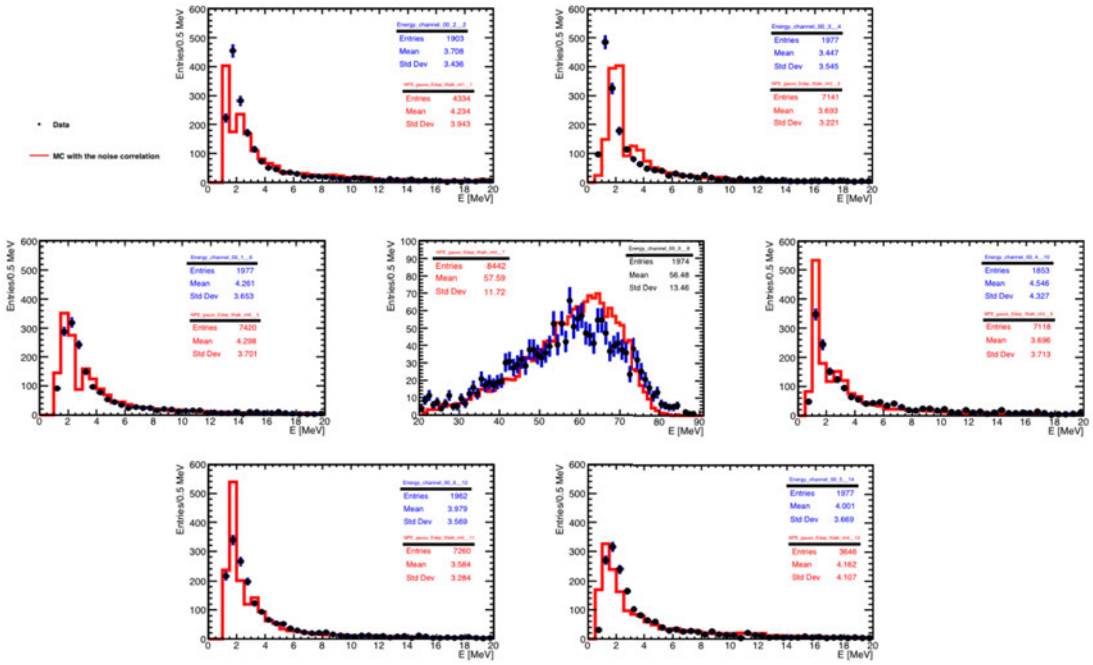

Figure 6.15: Data (black dots)-MC (red line) comparison of the energy deposit in the central crystal and the first surrounding ring

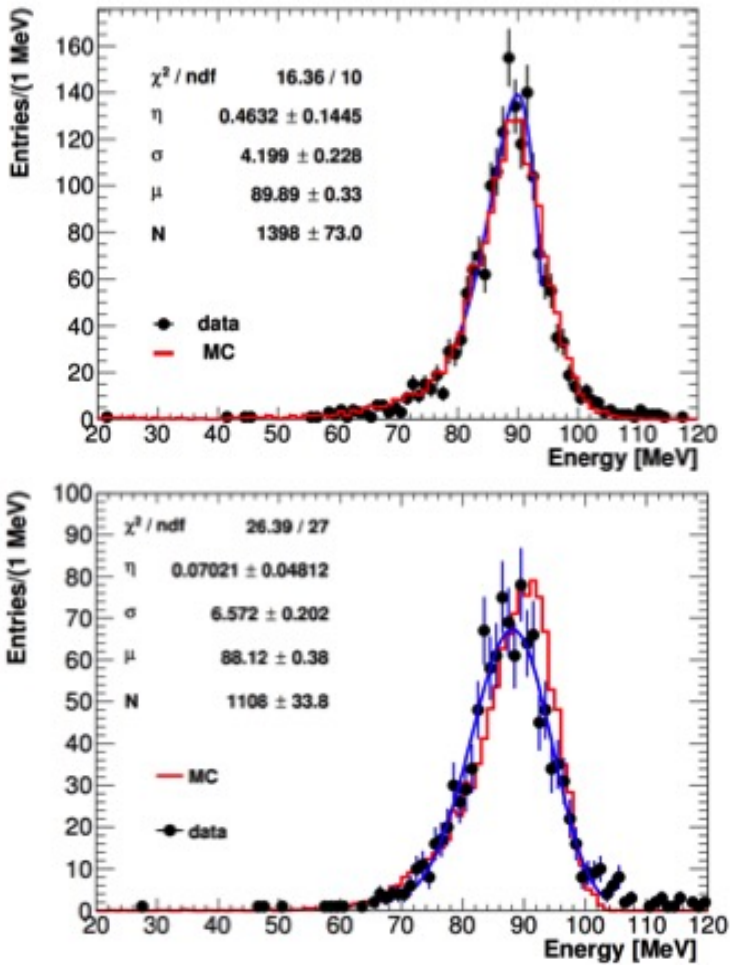

Figure 6.16: Energy reconstructed in the Module-0 by a 100 MeV electron beam impinging the Module-0 at 0 degree, on left, and at 50 degrees, on right.

The energy resolution at different beam energies is reported in Figure 6.17. The dependance of the energy resolution as a function of the deposited energy E_{dep} for single particle events has been parametrized by the function:

$$\frac{\sigma_E}{E_{dep}} = \frac{a}{\sqrt{E_{dep}[GeV]}} \oplus \frac{b}{E[GeV]} \oplus c \tag{6.2}$$

where a represents the stochastic term, b the noise term and c the constant term. The fit is rather insensitive to the stochastic term that is almost negligible and it has been fixed to 0.6% as estimated by the light yield contribution of 30 pe/MeV. The deterioration of resolution at increasing incidence angles is dominated by the increase of the leakage term fluctuation.

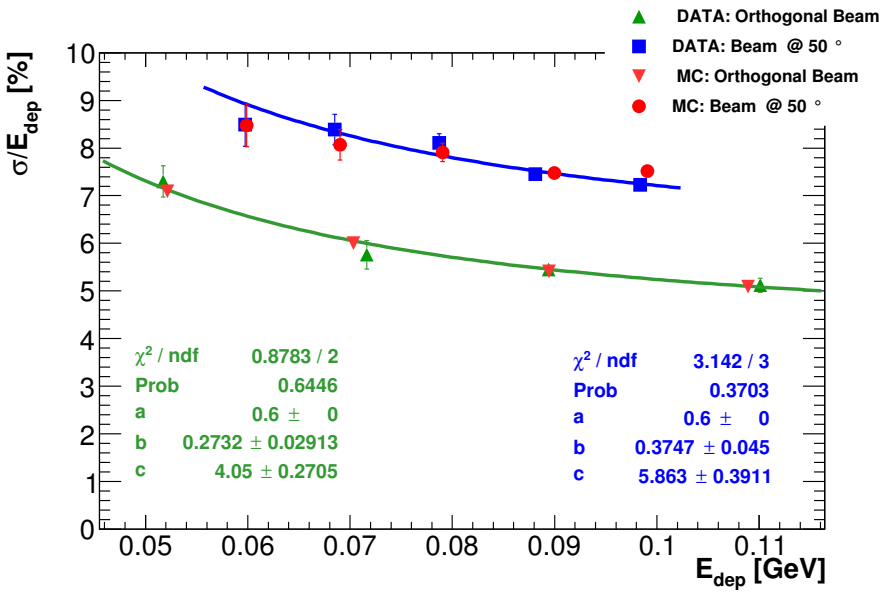

Figure 6.17: Energy resolution as a function of the deposited energy in Module-0. Blue points refers to the configuration with the beam entering at 0 degrees, green points at 50 degrees.

6.6 Time reconstruction

The signal time is determined by fitting the leading edge of the waveform with an analytic function and the best accuracy achieved by setting the signal time at a constant fraction (CF) of the pulse height. This is possible because the pulse shape is independent on the deposited energy in the crystals and assuming that it is the same for all photosensors used. Some waveform fit components have to be fixed:

- the fit function;
- the range where to perform the fit;
- the CF of the pulse height used to evaluate the time.

After studying several functions, the best result was obtained using an asymmetric log-Normal function defined as [114]:

$$f(t) = \exp\left(-\frac{\ln^2\left[1-\eta(t-t_p)/\sigma\right]}{2s_0^2} - \frac{s_0^2}{2}\right)\frac{\eta}{\sqrt{2\pi}\sigma s_0} \quad , \tag{6.3}$$

where t_p is the position of the peak, σ = FWHM/2.35, η is the asymmetry parameter, and s_0 can be written as:

$$s_0 = \frac{2}{\xi}\text{arcsinh}\left(\frac{\eta\xi}{2}\right), \quad \xi = 2.35\ . \tag{6.4}$$

The fit optimisation was performed on signals from the Hamamatsu SiPMs reading out the central crystal, by varying the fit range and the constant fraction threshold.

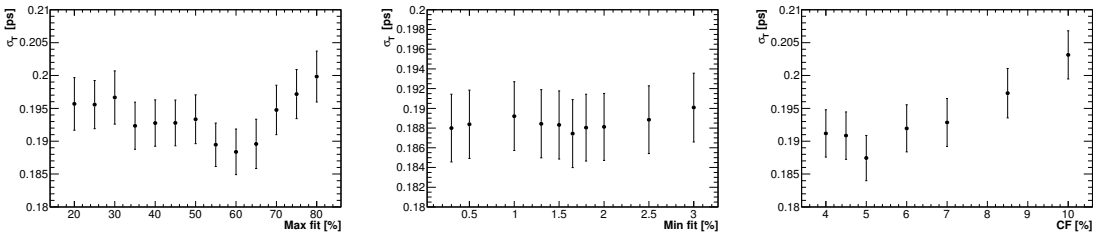

Figure 6.18: Optimisation scans of the time resolution as a function of the upper (lower) limit of the fit range on left (middle) and as a function of the Constant Fraction used to evaluate the time itself (right).

Results on fit range scan are reported on Figure 6.18. The upper (left) and lower (middle) limits have been set to 1.65% and 60% of the pulse maximum height respectively. Figure 6.19 (left) shows an example of a waveform fit by a log-Normal function in this range. Figure 6.18 shows the constant fraction scan results. The optimized threshold is set at 5% of the pulse height.

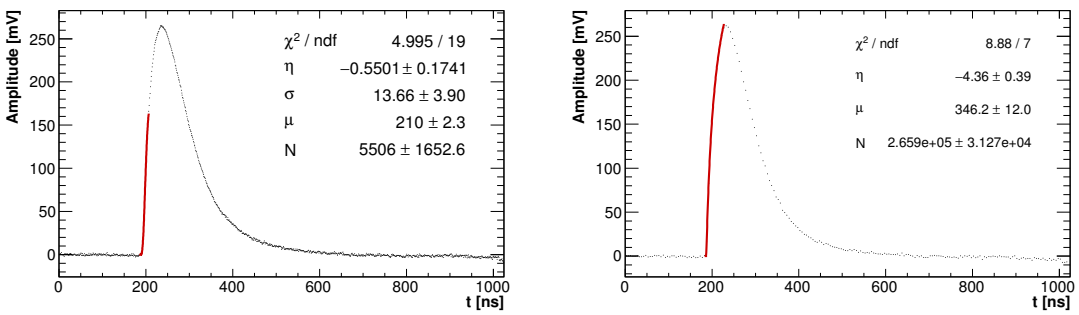

Figure 6.19: Example of the outcome of the optimized fit to a waveform at 1 Ghz sampling rate (left) and 200 MHz (right).

The fit procedure was checked by looking at the distribution of number of degrees of freedom and at the distribution of the normalized χ^2 (Fig. 6.20). The presence of systematic effects was investigated also looking at the distribution of the difference between the reconstructed time t_{CF} and the corresponding bin position: $t_{CF} - t_{bin}$, where t_{bin} is the time corresponding to the start of the digitizer sample where t_{CF} belongs to. The flat distribution of the t_{reco} - t_{bin} distribution (Figure 6.20) confirms a good uniformity inside the bin interval.

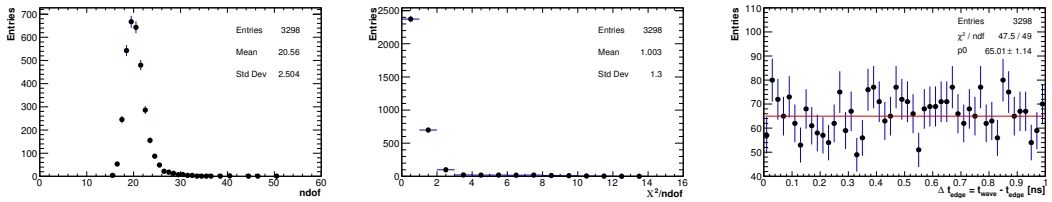

Figure 6.20: Left: Distribution of the number of degree of freedom for 1 GHz sampling frequency. Middle: Distribution of the normalized χ^2 for the 1 GHz sampling frequency. Right: Residuals distribution of the reconstructed time inside the sample for 1 GHz sampling frequency.

In the Mu2e experiment the sampling frequency of the calorimeter waveform digitizer boards will be 200 Msps, so that to evaluate the performance in this configuration, each waveform was re-sampled offline in 5 ns bins. Also at this sampling, we have enough points in the leading edge to allow a stable fit procedure. Figure 6.19 (right) shows an example of the fit performed on a re-sampled waveform at 200 Msps. In this case, the asymmetric parameter η of the log-Normal function has been fixed as a function of σ, in order to obtain enough degrees of freedom in the fit. Figure 6.21 shows the distribution of η as function of σ, for the two SiPMs reading out the central crystals. We fixed η thanks to a second order polynomial fit.

The optimization scan described above have been repeated also in this configuration. The fit range has been set between 1% and 95% of the peak and the best CF resulted to be 5% also in this case. Figure 6.22 shows the distributions of: ndof, χ^2/ndof and $t_{CF} - t_{bin}$. All these distributions confirm the absence of any systematic effect in the procedure.

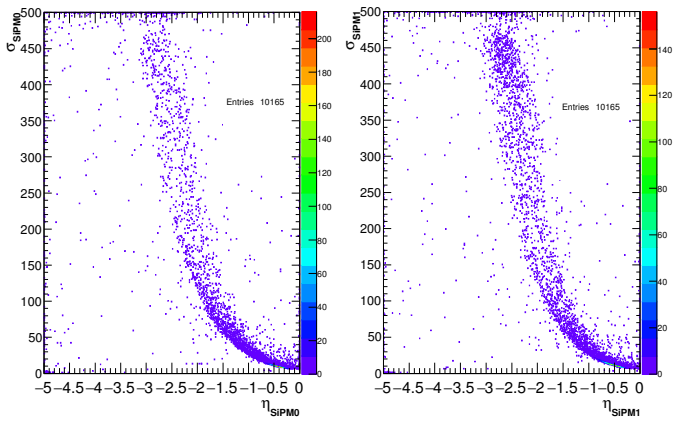

Figure 6.21: Asymmetric parameter η of the log-Normal function as a function of σ, both obtained applying the log-Normal fit on the 200 MHz re-sampled waveforms. A dependance is clearly visible and well represented by a second order polinomial function.

6.6.1 Time resolution

The time resolution was measured using the time difference between the signals of two SiPMs collecting light from the same crystal. For each event passing the single electron selection cuts, the crystal with the largest energy deposit was used to compute the time difference between the two SiPMs, $\Delta T = T_{left} - T_{right}$. Figure 6.23 shows the resulting distributions at 1 Gsps and 200 Msps sampling frequency for electrons impinging at 0° on the central crystal. The time resolution was deduced by applying a Gaussian fit on the distributions and dividing the σ by $\sqrt{2}$ to take into account the contribution of the two sensors. The resolution results to be $\sigma_t \sim 132$ ps for 1 Gsps sampling frequency and $\sigma_t \sim 195$ ps for 200 Msps.

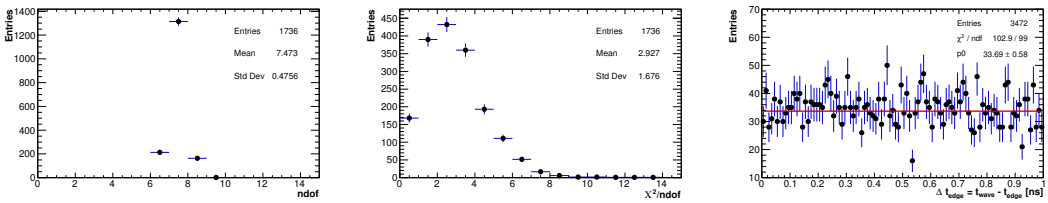

Figure 6.22: Left: Distribution of the number of degree of freedom for 200 MHz sampling frequency. Middle: Distribution of the normalised χ^2 for the 200 MHz sampling frequency. Right: Residuals distribution of the reconstructed time inside the sample for 200 MHz sampling frequency.

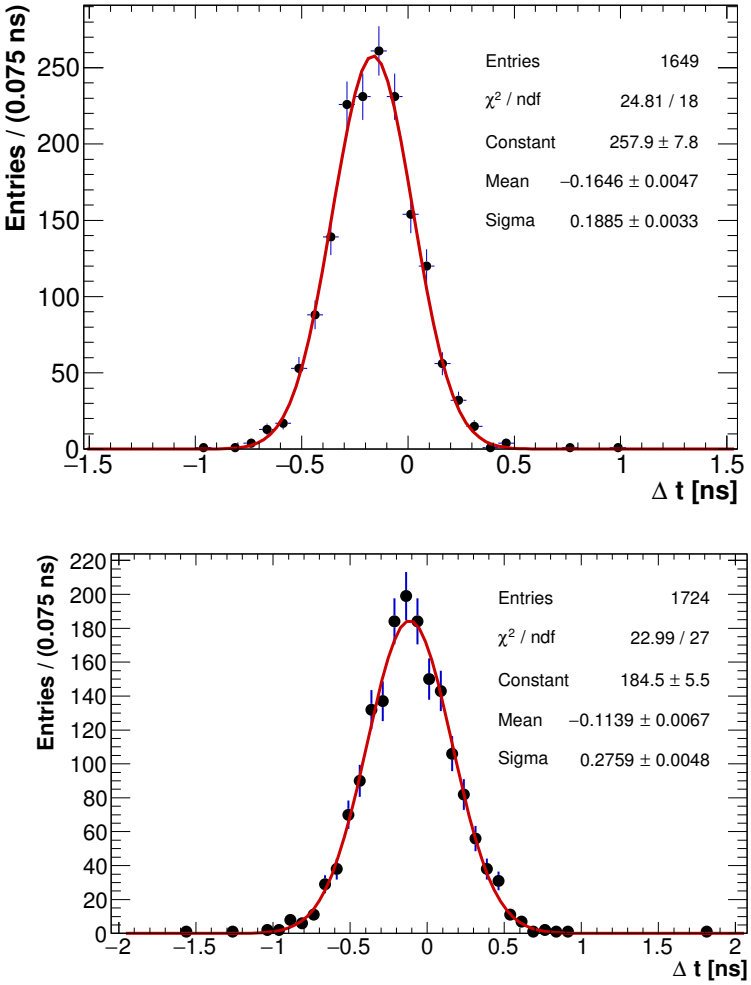

Figure 6.23: Time resolution of the central crystal readout by two Hamamatsu SiPM with a beam energy of 100 MeV. On left the sampling rate is at 1 GHz, on right the waveform has been resampled offline at 200 MHz. The red lines represent the Gaussian fit performed.

6.6.2 Comparison of vendor performances

As already described in section 6.1, three vendors provided us Silicon Photomultipliers. The sensors have been mounted on the Module-0 as shown in Figure 6.24 (left). Figure 6.24 shows the profiles of 1000 waveforms (normalized to their amplitudes) per vendor obtained during the calibration runs done with 100 MeV energy beam orthogonally perpendicular on each channel. Small differences on response is clearly visible: Hamamatsu shows the shortest rise time, about 29 ns, while the other two showed a similar rise time at the level of 38 ns. In addition to that, Hamamatsu

was also showing a shorter quenching time.

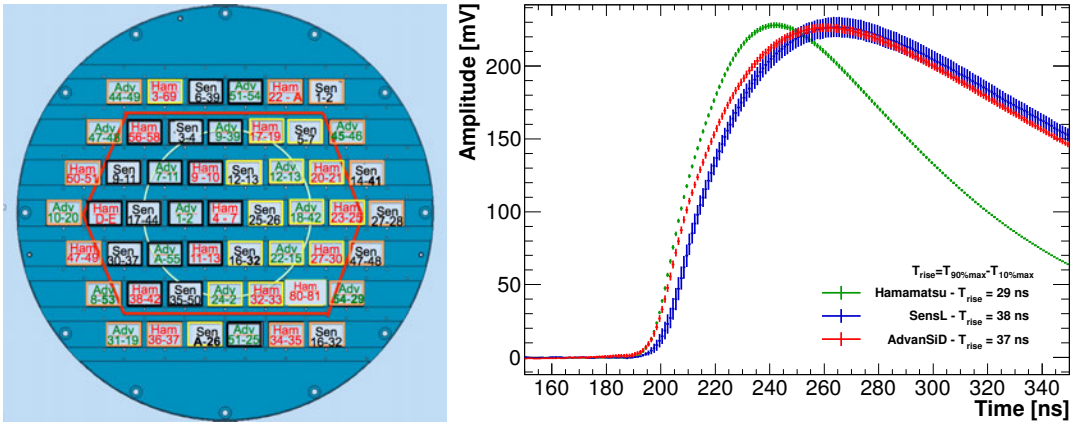

Figure 6.24: Left: Vendor SiPM map in the Module-0. Right: profiles of 1000 normalised waveforms per vendor obtained during the calibration runs done with 100 MeV energy beam impinging orthogonally on each crystal.

Figure 6.25 shows the time resolution obtained for AdvanSiD (left) and SensL (right) readout SiPMs. The same fit range and CF parameter obtained by the optimisation carried out on the crystals readout by Hamamatsu SiPM have been used. The Gaussian fits applied to these distributions show that a time resolution of about 151 ps and 163 ps was obtained with AdvanSiD and SensL readout SiPMs, respectively. The best time resolution performances have been obtained using Hamamatsu SiPMs. This is confirmed also at the sampling rate of 200 Msps. The time resolutions obtained in this configuration are shown in Figure 6.25 (bottom). We obtained a resolution of about 153 ps when using both AdvanSiD and SensL SiPMs, which corresponds to a 25% worst than the results obtained with Hamamatsu SiPM.

6.6.3 Time resolution as function of the energy

An energy scan has been performed from 60 MeV up to 120 MeV. In the tilted configuration, the channel with the highest energy deposit resulted to be the one readout by SensL SiPMs. Figure 6.26 shows the time resolution as a function of the deposited energy in the highest energetic crystal. The time resolution obtained with MIPs both with Hamamatsu and SensL SiPMs was also added in this plot.

The dependance of the single sensor time resolution σ_T as a function of the deposited energy E_{dep} was parametrized by the function:

$$\sigma_T = \frac{a}{E[GeV]} \oplus b \tag{6.5}$$

where a is proportional to the emission time constant of the undoped CsI and b represents the additional contribution due to the readout electronics.

Figure 6.27 shows the time resolution at 1 Gsps and 200 Msps sampling rate obtained with Hamamatsu SiPMs as a function the deposited energy. A deterioration lower than 30% is obtained. This demonstrates that the experiment timing requirement is well satisfied at the Mu2e sampling rate too.

We tried also to measure the time resolution between neighbouring crystals with similar reconstructed energies using the mean-time of SiPMs in the crystals involved and subtracting the trigger start, but we found that the DAQ system with the V1742 CAEN board had a serious synchronization problem between boards that spoiled the result. This is described in some details in Appendix A.

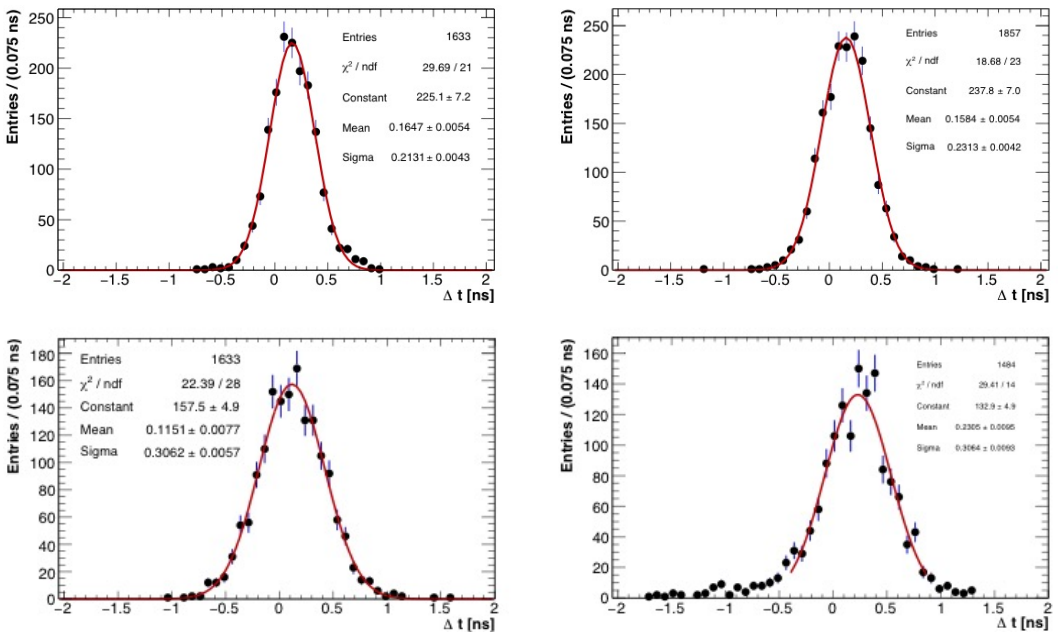

Figure 6.25: Time resolution of the crystals readout by AdvanSiD (left) and SensL (right) SiPMs. The top plots are related to the 1 GHz sampling rate, the bottom ones are obtained with the offline resampling at 200 MHz

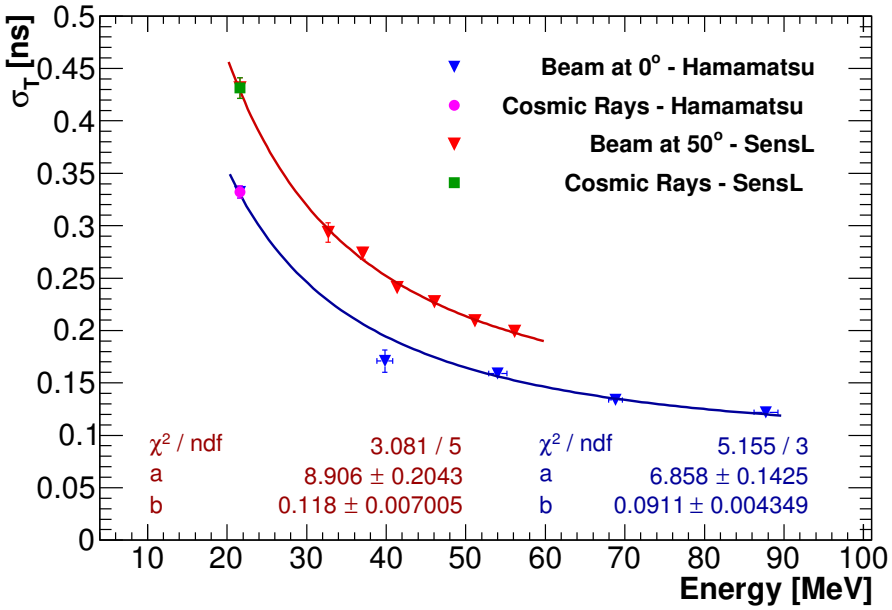

Figure 6.26: Time resolution as a function of the deposited energy in the highest energetic crystal.

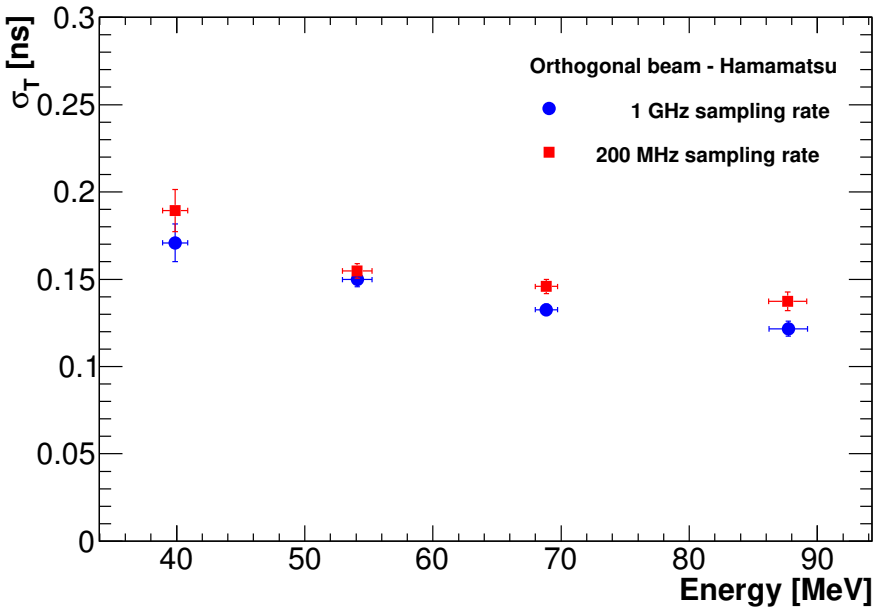

Figure 6.27: Time resolution as a function of the deposited energy in the highest energetic crystal.

Chapter 7

Calorimeter calibration strategies

We designed multiple calibration techniques in order to fully characterise and calibrate the calorimeter timing and energy response at different energy levels. A radioactive source for absolute crystal by crystal calibration at 6 MeV and a laser system for SiPM monitoring are techniques already integrated with the current construction plan (Chapter 3). Concerning the energy calibration, the laser will be used to monitor and correct variation of SiPMs' gains related to small temperature variation, in short time-frames, or to radiation damage in the long-term. The radioactive source running weekly, will allow to see the overall response change so to disentangle any eventual long term deterioration of the crystal response. The laser system will allow also to monitor the variation of the channels time offsets and time resolution along the running time. However, calibration at higher energies *in-situ* are needed, since the calorimeter will reconstruct 105 MeV electron. We propose, to use as calibration sources:

- a selected sample of cosmic rays (CRs);
- electrons from muon decay in orbit (DIOs) in the stopping target.

The contemporary usage of the source system and of the *in-situ* calibration events will allow us to disentangle the contribution due to the crystal changes, for example due to radiation damage, with respect to gain changes. A preliminary Monte Carlo study based on the Module-0 test beam results has been developed to estimate the

energy resolution degradation as a function of the calibration precision (Fig. 7.1). The starting value is related to the resolution simulated with 100 MeV electron beam impinging at 50 degrees and with a perfect crystal calibration. Then, miscalibration factors have been simulated, from 1 to 10%, both in a gaussian and in a uniform distribution. A calorimeter calibration accuracy better than 4% allows to introduce negligible contribution to the resolution.

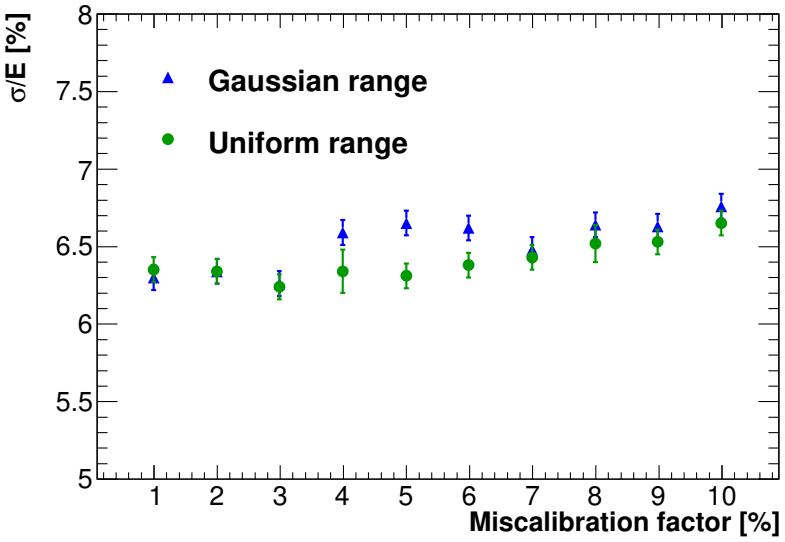

Figure 7.1: Energy resolution as a function of the miscalibration coefficient inserted in the MC simulation.

7.1 Calibration with cosmic ray muons

Cosmic muons represent an important calibration source for the Mu2e calorimeter. They have unique characteristics that make this calibration complementary to the other techniques previously described:

- they can be acquired during normal run operations, in the same experimental conditions of the physics data sample;
- their flux [136] is high enough to collect a large amount of calibration data in a relatively short time, allowing a better than daily monitoring of the detector response;

- their energy loss is practically independent of their initial energy, since the majority of them are minimum ionising particles (MIPs), and their energy deposition is constant along time and for the same path length;
- they are relativistic particles and, thanks to their negligible energy loss, their speed is practically always equal to the speed of the light c; the time they take to travel through the calorimeter can be used to align the time offsets of all the channels without any external time reference.

Cosmic muons crossing the calorimeter will be selected by a dedicated trigger. Basic selection methods are reported in the next sections.

The specific energy loss, dE/dx, of the selected muons is uniform along the calorimeter. Since the Mu2e calorimeter does not provide a measurement of the z coordinate, the total three-dimensional path length cannot be directly obtained by the crystal energy deposits. Nonetheless, if the two-dimensional path length in the transverse plane (which is independent by the z coordinate) is used instead of the total path length, the 2D specific energy loss has still a distribution with a good homogeneity along all the calorimeter. Preliminary simulation show that an equalisation of O(1-2%) can be achieved.

7.1.1 Cosmic simulation and trigger selection

A MC generator for Cosmic Rays has been developed by the collaboration. The sea level flux is described by a modified Gaisser's formula [137] to take into account the effects related to the Earth curvature and of the muon decay rate (Fig. 7.2, left). Moreover, the effects due to the external overburden of the experimental hall (approximated with a ceiling above the Mu2e experiment made by 1.8 m of concrete) and of the external neutron shield in the DS ($\sim$0.9 m of concrete) have been inserted in the generator. The generation plane used has a dimension of 2.2 $\times$ 7.5 m^2 and is located around 11 m above the beam axis. For the energy and angular distribution, we used the energy range between 0.5 and 500 GeV and the angles from 0 to 90 degrees. The lower limit of 0.5 GeV is a safe margin when considering the effective 1.5 GeV threshold observed on the muons energy reaching the calorimeter (Fig. 7.2, right). For energies below this threshold, the muons are absorbed in the concrete

located above the detector. The rate of generated events is obtained by integrating the flux on the generation plane and on the solid angle. The result is a rate of generated cosmic muons of $\sim$ 9.5 kHz, corresponding to a bandwidth of $\sim$8 kB/s, well within the allocated budget.

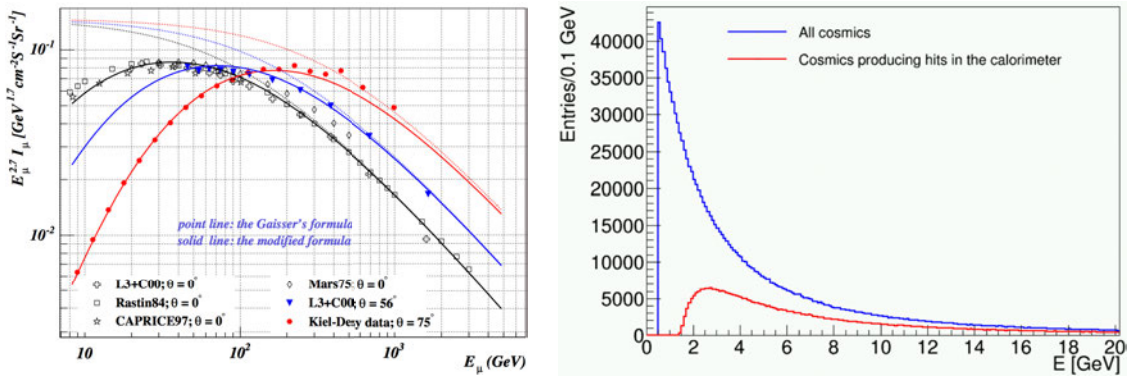

Figure 7.2: Left: fit results to the experimental data: the three dotted lines are the prediction of the standard Gaisser's formula and the solid lines are prediction of the modified formula. Right: generated energy distribution of all the cosmic muons in the horizontal production plane (blue line) and of cosmic muons producing hits in the calorimeter (red line).

The calorimeter is considered hit by a muon if at least one crystal is fired with an energy deposition of 1 MeV. The CR muons rate detected by the calorimeter is obtained as:

$$R = R_{plane} \cdot \frac{N_{E\,>\,1\ MeV}}{N_{TOT}}\ , \tag{7.1}$$

where $N_{E\,>\,1\ MeV}$ is the number of events with a deposit greater than 1 MeV in at least one crystal. The rate on the calorimeter results to be $R \sim 130$ Hz. This is clearly an upper limit for the rate of CR events that can be used to calibrate the calorimeter. This rate decreases down to $R = 15$ Hz considering the selection criteria needed to make the sample as homogeneous as possible. This rate allows to accumulate 1000 events/crystal after $\sim$ 5 hours of calibration run.

7.1.2 Golden MIP selection

The crystals hit by a CR muon are grouped in a cluster following the procedure described in Section 3.5.2. A digitization threshold of 1 MeV per crystal is applied. In order to have a reliable fit of the muon trajectory, the calorimeter cluster is

required to have an energy deposition above 6 MeV in at least three crystals. Three different topologies of calorimeter events are selected: *a*) muon tracks that do not cross the central hole (Fig. 7.3, left), but hit two crystals in the outer ring of the same disk; *b*) muon tracks crossing once the calorimeter disk passing trough the central hole (Fig. 7.3, middle), one crystal in the outer ring and one in the inner ring of the same disk are required; *c*) muon tracks that cross twice the calorimeter disk passing trough the central hole (Fig. 7.3, right), two crystals in the outer ring and two crystals in the inner ring of the same disk are required.

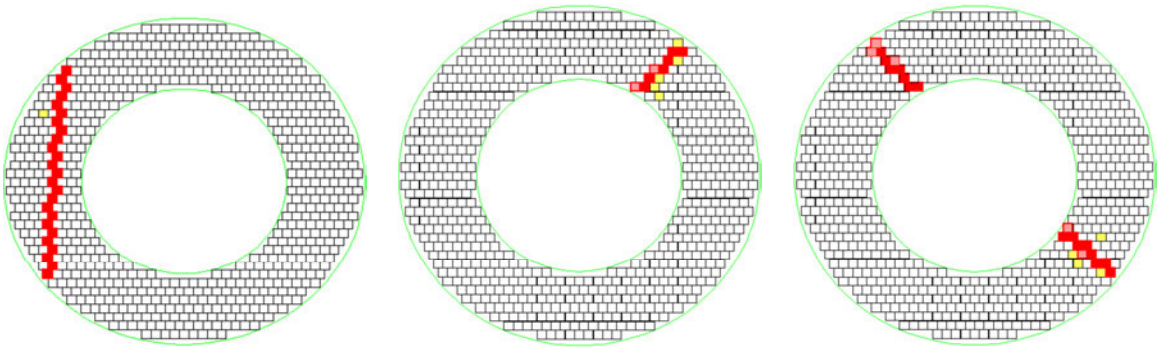

Figure 7.3: Example of cosmic muon passing the selection *a*) on left, *b*) on middle and *c*) on right.

Then, all the crystals above the clustering threshold are fit with a linear function in the x-y transverse plane. Their positions are weighted proportionally to the deposited energy. For each selected CR event, the least square method is used to perform this muon trajectory fit. A distribution of the energy deposited by CR muons in a single crystal is reported in Figure 7.4.

Moreover, only clusters with $0.6<\chi^2/\text{ndof}<1.4$ (from the linear fit) are accepted for the calibration and not all the hits used in the fit are used to calibrate. The hits are retained for calibration only if their crystal center has a distance lower than 1/2 of the crystal size (17 mm) from the fit linear trajectory. In addition, the hits are considered only if the corresponding path length (Fig. 7.5, left) in the transverse plane is longer than the crystal thickness (34 mm). The muon path length (dX) has been approximated by the path length in the transverse plane. In Figure 7.5 (right) the distribution of the specific energy loss (dE/dX) in the crystals before and after the event selection is reported. A clear reduction of the events with an anomalous

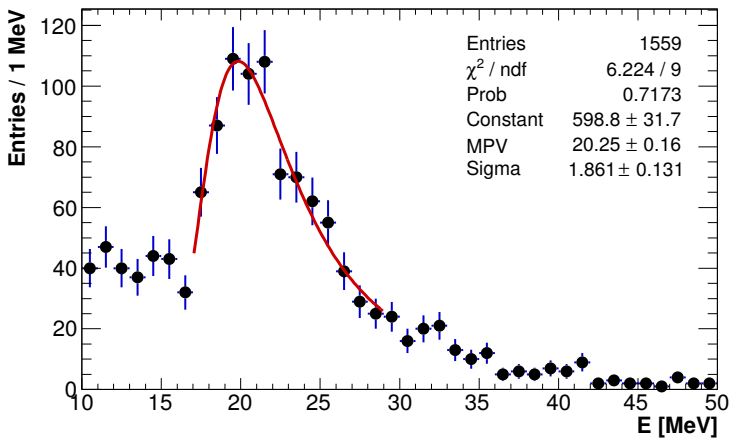

Figure 7.4: Distribution of cosmic muon energy deposition, as expected from simulation.

specific energy loss is observed after this selection.

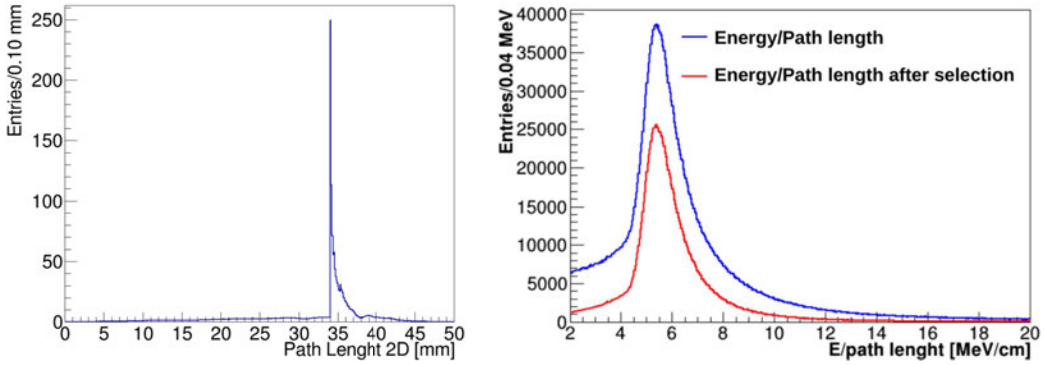

Figure 7.5: Left: distribution of the bidimensional path lenght in each crystal. Right: Specific energy loss (dE/dX) before and after the selection cuts.

7.1.3 Energy equalization

The specific energy deposit of cosmic muons is expected to be the same for all the crystals, as the majority of them are MIPs. The dE/dX differences due to the different material crossed before to hit a crystal can be considered negligible. A dedicated MC simulation study has been performed to check the validity of this assumption. Figure 7.6 shows the distribution of the peaks of the specific energy loss in a crystal, obtained with a Landau fit. The distribution is homogeneous

along all the calorimeter, with fluctuations at the level of ∼1%, compatible with the statistical error of the Landau fit.

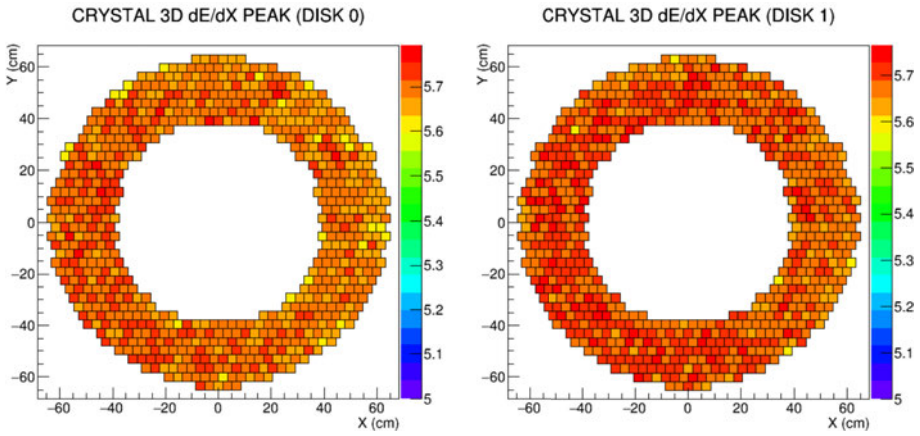

Figure 7.6: 3D specific energy loss in the crystals of the front (left) and back (right) calorimeter disks obtained by the MC simulation.

The Mu2e calorimeter does not provide a measurement along the crystal (z coordinate), so that the total three-dimensional path length cannot be directly obtained by the crystal energy deposits. Nonetheless, if the two-dimensional path length in the transverse plane, which is independent of the z-coordinate, is used instead of the total path length, the 2D specific energy loss has still a distribution with a good homogeneity along the calorimeter, as shown in Figure 7.7. Once again, the fluctuations of ∼1% are compatible with the statistical error of the peaks obtained with the Landau fit and the 2D specific energy loss can then be used to equalize the calorimeter channels.

Figure 7.8 shows the comparison between the CR muons specific energy loss obtained using the 3D and the 2D path length. The 2D specific energy loss distribution is shifted towards higher values because the path length is systematically underestimated, but the peak shift is relatively small because the cosmic muons angular distribution presents a sharp peak corresponding to the vertical direction [140].

All the calorimeter channels have a different energy scale factor, q_i, so that their measured energy is $E_i = q_i E_i^{DEP}$, where E_i^{DEP} is the energy deposit in the crystal according to GEANT4 [75]. A Landau fit on the reconstructed 2D specific energy loss (Fig. 7.8) gives the peak value dE/dX_{peak_i} for the i-th crystal. Then equalisation

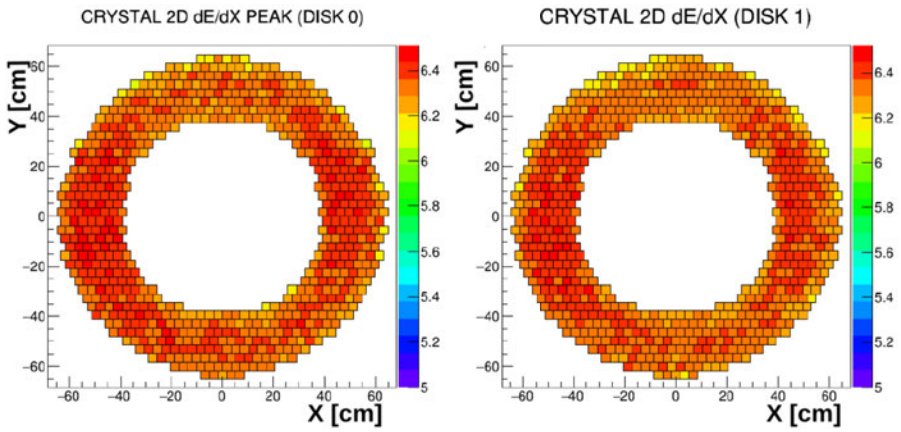

Figure 7.7: 2D specific energy loss in the crystals of the front (left) and back (right) calorimeter disks obtained by the MC simulation.

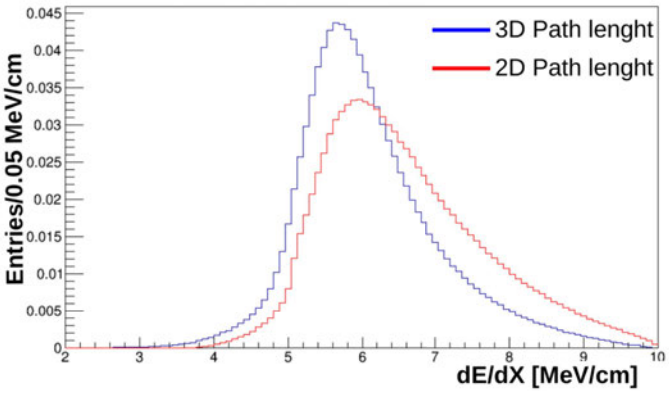

Figure 7.8: Comparison between the 2D and the 3D path length values.

factor is defined as:

$$\bar{q}_i = \frac{dE/dX_{peak_i}}{dE/dX_{peak}} \ , \tag{7.2}$$

where $dE/dX_{peak} \sim 6$ MeV/cm is the nominal energy loss expected by the simulation. Then the equalized energy can be obtained as follow:

$$\frac{E_i}{\bar{q}_i} = \frac{q_i}{\bar{q}_i} E_i^{DEP} \ . \tag{7.3}$$

The distribution of the calibrated specific energy loss $(dE/dX_{peak_i})/\bar{q}_i$ is reported in Figure 7.9 and has the correct mean value with a sigma of ∼1.7%.

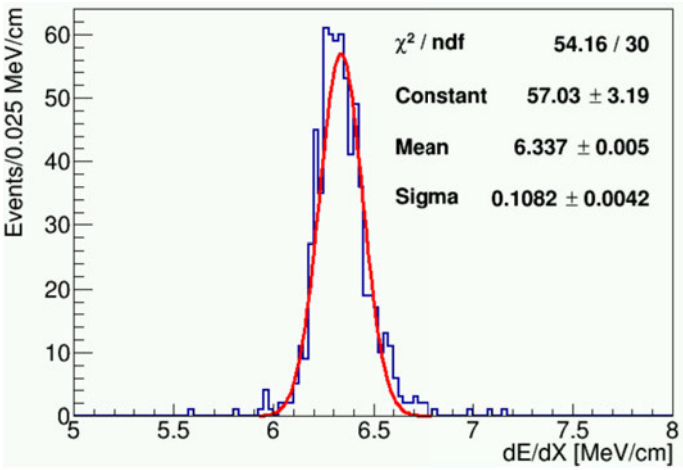

Figure 7.9: Distribution of the calibrated specific energy loss $(dE/dX_{peak_i})/\bar{q}_i$

7.1.4 Time offset alignment

The time offsets (T_0) between calorimeter channels can be caused by different factors, such as small differences on cable lengths, contributions due to different transit time of the SiPM signals or other electronics delays. These offsets must be evaluated and corrected in order to make negligible their contribution to the determination of the calorimeter time resolution. T_0s can be calibrated exploiting CR muons, using the following procedure:

- the 2D fit of the muon trajectory in the transverse plane is performed as previously described, and the angle θ in the x-y plane is calculated either using the fit slope or analytically, using cluster crystals coordinates;
- only the crystals having their center located at a distance lower than 1/2 of the crystal size (17 mm) from the fitted trajectory and a path length in the transverse plane longer than the crystal thickness (34 mm) are used;
- the crystal center position is converted in the distance travelled in the x-y plane:
$$\Delta y' = \frac{\Delta y}{sin\theta} = \frac{y - y_0}{sin\theta} \ , \tag{7.4}$$
where y_0 is the y coordinate of the cosmic muon starting point;
- the measured time in the crystal versus its distance $\Delta y'$ is fitted;

- considering all the calibration sample, the average value of the fit residuals is used to estimate the offset, T_0, for each crystal;
- the values of the measured time are corrected in all the crystals by subtracting their estimated T_0.

This procedure can be iterated many times to converge to stable results. The possibility to extract the time offset T_0 from this procedure needs some more justification. The time of a calorimeter channel can be expressed as the sum of the constant offset, the muon time-of-flight and the optical photons time-propagation inside the crystal:

$$t_i = T_{0i} + \frac{\Delta y'}{c \cdot sin\psi} + \frac{z}{v_c} \ , \tag{7.5}$$

where ψ is the inclination with respect to the z axis, v_c is the average velocity of the optical photons and z is the distance travelled by the optical photons to reach the SiPM. Equation 7.5 can also be written as:

$$t_i - \frac{\Delta y'}{c \cdot sin\psi} = T_{0i} + \frac{\Delta z}{v_c} + \frac{z_0 - L/2}{v_c} + \frac{L/2}{v_c} \ , \tag{7.6}$$

where z_0 is the z coordinate of the cosmic muon starting point and L = 20 cm is the crystal length. When a sufficient number of calibration events has been collected, the contributions of the $\frac{\Delta z}{v_c}$ (where $\Delta z = y' cot\psi$) and $\frac{z_0 - L/2}{v_c}$ terms are null. The correction to apply, $t_{corr} = t_i - \frac{\Delta y'}{c \cdot sin\psi}$, is therefore equal to the i-th crystal time offset, T_{0i}, in addition to a constant factor $(L/2)$, which is the same for all the calorimeter channels.

The T_0 alignment procedure has been tested on a CR muons MC sample in which all the channels were shifted by a different T_{0i} offset generated uniformly within the [-1,1] ns range and applying a 350 ps Gaussian smearing on signals time. This assumes that a good timing "hardware" offsets calibration and synchronization have been previously performed with the laser system.

Figure 7.10 shows the residual distributions between the offset T_0 and the correction T_{corr} at first iteration (left) and after the fifth iteration (right) for a single calorimeter crystal. The gaussian fit superimposed is needed to evaluate the mean value as correction, T_{corr}, to apply to the following iteration. In this crystal case, the mean (sigma) value improves from ∼-0.535 ps (∼381 ps) to ∼0.008 ps (∼343 ps).

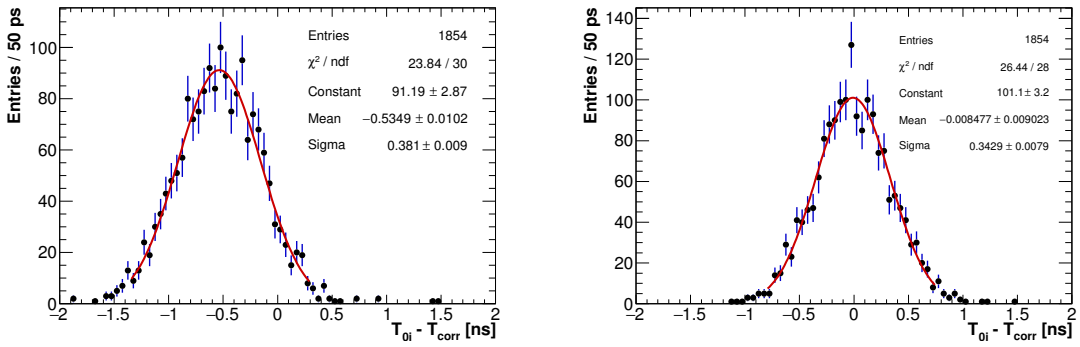

Figure 7.10: Distribution of the fit residuals for a single crystal at the first iteration (left) and after 5 iterations (right) considering all the calibration sample. A gaussian fit is performed to determine the corresponding T_{0i} value.

The residuals mean values distribution for each crystal i of a calorimeter disk obtained in such way and as a function of the crystal identification number is shown in Figure 7.11 (left), for five iterations. A good alignment is clearly visible. Figure 7.11 (right) reports the sigma values obtained from the same gaussin fit on residuals distributions. This method demonstrates already a good capability in monitoring timing resolutions: at first iteration the crystals resolutions are around 380 ps, arriving at < 350 ps after five iterations.

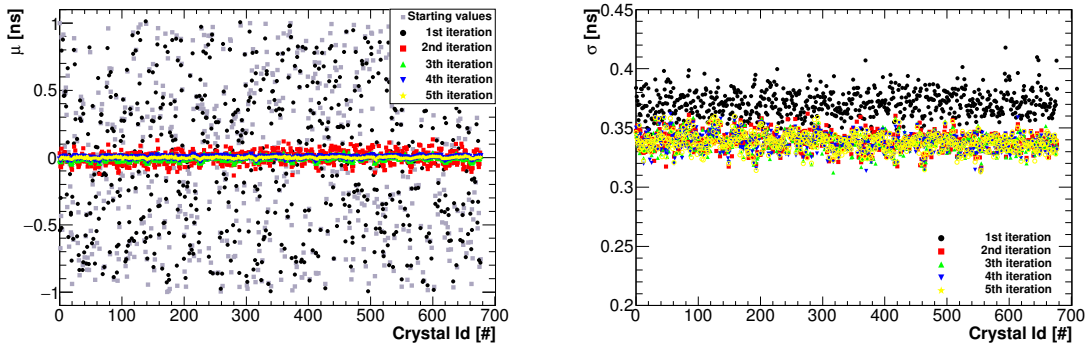

Figure 7.11: Left: mean values of the residuals distribution obtained from a Gaussian fit. Right: sigma values of the residuals distribution obtained from the same Gaussian fit.

The distribution of the difference between the initial T_0 and the correction to be applied at each iteration is reported in Figure 7.12. The values are distributed as a gaussian around zero and a sigma always lower iteration by iteration. At fifth iteration (yellow distribution) the mean value obtained with a gaussian fit is $\sim 3 \pm 1$ ps, with a sigma of $\sim 347 \pm 11$ ps. The same residuals distribution as a function of the crystal identification number of the front calorimeter disk is reported in Figure 7.13 (right). The great capability of correcting the offsets down to < 90 ps is clearly visible.

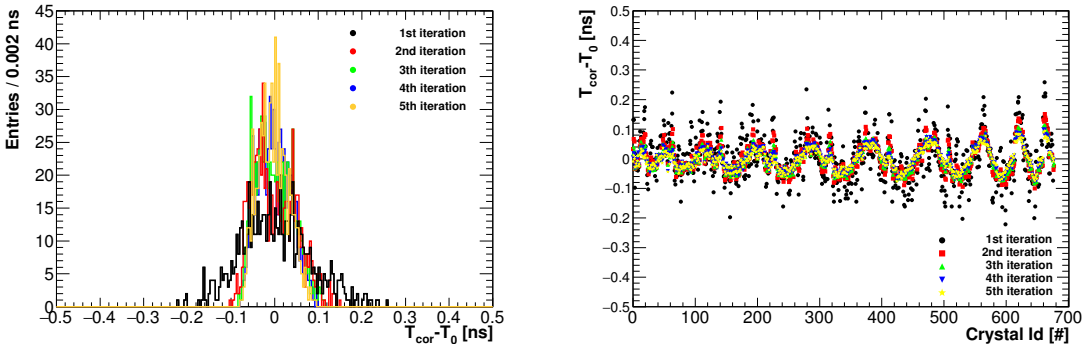

Figure 7.12: Left: difference between the initial T_0 and the correction to be applied at each iteration. Right: same distribution as a function of the crystal id.

Figure 7.13 shows the associated errors, as sigma divided by the square root of the number of entries. Statistical error on residuals evaluation is already better than 10 ps/channel with this statistics. A radius-modulation is visible and it is due to the events distribution involving calorimeter crystals as a function of their position, as shown in Figure 7.13 (right). The identification number associated to crystals starts from zero in the inner ring and increases spirally.

This simulation study has been repeated for several time offset spreads in addition to 350 ps: 250 ps, 500 ps and 750 ps. The timing monitor and T_0s alignment capabilities of the procedure are confirmed for all these values.

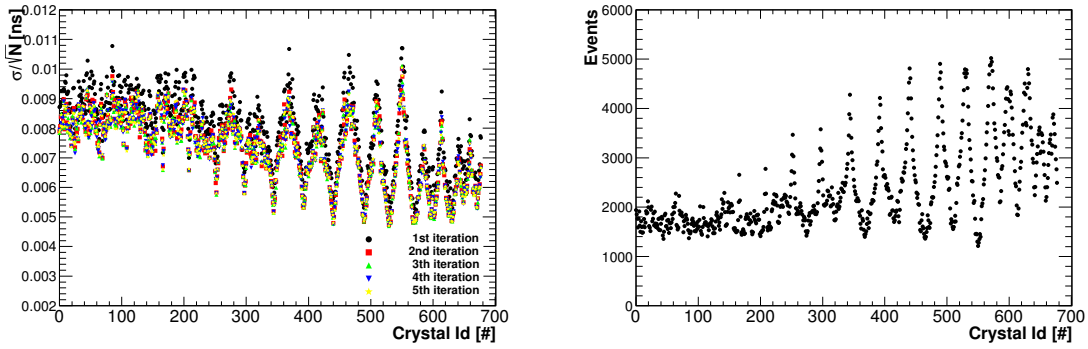

Figure 7.13: Left: error associated to the residuals evaluation. Right: events distribution as a function of the crystal identification number.

7.1.5 Experimental test on a prototype

On May 2018, the first test of the timing calibration with cosmics has been carried out with a central section of the Module-0. Figure 7.14 shows a map of the 16 channels used. Only three central crystals had both SiPMs biased and readout; the remaining 13 crystals were readout with a single SiPM.

To tag cosmic ray events, the Module-0 was positioned between two plastic scintillation counters, each one readout by two PMTs. The coincidence of the four PMT signals provided the DAQ trigger. The test lasted about a week, for a total of ∼80000 events acquired. Moreover, a random signal generated with a CAEN time unit has been used for dedicated pedestal run to evaluate the noise (about ∼1500 events/run).

Two 8-channels-CAEN-V1720 waveform digitizer boards were used to acquire data and digitize the waveforms at 250 Msps. The same FEE configuration used during the test beam was in place. The new DAQ boards were chosen to overcome the noise and jitter synchronization problems seen at the test beam.

7.1.6 Data analysis

To analyze data, the same procedure of the TB has been followed. The charge collected was estimated by numerical integration of the waveforms in a 250 ns integration gate (from 150 ns to 400 ns).

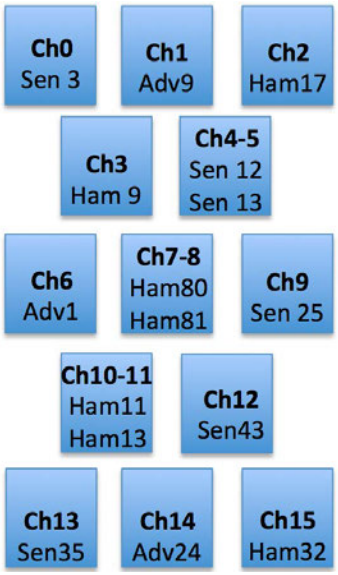

Figure 7.14: Map of the Module-0 channels used for the cosmic ray test.

In Figure 7.15 (left), the charge reconstructed in central channel of the system is reported. The peak due to cosmic ray muons is clearly visible. A landau fit has been applied to extract the most probable value that shows a statistical error determination better than 1%.

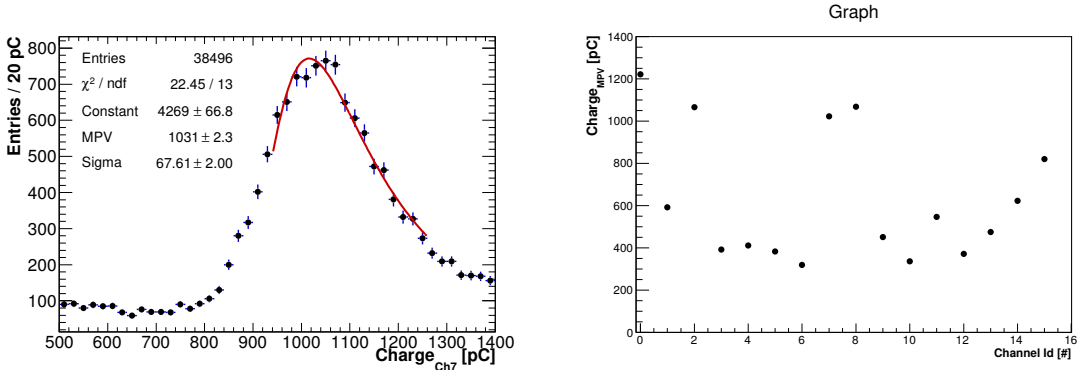

Figure 7.15: Left: example of the charge distribution reconstructed by a SiPM of the central channel. The peak due to CR events is clearly visible and fit with a Landau function. Right: MPV values obtained from the Landau fit on all the channels charge distributions.

However, due to the many modifications done to the electronics and to the SiPMs and crystals connection after the test beam, a large spread of response among different calorimeter channels is observed, as shown in Figure 7.15 (right). In order to improve the data analysis, an offline equalization of the response based on MIPs

was performed. For each channel, the charge MPV obtained from the Landau fit for each readout SiPM was used as calibration factor assuming: (i) a straight trajectory and (ii) a mean energy deposition value. This last value has been estimated with the MC simulation already developed for the Module-0 TB (see Ch. 6). The expected energy deposition by a MIP in a CsI crystal is ∼21.06 MeV. So that, the average pC/MeV conversion factor is of around 48.96 pC/MeV.

Figure 7.16 shows an example of energy distribution obtained after the calibration procedure. The red line superimposed represents the Landau fit used to extract the MPV. The MPV values of all the channels are reported in Figure 7.16 (right). The average is centered around 21.1 MeV with an RMS of about 0.3% (Fig. 7.17, left). Similar indication is shown in MeV when plotting the difference of the MPV energy values with respect to the central channel one. This residual fluctuation is assigned to the systematics of the Landau peak determination.

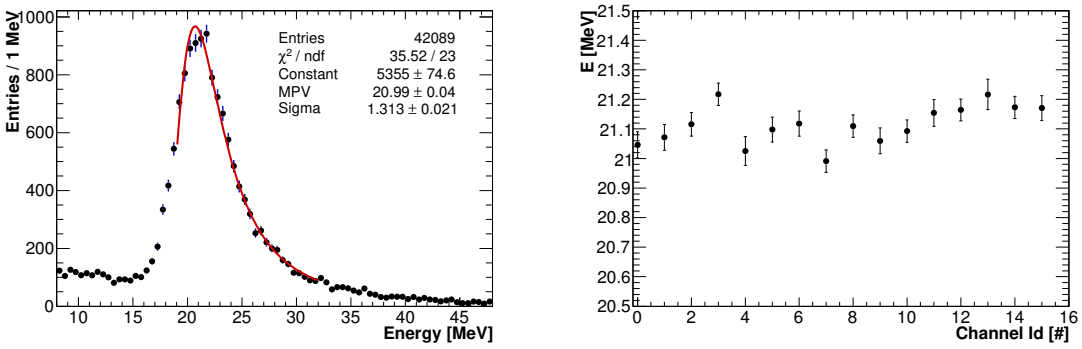

Figure 7.16: Left: example of energy distribution obtained after MC-based calibration. The peak due to CR events is fit with a Landau function. Right: MPV values obtained from the Landau fit on all the channels energy distributions.

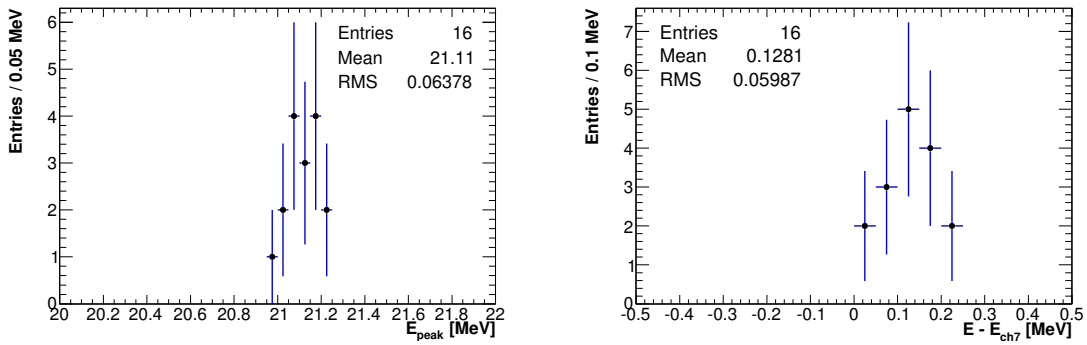

Figure 7.17: Left: distribution of the MPV energy value. Right: MPV energy value relative to the central channel.

To determine the noise level in the detector, a random signal has been used as a trigger. A total of ∼1500 events have been acquired. An example of the noise distribution of a single channel is reported in Figure 7.18 (left). The distribution is fit with a gaussian function. The mean, μ_{noise}, and sigma, σ_{noise} parameters extracted for all the channels are reported in Figure 7.18 (middle, right).

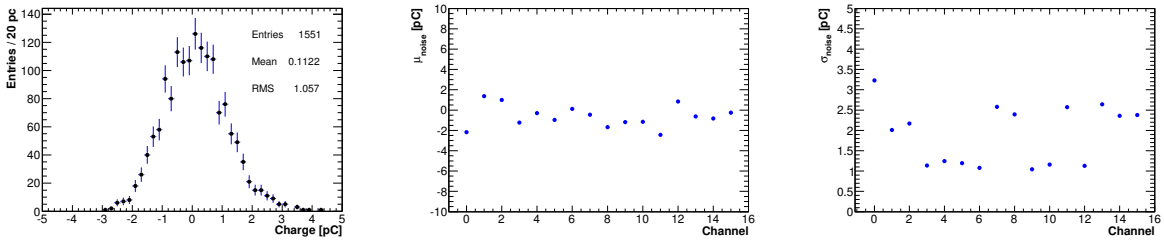

Figure 7.18: Left: example of charge distribution obtained during the pedestal run. Middle: peaks of the noise distributions of all the 16 channels obtained from a gaussian fit. Right: sigma of the noise distributions of all the 16 channels obtained from the gaussian fit.

Figure 7.19 shows the dependence of the noise value obtained when summing up several channels as a function of the number of channels. Differently from the TB, the behaviour is well represented by $1/\sqrt{(N)}$, where N is the number of channels in the sum. We realized that the TB problem was related to the input section of the CAEN V1742 digitizer boards used at BTF.

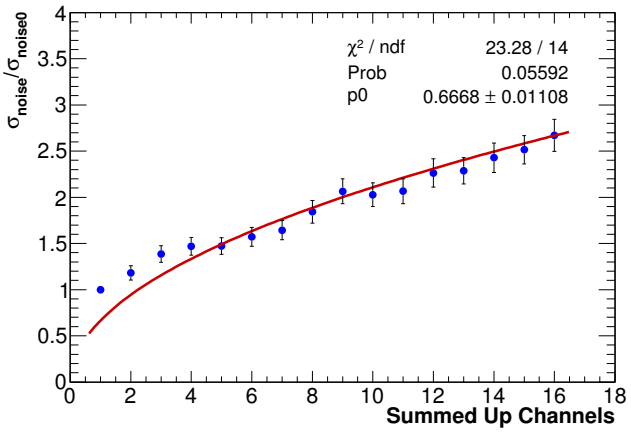

Figure 7.19: Noise value obtained summing up several channels noise as a function of the number of channels

Time reconstruction

For the time evaluation, the same analysis proceedure used at the BTF test beam has been followed. Figure 7.20 (left) shows a digitized signal, with a lognormal fit applied on the leading edge, between 1.65 and 98% of the maximum amplitude value. The time, T_{CF}, is evaluated using a CF threshold at 5% of the maximum. An example of the time distribution obtained after cutting around the MIP peak is reported 7.20 (right).

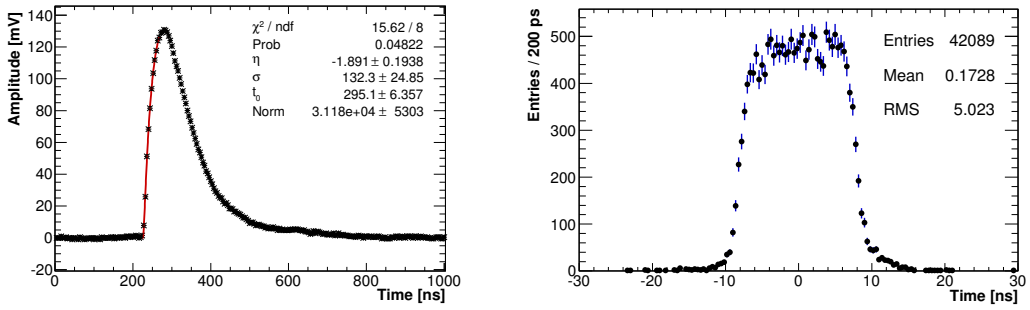

Figure 7.20: Left: example of a SiPM waveform due to a "golden" muon. Right: time distribution obtained fitting the waveforms with a lognormal function and applying the CF method described in the text.

Figure 7.21 shows the distribution of some parameters used to check the fit validity. These values are related to the two SiPMs (channel 7 on top and channel

8 on bottom) reading out the central crystal, which are connected to two different DAQ boards. The first plot shows the charge distribution, a cut of $\pm 3\ \sigma$ around the MIP peak has been used to select "golden" Cosmic Ray events. In the second plot, the $\chi^2/ndof$ distribution of the lognormal fit is reported. In the third plot, the number of degree of freedom (ndof) used for the same fit is shown. The last plot shows the differences between T_{CF} and the time position of the closest digitizer bin. The distribution obtained is flat, demonstrating that there is no bias in the leading edge reconstruction.

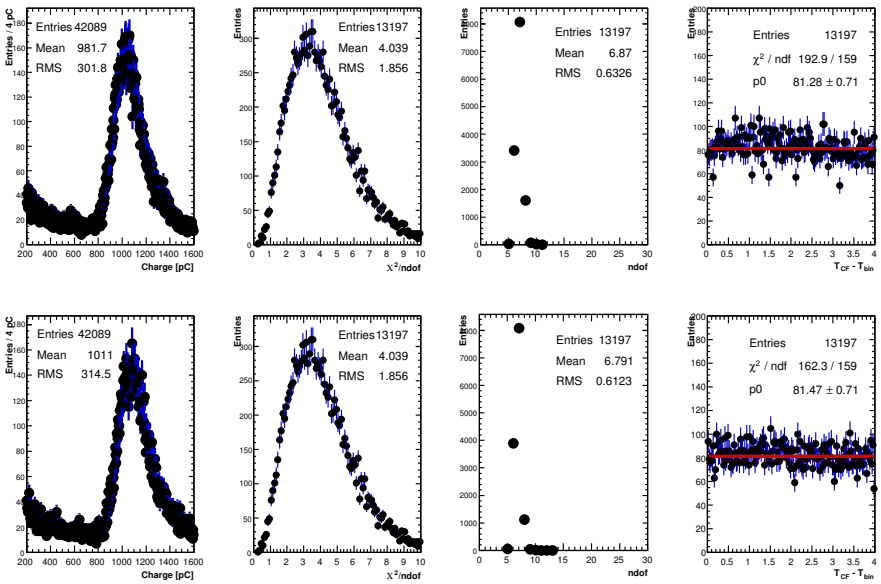

Figure 7.21: Parameters used to evaluate the consistency of the lognormal fit used to extract the signal time and select CR events.

Before to procede testing the T_0 calibration procedure, the time resolution has been estimated in the central channel to check consistency with the TB results. Figure 7.22 shows the time difference between the two SiPMs of the central channel. This grants a resolution for the single sensor of $\sim$315 ps, in well agreement with previous results.

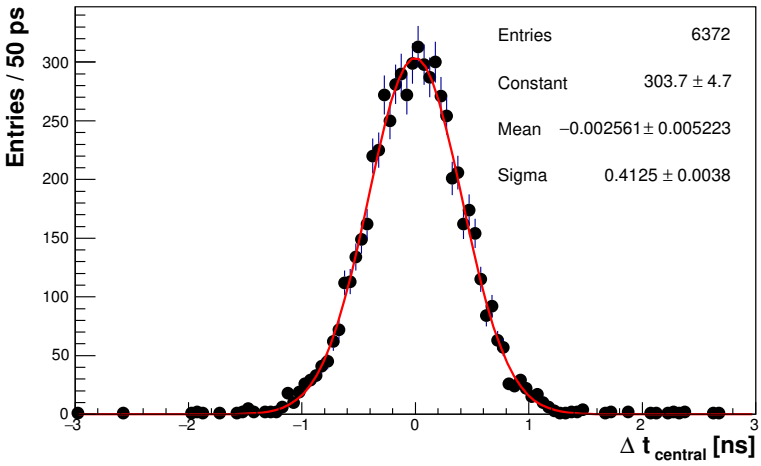

Figure 7.22: Time resolution of the central channel.

7.1.7 Time offset alignment

To check the T_0 calibration, the same iterative procedure presented in Section 7.1.4 has been applied on data.

7.1.8 Event selection

To identify CR events, an additional offline selection has been introduced by requiring the energy of the top layer (channel 0, 1, 2) to be in the [15, 40] MeV range. To identify a cosmic ray track, only the events with at least three fired crystals have been retained for further processing. A crystal is considered hit by a CR muon when its energy deposition is > 6 MeV. The energy distribution of the selected events is reported in Figure 7.23 as a function of the number of crystals in the track. The peak values for the different crystal multiplicity scales well with MC expectation.

Once the event is selected, the slope of the CR track has been evaluated analytically, weighting each crystal positions with its own energy deposition. The time correction, T_{corr} has been evaluated following Equation 7.6. Distribution of the residuals for a single crystal at the first iteration (left) and after five iterations (right) are reported in Figure 7.24. A gaussian fit is performed to determine the corresponding T_{0i} value, to be applied as correction to the following iteration.

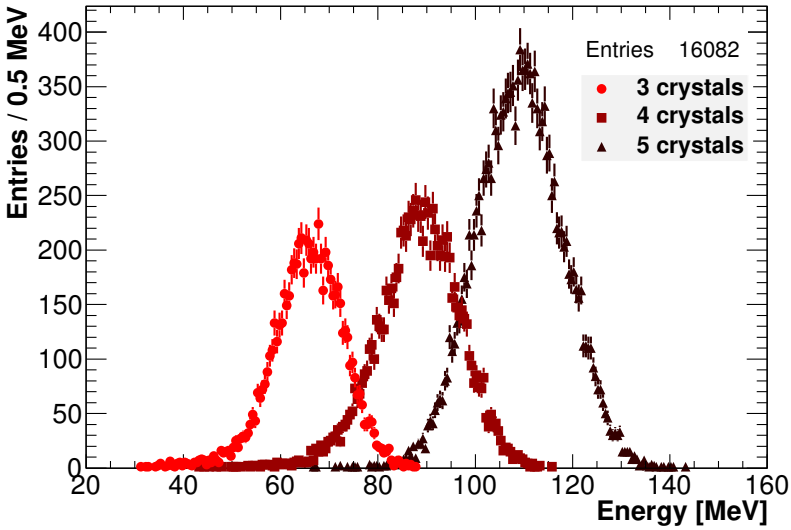

Figure 7.23: Energy distribution of cosmic ray events hitting three crystals at least.

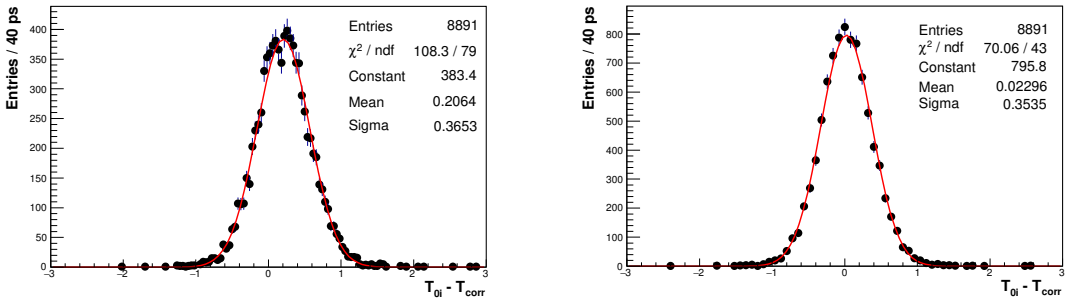

Figure 7.24: Distribution of the fit residuals for a single crystal at the first iteration (left) and after 5 iterations (right). A gaussian fit is performed to determine the corresponding T_{0i} value.

To check if five iterations are enough to obtain a good alignment, the correction, T_{corr} have been evaluated up to 10 iterations. Figure 7.25 shows these results for all the channels in both DAQ boards. After the fifth iterations, the corrections to apply are consistent with zero.

Therefore, the calibration iterative procedure has been applied on data only up to five iterations. Figure 7.26 shows the mean (left) and sigma (right) values of the residuals distribution, as obtained from a Gaussian fit. A good alignment is clearly visible and confirmed by Figure 7.27 (left). The orange distribution, corresponding to the last iteration, has a mean value of 6 ps with an RMS of 10 ps.

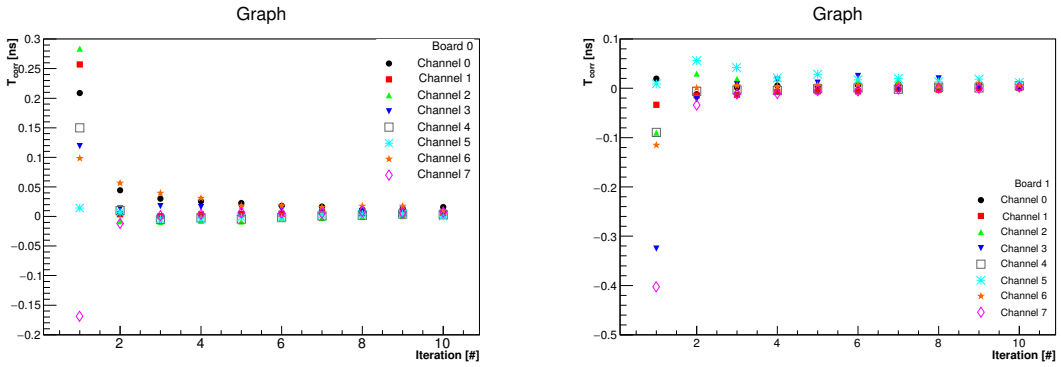

Figure 7.25: T_{corr} as a function of the iteration number for the channels of board 0 on left and of board 1 on right.

Figure 7.27 (right) shows that with 5 iterations an error smaller than 10 ps on the T_0 determination is achieved.

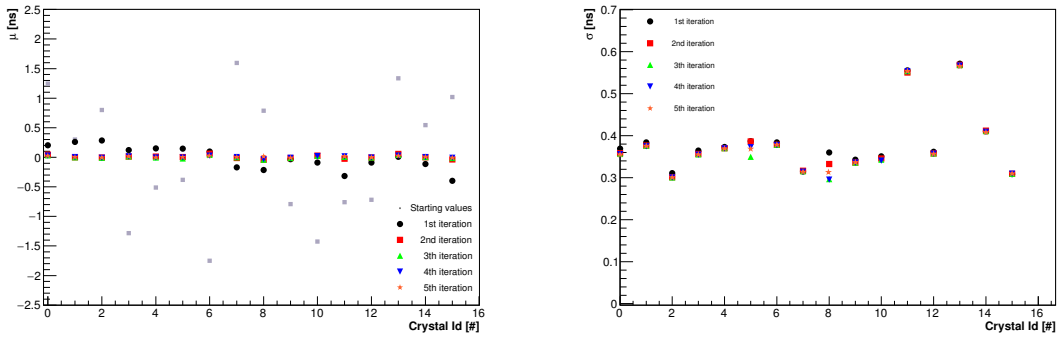

Figure 7.26: Mean (left) and sigma (right) values of the residuals distribution, obtained from a Gaussian fit.

The T_0 corrections are then applied at all channels time to evaluate the resolution between neighbouring crystals. As an example, the time differences between three crystals involved in the same events are reported in Figure 7.28; in addition to T_{corr} also the travel time difference between CsI crystals has been subtracted. A single photosensor per SiPM has been considered. All the three possible distributions of time differences are well aligned around zero, with a resolution of about ∼330 ps. This value is compatible with the one obtained by a single crystals readout by two SiPMs, as shown in Chapter 6.

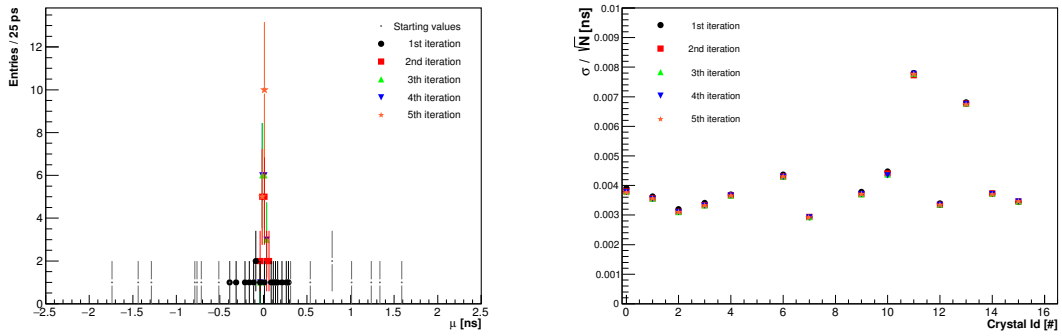

Figure 7.27: Left: mean values of residual distribution at each iteration. Right: erros associated to each channels.

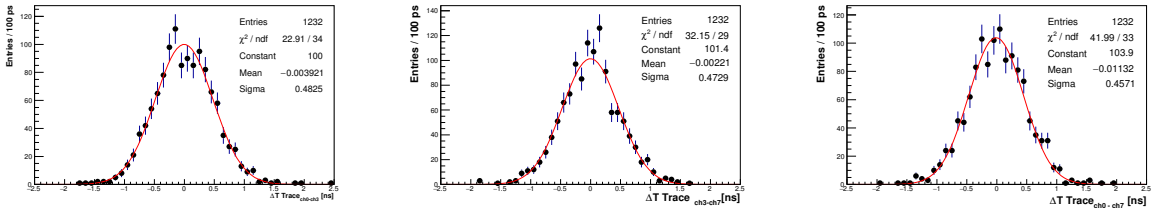

Figure 7.28: Time differences between three crystals (Channel 0, Channel 3, Channel 7) hit by the same CR events. The resolution between neighbouring crystals is evaluated as the sigma from the gaussian fits applied divided by $\sqrt{(2)}$.

7.2 Calibration with DIO electrons

Calibration with DIO electrons (Fig. 7.29, left), together with other calibration techniques, will help to realize the best possible performance of the calorimeter, providing an independent cross checks. These events are needed to define the absolute energy scale and timing of the calorimeter, using momentum measurements in the tracker. This relative calibration is possible due to the much higher resolution (>200 keV) of the tracker compared to the calorimeter one.

The energy calibration procedure is based on the comparison of the DIO electron cluster energies, E, to the electron track momenta measured in the tracker, P. The calibration constants can be computed by minimizing the RMS width of the E/P distribution and constraining it to peak at the MC predicted value. A timing calibration is also possible calculating the time offsets between DIO electron tracks

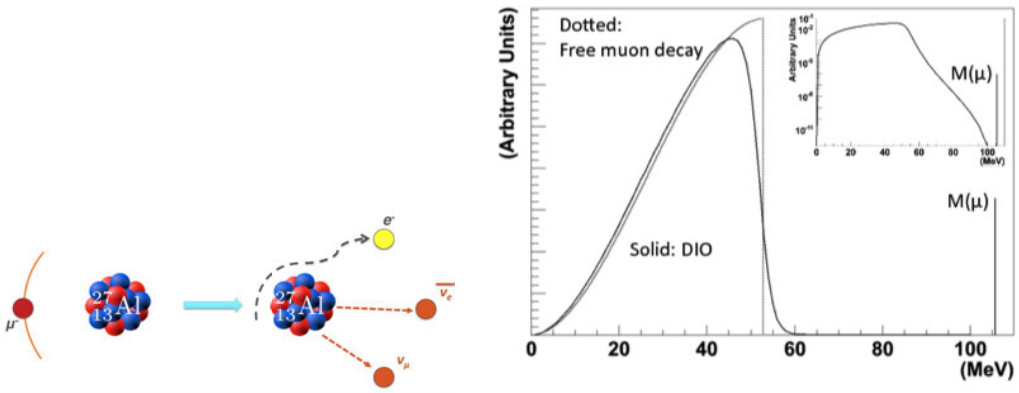

Figure 7.29: Left: topology of a decay in orbit muon, emitting an electron and two neutrinos in the final state. Right: Energy spectrum of the emitted electron.

and calorimeter clusters.

At the detector nominal magnetic field, B = 1 T, this method has to deal with very strong radial dependence of the occupancy and low statistics. Figure 7.29 (right) shows the DIO energy spectrum, which is peaked around 52 MeV with a long tail extended up to 100 MeV. So that, most of the hits are expected to be in the inner crystal layers, while there are no particles hitting the outer crystals. To provide uniform coverage and high statistics, the magnetic field should be reduced from 1 T to 0.5 T. This corresponds to shift the detectors acceptance around 50 MeV.

Given the narrow detector acceptance, δP/P$\sim$ 20%, several measurements at the intermediate magnetic fields are needed to translate the calibration from 0.5 T to the nominal field. Well modelling the behaviour of E/P vs the magnetic field, together with a high-statistics, could lead to a calibration accuracy of $\sim$ 0.2%.

7.2.1 Simulation and event selection

Using the Mu2e simulation software, electron samples within the DIO spectrum have been generated. As of today, the magnetic field values available for the DS are: 0.5 T, 0.7 T, 0.85 T and 1 T. For every field, a few large event samples with monochromatic DIO electrons have been generated. The momenta used for every field are reported in Table 7.1.

For calibration purpose, just events with a well reconstructed track are consid-

B-field [T]	Momentum [MeV]
0.5	40, 45, 50, 55
0.7	55, 60, 65, 70, 75, 85
0.85	85, 50, 95, 100
1	85, 90, 95, 100

Table 7.1: Summary of the momentum of the DIO electron samples generated at every magnetic field.

ered, with at least 25 hits and a good helical fit, $\chi^2_{trk}/ndof < 3$.

A clear dependance of the distributions on the track radius, R_{trk}, has been observed, for all the magnetic field used (see Figure 7.30). R_{trk} is correlated with the path of the electron inside the calorimeter, as shown in Figure 7.31. So a path larger than 280 mm is required, in order to exclude events with track entering the calorimeter disks from the inside or tracks hitting the inner edge of the calorimeter.

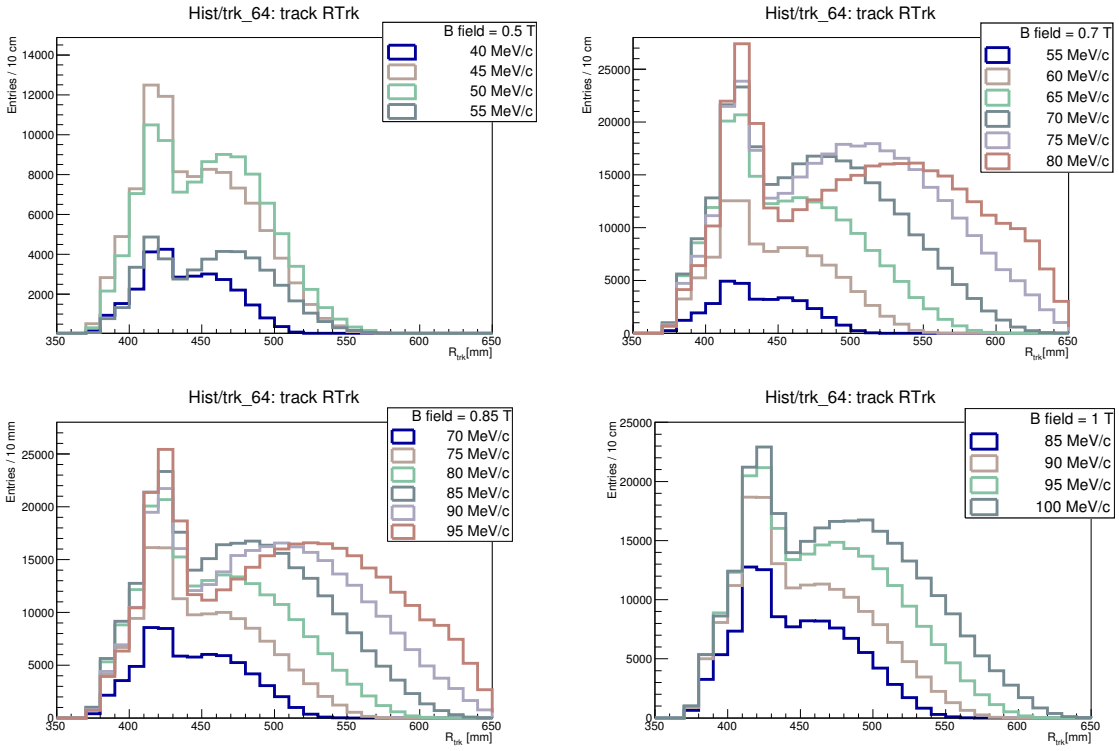

Figure 7.30: Distributions of the helical tracks radius of the DIO electrons hitting the calorimeter.

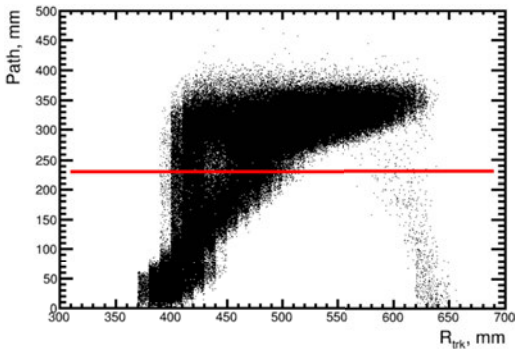

Figure 7.31: DIO electrons path inside the calorimeter as a function of their radius helical trajectory.

7.2.2 Calibration in reduced magnetic field

For calibration at B = 0.5 T, the statistics is limited only by the DAQ bandwidth. In principle, it is possible to achieve any desired statistical accuracy, but to keep the occupancy at a low level, the rate of stopped muons has to be reduced by factor of 200.

A large sample of DIO electrons has been simulated ($\sim 1 \times 10^5$) at B = 0.5 T. Half of the generated sample is used to produce a miscalibrated "data" sample, while the other half is used as a "reference MC" sample. The calibration procedure is trying to reproduce the reference MC by applying calibrations to the "data" sample, considering a linear miscalibration model. For each event in the calibration sample the energy deposition in crystal U_i is "miscalibrated" by the perturbation coefficient λ_i:

$$U_i = \frac{U_i'}{\lambda_i} \quad , \tag{7.7}$$

where the index i runs over the crystals in a calorimeter disk and U_i' is an actual energy deposition. In this study, the values of the perturbation coefficient, λ_i, are drawn from a gaussian distribution with a fixed mean and sigma of 0.1. A correct calibration procedure should reconstruct the calibration constants $C_i = \lambda_i$. The stability of the method is studied for the gaussian mean in the range of [0.8, 1.2]. Here we assume that the calorimeter has been already calibrated using the 6 MeV photons emitted by the radioactive source system and the "raw" energy scale of calorimeter has been determined, so the range chosen for this study seems to be sufficient.

The calculation of the calibration constants starts from the minimization of the following function [141] [142]:

$$f(C_i) \;=\; \sum_j \left(\sum_i \frac{U_{ij} C_i}{p_j} - < E/p > \right)^2 \quad , \tag{7.8}$$

where the index j runs over the events in our sample, the index i runs over the crystals in a cluster, U_{ij} is the energy deposition during the jth event in the ith crystal, p_j is the DIO electron track momentum at the trajectory end, <E/p> is the average ratio between the electron energy deposition in the calorimeter and the electron track momentum. The minimum of the function is determined by the following conditions [143]:

$$\frac{df(C_i)}{dC_i} = 0 \quad . \tag{7.9}$$

Uncertainty in the definition of <E/p> and effects leading to non-constant <E/p> for different parts of the calorimeter could bias the values of the calibration constants determined. Also the selection requirements on the energy deposition in crystals and the energy thresholds used for calorimeter clustering algorithm can bias the calibration procedure. To remove any bias, an iterative approach is used and at each iteration the energy deposited in the ith crystal is calculated using the value of calibration constant C_i determined at the previous iteration as:

$$C_i = \frac{C_i^{cal}}{C_i^{ref}} \quad . \tag{7.10}$$

In this way, the accuracy of the calibration is determined by the accuracy of the MC detector modelling. Figure 7.32 (left) shows the $E_{cluster}/p_{track}$ distributions, before calibration, after first iteration, and at the end of calibration procedure. These distributions are compared to the E/P distribution corresponding to "ideal" calibrations, $C_i = \lambda_i$. To test correctness of the calibrations, the $(C_i - \lambda_i)/\lambda_i$ distribution is fit with a gaussian function, as reported in Figure 7.32 (right). The resulting mean value is consistent with zero and confirms that the calibration procedure used does not introduce a bias.

Varying the average perturbation factor in the range of [0.8, 1.2], the mean values of $(C_i - \lambda_i)/\lambda_i$ are again consistent with zero, while the calibration accuracy has no dependence on perturbation factor and it is about 0.3% for both disks.

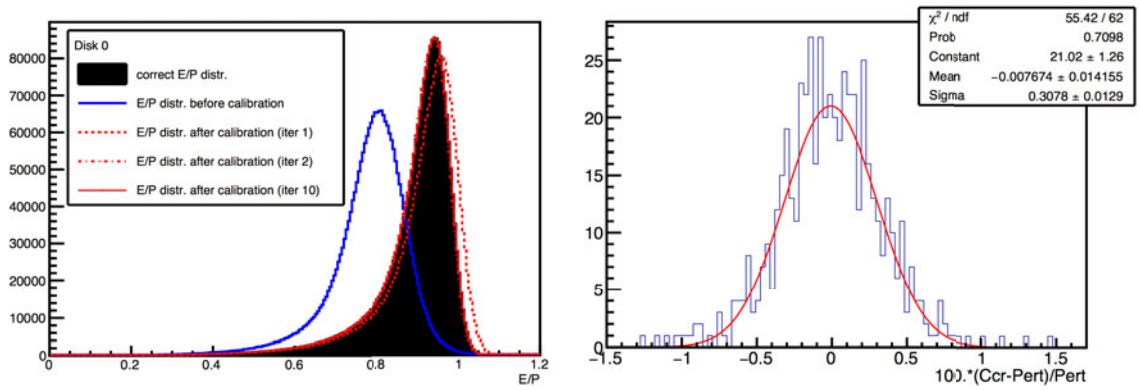

Figure 7.32: Left: distribution of the cluster energy, E, and tracker momentum measurement, P, ratio. Right: distribution of the difference between the iterative calibration constant and the perturbation coefficient, λ_i, normalized to λ_i.

Due to the non-uniform coverage, the calibration accuracy depends on the crystal radius. Compared to the central region, the calibration accuracy near the internal and external edges of disks is lower. By the way, simulations show that the mean values of the $(C_i - \lambda_i)/\lambda_i$ distributions remains consistent with zero for all the crystals at every radius.

Well modelling the calibration with DIO electrons at B = 0.5 T, the calorimeter can be calibrated using the data with the statistical accuracy better then 0.5%. An appropriate sample of DIO electrons can be obtained during the 10-20 minute long calibration run. The systematic accuracy of the calibration is determined by the accuracy of the MC detector modelling.

7.2.3 Calibration extrapolation from 0.5 T to 1 T

Given the narrow detector acceptance, several measurements are needed to connect the calibration at 0.5 T to the nominal field. We also assume no relative channel-to-channel change in the gain as a function of the magnetic field.

So that, in addition to 0.5 T and 1 T, measurements at two additional magnetic field values are needed (Tab. 7.1). The $E_{cluster}/P_{traker}$ distribution is used to extract the calorimeter energy scale at nominal field. Example of these distributions obtained at 0.7 T are reported in Figure 7.33.

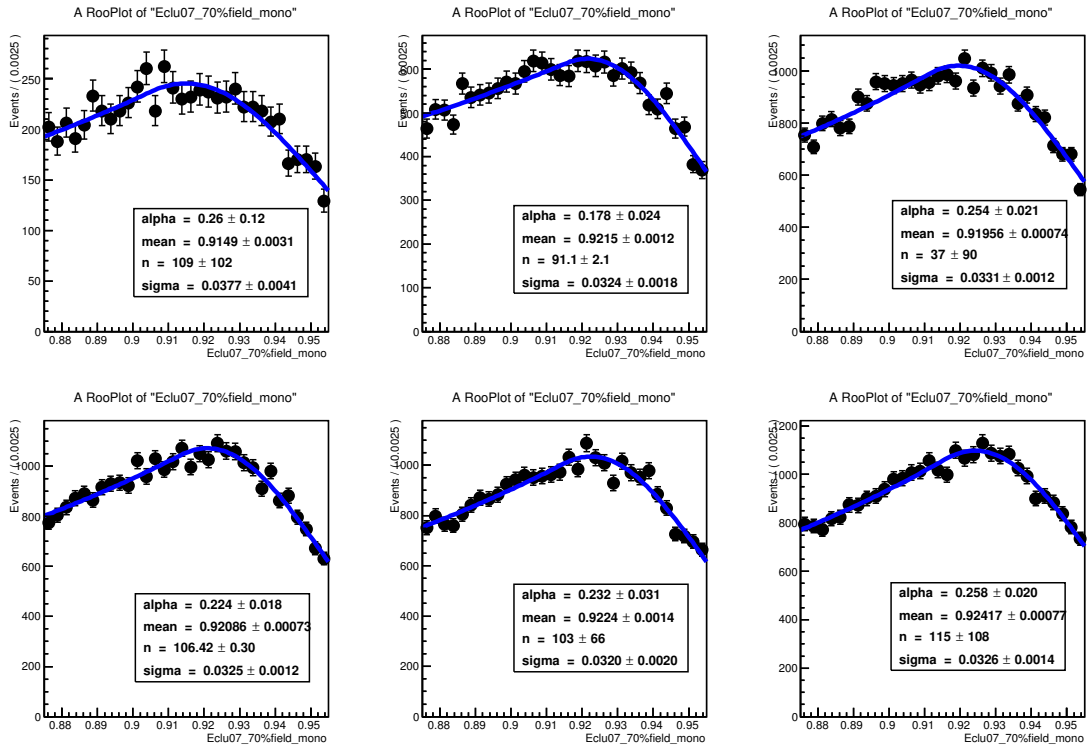

Figure 7.33: $E_{cluster}/P_{traker}$ distribution obtained at 0.7 T for the six momentum values used in the simulations, as reported in Table.

The most probable value, X_0, for $E_{cluster}/P_{traker}$ distribution is defined by the fit with the modified crystal ball function:

$$f(x;\alpha,n,X_0,\sigma_L,\sigma_R) = \frac{N}{1+0.5S_1-0.5S_2}\times\begin{cases} CB(x;\alpha,n,X_0,\sigma_L), & for\ x\ <\ X_0, \\ S_1\times\frac{1}{\sqrt{2\pi\sigma_R^2}}e^{-\frac{(x-X_0)^2}{2\sigma_R^2}} & ,for\ x\ >\ X_0\ , \end{cases} \tag{7.11}$$

where $\alpha,\ n,\ X_0,\ \sigma_L$, and σ_R are the fit parameters and N is the normalization factor. The Crystal Ball pdf [144] is denoted as as $CB()$, $S_1 = \sqrt{2\pi\sigma_R^2}\times CB(x;\alpha,n,X_0,\sigma_L)$ and $S_2 = \sqrt{2\pi\sigma_L^2}\times CB(x;\alpha,n,X_0,\sigma_L)$. Since we are mostly interested in finding the most probable value of the distribution, the fit uses only events around the peak.

In Figure 7.34, the X_0 values obtained using the modified CB fit are reported as a function of the momentum values used to generate the DIOs samples.

At the beginning of this calibration algorithm study, a full spread of about 2% was observed. The 1.5% spread (circle points) has been obtained considering the tracker

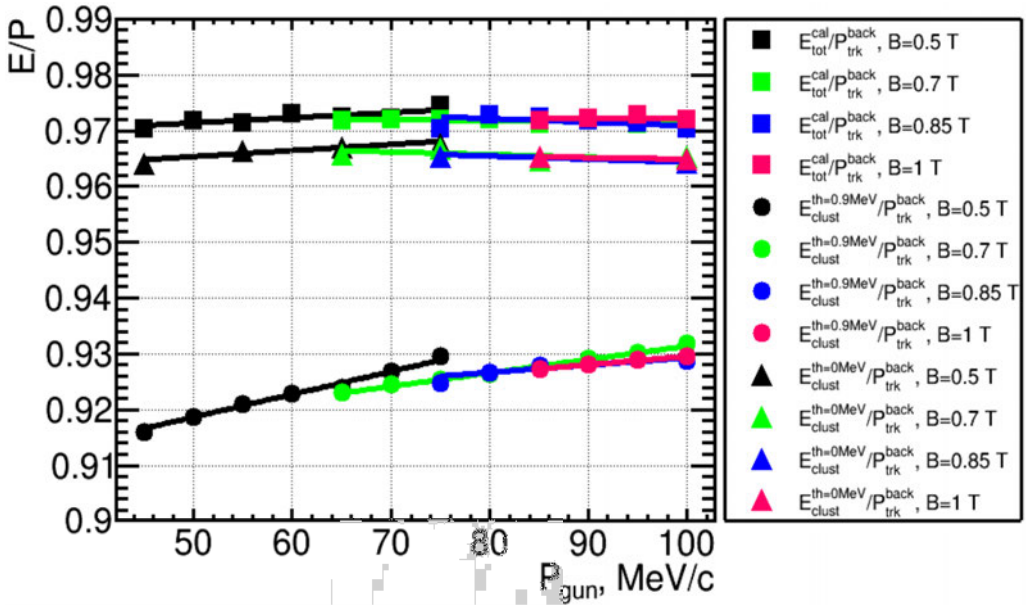

Figure 7.34: E/P distribution for three different clustering threshold as a function of the generated momentum value.

momentum at the end of the tracker, instead at the beginning. The distribution of the momentum both at front and back of the tracker is reported in Figure 7.35. A shift of about 1% is clearly visible.

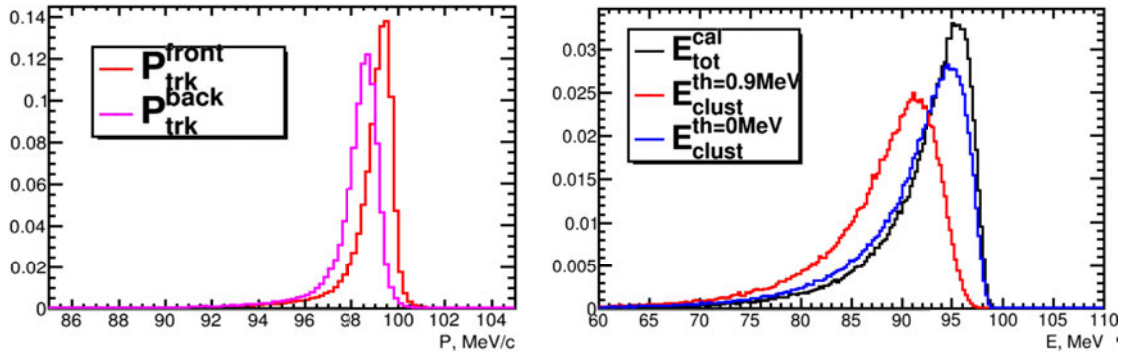

Figure 7.35: Left: distribution of the momentum at the beginning and at the end of tracker, for a generated momentum value of 100 MeV. Right: energy reconstructed by the calorimeter considering three different clustering threshold considering a generated momentum value of 100 MeV.

The clustering threshold can also affect the E/P behaviour. For the circle points distribution is 0.9 MeV. Two more configuration have been investigated (Fig. 7.35, right):

- cluster energy calculated with threshold of 0 MeV (blue distribution);
- total energy deposition in the calorimeter (black distribution);

In Figure 7.34, the X_0 values are reported also for this cases. It is clear the thresholds applied in cluster finding algorithm define the E/P versus P trend. As this effect is well modelled, the calibration extrapolation to nominal field can be done with precision of 0.2%.

Conclusions

The work of this thesis focused on the Mu2e calorimeter R&D phase and on the experimental tests needed to check that the Mu2e crystal calorimeter requirements are satisfied. The calorimetric information on time, energy and position are needed for a good Particle Identification capability and can also be used to improve the track reconstruction performance. After participating to a long R&D phase, a final down select of the calorimeter components was done: undoped CsI as scintillating crystals and a custom array of UV extended SiPMs as photosensor. A large size calorimeter prototype (Module-0) was tested with an electron beam in the energy range 60-120 MeV. This test demonstrated that the proposed detector satisfies the Mu2e requirements both for timing and energy response and resolution ($\sigma_T < 500$ ps, and $\sigma_E/E<10\%$, at 100 MeV). I contributed personally on the data analysis of the test beam data with an emphasis on timing reconstruction and determination of the timing resolution. Module-0 is now used to test all technical calorimeter functionality in vacuum and at low temperature. I am personally in charge of the data taking with cosmic rays inside the vacuum chamber. After completing the Module-0 test beam, I worked on the realization of the Quality Assurance stations for crystals and sensors and on the direct test of their quality. The calorimeter production phase started on March 2018 and the results found so far for the CsI and SiPM properties are excellent. We expect to conclude production in late spring 2019, in order to complete the detector assembly for middle 2020.

During commissioning and then physics running, an accurate equalization and calibration of all calorimeter channels will be needed in order to obtain the expected timing and energy performance. Two calibration algorithms exploiting the main experimental source of backgrounds have been developed and discussed in this thesis:

(i) The cosmic rays based calibration will provide an energy equalization using the specific energy loss (∼21 MeV) in the calorimeter cells, with an estimated precision of ∼1.5%. Moreover cosmic muons tracks will be used to align the time offsets between channels. This can be performed with an expected accuracy (estimated with the RMS) lower than 90 ps, which is an acceptable value with respect to the achievable time resolution. (ii) Electrons coming from muons decay in orbit (DIO) in the Stopping Target can provide an additional calorimeter calibration source. The energy calibration procedure is based on the comparison between the DIO electron cluster energies, E, and the electron track momenta measured in the tracker, P. At the nominal 1 T magnetic field, this method has to deal with a very strong radial dependence of the occupancy and therefore with a low statistics at higher radii. To provide a more uniform coverage and high statistical samples, the magnetic field should be reduced from 1 T to 0.5 T, during dedicated calibration runs. A Monte Carlo study demonstrated that a calibration accuracy of about ∼0.3% is achievable at 0.5 T. At least two additional runs at reduced magnetic fields need to be done in order to extrapolate the E/P calibration up to 1 T. As the behaviour of E/P versus the magnetic field and electron momentum is well modelled, a high-statistics set of datasets can provide a calibration accuracy of ∼0.2%.

Bibliography

[1] L. Bartoszek et al., *Mu2e Technical Design Report*, [physics.ins-det] (2014) [arXiv:1501.05241]

[2] G. Altarelli, *The Standard Model of Particle Physics* (2005) [arXiv:hep-ph/0510281]

[3] L. Calibbi and G. Signorelli, *Charged Lepton Flavour Violation: an Experimental and Theoretical Introduction*, Riv.Nuovo Cim. 41 (2018) no.2, 1 (2018-02) [DOI:10.1393/ncr/i2018-10144-0, arXiv:1709.00294]

[4] ATLAS collaboration home page, `http://atlas.ch`.

[5] CMS collaboration, *Observation of a new boson at a mass of 125 GeV with the CMS experiment at the LHC*, Phys. Lett. B, Vol 716, Issue 1, Pag. 30-61 (arXiv:1207.7235) - 2012.

[6] G. Aad et al. [ATLAS Collaboration], *Observation of a new particle in the search for the Standard Model Higgs boson with the ATLAS detector at the LHC*, Phys. Lett. B, Vol. 716, 1, Pag. 1-29 (2012) [arXiv:1207.7214]

[7] Super-Kamiokande Collaboration, Y. Fukuda et al, *Evidence for oscillation of atmospheric neutrinos*, Phys. Rev. Lett. 81, 1562 (1998) [arXiv:hep-ex/9807003]

[8] J.N. Bahcall, M.C. Gonzalez-Garcia and C. Peña-Garay, *Global analysis of solar neutrino oscillations including SNO CC measurement*, Journal of High Energy Physics, Volume 2001, JHEP08

[9] Z. Maki, M. Nakagawa and S. Sakata, *Remarks on the unified model of elementary particles*,Prog. Theor. Phys. 28 (1962) 870

[10] Olive K. A. et al. Review of Particle Physics. Chin. Phys. C38, 090001 (2014)

[11] Marciano W. J., Mori T. and Roney J. M., *Charged Lepton Flavor Violation Experiments*, Annual Review of Nuclear and Particle Science 58, 315-341 (2008)

[12] A.M. Baldini et al., *Search for the lepton flavour violating decay* $\mu^+ \to e^+\gamma$ *with the full dataset of the MEG experiment*, Eur. Phys. J. C, 76 (2016) 434

[13] U. Bellgardt et al., *Search for the decay* $\pi^+ \to e^+e^+e$, Nuclear Physics B 299, 1-6 (1998) ISSN: 0550-3213

[14] A. Van der Schaaf et al., NOON03 Conference Proceedings (2003)

[15] W. Bertl et al., *A search for* $\mu \to e$ *conversion in muonic gold*, EPJ C, 47(2):337:346 - 2006.

[16] B. Aubert et al., *Searches for Lepton Flavor Violation in the Decays* $\tau^\pm \to e^\pm\gamma$ *and* $\tau^\pm \to \mu^\pm\gamma$, Phys. Rev. Lett. 104 (2010) 021802

[17] K. Hayasaka et al., *Search for lepton-flavor-violating* τ *decays into three leptons with 719 million produced pairs*, Physics Letters B 687 (2010) 139 -143, ISSN: 0370-2693

[18] P. Krolak et al., *A limit on the lepton-family number violating process* $\pi^0 \to \pi^\pm e^\mp$, Physics Letters B 320 (1994) 407-410, ISSN:0370-2693

[19] D. Ambrose et al., *New Limit on Muon and Electron Lepton Number Violation from* $K_L^0 \to \mu^\pm e^\mp$ *Decay*, Phys. Rev. Lett. 81 (1998) 5734-5737

[20] A.M. Lee et al., *Improved limit on the branching ratio of* $K^+ \to \pi^+\mu^+e^-$, Phys. Rev. Lett. 64 (1990) 165-168

[21] L. Bellantoni, *Recent results from KTeV*, 36^{th} Rencontres de Moriond on Electroweak Interactions and Unified Theories, Les Arcs, France (2001) [arXiv: hep-ex/0107045]

[22] R. Akers et al., *A search for lepton flavour violating Z0 decays*, English. Zeitschrift fur Physik C Particles and Fields 67 (1995) 555-563, ISSN:0170-9739

[23] P. Abreu et al., *Search for lepton flavor number violating Z0 decays*, Z. Phys. C73 (1997) 243-251

[24] A. de Gouvea and P. Vogel, *Lepton Flavor and Number Conservation, and Physics Beyond the Standard Model*, Progress in Particle and Nuclear Physics, Vol 71 (2013) pag. 75-92 [arXiv:1303.4097]

[25] Fermilab, Proton Improvement Plan-II (PIP-II), `https://pip2.fnal.gov` - 2015.

[26] Yoshitaka Kuno and Yasuhiro Okada, *Muon decay and physics beyond the standard model*, Rev. Mod. Phys. 73, (2001) p.151

[27] R. N. Mohapatra, *Seesaw Mechanism and Its Implications*, (2004) [arXiv:hep-ph/0412379]

[28] L. Calibbi et al., *Status of supersymmetric type-I seesaw in SO(10) inspired models* JHEP, 1211:040 - 2012.

[29] E. P. Hincks and B. Pontecorvo, *Search for Gamma-Radiation in the 2.2-Microsecond Meson Decay Process*, Phys. Rev. 73 (1948) 257

[30] J. Adam et al., *New constraint on the existence of the $\mu \to e\gamma$ decay*, Phys. Rev. Lett., 110:201801 - 2013.

[31] A.M. Baldini et al., *MEG Upgrade Proposal*, Paul Scherrer Institute Research Committee - 2013.

[32] MEG collaboration, J.Adam et al., *New Constraint on the Existence of the $\mu \to e\gamma$ Decay*, Phys. Rev. Lett., 110:201801 - 2013.

[33] R. Harnik, J. Kopp, and J. Zupan, *Flavor Violating Higgs Decays*, JHEP, 1303:026 - 2013.

[34] J.Hubisz and P. Meade, *Phenomenology of the Littlest Higgs with T-Parity*, Phys.Rev. D71 (2005) 035016 [DOI: 10.1103/PhysRevD.71.035016, arXiv:hep-ph/0411264]

[35] M. Blanke et al., *FCNC Processes in the Littlest Higgs Model with T-Parity: a 2009 Look*, Acta Phys. Polon., B41:657:683 - 2010.

[36] R.N. Mohapatra et al., *Theory of Neutrinos: A White Paper*, Rept.Prog.Phys.70 (2007) 1757-1867 [DOI:10.1088/0034-4885/70/11/R02, arXiv:hep-ph/0510213]

[37] J. M. Arnold, B. Fornal, and M. B. Wise, *Phenomenology of scalar lepto-quarks*, Phys. Rev., D88:035009 - 2013.

[38] P.S. Bhupal Dev, C.H. Lee and R. N. Mohapatra, *Natural TeV-Scale Left-Right Seesaw for Neutrinos and Experimental Tests*, Phys. Rev., D88(093010) - 2013

[39] U. Bellgardt et al., *Search for the decay* $\pi^+ \to e^+e^+e^-$, Nuclear Physics B 299, (1998), 1-6. ISSN: 0550-3213

[40] N. Berger for the Mu3e collaboration, *The Mu3e experiment*, Nuclear Physics B Proceedings Supplement 00 16 - 2013.

[41] SINDRUM II Collaboration (Bertl, Wilhelm H. et al.), *A Search for muon to electron conversion in muonic gold*, Eur. Phys. J. C47 337-346 - 2006.

[42] A. Czarnecki, X. Garcia i Tormo and W. J. Marciano, *Muon decay in orbit spectra for* $\mu - e$ *conversion experiments*, Hyperfine Interact, 210 19 - 2012.

[43] S. Ahmad et al., *Searches for muon-electron and muon-positron conversion in titanium*, Phys. Rev. Lett. 59 (1987) 970

[44] A. Czarnecki, X. G. Tormo and W. J. Marciano, *Muon decay in orbit: spectrum of high-energy electrons*, Phys. Rev. D84 013006 - 2011.

[45] A. Czarnecki, M. Dowling et al., *Michel decay spectrum for a muon bound to a nucleus*, Phys. Rev. D 90, 093002 (arXiv:1406.3575) - 2014.

[46] P.Derwent, *Accelerators for Intensity Frontier Research*, Conf.Proc. C1205201 (2012) 4185-4189

[47] `http://muon-g-2.fnal.gov`

[48] R.M. Djilkibaev and V.M. Lobashev, *The solenoid muon capture system for the MELC experiment*, AIP Conference Proceedings 372, 53 (1996) [doi:10.1063/1.50918]

[49] IPAC, Proc. 2nd International Particle Accelerator Conference, IPAC 2011, San Sebastian, Spain - 2011.

[50] Y. Hine et al.*A Highly intense DC muon source, MuSIC and muon CLFV search* Nuclear Physics B - Proceedings Supplements 253-255. The Twelfth International Workshop on Tau-Lepton Physics (TAU2012), 206-207 (2014) [ISSN: 0920-5632]

[51] P. Fabbricatore et al., *Mu2e Transport Solenoid Prototype Design and Manufacturing* IEEE Transactions on Applied Superconductivity Vol. 26 (2016) Issue 4 [DOI:10.1109/TASC.2016.2527502]

[52] AlCap collaboration, http://muon.npl.washington.edu/exp/AlCap

[53] M.J. Lee on behalf of the Mu2e collaboration, *The Straw-tube Tracker for the Mu2e Experiment*, Nuclear and Particle Physics Proceedings Vol. 273-275 (2016) Pag. 2530-2532 [DOI:10.1016/j.nuclphysbps.2015.09.448]

[54] G. Pezzullo, *The Mu2e Tracker*, submitted to PoS, ICHEP 2018

[55] R.C. Group and Y. Oksuzian, *Design considerations for the cosmic-ray-veto system of the Mu2e experiment at Fermilab*, Instrumentation and Detectors (hep-ex) Report number: FERMILAB-CONF-13-591-E [arXiv:1310.1377]

[56] A. Artikov et al., *Photoelectron Yields of Scintillation Counters with Embedded Wavelength-Shifting Fibers Read Out With Silicon Photomultipliers*, NIM A 890, 85-95 (2018) [DOI:10.1016/j.nima.2018.02.023, arXiv:arXiv:1709.06587]

[57] R.Donghia, *Performance studies for the electromagnetic calorimeter of the Mu2e experiment at Fermilab*, Master Thesis (2015)

[58] O.Atanova et al., *Measurement of the energy and time resolution of a undoped CsI + MPPC array for the Mu2e experiment*, JINST 12 (2017) no.05, P05007 [DOI:10.1088/1748-0221/12/05/P05007, arXiv:1702.03720]

[59] N. Atanov et al., *Measurement of time resolution of the Mu2e LYSO calorimeter prototype*, NIM A 812 (2016) 104-111 [DOI: 10.1016/j.nima.2015.12.055, arXiv:1509.04468]

[60] N. Atanov et al., *Design and status of the Mu2e electromagnetic calorimeter*, NIM A 824 (2015), ISSN:0168-9002

[61] L. Bartoszek et al., *Mu2e Conceptual Design Report* physics.ins-det (2012) [arXiv: 1211.7019]

[62] R. Donghia on behalf of the Mu2e calorimeter group, *Design, R&D and status of the crystal calorimeter for the Mu2e experiment*, YRW 2016, Frascati Physics Series, Vol. LXIII, pag. 37 (2016) [arXiv:1607.01301]

[63] R. Donghia on behalf of the Mu2e calorimeter group, *Performance study of single undoped CsI crystals for the Mu2e experiment*, Nuovo Cimento 39 C 276 (2016) [arXiv:1602.02983, DOI: 10.1393/ncc/i2016-16276-y]

[64] R. Donghia on behalf of the Mu2e calorimeter group, *Performance study of single undoped CsI crystals for the Mu2e experiment*, Nuovo Cimento 39 C 276 (2016) [arXiv:1602.02983, DOI: 10.1393/ncc/i2016-16276-y]

[65] R. Donghia et al., *Longitudinal uniformity, time performance and irradiation test of pure CsI crystals*, NIM A824, 678-680, ISSN 0168-9002 (2015) [arxiv:1606.07110, DOI: 10.1016/j.nima.2015.11.042]

[66] S.H. Byun, *Radioisotopes and Radiation Methodology - Scintillation Detectors*, Med Phys 4R06/6R03 lectures (2017)

[67] Saint Gobain web page, `www.crystals.saint-gobain.com`

[68] Hamamatsu PMT R2059 datasheet, `www.hamamatsu.com/resources/pdf/etd/R1828-01_R2059_TPMH1259E.pdf`

[69] V. Saveliev, `Advancesinopticalandphotonicdevices`, InTech (2010)

[70] Hamamatsu, *TSV MPPC array*, production flyer 2015.05 KSX-I50080-E-S13361-3050xx-04

[71] N. Yahlali et al., *Imaging with SiPMs in noble-gas detectors*, physics.ins-det (2012) [arXiv: 1501. 05241]

[72] S. Di Falco et al., *Components Qualification for a Possible use in the Mu2e Calorimeter Waveform Digitizers*, JINST 12 (2017) no.03, C03088 [DOI:10.1088/1748-0221/12/03/C03088, arXiv:1710.01981]

[73] K. Terada and T. Okano, *Conductance modulation method for the measurement of the pumping speed and outgassing rate of pumps in ultrahigh vacuum*, Journal of Vacuum Science & Technology A 7 (1998) 2397 [doi.org/10.1116/1.575907]

[74] G. Pezzullo et al., *Progress status for the Mu2e calorimeter system*, Journal of Physics: Conference Series 587, 012047 (2015)

[75] S. Agostinelli et al., *Geant4-a simulation toolkit*, NIM A 506, 250 303 (2003) ISSN: 0168-9002

[76] C. Leroy and P.G. Rancoita, *Particle interaction and displacement damage in silicon devices operated in radiation environments*, Reports on Progress in Physics 70, (2007) 493

[77] Y. Qiang et al., *Radiation hardness tests of SiPMs for the JLab Hall D Barrel calorimeter*, NIM A 698, 234 241 (2013) ISSN: 0168-9002

[78] R. Ehrlich, *Update on the cosmic background simulation*-doc-4184 - 2014.

[79] F. Cervelli et al., *Study of the DIO rate for a calorimeter based trigger*, Mu2e-doc-3456-v1 - 2013

[80] P. Murat, *Particle Identification with the Mu2e Detector and Rejection of the Cosmics-Induced Background*, Mu2e-doc-2992 - 2013

[81] S. Di Falco et al., *Mu2e standalone calorimeter trigger studies*, Mu2e-doc-12272 - 2017

[82] D. Brown, *Tracker Selection Cut-set C* Mu2e-doc-3996-v3 - 2014

[83] R.-Y. Zhu, *Radiation damage in scintillating crystals*, Nucl. Inst. And Meth. A413 297-311 - 1998

[84] S. Nikzad et al., *Delta-doped electron-multiplied CCD with absolute quantum efficiency over 50% in the near to far ultraviolet range for single photon counting applications*, Appl. Opt., 51:365:369 - 2012

[85] Gordon Gilmore, *Practical Gamma-ray Spectroscopy*, Wiley editor - 2008

[86] C.M.Hawkes et al., *Decay time and Light Yield measurements for plastic scintillating fibers*, NIM A 292 (1990) 329-336

[87] G. Pezzullo and B. Echenard, *Study of the radiation dose and neutron flux on the calorimeter*, Mu2e-doc-2853

[88] Hamamatsu, *TSV MPPC array*, production flyer 2015.05 KSX-I50080-E-S13361-3050xx-04

[89] Advanced RISC Machines, `http://foldoc.org/Advanced%20RISC%20Machines` - 1997

[90] I. Sarra, R. Donghia et al., LNF Mu2e calorimeter group, *The backup option - CsI+MPPC: Tests, measurements and plans*, Mu2e Document 5701-v6 - 2015.

[91] S. Baccaro, A. Cecilia and A. Pasquali, γ *irradiation facility at ENEA-Casaccia Centre, Roma*, ENEA Report RT/2005/28/FIS - 2005.

[92] M. Martone. M. Angelone and M. Pillon, *The 14 MeV Frascati neutron Generator*, Journal of Nuclear Materials 212-215 (1994) 1662-1664.

[93] R.Y. Zhu, *Radiation damage in scintillating crystals*, NIM A Vol. 413 (1998) Issues 2-3 [DOI:10.1016/S0168-9002(98)00498-7]

[94] Z.Y. Wei and R.Y. Zhu, *A study on undoped CsI crystals*, NIM A 326 (1993) 508

[95] G.Pezzullo et al., *Status report on dose estimates and future plan*, Mu2e-doc-18417 - 2018

[96] R.Y. Zhu, *Crystals: optical, scintillation properties and radiation hardness*, Mu2e-doc-5699 - 2015

[97] J.O.Gichaba, *Measurements of TYVEK Reflective Properties for the Pierre Auger Project*, The University of Mississipi, 1998

[98] Filar optoMaterials s.r.l., `http://www.filaroptomaterials.com` - 2015

[99] Institute for Scintillation Materials, `http://www.isma.kharkov.ua/eng/` - 2015

[100] M.Cordelli, R.Donghia et al., *Irradiation tests with ionization dose and neutrons for undoped CsI and BaF_2 crystals*, Mu2e-doc-5800 - 2015.

[101] B.Buonomo, G.Mazzitelli and P.Valente, *Performance and Upgrade of the DAFNE Beam Test Facility (BTF)*, Nuclear Physics B - Proceedings Supplements, 150:362-365 - 2006

[102] O. Atanova et al., *Experimental test of an undoped CsI+MPPC calorimeter prototype with electron beam in the energy range 80 to 140 MeV*, Mu2e-doc-5816-v1

[103] A. Hoecker et al., *TMVA-Toolkit for multivariate data analysis*, (2007) [arXiv: physics/0703039]

[104] M. Cordelli et al., *Measurement of the slow component for undoped CsI crystals*, Mu2e internal note DocDB 6813

[105] Z.Y. Wei and R.Y. Zhu, *A study on undoped CsI crystals*, NIM A 326 (1993) 508-512

[106] S. Baccaro et al., *Radiation hardness test of un-doped CsI crystals and Silicon Photomultipliers for the Mu2e calorimeter*, CALOR 2016, J.Phys Conf. Ser. 928, conference 1, (2016) 928 012041 [arxiv:1606.07255, DOI: 10.1088/1742-6596/928/1/012041]

[107] A. Sperduti et al., *Results of the first user program on the Homogenous Thermal Neutron Source HOTNES (ENEA / INFN)*, JINST 12 (2017) P12029 [arXiv: 1802.08132, DOI 10.1088/1748-0221/12/12/P12029]

[108] Labview official page`http://www.ni.com/it-it/shop/labview.html`

[109] Julabo Chiller datasheet, https://www.julabo.com/it/prodotti/ricircolatori-di-raffre

[110] Model 6485 Picoammeter - Model 6487 Picoammeter/ Voltage Source User's Manual, 6487-900-01 Rev. B (2003), www.keythley.com

[111] Arduino official webpage, https://store.arduino.cc/usa/arduino-mega-2560-rev3

[112] 6zi-oscilloscopes datasheet, Lecroy, http://teledynelecroy.com/oscilloscope/waverunner-

[113] F. Nagy et al., *A model based DC analysis of SiPM break-down voltages*, NIM A 849 (2017) [DOI: 10.1016/j.nima.2017.01.002, arXiv:1606.07805]

[114] C. Grupen and B. Shwartz, *Particle detectors*, Cambridge university press (2008).

[115] V. Chmill et al., *On the characterisation of SiPMs from pulse-height spectra*, NIM A 854 (2017) 70-81 [DOI:10.1016/j.nima.2017.02.049, arXiv:1609.01181]

[116] A. Nagai et al., *SENSE: photon detection efficiency and optical crosstalk of various SiPM devices* (2017) [arXiv:1712.03703]

[117] L.Gruber et al., *Recovery Time Measurements of Silicon Photomultipliers Using a Pulsed Laser*, PoS (EPS-HEP2015) 234 (2016) [DOI: 10.22323/1.234.0249, arXiv:1510.06906]

[118] http://www.enea.it/it/laboratori-impianti/schede-laboratori/CALLIOPE.pdf

[119] https://www.hzdr.de/db/Cms?pNid=0

[120] https://www.hzdr.de/db/Cms?pNid=3225

[121] http://www.fluka.org/fluka.php

[122] Datasheet: https://literature.cdn.keysight.com/litweb/pdf/34972-90010.pdf

[123] N. Atanov et al., *Quality Assurance on Un-Doped CsI Crystals for the Mu2e Experiment*, IEEE Trans. Nucl. Sci. 65 (2017) 752-757 [DOI: 10.1109/TNS.2017.278608, arXiv:1802.08247]

[124] M. Cordelli et al., *Pre-Production and Quality Assurance of the Mu2e Calorimeter Silicon Photomultipliers*, submitted to NIM A (2017), [doi:10.1016/j.nima.2017.12.039, arXiv:1712.04749]

[125] `http://www.lnf.infn.it/acceleratori/btf/`

[126] `http://www.matweb.com/search/GetMatlsByTradename.aspx?navletter=z&tn=ZEDEX`

[127] L. Lucchesi Master Thesis, *Design, thermal analysis and validation test of the Mu2e electromagnetic calorimeter cooling system at Fermilab*, 2017 [http://www.infn.it/thesis/PDF/getfile.php?filename=11776–.pdf]

[128] Acrylonitrile styrene acrylate, `https://plastics.ulprospector.com/generics/8/acrylonit`

[129] `https://www.masterbond.com/tds/ep21tdcanht`

[130] B. Buonomo et al., *THE FRASCATI LINAC BEAM-TEST FACILITY (BTF) PERFORMANCE AND UPGRADES*, Proceedings of IBIC2016, TUPG29

[131] `https://medipix.web.cern.ch`

[132] `https://www.psi.ch/drs/`

[133] `http://www.caen.it/csite/CaenProd.jsp?idmod=450&parent=15#`

[134] `https://root.cern.ch`

[135] `https://geant4.web.cern.ch`

[136] K.A. Olive et al., Review of Particle Physics. Chin. Phys. C38 (2014) 090001

[137] M. Guan et al., *A parametrization of the cosmic-ray muon flux at sea-level* Chinese Physics C (2015) [arXiv:1509.06176]

[138] T. K. Gaisser and T. Stanev, Cosmic Rays, Phys. Lett. B 592 (2004) 1

[139] M. Guan et al., *Muon simulation at the Daya Bay site*, Lawrence Berkeley National Laboratory Paper LBNL-4262E http://escholarship.org/uc/item/6jm8g76d (2011)

[140] P. Shukla and S. Sankrith, *Energy and angular distributions of atmospheric muons at the Earth*, (2016) [arXiv:1606.06907]

[141] Y. Kubota et al. (CLEO), NIM A 320 (1992)

[142] M.N. Achasov et al., *Energy calibration of the NaI(Tl) calorimeter of the SND detector using e+e- -> e+e- events*, NIM A 411 (1998) 337-342

[143] P. Murat et al., *Calorimeter energy calibration with DIO electrons at B=0.5 T*, Mu2e internal note DocDB:15600 v1 (2018)

[144] https://en.wikipedia.org/wiki/Crystal Ball function

Appendix A

7.3 CAEN V1742 boards synchronisation

As already explained, the 32-channels WF digitizer boards used have a DRS4 based technology. A fan-in Fan out Module is used to make two copies of the trigger signal, one per board. When the board receives the trigger input, this NIM signal is automatically copied 4 times, one per DRS4 chip, by the digitizer itself. In addition each DRS4 chip samples and acquires also the input trigger signal. An example of an acquired NIM trigger signal is reported in FIgure 7.36.

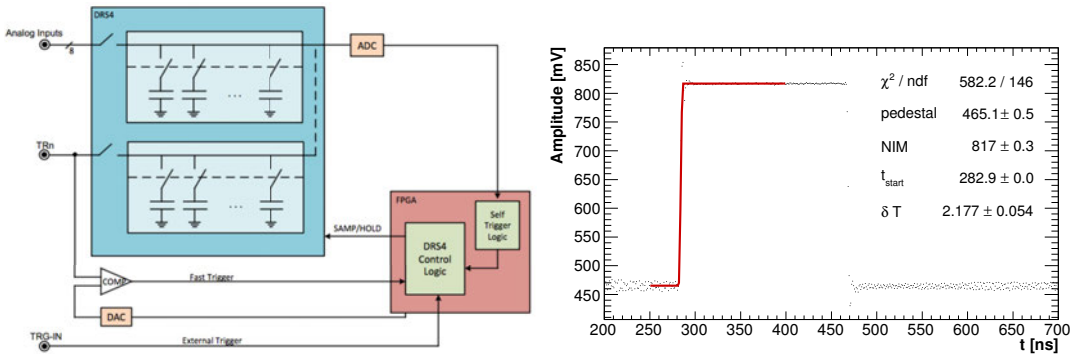

Figure 7.36: Left: Trigger scheme of the DRS4 chip used in the V1742 CAEN digitizer board. Right: NIM trigger signal digitized at 1 GHz sampling rate. The red line represents the fit used to evaluate the signal time.

This trigger signal can be used to synchronise the analog signals. The following function is used to fit the trigger waveform and extrapolate the time, t_{TRG}, at 10%

above the pedestal:

$$fit(t) = \begin{cases} pedestal & \text{if } t < t_{start} \\ pol1 & \text{if } t_{start} < t < t_{start} + \delta t \\ (3n+1)/2 & \text{if } t > t_{start} + \delta t \end{cases} . \tag{7.12}$$

In Figure 7.37, the trigger time distribution of the first chip of the first board is shown (top left). This channel has been chosen as reference. The other distributions report the time differences between the trigger time of the other 7 channels with the reference one. The top plots are related to the DRS4 chips of the first board and the bottom ones refers to the the second board's chips. Non-costant time offsets are observed between chips, making difficult to understand the contributions, in particular for the second board.

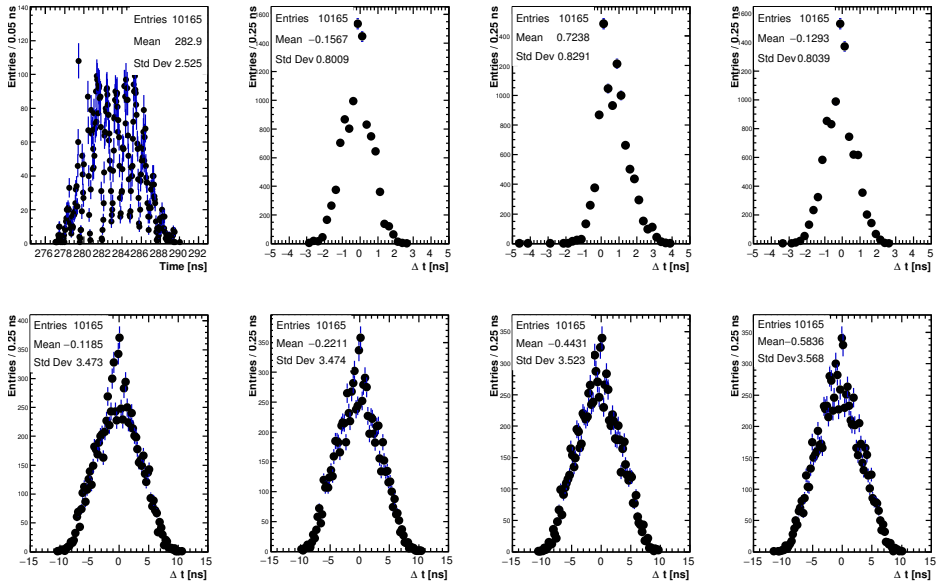

Figure 7.37: Top left: time distribution of the trigger signal of the first chip of the first digitizer board, which is the reference signal. The other distributions on top (bottom) are the time differences between the trigger time of the other DRS4 chips of the first (second) board and the reference.

The correction on trigger time is needed to evaluate the time differences among channels read out by different chips. An example is the time difference between the small counters and the central channel SiPMs, as reported in Figure 7.38. On left,

the time difference before trigger correction is shown, where $t_{crystal}$ is the average time between the two Hamamatsu SiPM of the central channel and t_{beam} is the counters average time. A time offset of about 24 ns is observed, in addition to a huge jitter.

On right the same distribution after correction is reported. The times are now evaluated as:

- $t^*_{crystal} = (t_{SiPM-L} - t_{TRG-1-0} + t_{SiPM-R} - t_{TRG-1-0}) / 2$;
- $t^*_{beam} = (t_{counter1} - t_{TRG-2-4} + t_{counter2} - t_{TRG-2-4}) / 2$;

where $t_{SiPM-L/R}$ are the times of the two SiPMs coupled with the central crystal (on left and right respectively), extracted with the CF procedure, $t_{TRG-1-0/TRG-2-4}$ are the times of the trigger signals in input to digitizer board-1 DRS4-0 and digitizer board-2 DRS4-4 respectively, $t_{counter1/2}$ are the two fingers time.

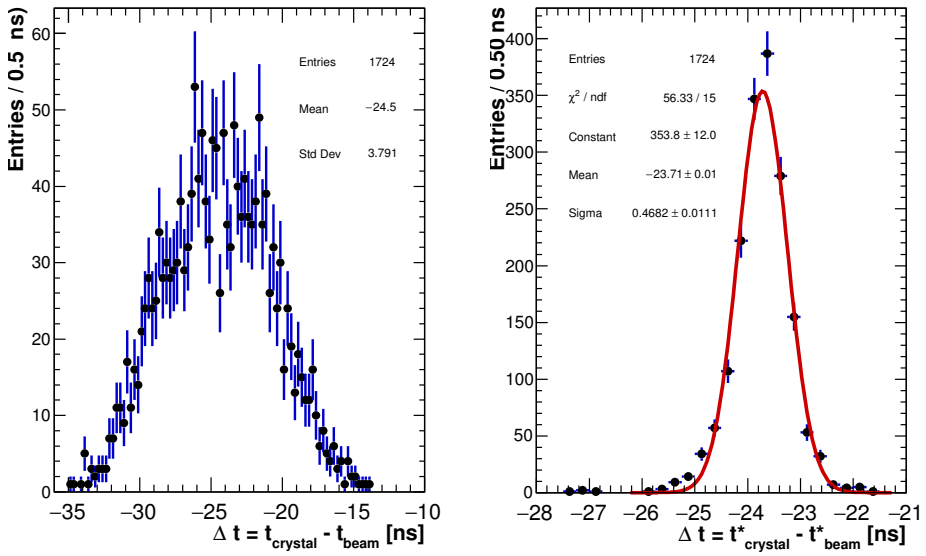

Figure 7.38

The jitter is $\sim$ 468 ps when subtracting the trigger time. This value should be the quadratic sum of the fingers jitter, crystal resolution and DRS4 chips jitter convoluted with the slewing effect. We measured a time jitter between the counters of about 100 ps, in agreement with the 2015 test beam results [58] where the

same scintillators where used. Considering the resolution of the central channel of 132 ps, the jitter between the DRS4 chips, of two different digitizer boards, results of about 435 ps. A slewing study has been also performed, but no reconstructed time dependance to the signals charge has been observed.

7.4 Tilted runs

Another case in which the trigger correction is needed is the study of the time propagation among neighbouring crystals, when the beam impinges the Module-0 front face at 50° degrees-

Figure 7.39 shows the energy deposit for the 100 MeV energy beam. One of the two crystals with the highest energy deposit is read out by just one AdvanSiD SiPM, for convenience we refer to this as crystal A. The other channel, crystal B, is read out by two SensL SiPMs. The results is already discussed and shown in Figure 6.25, the time resolution obtained is $\sim$ 230 ps.

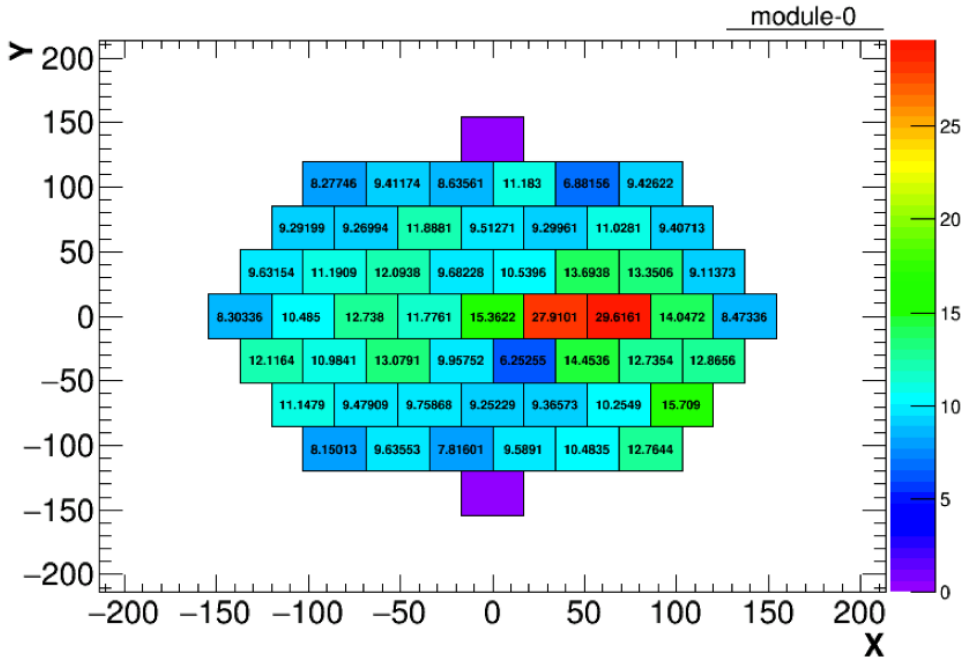

Figure 7.39: Module-0 energy map when a 100 MeV electron beam impinges at 50 degrees.

We evaluated the time resolution just for the events in which there is a similar

energy deposition in the two crystals, requiring an energy ratio in the [0.8,1.2] range.

Figure 7.40 shows the time differences between the two crystals before and after the trigger time correction, on left and right respectively.

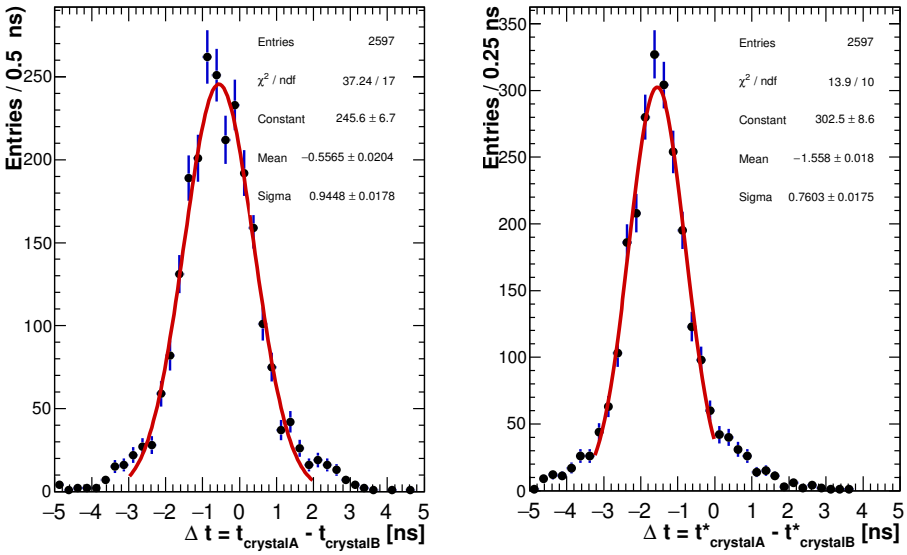

Figure 7.40: Time difference between crystal A and B before (after) trigger time correction on left (right).

The resolution is estimated as $\sigma/\sqrt{(3/2)}$ and it is $\sim$ 620 ps. In this value there are contributions both due to the DRS4 trigger jitter and to the shower propagation time.

In Figure 7.41 the timing resolution as a function of the deposited energy in the crystal with the highest deposit is reported.

In conclusion, the huge jitter introduced by the CAEN WF digitizer boards made the neighbouring crystals time resolution evaluation impossible, because this jitter is more than 2 times larger the the single channel resolution.

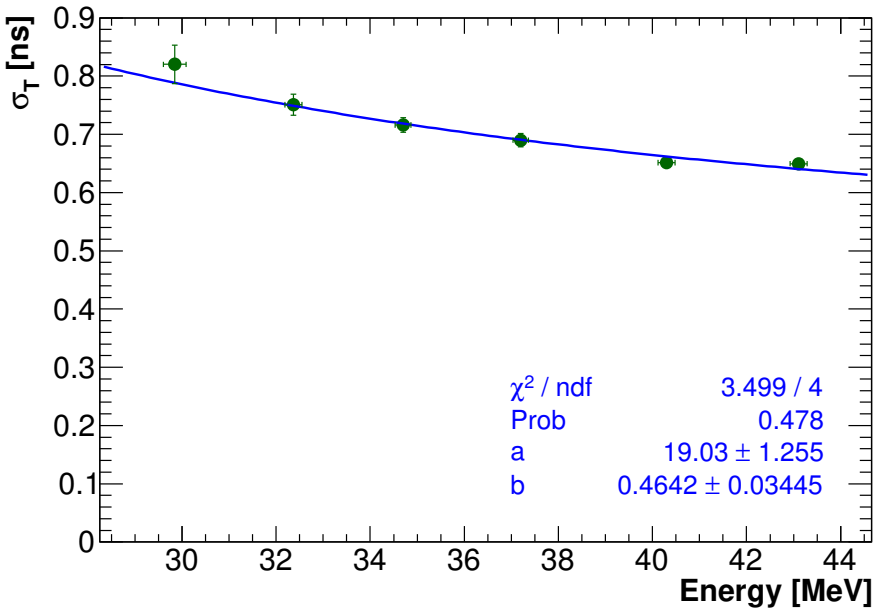

Figure 7.41: Time resolution as a function of the deposited energy obtained for the most energetic neighbouring crystals when the beam impinges at 50 degrees the Module-0.